Exploring X-ray photon-counting scintillation detectors with silicon photomultiplier readout for medical imaging

van der Sar, S.J.

DOI
10.4233/uuid:370aa87c-3055-4b2d-9e9e-ca74f2fab2e4

Publication date
2023

Document Version
Final published version

Citation (APA)
van der Sar, S. J. (2023). *Exploring X-ray photon-counting scintillation detectors with silicon photomultiplier readout for medical imaging*. [Dissertation (TU Delft), Delft University of Technology]. https://doi.org/10.4233/uuid:370aa87c-3055-4b2d-9e9e-ca74f2fab2e4

Important note
To cite this publication, please use the final published version (if applicable).
Please check the document version above.

Exploring X-ray photon-counting scintillation detectors with silicon photomultiplier readout for medical imaging

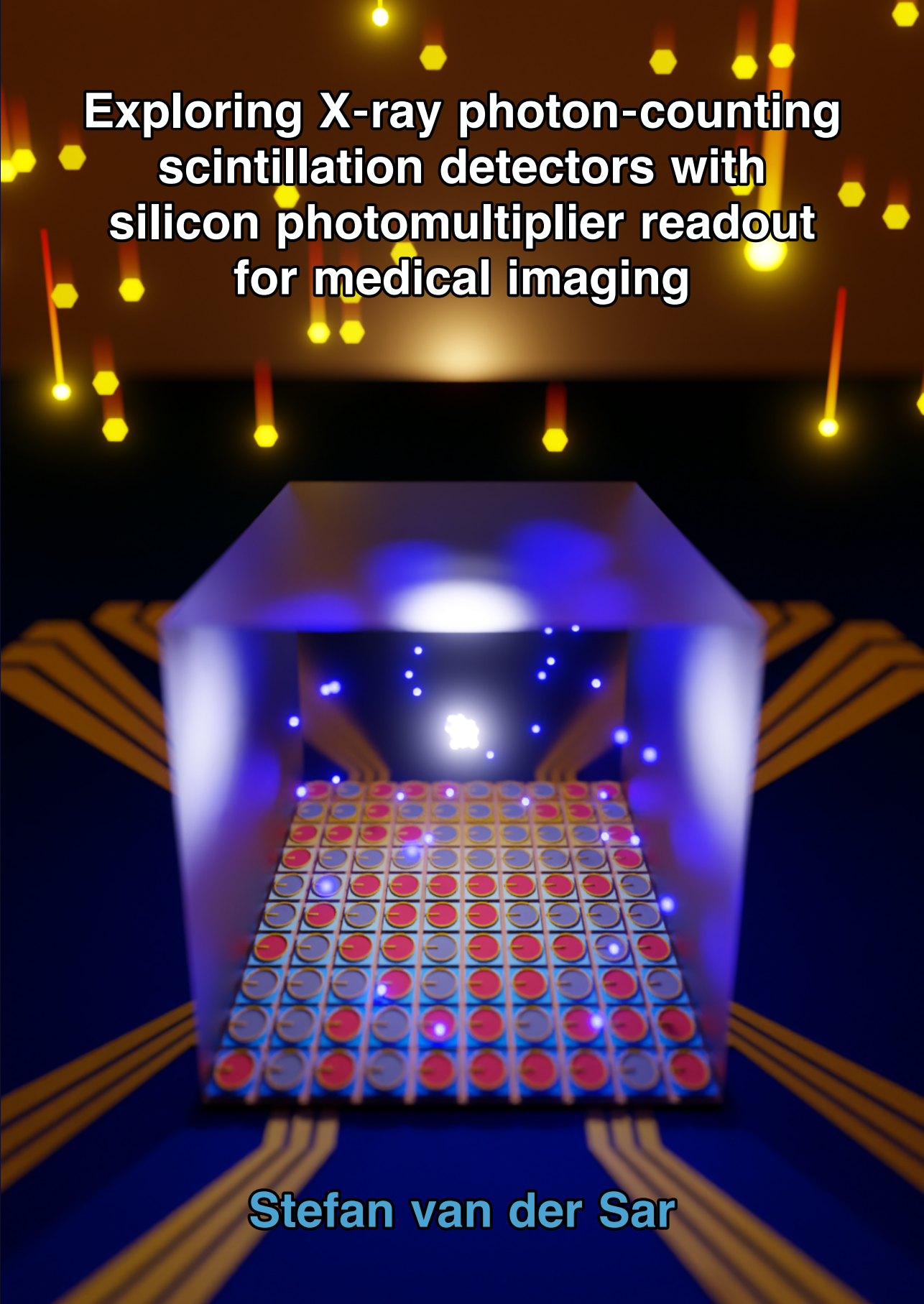

Stefan van der Sar

Exploring X-ray photon-counting scintillation detectors with silicon photomultiplier readout for medical imaging

Exploring X-ray photon-counting scintillation detectors with silicon photomultiplier readout for medical imaging

Proefschrift

ter verkrijging van de graad van doctor
aan de Technische Universiteit Delft,
op gezag van de Rector Magnificus, prof. dr. ir. T.H.J.J. van der Hagen,
voorzitter van het College voor Promoties,
in het openbaar te verdedigen op
donderdag 12 oktober 2023 om 15:00 uur

door

Stefan Jens VAN DER SAR

Master of Science in Applied Physics,
Technische Universiteit Delft, Nederland,
geboren te Rotterdam, Nederland.

Dit proefschrift is goedgekeurd door de promotoren.

De promotiecommissie bestaat uit:

Rector Magnificus	voorzitter
Prof. dr. P. Dorenbos	Technische Universiteit Delft, promotor
Dr. ir. D.R. Schaart	Technische Universiteit Delft, promotor
Dr. ir. M.C. Goorden	Technische Universiteit Delft, copromotor
Onafhankelijke leden:	
Em. prof. dr. ir. P. Kruit	Technische Universiteit Delft
Prof. dr. ir. H.W.A.M. de Jong	Universitair Medisch Centrum Utrecht
Prof. dr. K. Taguchi	Johns Hopkins University School of Medicine
Dr. V.O. Ouspenski	Saint Gobain Recherche
Prof. dr. ir. W.A. Serdijn	Technische Universiteit Delft, reservelid

The research described in this thesis was conducted in the Medical Physics and Technology section, department of Radiation Science and Technology, faculty of Applied Sciences, Delft University of Technology, Delft, the Netherlands. The work described in this thesis has been supported by Broadcom Inc. (in-cash and in-kind) and Luxium Solutions (in-kind, formerly Saint Gobain Crystals).

Printed by Proefschriftspecialist in Zaandam, the Netherlands.

Cover design by David Leibold.
An artistic impression of a single-pixel (front cover) and a multi-pixel (back cover) silicon photomultiplier-based scintillation detector exposed to X-ray photons.

ISBN: 978-94-6384-485-7

An electronic version of this thesis is available at: https://repository.tudelft.nl

Delft, Zuid-Holland, 26 juni 2022. Warm, bewolkt weer.
Ik stop mijn spullen in mijn tas en fiets haastig naar het lab.
Vanaf terrasjes kijken toeristen en inwoners toe. Niet-wetenschappers.
De leegheid van die levens schokt me.

Een bewerking van de openingszinnen van
de roman De Renner (Tim Krabbé, 1978).

Table of contents

Summary

Photon-counting detectors (PCD) for medical X-ray computed tomography (CT) are designed to measure the number of X-ray photons incident on a detector pixel as well as the energy of the individual X-rays. They are expected to yield improvements in image quality for a given radiation dose, and to offer opportunities for spectral imaging beyond dual-energy techniques. However, the fluence rate incident on the detector can exceed 10^8 mm^{-2} s^{-1} in CT, so that the detector pulses generated by the X-rays likely pile up on each other, which distorts the measurement. The semiconductors CdTe and $Cd_{1-x}Zn_xTe$ (CZT, $x \approx 0.1$-0.2) are commonly considered efficient X-ray absorbers that provide sufficient rate capability (fast pulses in the order of 10^1 ns and a high pixel density ≥ 4 mm^{-2}) and energy resolution (8-20% FWHM at 60 keV). In such detectors, an X-ray is converted into electron-hole pairs, which travel to (pixelated) electrodes, on which they induce a current pulse. However, the cost-effective synthesis of material of sufficient quality to make this a stable and reliable detection process appears to remain an issue. Thus, the aim of this thesis is to explore the photon-counting performance, e.g., the rate capability and energy resolution, of an alternative detector concept based on a scintillator, which converts an X-ray into a light pulse, and a silicon photomultiplier (SiPM), which detects the light. Since such a detector relies on light rather than charge transport, it may enable cost-effective manufacturing of stable and reliable PCDs.

Firstly, a pulse shape model that calculates the best achievable pulse duration and associated rate capability as well as the best achievable energy resolution, as a function of pixel size and scintillator and SiPM characteristics, is developed and experimentally validated in Chap. 2. The model is run for the readily available scintillators $LaBr_3$:Ce, $LuAlO_3$:Ce (LuAP:Ce), $Lu_{1.8}Y_{0.2}SiO_5$:Ce (LYSO:Ce) and $YAlO_3$:Ce (YAP:Ce), coupled to either a standard or an ultrafast SiPM. The results indicate that $LaBr_3$:Ce and LuAP:Ce, both coupled to the ultrafast SiPM, can provide pulse durations in the same order of magnitude as CdTe/CZT, and that $LaBr_3$:Ce and YAP:Ce can yield energy resolutions comparable to the semiconductors. Importantly, the model shows that the saturation of the ultrafast SiPMs is sufficiently low to prevent performance degradation for pixel sizes $\leq 0.5 \times 0.5$ mm^2, which help to increase the count rate capability per mm^2.

In practical detectors with a count detection threshold, pulse trains must often be filtered to ensure accurate counting. This makes it hard to obtain the best rate capability and energy resolution at the same time. Therefore, Chap. 3 concerns experiments into the effect of 2nd-order low-pass filters with cut-off frequencies f_c of 5, 10, and 20 MHz on the performance at 60 keV (Am-241) of 1×1 mm^2 single-pixel detectors consisting of LYSO:Ce and YAP:Ce coupled to the ultrafast SiPMs, as a function of input count rate (ICR). As expected, $f_c = 20$ MHz yields the best counting performance. The spectral

performance is also optimal for f_c = 20 MHz as soon as the ICR exceeds only a few Mcps/pixel, due to less pile-up for a higher f_c at a given ICR. This is quantified by the proposed *spectral degradation factor*, which is a better measure of spectral performance in the presence of pile-up than the FWHM energy resolution. The highest ICR obtained in these experiments is only 4.6 Mcps/pixel, but it is shown that this is nevertheless a relevant ICR, because it is about the peak ICR in cone-beam CT for radiotherapy.

The above-mentioned LYSO:Ce and YAP:Ce detectors as well as a 1×1 mm^2 single-pixel $LaBr_3$:Ce detector, all with an as a high as possible f_c, are characterized for use in medical photon-counting systems in Chap. 4. This means that the low-rate FWHM energy resolution at 60 keV, the proportionality of the energy response in the 14-122 keV range, and the output count rate (OCR) as a function of the ICR generated by a 120 kVp X-ray tube are measured. Only the $LaBr_3$:Ce detector comes close to CdTe/CZT detectors optimized for photon-counting CT. An energy resolution of about 20% FWHM at 60 keV is measured, comparable to at least one such CdTe detector, and the energy response is very proportional. Moreover, paralyzable-like counting with a 30 keV count detection threshold yields a peak OCR of 10.5 Mcps/pixel, while the OCR approaches an asymptotic value of 22 Mcps/pixel for nonparalyzable-like counting. The corresponding values for CdTe/CZT are 13 and 28-29 Mcps/pixel, respectively.

Not only pulse duration/rate capability and energy resolution, but also inter-pixel X-ray crosstalk affects detector performance. Crosstalk refers to the absorption of secondary X-rays in other pixels than the one in which the primary X-ray interacted. It is studied by means of Monte-Carlo simulations in Chap. 5 for the earlier-mentioned X-ray absorbers, a detection threshold of 25 keV, and fixed pixel sizes (1×1 mm^2) as well as absorber-specific ones (≤0.5×0.5 mm^2). The latter are expected to yield similar rate capability per mm^2. Counting performance is quantified by the zero-frequency detective quantum efficiency DQE(0). YAP:Ce has the best DQE(0), even when it has smaller pixels than CZT and $LaBr_3$:Ce, because crosstalk counts due to its 15 keV K X-rays are rejected by the 25 keV threshold. However, this does not prevent spectral degradation as quantified by the full-energy peak fraction, and CZT is best in this respect. $LaBr_3$:Ce in general performs slightly worse than CZT, and Lu-based materials considerably worse.

This research implies that the performance of YAP:Ce and Lu-based, e.g., LYSO:Ce, detectors with SiPM readout does not approach that of CdTe/CZT detectors for photon-counting diagnostic CT. These detectors are more useful for less demanding modalities, e.g., cone-beam CT in radiotherapy, for which building 1×1 mm^2 pixel arrays is a good way to move forward with this detector concept. While YAP:Ce is expected to perform better, LYSO:Ce is more mature (being widely used in positron emission tomography detectors). The SiPM-based $LaBr_3$:Ce detector performance approaches that of high-end CdTe/CZT detectors. Thus, it can be a viable detector for photon-counting diagnostic CT, provided that pixels smaller than 0.5×0.5 mm^2 with a high dose efficiency can be made. Laser-induced optical barriers are promising in this respect. Given the small gap between the $LaBr_3$:Ce and semiconductor detectors, the further development of faster scintillators that outperform CdTe/CZT in terms of rate capability appears warranted.

Samenvatting

Photon-counting detectoren (PCD) voor medische röntgencomputertomografie (CT) zijn ontworpen om het aantal röntgenfotonen te meten dat op een detectorpixel valt, evenals de energie van de individuele röntgenstralen. Verwacht wordt dat ze verbeteringen in beeldkwaliteit opleveren voor een gegeven stralingsdosis, en spectrale beeldvorming mogelijk maken die verder gaat dan de huidige dual-energy techniek. Het fluentietempo dat op de detector valt, kan echter hoger zijn dan 10^8 mm^{-2} s^{-1}, zodat de kans aanzienlijk is dat de detectorpulsen die door de röntgenfotonen worden gegenereerd, overlappen. Dit verstoort de meting. De halfgeleiders CdTe en $Cd_{1-x}Zn_xTe$ (CZT, $x \approx 0.1$-0.2) worden algemeen beschouwd als materialen die röntgenstraling efficiënt absorberen en die voldoende teltempo-capaciteit (snelle pulsen in de orde van 10^1 ns en een hoge pixeldichtheid ≥ 4 mm^{-2}) en energieresolutie (8-20% FWHM bij 60 keV) bieden voor CT. In dergelijke detectoren wordt een röntgenfoton omgezet in elektron-gat paren die aangetrokken worden door (uit pixels bestaande) elektroden waarop ze een stroompuls induceren. De kosteneffectieve synthese van materiaal van voldoende kwaliteit om dit tot een stabiel en betrouwbaar detectieproces te maken, lijkt echter een probleem te blijven. Het doel van dit proefschrift is dan ook om de prestaties, zoals de teltempo-capaciteit en de energieresolutie, van een alternatief detectorconcept gebaseerd op een scintillator, die een röntgenstraal omzet in een lichtpuls, en een silicium photomultiplier (SiPM), die het licht detecteert, te onderzoeken. Aangezien een dergelijke detector gebaseerd is op lichttransport in plaats van ladingstransport, kan het de kosteneffectieve productie van stabiele en betrouwbare PCD's mogelijk maken.

Als eerste wordt er in Hoofdstuk 2 een model voor de te verwachten pulsen ontwikkeld en experimenteel gevalideerd. Het model wordt toegepast op de thans verkrijgbare scintillatoren $LaBr_3$:Ce, $LuAlO_3$:Ce (LuAP:Ce), $Lu_{1.8}Y_{0.2}SiO_5$:Ce (LYSO:Ce) en $YAlO_3$:Ce (YAP:Ce), alle gekoppeld aan een standaard of een ultrasnelle SiPM. De resultaten geven aan dat $LaBr_3$:Ce en LuAP:Ce, beide gekoppeld aan de ultrasnelle SiPM's, een duur van de puls kunnen geven die in dezelfde orde van grootte is als die van CdTe en CZT, en dat $LaBr_3$:Ce en YAP:Ce energieresoluties kunnen bieden die vergelijkbaar zijn met die van de halfgeleiders. Belangrijk is dat het model laat zien dat de verzadiging van de ultrasnelle SiPM's laag genoeg is om prestatieverlies te voorkomen in het geval van pixelgroottes $\leq 0.5 \times 0.5$ mm^2, die nodig zijn om de teltempo-capaciteit per mm^2 voldoende te verhogen voor CT.

In de praktijk moeten detectorpulsen worden gefilterd om hen nauwkeurig te kunnen tellen op basis van het overschrijden van een detectiedrempelwaarde. Dit maakt het moeilijk om tegelijkertijd de beste teltempo-capaciteit en energieresolutie te verkrijgen.

Daarom betreft Hoofdstuk 3 experimenten over het effect van tweede orde laagdoorlaatfilters met cut-off frequenties f_c van 5, 10 en 20 MHz op de prestaties bij 60 keV (Am-241) van 1×1 mm^2 single-pixel detectoren bestaande uit LYSO:Ce en YAP:Ce, beide gekoppeld aan de ultrasnelle SiPM's, als functie van de input count rate (ICR). Zoals verwacht geeft f_c = 20 MHz de beste telprestaties. De spectrale prestaties zijn ook optimaal in het geval van f_c = 20 MHz al zodra de ICR boven een paar Mcps/pixel uitkomt, vanwege minder overlappende pulsen in het geval van een hogere f_c bij een gegeven ICR. Dit wordt gekwantificeerd met de in dit proefschrift geponeerde *spectrale degradatiefactor*, die een betere maatstaf is voor de spectrale prestaties in de aanwezigheid van overlappende pulsen dan de FWHM energieresolutie. De hoogste ICR verkregen in deze experimenten is slechts 4.6 Mcps/pixel, maar er wordt aangetoond dat dit toch een relevante ICR is, omdat het overeenkomt met de maximale ICR in een toepassing als cone-beam CT voor de radiotherapie.

De bovengenoemde LYSO:Ce en YAP:Ce detectoren, alsmede een 1×1 mm^2 single-pixel $LaBr_3$:Ce detector, alle met een zo hoog mogelijke f_c, worden gekarakteriseerd voor gebruik in medische photon-counting systemen in Hoofdstuk 4. Dit betekent dat de FWHM energieresolutie bij een laag fluentietempo van 60 keV fotonen, de evenredigheid van de energierespons in het bereik van 14 tot 122 keV, en de output count rate (OCR) als functie van de ICR gegenereerd door een 120 kVp röntgenbuis worden gemeten. Alleen de $LaBr_3$:Ce detector komt in de buurt van CdTe en CZT detectoren die zijn geoptimaliseerd voor photon-counting CT. Er wordt een energieresolutie van ongeveer 20% FWHM bij 60 keV gemeten, vergelijkbaar met ten minste één zo'n CdTe detector, en de energierespons is zeer proportioneel. Bovendien levert op een paralyseerbare manier tellen met een detectiedrempel van 30 keV een maximale OCR op van 10.5 Mcps/pixel, terwijl de OCR een asymptoot van 22 Mcps/pixel benadert bij een niet-paralyseerbare manier van tellen. De corresponderende waarden voor CdTe/CZT zijn respectievelijk 13 en 28-29 Mcps/pixel.

Naast teltempo-capaciteit en energieresolutie beïnvloedt ook overspraak tussen pixels de prestaties van de detector. Overspraak verwijst naar de absorptie van secundaire röntgenfotonen in andere pixels dan die waarin het primaire röntgenfoton een interactie had. Dit wordt bestudeerd middels Monte Carlo simulaties in Hoofdstuk 5 voor de eerder genoemde detectormaterialen, een detectiedrempel van 25 keV, en zowel vaste (1×1 mm^2) als materiaal-specifieke (≤0.5×0.5 mm^2) pixelgroottes. Van de laatste wordt verwacht dat ze een vergelijkbare teltempo-capaciteit per mm^2 opleveren. De telprestaties worden gekwantificeerd middels de zero-frequency detective quantum efficiency DQE(0). YAP:Ce heeft de beste DQE(0), zelfs als het kleinere pixels heeft dan CZT en $LaBr_3$:Ce, omdat overspraak via zijn 15 keV karakteristieke röntgenstralen niet meegeteld wordt vanwege de detectiedrempel van 25 keV. Dit voorkomt echter geen spectrale degradatie zoals gekwantificeerd door de fotopiekfractie, zodat CZT in dit opzicht het beste materiaal is. $LaBr_3$:Ce presteert over het algemeen iets slechter dan CZT, terwijl op Lu gebaseerde materialen aanzienlijk slechter presteren.

Dit promotieonderzoek impliceert dat de prestaties van YAP:Ce en op Lu gebaseerde, zoals LYSO:Ce, detectoren met SiPM uitlezing niet in de buurt komen van die van CdTe/CZT detectoren ontwikkeld voor diagnostische photon-counting CT. Deze detectoren zijn geschikter voor minder veeleisende modaliteiten. Een voorbeeld hiervan is cone-beam CT in de radiotherapie, waarvoor het bouwen van arrays bestaande uit 1×1 mm^2 pixels een goede manier is om verder te gaan met dit detectorconcept. Terwijl YAP:Ce naar verwachting beter zal presteren, is LYSO:Ce al verder ontwikkeld (het wordt namelijk veel gebruikt in positronemissietomografiedetectoren). De prestaties van een op SiPM's gebaseerde $LaBr_3$:Ce detector benaderen wel die van de CdTe/CZT-detectoren. Dit kan dus een goede alternatieve detector zijn voor diagnostische photon-counting CT, op voorwaarde dat er pixels kleiner dan 0.5×0.5 mm^2 met een hoge dosisefficiëntie kunnen worden gemaakt. Laser-geïnduceerde optische barrières zijn in dit opzicht veelbelovend. Gezien het kleine verschil tussen de $LaBr_3$:Ce detector en de halfgeleiderdetectoren is de verdere ontwikkeling van snellere scintillatoren die beter kunnen presteren dan CdTe en CZT in termen van teltempo-capaciteit gerechtvaardigd.

1 General introduction

1.1 Medical X-ray imaging

Medical imaging using X-rays comes in two flavours: projection radiography and computed tomography (CT). In both modalities, an X-ray tube on one side of the patient generates a poly-energetic X-ray beam (diagnostic energy range: 25 keV-150 keV). This beam is aimed at the patient's body. Some X-ray photons are absorbed in the body via photo-electric and Compton interactions, giving rise to a radiation dose to the patient, whereas others are not. The as-such attenuated X-ray beam is measured by a pixelated detector on the other side of the patient [1]. A schematic drawing of the imaging geometry can be found in Fig. 1.1.

An X-ray photon that is absorbed in the detector is ultimately converted into electric charges, the number of which increases with energy deposited by the X-ray photon. Together, the charges generated in a pixel form a small current pulse. Each pixel has its own read-out channel, in which all current pulses generated during the exposure time are integrated. The output signal from each pixel therefore increases with the total charge generated during the exposure time, and therefore with the total energy deposited by all X-ray photons. Because of this operating principle, the detector is called an energy-integrating detector (EID).

Dividing the detector signal measured with a patient in the beam by the signal measured without patient yields the attenuation of the X-ray beam intensity along the paths from the X-ray tube to each pixel. Such data is called projection data. In planar radiography, two-dimensional projection data are obtained, which directly constitute the image. In computed tomography, the X-ray tube and detector rotate around the patient and projection data are obtained for many angular positions. These data are fed into an image reconstruction algorithm, which generates two-dimensional slices or three-dimensional volumes of the patient [1].

Image contrast is provided by the fact that the attenuation depends on tissue type. As can be appreciated in Fig. 1.2, the so-called linear attenuation coefficients of air (e.g., the lungs), soft tissues (e.g., adipose (fatty) tissue and muscles) and bone are

Section 1.1 till 1.4 are based on S. J. van der Sar and D. R. Schaart, "Silicon Photomultiplier-Based Scintillation Detectors for Photon-Counting X-Ray Imaging," in *Radiation Detection Systems*. Boca Raton, FL, USA: CRC Press, 2021, pp. 289-312.

considerably different. Therefore, these tissue types can be clearly distinguished in an X-ray image. However, Fig. 1.2 also shows that the two soft tissues have very similar attenuation coefficients. Hence, the soft tissue contrast in an X-ray image is typically limited. In order to make certain anatomical structures in soft tissues more visible, contrast agents are often administered to patients. Examples are iodine-based contrast agents for blood vessels/perfusion, and barium-based agents for the gastrointestinal tract [1]. In this way, X-ray imaging has become a very useful and widely used medical imaging modality. However, it has not reached its full potential yet, in particular due to the use of EIDs [2].

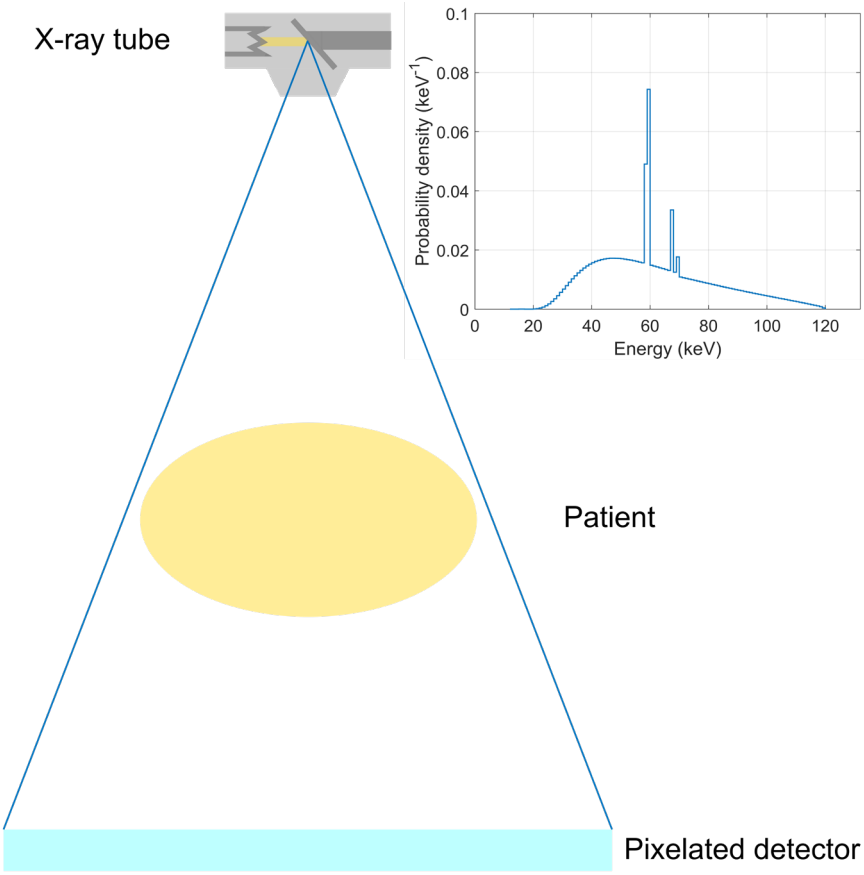

Fig. 1.1. Schematic cross-section of the imaging geometry of a medical X-ray imaging system. An X-ray tube generates a poly-energetic X-ray beam on one side of the patient. A typical X-ray spectrum is shown in the diagram. The X-ray beam is aimed at the patient, in whom tissue-dependent beam attenuation takes place. The attenuated beam is measured on the other side of the patient by a pixelated detector. In diagnostic CT, the detector is slightly curved. Furthermore, the tube and detector rotate around the patient, and measurements are done at many angular positions. The data are used to reconstruct slices or volumes of the patient.

In an EID, the higher-energy X-ray photons contribute more to the detector signal than the lower-energy X-ray photons, because they typically generate more charges and stronger current pulses. This type of energy-weighting leads to sub-optimal image contrast, because the differences in the linear attenuation coefficients of tissues and contrast agents are more pronounced at lower X-ray energies, as can be appreciated in Fig. 1.2. Moreover, any kind of energy-weighting causes the mean signal to be less than the variance of the signal, so the signal-to-noise ratio (SNR) is worse than predicted by Poisson statistics. This is quantified by the Swank factor [3]. Lastly, EIDs integrate all noise during the exposure time, which also negatively affects the SNR. As a result, the contrast-to-noise ratio (CNR), i.e., the product of image contrast and SNR, of X-ray imaging systems equipped with EIDs is sub-optimal. This implies that unnecessarily high radiation doses and/or contrast agent loads are delivered to patients in order to obtain the desired image quality. This gives rise to an increased chance of developing cancer, or allergic reactions, such as thyroid dysfunction in the case of iodine-based contrast agents [4], respectively.

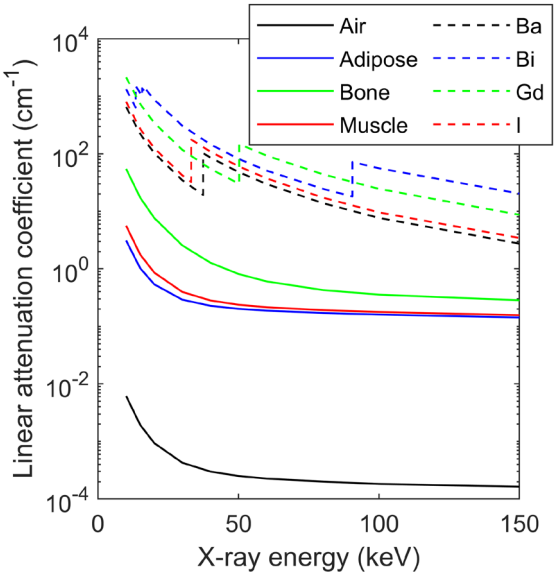

Fig. 1.2. Contrast in medical X-ray imaging is based on differences in the linear attenuation coefficients of tissues. Therefore, air (e.g., the lungs), soft tissues (e.g., adipose (fatty) tissue and muscles) and bone can be well distinguished from each other. The contrast between two soft tissues is limited, however. Therefore, contrast agents based on iodine (I) and barium (Ba) are commonly administered to enhance contrast within soft tissues. Notice that the curves for the contrast agents contain a K-edge discontinuity. Since quantitative imaging of one or more contrast agents, facilitated by photon-counting detectors, works better if this K-edge lies halfway the diagnostic energy range, new contrast agents for X-ray imaging, e.g., based on gadolinium (Gd) and bismuth (Bi), are under investigation [5]. Also note that the differences in the linear attenuation coefficients tend to increase with decreasing X-ray energy, which gives photon-counting detectors an advantage over energy-integrating detectors in terms of achievable image contrast for a given radiation dose and/or contrast agent load. Data were obtained from the NIST databases 8 and 126.

1.2 X-ray photon-counting detectors

Photon-counting detectors (PCD) measure the number of X-ray photons during the exposure time rather than the intensity of the X-ray beam. Hence, attenuation must be defined in terms of photon numbers with and without patient in the beam. The number of counts is incremented by one every time the train of detector pulses crosses a pre-defined threshold (see Fig. 1.3(a)). In this way, all X-ray photons equally contribute to the output signal, regardless of their energy. In addition, noise does not contribute to the output signal, provided that the threshold is set above the noise level. As a result, the contrast, the SNR, and the CNR of the resulting image are better than those obtained with an EID for a given radiation dose and contrast agent load. Alternatively, this can be used to reduce the radiation dose and contrast agent load without sacrificing image quality [2].

1.2.1 Spectral X-ray imaging

Since the pulse height is typically a measure of the energy deposited by an X-ray photon, implementing a second, higher threshold allows to assign the counts to either a lower-energy bin or a higher-energy bin (see Fig. 1.3(a)). In this way, it becomes possible to do dual-energy X-ray imaging with PCDs. This imaging technique already has many clinical applications with EIDs [6] However, compared to the various dual-energy systems based on EIDs described in [7], PCD-based systems offer the advantages of a simple system design, i.e., a single, conventional X-ray tube and a single detector, and a truly simultaneous acquisition of the lower-energy and the higher-energy projection data. Furthermore, the degree of spectral separation between both data sets is only limited by the spectral response function of the detector [6,7].

In dual-energy CT, a lower-energy and a higher-energy image are reconstructed and the values of the image voxels represent the local linear attenuation coefficient in these two energy ranges. Since two measurements at different energies are available, a unique decomposition of the attenuation coefficient into a photo-electric effect component and a Compton scattering component can be done [8,9]. This can be used to derive the local electron density and effective atomic number, which finds applications in treatment planning for proton radiotherapy, for example [10]. However, the linear attenuation coefficient curves of contrast agents have a K-edge discontinuity within the diagnostic energy range (see Fig. 1.2), which is not taken into account by the photo-electric and Compton components. An accurate decomposition in the presence of n contrast agents therefore requires $2+n$ components, where the n additional components represent attenuation due to each of the n contrast agents. Consequently, measurements at (at least) $2+n$ energies are required for a unique decomposition. PCDs with $2+n$ thresholds, which assign the counts to $2+n$ energy bins, offer a straightforward way to do these measurements. However, this so-called K-edge imaging technique, which allows to quantify simultaneously the concentrations of n contrast agents, works best when the X-ray spectrum has similar numbers of photons on both sides of the K-edge energies of the contrast agents [9]. Therefore, traditional contrast agents based on iodine and barium,

which have a relatively low K-edge energy, are less suited for this purpose, whereas others, such as gadolinium and bismuth (see Fig. 1.2), are increasingly considered [11].

Alternatively, the two measurements of the linear attenuation coefficient at different energies obtained in dual-energy CT can be used to decompose the attenuation coefficient into two basis material components, which represent the attenuation due to

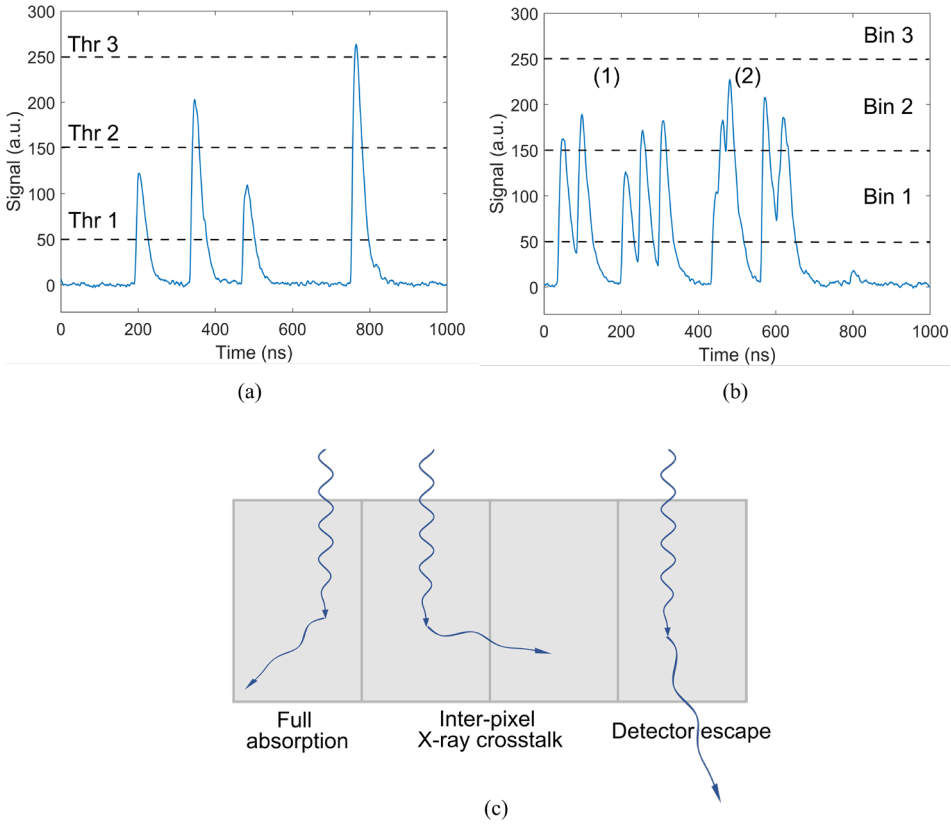

Fig. 1.3. (a) A photon-counting detector counts the number of detector pulses, by counting the number of positive threshold (thr) crossings, for example. Since the pulse height typically increases with energy deposited by an X-ray photon, implementing multiple thresholds yields energy-resolved data. (b) Under pulse pile-up conditions, (1) the pulse height measurements are distorted, and (2) some pulse do not cross the first threshold anymore, for example. This leads to incorrect numbers of counts. If binned data is generated by subtracting the number of pulses crossing threshold 1 from the number of pulses crossing threshold 2, for example, one may end up with a negative number. (c) The counting and spectral detector performance is also degraded by characteristic and Compton-scattered X-ray photons escaping the pixel in which the corresponding primary X-ray photon interacted, either to be absorbed in another pixel (inter-pixel X-ray crosstalk) or to escape the pixel array (detector escape).

these two materials [12]. This is called material decomposition and yields two material-specific images. However, if, e.g., soft tissue and a contrast agent are used as basis materials, all other materials in the patient's body will be regarded as a combination of these two materials. PCDs with *n* thresholds allow to decompose into *n* basis materials, offering more specific basis material images.

The use of two or more thresholds also allows to further improve the image contrast by giving more weight to the lower-energy X-ray photons [2]. However, weighting some photons more than others also leads to a reduction of the SNR, similar to the Swank factor mentioned in Sec. 1.1 for energy-integrating detectors [13]. Therefore, sets of weights that optimize the CNR for specific imaging tasks must be found [14].

1.2.2 Detector requirements

Despite the numerous advantages of photon-counting detectors over energy-integrating detectors, PCDs are not widely implemented in medical X-ray imaging systems (yet). An important reason is the generally high X-ray fluence rate incident on the detector. As a result, two or more X-ray photons may be detected in the same pixel with such a short period of time between them, that the resulting pulses are superimposed on each other. This is called pulse pile-up and is visualized in Fig. 1.3(b). It can lead to a pulse not being registered as a count. The higher the input rate, the more pile-up, and the more pulses not counted. For some input count rate, the output count rate saturates, which limits the maximum input rate the detector can be exposed to. Pile-up can also affect the pulse height, potentially causing a count to end up in the wrong energy bin. This reduces the spectral separation between energy bins and the material decomposition performance, for example.

So far, PCDs have mainly been considered for diagnostic CT systems, which are very demanding in terms of X-ray fluence rate incident on the detector. The maximum fluence rate for standard, clinical CT protocols was found to be about 3.5×10^8 photons/s/mm^2, provided that the patient is properly aligned [15]. However, it was also found that such high rates mainly occur in beam paths that pass just below the skin, which are not the most relevant ones from an imaging perspective. If only paths that go deeper than 1 cm below the skin are considered, the maximum fluence rate incident on the detector drops to around 2.5×10^8 photons/s/mm^2. Moreover, the 95th percentile fluence rate is about 2.0×10^8 photons/s/mm^2 in the most demanding protocol. Nevertheless, these numbers means that, even if the detector pulses last only tens of nanoseconds, the pixels must be reduced to 0.5×0.5 mm^2 or smaller, so that the incident photons are distributed over multiple pixels per mm^2 and pulse pile-up in a pixel is lowered to an acceptable level.

However, the smaller the pixel size, the more likely the escape of characteristic and Compton-scattered X-ray photons from a detector pixel. As shown in Fig. 1.3(c), these secondary X-rays can either leave the detector or be absorbed in another pixel (inter-pixel X-ray crosstalk). As a result, some primary X-rays do not give rise to a count at all, e.g., when the energy deposition in the first interaction in the detector is below the

threshold energy and the secondary X-ray escape the detector, whereas others yield more than one count in multiple pixels. The latter is called count multiplicity. It can be seen as a number weighting of X-ray photons and reduces the zero-frequency SNR [16]. It also leads to pixel-to-pixel correlations and a non-white noise power spectrum [17]. Another consequence of the escape of a secondary X-ray is an incorrect energy measurement, so the counts may end up in the wrong energy bin. In addition, inter-pixel crosstalk increases the pile-up level in a pixel for a given incident rate of X-ray photons and has a negative effect on the spatial resolution [13]. A careful analysis of this trade-off between pulse pile-up and escape of secondary X-rays must thus be done.

Other requirements on X-ray photon-counting detectors include sufficient energy resolution to assign a large fraction of the X-ray photons that are fully absorbed in a single pixel to the correct energy bin, and room temperature operation. High density of the detection material is also preferred. It allows for thin detectors, which is beneficial from a spatial resolution point-of-view, for example.

1.3 CdTe and CZT detectors

The requirements on medical X-ray PCDs such as short pulse duration and sub-mm pixels (to reduce pulse pile-up) and good energy resolution point in the direction of direct-conversion detectors in general, and those based on the semiconductors CdTe and $Cd_{1-x}Zn_xTe$ (CZT, x typically being 0.1-0.2) in particular, because they can be operated at room-temperature and offer a high density of 5.8 g cm^{-3}. See Fig. 1.4(a) for a schematic drawing of this detector concept. An X-ray photon absorbed in a CdTe/CZT detector is directly converted into approximately 200 electron-hole pairs per keV of energy deposited. Under the influence of an electric field (bias voltage 800-1000 V, detector thickness around 2 mm), the electrons and holes drift to opposite electrodes, on which they induce a current pulse. Since the electric field confines the charges to a certain region of the detector, the detection layer can be monolithic. Usually, only the anode is pixelated and read out. This allows for relatively easy fabrication of sub-mm pixels. The pulses are further processed in an application specific integrated circuit (ASIC), in which voltage pulses with a height that in general increases with deposited energy are created and counted. These pulses typically last tens of nanoseconds and FWHM energy resolution in the 10-20% range at 60 keV can be achieved [18,19].

1.3.1 Photon-counting CT systems

Recent progress in the growth of high-quality CdTe and CZT as well as in ASIC design has brought photon-counting X-ray imaging within reach [2]. Most vendors of diagnostic CT scanners have built prototype photon-counting CT systems, which are used to evaluate the benefits of PCDs in clinical practice. Overviews of the findings so far can be found in recent review papers [2,20].

For example, the first Siemens prototypes are equipped with 1.6 mm thick CdTe detectors. The anodes of these detectors consist of 0.225×0.225 mm^2 pixels, which are all connected to their own, in-house developed ASIC that has two thresholds. Pixels can also be read out in groups of 2×2 pixels (high-resolution mode) or 4×4 pixels (macro-mode). The latter yields an effective pixel size of 0.9×0.9 mm^2, comparable to the pixel size in energy-integrating CT detectors (and the pitch of the anti-scatter grid), whereas the high-resolution mode potentially allows for improved spatial resolution [2,21]. However, spatial resolution is also determined by the focal spot size of the X-ray tube, for example. Reducing the spot size usually means that the tube current has to be reduced, as well. This may limit the applicability of improved spatial resolution in CT imaging [2]. Two different sets of threshold values can be assigned to two adjacent pixels in a group of 2×2 or 4×4 pixels in order to increase the number of energy bins to four. However, this comes at the cost of some dose-efficiency [21]. In a second Siemens system with a 1.6 mm thick CdTe detector, each pixel is equipped with four thresholds, so this is not an issue anymore. The pixel size of this system is 0.151×0.176 mm^2 at the isocenter [22]. This likely corresponds to about 0.27×0.32 mm^2 at the detector level [2,23]. The system was cleared for clinical use by the FDA in 2021 [24].

Philips has built a prototype scanner based on a 2 mm thick CZT detector. The anode is divided into pixels of 0.5×0.5 mm^2, each of which is coupled to an in-house developed ASIC called ChromAIX2 with five thresholds [19]. United Imaging has also built a prototype based on a 2 mm thick CZT detector. However, this scanner has pixels of 0.334×0.334 mm^2 and six energy thresholds [25]. Canon is currently developing a prototype system based on a CZT detector, as well [26].

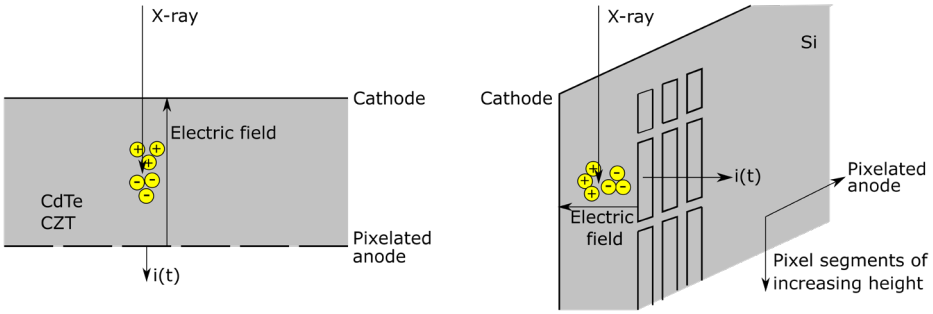

Fig. 1.4. (a) Schematic cross-section of a face-on CdTe/CZT detector with a pixelated anode. The interaction of an X-ray photon results in about 200 electron-hole pairs per keV of energy deposited, although only three are shown here. The electrons and holes drift to opposite electrodes under the influence of an externally applied electric field. The current pulse *i(t)* induced on the anodes is fed into an ASIC. (b) Schematic drawing of an edge-on silicon detector, which is being investigated as an alternative to face-on CdTe/CZT detectors. Edge-on means that the semiconductor wafer is put on its side, so that the electric field is perpendicular to the direction of the impinging X-ray photons. The pixelated anode is divided into segments of increasing height. If an X-ray photon deposits energy in a pixel, a current pulse *i(t)* will be induced in one of the pixel segments, depending on the depth-of-interaction.

1.3.2 Difficulties with CdTe/CZT detectors

Despite the above-mentioned developments, some difficulties with CdTe/CZT detectors remain.

The first one is related to the small pixel size and applies to any direct-conversion detector. The initial charge cloud resulting from an X-ray interaction in the CdTe/CZT layer has a finite size, and it grows along its way to the electrodes, due to diffusion and mutual Coulomb repulsion of the charges, despite the electric field. Consequently, a current pulse will be induced on more than one pixel, if an X-ray photon deposits (part of) its energy in the proximity of a virtual pixel border in the CdTe/CZT layer. This phenomenon is referred to as charge sharing. It leads to a broadening of the low-energy side of the full-energy peak in a spectrum of a mono-energetic source, and therefore to a degradation of the FWHM energy resolution of the detector. The other consequences of charge sharing are the same as those of X-ray crosstalk described in Sec. 1.2.2. Charge sharing becomes more important as the detector thickness increases and the pixel size decreases. Hence, not only the escape of secondary X-rays, but also charge sharing discourages further reduction of the pixel size for count rate capability reasons. It is interesting to note that Philips previously used a 3 mm thick CdTe detector with 0.3×0.3 mm^2 pixels for its prototype photon-counting CT scanner [18]. However, a 2 mm thick CZT detector with a pixel size of 0.5×0.5 mm^2 was later chosen, because of better spectral performance [19]. FWHM energy resolutions of 18% and 8% at 60 keV were reported for the 0.3×0.3 mm^2 and 0.5×0.5 mm^2 pixels, respectively.

The second difficulty also applies to any direct-conversion detector and concerns the intrinsically weak raw pulses from such a detector (~200 electron-hole pairs per keV in the case of CdTe and CZT). As a result, an elaborate read-out channel is needed, consisting of a charge-sensitive amplifier (integration and amplification), a pulse shaping circuit with pole-zero cancellation and baseline restoration circuits (as the shaper contains a differentiator), leakage current compensation, and pulse height discriminators with associated counters [19]. Ideally, there is also a direct physical interconnection between an anode pixel and its read-out channel in the ASIC and the pixel pitch and the pitch of the read-out channels are the same (hybrid pixel technology). This offers low noise and high bandwidth at a given power consumption, but the costs of the interconnection process are high for relatively small volumes [27].

Thirdly, there is the relatively low hole mobility (about ten times lower than the electron mobility) and the charge trapping in CdTe and CZT. Especially holes are likely to get trapped in defects and impurities in the CdTe/CZT layer while drifting to the cathode. Frequently-mentioned defects in literature include (sub-)grain boundary networks and Te inclusions [28,29]. Low hole mobility and charge (de)trapping affect the detector pulse characteristics. If defects are not uniformly distributed throughout the detector, the pulse characteristics will be pixel-dependent and pixel-specific calibrations will be needed. Low hole mobility and charge (de)trapping are also the reasons why a net positive charge may be present in the CdTe/CZT layer when the next X-ray photon arrives. This is called polarization. The electric field in the detector is distorted, and the

pulse characteristics are affected. Polarization becomes more severe at higher fluence rates incident on the detector, when a larger net positive charge builds up in the CdTe/CZT layer. Hence, the pulse characteristics of a pixel may depend on the irradiation history of that pixel. As a consequence, the calibrations may not hold anymore during image acquisition, which may lead to ring artifacts and less accurate material decomposition, for example [2,30]. Therefore, stable and reliable detector performance requires CdTe/CZT with a very low density of trapping centers, uniformly distributed throughout the layer. However, it remains an issue if the production of large-area detectors of such high quality is cost-effective. Furthermore, the number of manufacturers that can grow detector-grade CdTe and CZT is very limited, and acquisitions by vendors of diagnostic CT scanners have taken place. For example, Acrorad, a manufacturer of CdTe detectors, is a daughter company of Siemens [31], and Redlen Technologies, a manufacturer of CZT detectors, was acquired by Canon in 2021 [26]. These developments may limit the availability of high-quality CdTe and CZT detectors to other developers of X-ray imaging systems.

Instead of trying to improve the detection material, using Ohmic (conducting) electrode contacts instead of Schottky (blocking) contacts has also been investigated [32]. The rationale behind using Ohmic contacts is that these contacts inject electrons into the CdTe/CZT layer when there is a net positive charge, thereby combatting polarization. However, it was observed that this results in a distortion of the counting statistics that is considered unacceptable for X-ray imaging. This is because the injection of electrons leads to a baseline shift that is not constant in time, but contains high-frequency components, which can lead to crossings of the counting threshold. Using a baseline restorer does not solve the problem, because the restorer can only eliminate low-frequency changes in the baseline. Otherwise, it would also eliminate the X-ray photon-induced pulses.

Lastly, it is unclear how continuous exposure to high X-ray fluence rates affects CdTe/CZT detector performance in the long term [33], and if further improvements of the material are even possible, given the inherent, poor thermo-physical properties of CdTe and CZT near and below the melting point, which are responsible for (some of) the above-mentioned defects [28,29].

1.4 Silicon detectors

A room-temperature direct-conversion detector based on silicon has been proposed and developed by researchers from KTH Royal Institute of Technology as an alternative to CdTe/CZT detectors [34]. Si is a very mature semiconductor material, thanks to its widespread use in the electronics industry, so high-quality Si detectors, in which hole (de)trapping and polarization effects are of little concern, can be produced in a cost-effective way. Indeed, the density of trapping centers in Si must be considerably lower than in CdTe and CZT, given that the mobility-lifetime product of Si is three to four orders of magnitude better, while the mobilities are in the same order of magnitude [27].

On the other hand, the density (2.3 g cm^{-3}) and atomic number (14) of Si are rather low. This means that a few centimetres (3 – 6 cm) of material is needed to absorb enough X-ray photons in the diagnostic energy range, which may have negative consequences for the spatial resolution of the detector. The required thickness is achieved by placing Si wafers with a thickness of 0.5 mm on their sides. As shown in Fig. 1.4(b), the electrode configuration is such that the charge carriers drift perpendicular to the direction of the incident X-ray photons (edge-on geometry). In this way, charge carriers do not need to travel several centimetres through the material. The anodes are divided into multiple segments with a constant width of 0.4 mm and an exponentially increasing length along the depth direction of the pixel, ensuring that similar numbers of X-ray photons are detected in each segment. This geometry dramatically increases the count rate capability of a 0.4×0.5 mm^2 pixel. Furthermore, the smallest segment is much longer than 0.4 mm, so charge sharing is practically reduced to only one dimension. However, this geometry increases the power consumption per unit detection area to a level much higher than that of other photon-counting and conventional energy-integrating detectors [27]. Moreover, hybrid pixel detector technology cannot be used, so relatively long interconnections between anode and ASIC are needed, which further increases the power consumption. The associated additional demand for active cooling increases the operating costs [35].

The relatively low density and atomic number of Si also imply that Compton scattering is the dominant X-ray interaction mechanism in the detector. The initial energy deposition is therefore relatively small. Consequently, the lowest-energy threshold must be set lower than in CdTe/CZT detectors for dose-efficient X-ray detection. This puts heavier requirements on the noise performance of the ASIC. The escape of secondary X-rays is also more of a concern. In order to reduce it, 20 μm thick tungsten foils are placed between the wafers [34].

A prototype photon-counting CT scanner based on this technology was built in 2019 [36], and the technology was adopted by GE Healthcare in 2020 [37]. Clearly, both CdTe/CZT detectors and Si detectors have their advantages and difficulties, so it remains unclear what the best choice of detector is. Moreover, there may be X-ray imaging applications other than diagnostic CT, which are less demanding in terms of incident fluence rate, for example. This leaves room for the development of alternative detector concepts.

1.5 Thesis objective

In this thesis, silicon photomultiplier (SiPM)-based scintillation detectors are investigated as another potential alternative to CdTe/CZT detectors for medical X-ray photon-counting applications. These detectors are based on the principle of indirect conversion, i.e., energy deposited by an X-ray photon in a scintillator leads to a pulse of optical photons, which is converted into a current pulse by a light sensor (see Fig. 1.5(a)). In this work, the SiPM is the light sensor of choice. Since SiPMs are four-side

buttable, arrays of light sensors suitable for pixelated radiation detectors can be manufactured. Fig. 1.5(b) contains a picture of an array of 4×4 SiPMs to illustrate this.

A single SiPM is a two-dimensional array of single-photon avalanche diodes (SPAD) at a pitch in the order of 10^0-10^1 µm. SPADs are photodiodes biased above their breakdown voltage. Consequently, a single electron-hole pair resulting from the absorption of an optical photon is multiplied without limit. A series resistor is used to quench the discharge, and a stable gain in the order of 10^5 -10^7 is achieved. The internal gain of the SiPM raises the weak intrinsic signal from a scintillator in the order of 10^0-10^1 optical photons per keV well above the noise level of the detector, which is crucial for operation in X-ray photon-counting mode and allows for simpler pulse processing than possible with CdTe/CZT detectors (see Sec. 1.3.2). It should be noted that other light sensors with internal gain exist, e.g., avalanche photodiodes (APD) and photomultiplier tubes (PMT). However, the gain of the former strongly depends on bias voltage and temperature, requiring accurate stabilization of both, while the latter is a bulky device that cannot be miniaturized to the sub-mm level.

Both scintillators and SiPMs work well at room temperature. Furthermore, many scintillators with high density (and high effective atomic number) are readily available. Moreover, a scintillation detector relies on optical photon transport rather than charge transport, so detector performance is not degraded by polarization (and charge sharing).

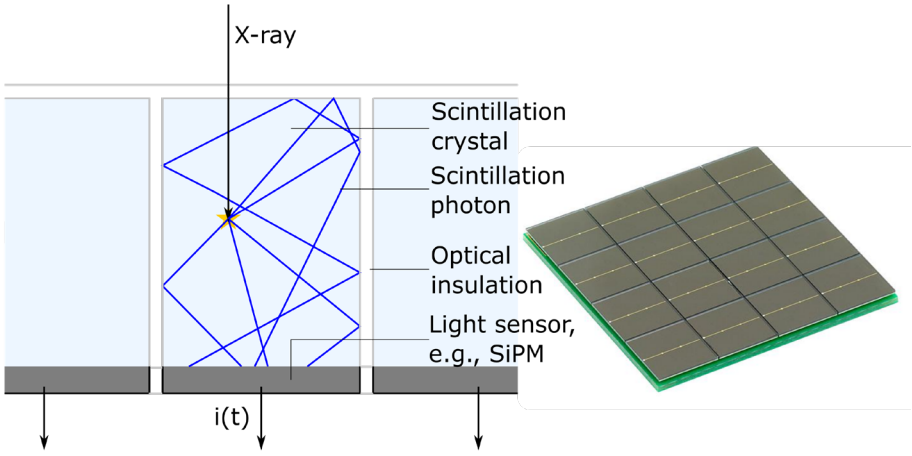

Fig. 1.5. (a) Schematic cross-section of the most common implementation of a pixelated scintillation detector: Each pixel consists of a scintillation crystal one-to-one coupled to a light sensor, such as a silicon photomultiplier (SiPM), which converts the pulse of optical photons generated by the interaction of an X-ray in the scintillator into a current pulse *i(t)*. Only 5 optical photons are shown, although typically in the order of 10^0-10^1scintillation photons are generated per keV of energy deposited. The reflective optical insulation guides the photons towards the light sensor and prevents light sharing with nearby pixels. (b) SiPMs are four-side buttable, enabling the production of two-dimensional arrays of SiPMs, such as the 4×4 array of SiPMs from Broadcom Inc. shown here. Such arrays are suitable for use in pixelated scintillation detectors.

This could make it easier to manufacture stable and reliable detectors in a cost-effective way. Such a claim is supported by the fact that most detectors used in medical imaging these days are scintillation detectors, either being operated in energy-integrating mode (X-ray imaging) or in photon-counting mode (nuclear medicine). Moreover, SiPMs have become the preferred light sensors for the positron emission tomography (PET) scanners of all major vendors.

All in all, SiPM-based scintillation detectors may combine a high density (and effective atomic number), as offered by CdTe and CZT, with cost-effective manufacturing of stable and reliable detectors, as offered by silicon. However, this particular detector concept has not been widely investigated yet. Researchers in Japan built a 1×64 array of 1×1 mm^2 pixels, based on the ceramic yttrium-gadolinium-aluminium-gallium garnet scintillator (YGAG) [38]. Ceramic scintillators surely enable cost-effective detector manufacturing, and it was shown that, despite a moderate energy resolution of 32% FWHM at 60 keV [38], it is possible to do material decomposition with images acquired with this prototype X-ray photon-counting detector under low fluence-rate conditions [39]. However, the response of the YGAG scintillator to an X-ray photon is quite slow, thereby severely limiting the count rate capability [40]. As such, the detector performance seems to be inferior to that of state-of-the-art CdTe/CZT detectors, and insufficient for photon-counting medical X-ray imaging.

The main objective of this thesis is therefore to investigate if it is feasible to obtain sufficient detector performance for medical X-ray photon-counting applications with SiPM-based scintillation detectors, with particular emphasis on count rate capability, energy resolution, inter-pixel X-ray crosstalk, and how these compare to those of state-of-the-art CdTe/CZT detectors developed and optimized for these applications.

1.6 Thesis outline

In Chap. 2, a model that allows to calculate the best achievable pulse duration (and associated count rate capability) as well as the best achievable energy resolution for any combination of scintillator and SiPM is presented and experimentally validated. Four scintillators are included in this study, namely $LaBr_3$:Ce ($LaBr_3$), $LuAlO_3$:Ce (LuAP), $(Lu_{1-x}Y_x)_2SiO_5$:Ce (L(Y)SO), and $YAlO_3$:Ce (YAP), as well as two different SiPMs. Expected pulse durations/count rate capabilities and energy resolutions are calculated as a function of pixel size and compared to those reported for CdTe and CZT detectors developed and optimized for photon-counting CT prototype scanners. The model contains a detailed description of SiPM saturation, which may increasingly degrade the energy resolution in particular as the pixel size becomes smaller. Since the smallest SiPM currently available is 1×1 mm^2, the model is useful to determine which SiPM properties are needed in order not to suffer from saturation when sub-mm SiPMs are manufactured.

Chap. 3 concerns experiments with two 1×1 mm^2 single-pixel detectors consisting of either a LYSO or YAP scintillation crystal coupled to one of the two SiPMs included in the study of Chap. 2. These detectors are exposed to a 10 GBq mono-energetic Am-241 source, which emits 60 keV photons, at various source-detector distances. In this way, output count rate and spectral detector performances are evaluated as a function of input count rate, for various simple pulse processing methods and counting modes. Another measure for spectral performance than the FWHM energy resolution is proposed here. This *spectral degradation factor* better describes spectral performance under clinically realistic pulse pile-up conditions.

The results of common characterization experiments for X-ray photon-counting detectors are presented in Chap. 4 for the LYSO and YAP detectors as well as for a third 1×1 mm^2 single-pixel detector based on the $LaBr_3$ scintillator. Only the pulse processing method from Chap. 3 optimized for counting performance is used in this chapter. Count rate curves measured at an X-ray tube facility are shown, as well as the low-rate spectra of three radioisotopes with emissions in the diagnostic energy range. The FWHM energy resolutions are derived from the Am-241 spectra. Lastly, the measured performances are compared to those of CdTe and CZT detectors developed and optimized for photon-counting CT prototype scanners.

In Chap. 5, two first-order effects of the escape of secondary X-rays from the pixel in which a primary X-ray interacted are studied by means of Monte Carlo simulations. The effect on the counting performance is quantified by the zero-frequency detective quantum efficiency, and the effect on the spectral performance by the full-energy peak fraction under uniform detector irradiation. Not only pixelated LYSO, YAP, and $LaBr_3$ detectors are simulated, but also a pixelated CZT detector, which allows for a comparison.

This thesis in concluded in Chap. 6. An overview of the most important findings is given. Furthermore, it is discussed how the results obtained in Chap. 2, 3, and 4 relate to each other, and which steps have to be taken in future research to go from simulating pixel arrays as in Chap. 5 to building pixelated detectors.

References

[1] J. L. Prince and J. M. Links, *Medical Imaging Signals and Systems*. Upper Saddle River: Pearson Prentice Hall, 2015.

[2] T. Flohr, M. Petersilka, A. Henning, S. Ulzheimer, J. Ferda, and B. Schmidt, "Photon-counting CT review," *Physica Medica,* vol. 79, pp. 126-136, 2020, doi: https://doi.org/10.1016/j.ejmp.2020.10.030.

[3] R. K. Swank, "Absorption and noise in x-ray phosphors," *Journal of Applied Physics,* vol. 44, no. 9, pp. 4199-4203, 1973, doi: https://doi.org/10.1063/1.1662918.

[4] S. Y. Lee, C. M. Rhee, A. M. Leung, L. E. Braverman, G. A. Brent, and E. N. Pearce, "A review: radiographic iodinated contrast media-induced thyroid dysfunction," *The Journal of Clinical Endocrinology & Metabolism,* vol. 100, no. 2, pp. 376-383, 2015, doi: https://doi.org/10.1210/jc.2014-3292.

[5] S. Tao, K. Rajendran, C. H. McCollough, and S. Leng, "Feasibility of multi-contrast imaging on dual-source photon counting detector (PCD) CT: An initial phantom study," *Medical physics,* vol. 46, no. 9, pp. 4105-4115, 2019, doi: https://doi.org/10.1002/mp.13668.

[6] C. H. McCollough, S. Leng, L. Yu, and J. G. Fletcher, "Dual-and multi-energy CT: principles, technical approaches, and clinical applications," *Radiology,* vol. 276, no. 3, pp. 637-653, 2015, doi: https://doi.org/10.1148/radiol.2015142631.

[7] R. Forghani, B. De Man, and R. Gupta, "Dual-energy computed tomography: physical principles, approaches to scanning, usage, and implementation: part 1," *Neuroimaging Clinics,* vol. 27, no. 3, pp. 371-384, 2017, doi: https://doi.org/10.1016/j.nic.2017.03.002.

[8] R. E. Alvarez and A. Macovski, "Energy-selective reconstructions in x-ray computerised tomography," *Physics in Medicine & Biology,* vol. 21, no. 5, p. 733, 1976, doi: https://doi.org/10.1088/0031-9155/21/5/002.

[9] E. Roessl and R. Proksa, "K-edge imaging in x-ray computed tomography using multi-bin photon counting detectors," *Physics in Medicine & Biology,* vol. 52, no. 15, p. 4679, 2007, doi: https://doi.org/10.1088/0031-9155/52/15/020.

[10] W. van Elmpt, G. Landry, M. Das, and F. Verhaegen, "Dual energy CT in radiotherapy: current applications and future outlook," *Radiotherapy and Oncology,* vol. 119, no. 1, pp. 137-144, 2016, doi: https://doi.org/10.1016/j.radonc.2016.02.026.

[11] C. Amato *et al.*, "Potential of contrast agents based on high-Z elements for contrast-enhanced photon-counting computed tomography," *Medical physics,* vol. 47, no. 12, pp. 6179-6190, 2020, doi: https://doi.org/10.1002/mp.14519.

[12] J. Wang, X. Duan, and C. H. McCollough, "Material Decomposition and Post-processing: History and Basic Principles," in *Spectral Imaging*: Springer, 2022, pp. 3-14, doi: https://doi.org/10.1007/978-3-030-96285-2_1.

[13] M. Danielsson, M. Persson, and M. Sjölin, "Photon-counting x-ray detectors for CT," *Physics in Medicine & Biology,* vol. 66, no. 3, p. 03TR01, 2021, doi: https://doi.org/10.1088/1361-6560/abc5a5.

[14] T. G. Schmidt, "Optimal “image-based” weighting for energy-resolved CT," *Medical physics,* vol. 36, no. 7, pp. 3018-3027, 2009, doi: https://doi.org/10.1118/1.3148535.

[15] M. Persson *et al.*, "Upper limits of the photon fluence rate on CT detectors: Case study on a commercial scanner," *Medical physics,* vol. 43, no. 7, pp. 4398-4411, 2016, doi: https://doi.org/10.1118/1.4954008.

[16] T. Michel *et al.*, "A fundamental method to determine the signal-to-noise ratio (SNR) and detective quantum efficiency (DQE) for a photon counting pixel detector," *Nuclear Instruments and Methods in Physics Research Section A: Accelerators, Spectrometers, Detectors and Associated Equipment,* vol. 568, no. 2, pp. 799-802, 2006, doi: https://doi.org/10.1016/j.nima.2006.08.115.

[17] J. Xu *et al.*, "Cascaded systems analysis of photon counting detectors," *Medical physics,* vol. 41, no. 10, p. 101907, 2014, doi: https://doi.org/10.1118/1.4894733.

[18] R. Steadman, C. Herrmann, O. Mülhens, and D. G. Maeding, "ChromAIX: Fast photon-counting ASIC for spectral computed tomography," *Nuclear Instruments and Methods in Physics Research Section A: Accelerators, Spectrometers, Detectors and Associated Equipment,* vol. 648, pp. S211-S215, 2011, doi: https://doi.org/10.1016/j.nima.2010.11.149.

[19] R. Steadman, C. Herrmann, and A. Livne, "ChromAIX2: A large area, high count-rate energy-resolving photon counting ASIC for a spectral CT prototype," *Nuclear Instruments and Methods in Physics Research Section A: Accelerators, Spectrometers, Detectors and Associated Equipment,* vol. 862, pp. 18-24, 2017, doi: https://doi.org/10.1016/j.nima.2017.05.010.

[20] A. Esquivel *et al.*, "Photon-Counting Detector CT: Key Points Radiologists Should Know," *Korean Journal of Radiology,* vol. 23, 2022, doi: https://doi.org/10.3348/kjr.2022.0377.

[21] Z. Yu *et al.*, "Evaluation of conventional imaging performance in a research whole-body CT system with a photon-counting detector array," *Physics in Medicine & Biology,* vol. 61, no. 4, p. 1572, 2016, doi: https://doi.org/10.1088/0031-9155/61/4/1572.

[22] K. Rajendran *et al.*, "First clinical photon-counting-detector CT system: Technical evaluation," *Radiology,* vol. 303, no. 1, p. 130, 2022, doi: https://doi.org/10.1148/radiol.212579.

[23] J. Ferda *et al.*, "Computed tomography with a full FOV photon-counting detector in a clinical setting, the first experience," *European Journal of Radiology,* vol. 137, p. 109614, 2021, doi: https://doi.org/10.1016/j.ejrad.2021.109614.

[24] Siemens. "Siemens Healthineers announces FDA 510(k) clearance of Naeotom Alpha, the world's first photon-counting CT." https://www.siemens-healthineers.com/press/releases/naeotomfda (accessed 17 October, 2022).

[25] T. Fan *et al.*, "Preliminary performance evaluation of a prototype whole body photon counting CT using moderate detector pixel design," presented at the 2022 IEEE Nuclear Science Symposium and Medical Imaging Conference (NSS/MIC), 2022. [Online]. Available: https://www.eventclass.org/contxt_ieee2022/scientific/online-program/session?s=M-10#e381.

[26] Canon. "Canon Inc. completes acquisition of Redlen Technologies as a wholly owned subsidiary." https://global.canon/en/news/2021/20210929.html (accessed 17 October, 2022).

[27] R. Ballabriga *et al.*, "Photon counting detectors for X-ray imaging with emphasis on CT," *IEEE Transactions on Radiation and Plasma Medical Sciences,* 2020, doi: https://doi.org/10.1109/TRPMS.2020.3002949.

[28] U. N. Roy, G. S. Camarda, Y. Cui, R. Gul, G. Yang, and R. B. James, "Charge-transport properties of as-grown $Cd_{1-x}Zn_xTe_{1-y}Se_y$ by the traveling heater method," *AIP Advances,* vol. 8, no. 12, p. 125015, 2018, doi: https://doi.org/10.1063/1.5064373.

[29] U. N. Roy *et al.*, "Role of selenium addition to CdZnTe matrix for room-temperature radiation detector applications," *Scientific reports,* vol. 9, no. 1, pp. 1-7, 2019, doi: https://doi.org/10.1038/s41598-018-38188-w.

[30] M. Sjölin and M. Danielsson, "Relative calibration of energy thresholds on multi-bin spectral x-ray detectors," *Nuclear Instruments and Methods in Physics Research Section A: Accelerators, Spectrometers, Detectors and Associated Equipment,* vol. 840, pp. 1-4, 2016, doi: https://doi.org/10.1016/J.NIMA.2016.09.045.

[31] Siemens. "About Acrorad. We continue to challenge the innovation of the radiation applications." https://www.siemens-healthineers.com/jp/acrorad-en (accessed 17 October, 2022).

[32] C. Herrmann, I. Blevis, R. Steadman, and A. Livne, "Issues of ohmic contacts in Human Medical photon-counting CT detectors," *IEEE Transactions on Radiation and Plasma Medical Sciences,* 2020, doi: https://doi.org/10.1109/TRPMS.2020.3026832.

[33] K. Taguchi and J. S. Iwanczyk, "Vision 20/20: Single photon counting x-ray detectors in medical imaging," *Medical physics,* vol. 40, no. 10, 2013, doi: https://doi.org/10.1118/1.4820371.

[34] H. Bornefalk and M. Danielsson, "Photon-counting spectral computed tomography using silicon strip detectors: a feasibility study," *Physics in Medicine & Biology,* vol. 55, no. 7, p. 1999, 2010, doi: https://doi.org/10.1088/0031-9155/55/7/014.

[35] C. Sundberg, M. U. Persson, M. Sjölin, J. J. Wikner, and M. Danielsson, "Silicon photon-counting detector for full-field CT using an ASIC with adjustable shaping time," *Journal of Medical Imaging,* vol. 7, no. 5, p. 053503, 2020, doi: https://doi.org/10.1117/1.JMI.7.5.053503.

[36] J. da Silva *et al.*, "Resolution characterization of a silicon-based, photon-counting computed tomography prototype capable of patient scanning," *Journal of Medical Imaging,* vol. 6, no. 4, p. 043502, 2019, doi: https://doi.org/10.1117/1.JMI.6.4.043502.

[37] GeneralElectric(GE). "GE Healthcare Pioneers Photon Counting CT with Prismatic Sensors Acquisition." https://www.ge.com/news/press-releases/ge-healthcare-pioneers-photon-counting-ct-with-prismatic-sensors-acquisition (accessed 17 October 2022).

[38] M. Arimoto *et al.*, "Development of LSI for a new kind of photon-counting computed tomography using multipixel photon counters," *Nuclear Instruments and Methods in Physics Research Section A: Accelerators, Spectrometers, Detectors and Associated Equipment,* vol. 912, pp. 186-190, 2018, doi: https://doi.org/10.1016/j.nima.2017.11.031.

[39] H. Kiji *et al.*, "64-channel photon-counting computed tomography using a new MPPC-CT system," *Nuclear Instruments and Methods in Physics Research Section A: Accelerators, Spectrometers, Detectors and Associated Equipment,* vol. 984, p. 164610, 2020, doi: https://doi.org/10.1016/j.nima.2020.164610.

[40] T. Maruhashi *et al.*, "Evaluation of a novel photon-counting CT system using a 16-channel MPPC array for multicolor 3-D imaging," *Nuclear Instruments and Methods in Physics Research Section A: Accelerators, Spectrometers, Detectors and Associated Equipment,* vol. 936, pp. 5-9, 2019, doi: https://doi.org/10.1016/j.nima.2018.11.018.

2 A model to investigate the feasibility of silicon photomultiplier-based scintillation detectors for photon-counting CT

Abstract

The implementation of photon-counting detectors is widely expected to be the next breakthrough in X-ray computed tomography (CT) instrumentation. A small number of prototype scanners equipped with direct-conversion detectors based on room-temperature semiconductors, such as CdTe and CdZnTe (CZT), are currently installed at medical centers. Here, we investigate the feasibility of using silicon photomultiplier (SiPM)-based scintillation detectors in photon-counting computed tomography (PCCT) scanners, as a potential alternative to CdTe and CZT detectors.

We introduce a model that allows us to compute the expected energy resolution as well as the expected pulse shape and associated rate capability of SiPM-based PCCT detectors. The model takes into account SiPM saturation and optical crosstalk, because these phenomena may substantially affect the performance of SiPM-based PCCT detectors with sub-mm pixels. We present model validation experiments using a single-pixel detector consisting of a 0.9×0.9×1.0 mm^3 LuAP:Ce scintillation crystal coupled to a 1×1 mm^2 SiPM. We subsequently use the validated model to compute the expected performance of the fast scintillators LYSO:Ce, LuAP:Ce, and $LaBr_3$:Ce, coupled to currently available SiPMs, as well as to a more advanced SiPM prototype with improved dynamic range, for sub-mm pixel sizes.

The model was found to be in good agreement with the validation experiments, both with respect to energy resolution and pulse shape. It shows how saturation progressively degrades the energy resolution of detectors equipped with currently available SiPMs as the pixel size decreases. Moreover, the expected pulse duration is relatively long (~200 ns) with these SiPMs. However, when LuAP:Ce and $LaBr_3$:Ce are coupled to the more advanced SiPM prototype, the pulse duration improves to less than 60 ns, which is in the same order of magnitude as pulses from CdTe and CZT detectors. It follows that sufficient rate capability can be achieved with pixel sizes of 400 μm or smaller. Moreover, $LaBr_3$:Ce detectors can provide an energy resolution of 11.5%-13.5% at 60 keV, comparable to CdTe and CZT detectors.

This work provides first evidence that it may be feasible to develop SiPM-based scintillation detectors for PCCT that can compete with CdTe and CZT detectors in terms of energy resolution and rate capability.

This chapter is based on S. J. van der Sar, S. E. Brunner, and D. R. Schaart, "Silicon photomultiplier-based scintillation detectors for photon-counting CT: A feasibility study," *Medical Physics,* vol. 48, no. 10, pp. 6324-6338, 2021.

2.1 Introduction

The implementation of photon-counting X-ray detectors is widely expected to be the next technological breakthrough in CT scanner development. Several vision and review papers were published in the last ten years [1,2,3,4]. These highlight the potential benefits of replacing conventional energy-integrating detectors by photon-counting detectors. For example, image quality (contrast-to-noise ratio) can be improved and/or the radiation dose and contrast agent load can be reduced. Moreover, truly simultaneous acquisition of dual-energy data with good spectral separation becomes possible. Even multi-energy data can be acquired, which opens up opportunities to perform K-edge imaging, for example. Photon-counting detectors enable such benefits by measuring the number of X-ray photons and assigning each X-ray photon to one of a finite number of energy bins. To do so accurately, detectors must be able to handle an incident X-ray photon fluence rate in the order of 10^2 Mcps/mm^2 and have sufficient energy resolution. Therefore, direct-conversion detectors with sub-mm pixels based on room-temperature semiconductors with a high density and a high effective atomic number, such as CdTe and $Cd_{1-x}Zn_xTe$ (CZT, $x \approx 0.1$-0.2), are generally considered promising for this application. Specific drawbacks of these detectors are the occurrence of charge sharing and charge trapping. The latter can lead to unstable and unreliable detector operation [1,4]. High purity materials with a very low defect concentration are required to reduce this effect. This may negatively affect the cost-effectiveness of production. Nevertheless, a small number of prototype scanners equipped with CdTe or CZT detectors have been installed at medical centers to investigate the benefits of photon-counting computed tomography (PCCT) in clinical practice. The first results were published in 2016 [5,6]. An overview of studies conducted since then can be found in a recent review paper [4].

Scintillation detectors could be an alternative to the aforementioned direct-conversion detectors. Although the latter type of detector is commonly considered most suitable for applications that require short pulse duration and good energy resolution [7], scintillation detectors are successfully employed in most commercial radiological and nuclear medicine imaging systems. Here, we aim to show that fast scintillators with state-of-the-art energy resolution, in combination with recent developments in silicon photomultiplier (SiPM) technology, may enable the application of scintillation detectors in PCCT scanners. We do so by describing the basic principles of SiPM-based scintillation detectors in Sec. 2.2. In the same section, we introduce a model that allows us to compute two fundamental properties of such detectors for PCCT, viz. the rate capability and the (low-rate) energy resolution. The model considers the raw detector pulses, in other words no particular way of pulse processing and counting is assumed. In Sec. 2.3 and 2.4, we experimentally validate the model and use it to compute the expected performance of SiPM-based scintillation detectors with sub-mm pixels for PCCT. We discuss the results and draw conclusions in Sec 2.5 and 2.6.

2.2 Theory

Scintillation detectors are also known as indirect-conversion detectors, because a scintillator first converts an X-ray photon into a tiny light pulse, which in turn is converted into a current pulse by a light sensor. Obviously, a pixelated detector is needed for CT imaging. As shown schematically in Fig. 2.1(a), this can be achieved by optically coupling an array of scintillation crystals one-to-one to an array of light sensors. Some form of optical isolation between the individual crystals is useful to guide the optical photons towards the sensor and to prevent light sharing between pixels. It is noted that conventional reflectors applied to sub-mm pixels can result in a relatively large dead area and a loss of dose efficiency (see Sec. 2.5). On the other hand, optical photons rather than charge carriers are transported in a scintillation detector, so typical issues associated with direct-conversion detectors, such as charge sharing and charge trapping, do not play a role. The escape of secondary X-rays from sub-mm pixels may occur in both types of detector (also see Sec. 2.5).

Various types of light sensor are available [8]. Photodiodes are used in the energy-integrating scintillation detectors of conventional CT scanners. Since photodiodes do not provide internal amplification (gain), the signal-to-noise ratio (SNR) of the detector output signal in response to a single X-ray photon tends to be poor, which makes them unsuitable for photon-counting detectors. Photomultiplier tubes (PMTs) provide a high internal gain (in the order of 10^6 – 10^8), but do not offer sub-mm pixelated readout as required for photon-counting CT. The silicon photomultiplier (SiPM) is a more recent type of light sensor, which has successfully replaced PMTs in commercial positron emission tomography (PET) scanners [9]. SiPMs combine high internal gain (typically 10^6 at a bias voltage of only a few tens of volts) with the possibility of pixel miniaturization. Hence, we choose the SiPM as the light sensor for photon-counting CT.

As shown in Fig 2.1(b), an SiPM consists of a two-dimensional array of single-photon avalanche diodes (SPADs) [10]. These are small photodiodes (pitch ≤ 100 μm) that are reverse-biased a few volts above their breakdown voltage. Consequently, the electron-hole pair created by the absorption of an optical photon in one of the SPADs can trigger an avalanche multiplication process. When that happens, the SPAD is said to fire, or discharge. The rapidly increasing current through the quenching resistor causes the voltage across the diode to drop, resulting in the quenching of the avalanche. Thus, SPADs are photodiodes operated in Geiger-mode and the total amount of charge released in response to a single trigger is nearly constant. Fig. 2.2(a) shows the resulting pulse from the SiPM (the single-SPAD response, or SSR), which can be described as a fast spike (few ns width) followed by an exponential decay characterized by the recharge time constant τ_r [11]. Typical values of τ_r are in the order of 10^1 ns. All of the SPADs on an SiPM are connected in parallel (see Fig. 2.1(b)). Thus, if multiple optical photons trigger avalanches in multiple SPADs, all of these SPADs fire and the resulting SiPM output pulse equals the superposition of the pulses from the individual SPADs. An example of an output pulse resulting from three fired SPADs is shown in Fig. 2.2(b).

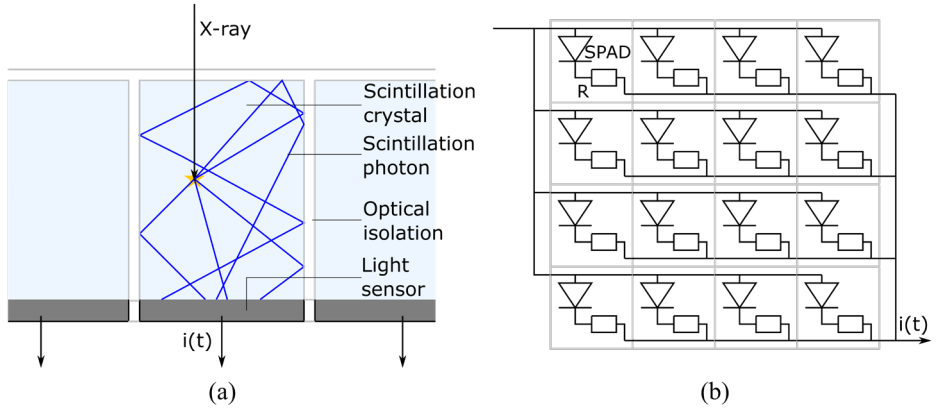

Fig. 2.1. (a) Schematic cross-section of a pixelated scintillation detector for PCCT. Each scintillation crystal is one-to-one coupled to a light sensor, such as a silicon photomultiplier (SiPM), which converts the pulse of optical photons generated by the interaction of an X-ray photon in the scintillator into a current pulse *i(t)*. The paths of 5 scintillation photons are represented here by the blue lines; in reality the number of photons can be much larger. (b) Schematic top view of an SiPM, a light sensor that consists of a two-dimensional array of single-photon avalanche diodes (SPADs). The SPADs of a single SiPM are connected in parallel and each SPAD is equipped with a quenching resistor (R). Only a 4×4 array of SPADs is shown here; practical SiPMs consist of 10^2-10^5 SPADs. Each detector pixel consists of a scintillation crystal coupled to its own SiPM, i.e. to its own two-dimensional array of SPADs, which generates the current pulse *i(t)*.

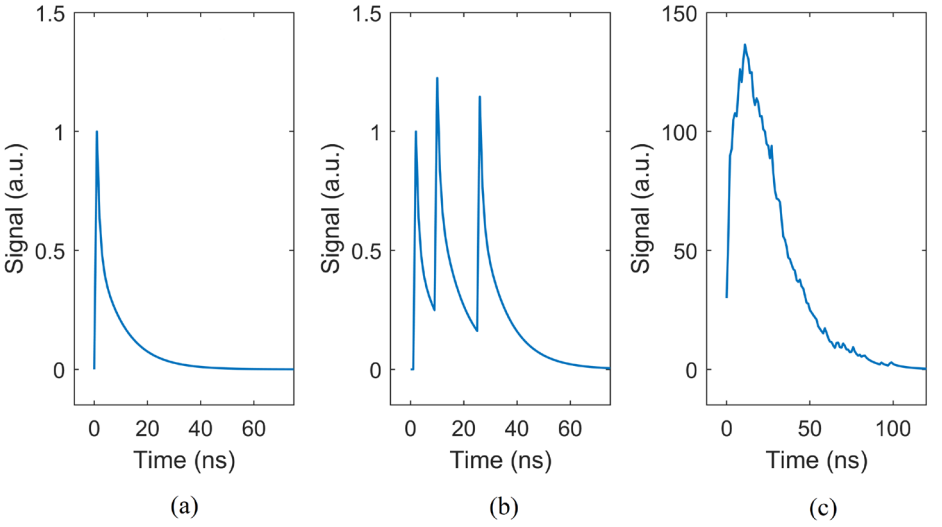

Fig. 2.2. (a) A typical SiPM output pulse in response to a single trigger (single-SPAD response, SSR). (b) A typical SiPM output pulse in response to three triggers in three different SPADs at three different moments in time. (c) A typical SiPM output pulse in response to an X-ray interaction in a scintillator, i.e. in response to many (e.g., 750) triggers occurring at different moments in time distributed according to Eqn. (2.2).

2.2.1 Pulse formation in SiPM-based scintillation detectors

After an X-ray interaction in a scintillator, many optical photons will be detected by the SiPM. The expected number of scintillation photon-induced triggers $\overline{n}_{\mathrm{tr,sc}}$ is given by:

$$\overline{n}_{\mathrm{tr,sc}} = E \cdot Y \cdot f \cdot \eta_{\mathrm{lc}} \cdot \eta_{\mathrm{pd}} \tag{2.1}$$

Here, E is the deposited X-ray energy in the scintillator [keV] and Y is the light yield of the scintillator [photons/keV]. Y is often a function of E. This phenomenon is called light yield non-proportionality. Values of Y are commonly measured at 662 keV. Non-proportionality factors f, describing the ratio between the value of Y at the energy of interest and at 662 keV, must then be known to calculate the absolute photon yield at other energies. The light collection efficiency η_{lc} describes the fraction of scintillation photons that reaches the SiPM. Only a fraction of these photons trigger avalanches. This is quantified by the photodetection efficiency η_{pd}. For detected X-rays in the diagnostic energy range, $\overline{n}_{\mathrm{tr,sc}}$ is typically in the order of 10^2-10^3.

Scintillation photons are not emitted instantaneously upon the interaction of an X-ray photon. In first-order approximation, the probability $P(\Delta t)$ that a scintillation photon is emitted a period of time Δt after the X-ray interaction can be assumed to follow an exponential distribution, characterized by the scintillation decay time constant τ_{d}:

$$P\left(\Delta t\right) = \frac{1}{\tau_{\mathrm{d}}} \exp\left(-\frac{\Delta t}{\tau_{\mathrm{d}}}\right) \tag{2.2}$$

Fast scintillators may have a decay time constant in the order of ns, whereas τ_{d} may be in the order of μs or more for a slow scintillator, such as GOS, which is used in energy-integrating CT detectors ($\tau_{\mathrm{d}} \sim 2.5$ μs). The triggering of the SPADs can be assumed to follow the same probability distribution (Eqn. (2.2)), because the transfer time spread of optical photons in sub-mm scintillation crystals is typically much smaller than τ_{d}. Fig. 2.2(c) shows an example of the resulting SiPM output pulse in response to an X-ray interaction in the scintillator. Due to the high internal gain of SiPMs, the use of charge-sensitive amplifiers and carefully optimized pulse-shaping circuitry, as required for direct-conversion detectors, is no longer mandatory. Good results can be obtained, for example, by feeding the SiPM current pulses directly into a trans-impedance amplifier and performing pulse height analysis on the resulting voltage pulses.

2.2.2 Noise sources in SiPMs

Thermal energy can release charge carriers that trigger discharges in SPADs. These are called dark triggers. A dark trigger gives rise to the same signal as shown in Fig. 2.2(a), i.e., the single-SPAD response. Such a pulse is much weaker than a typical X-ray induced pulse (Fig. 2.2(c)), so it typically does not cross the counting threshold of a photon-counting X-ray detector. If a dark trigger occurs during an X-ray induced pulse, the effect on that pulse is very small. Moreover, the typical rate of dark triggers in modern SiPMs is in the order of 10^4-10^5 per second per mm^2, which is much lower than the typical rate of X-ray photons, so most X-ray induced pulses will not at all be affected by dark triggers.

Another source of noise is afterpulsing. This concerns delayed avalanches triggered by trapped charge carriers escaping their traps some time after an optical photon-induced discharge. Afterpulses rarely occur in modern SiPMs and their effect on an X-ray photon-counting detector is similar to the effect of dark triggers, so they are neglected in this research.

When a SPAD fires, some of the charge carriers involved in the avalanche multiplication process produce infrared photons. These can nearly-instantaneously trigger avalanches in nearby SPADs on the same SiPM. Each of these secondary triggers in turn can cause tertiary triggers, and so on. This phenomenon is called optical crosstalk. The probability that a single trigger causes a total of $n_{\mathrm{tr,oc}}$ triggers (including itself) is given by the Borel distribution with parameter λ [12]:

$$P(n_{\mathrm{tr,oc}}) = \frac{(\lambda \cdot n_{\mathrm{tr,oc}})^{n_{\mathrm{tr,oc}}-1} \cdot \exp(-\lambda \cdot n_{\mathrm{tr,oc}})}{n_{\mathrm{tr,oc}}!} \tag{2.3}$$

The physical meaning of λ is the average number of directly-succeeding triggers caused by a single preceding trigger Under normal operation conditions, $0 < \lambda < 1$, more typically $0 < \lambda < 0.5$. Fig. 2.3(a) shows the typical SiPM output pulse for the case of a single scintillation photon-induced trigger (or dark trigger) causing one crosstalk photon-induced trigger. The pulse amplitude and integral are twice those of the single-SPAD response (Fig. 2.2(a)).

If the number of scintillation photon-induced triggers is assumed to be Poisson-distributed with mean $\overline{n}_{\mathrm{tr,sc}}$ given by Eqn. (2.1), the probability of having $n_{\mathrm{tr,tot}}$ triggers in total (scintillation photon- plus crosstalk photon-induced triggers) will follow a generalized Poisson distribution [12]:

$$P(n_{\mathrm{tr,tot}}) = \frac{\overline{n}_{\mathrm{tr,sc}} \cdot \left(\overline{n}_{\mathrm{tr,sc}} + \lambda \cdot n_{\mathrm{tr,tot}}\right)^{n_{\mathrm{tr,tot}}-1} \cdot \exp\left(-\overline{n}_{\mathrm{tr,sc}} - \lambda \cdot n_{\mathrm{tr,tot}}\right)}{n_{\mathrm{tr,tot}}!} \tag{2.4}$$

This distribution has the following mean value [12]:

$$\overline{n}_{\mathrm{tr,tot}} = \frac{\overline{n}_{\mathrm{tr,sc}}}{1-\lambda} \tag{2.5}$$

and variance [12]:

$$\mathrm{var}\left(n_{\mathrm{tr,tot}}\right) = \frac{\overline{n}_{\mathrm{tr,sc}}}{(1-\lambda)^3} \tag{2.6}$$

Eqn. (2.5) and (2.6) show that optical crosstalk increases the total number of triggers, but at the cost of a more strongly increasing variance in the total number of triggers.

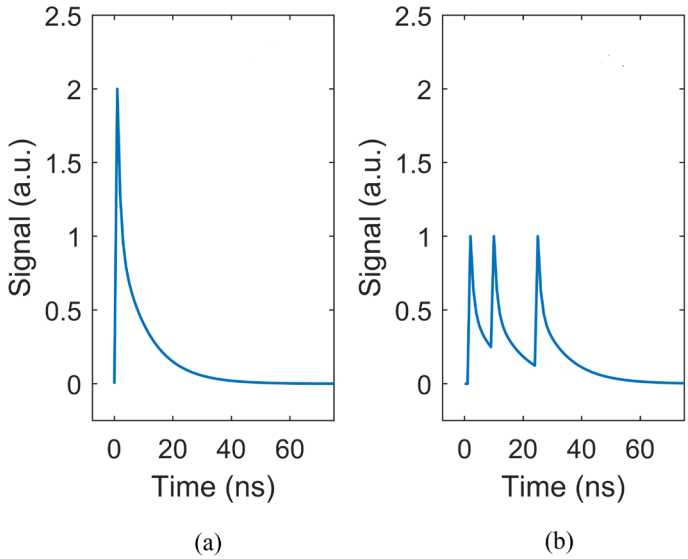

Fig. 2.3. (a) A typical SiPM output pulse in response to a single scintillation photon-induced trigger (or dark trigger) causing one crosstalk photon-induced trigger. (b) A typical SiPM output pulse in response to three triggers in the same SPAD shortly after one another, giving rise to partial SPAD pulses.

2.2.3 Non-proportional response of SiPMs

Sub-mm pixels, required to handle the high incident fluence rate of X-ray photons in photon-counting CT, can accommodate a limited number of SPADs. This makes it more likely that two or more optical photons fire the same SPAD, which can lead to the phenomenon of partial SPAD pulses as shown in Fig. 2.3(b). A partial pulse occurs when an optical photon triggers a new avalanche in a SPAD before that SPAD has fully recharged after the previous discharge [13]. A quantity called the equivalent number of fired SPADs, $n_{\mathrm{f,eq}}$, can be obtained by dividing the integral of an SiPM output pulse by the integral of the single-SPAD response (Fig. 2.2(a)). For three triggers in three different SPADs (Fig. 2.2(b)), $n_{\mathrm{f,eq}}$ equals 3, whereas it is less than 3 for three triggers occurring shortly after one another in the same SPAD (Fig. 2.3(b)). Due to the occurrence of partial pulses, the relationship between $n_{\mathrm{f,eq}}$ and the number of scintillation photon-induced triggers $n_{\mathrm{tr,sc}}$ becomes supra-proportional. As the number of partial pulses in an SiPM output pulse increases, the deviation from proportional behavior increases and the SiPM is said to saturate.

Van Dam et al. [13] developed an analytical expression for the non-proportional relationship between the expected value $\overline{n}_{\mathrm{f,eq}}$ of the equivalent number of fired SPADs and the expected value $\overline{n}_{\mathrm{tr,sc}}$ of the Poisson-distributed number of scintillation photon-induced triggers given by Eqn. (2.1). They took into account afterpulsing and optical crosstalk (both of which tend to increase $\overline{n}_{\mathrm{f,eq}}$), as well as saturation (which tends to decrease $\overline{n}_{\mathrm{f,eq}}$) and showed that their model was in good agreement with experimental

data up to very high saturation levels [13]. Here, we use a slightly adapted version of this model that is briefly explained in the following.

1. According to Eqn. (2.5), $\overline{n}_{\mathrm{tr,sc}}$ scintillation photon-induced triggers on average give rise to $\overline{n}_{\mathrm{tr,tot}}$ triggers in total. Note that our use of Eqn. (2.5) to calculate $\overline{n}_{\mathrm{tr,tot}}$ may be more accurate than the approximation originally used by Van Dam et al. [13], in particular when the crosstalk parameter λ is large.

2. Assuming a uniform distribution of $\overline{n}_{\mathrm{tr,tot}}$ triggers over the number of SPADs N_{SPAD}, the probability $P(i)$ that a single SPAD is triggered i times is given by a binomial distribution with $\overline{n}_{\mathrm{tr,tot}}$ trials and a success probability of $1/N_{\mathrm{SPAD}}$. This can be approximated by a Poisson distribution with a mean of $\overline{n}_{\mathrm{tr,tot}} / N_{\mathrm{SPAD}}$.

3. If afterpulsing is neglected, the expression in Van Dam et al. [13] for the expected value $\overline{n}_{\mathrm{f,eq,1}}(i)$ of the equivalent number of fired SPADs for a single SPAD that is triggered i times reduces to:

$$\overline{n}_{\mathrm{f,eq,1}}(i) = \overline{n}_{\mathrm{f,eq,1}}(i-1) + 1 - \frac{(i-1)\tau_{\mathrm{r}}}{(i-1)\tau_{\mathrm{r}} + \tau_{\mathrm{d}}} \text{ with } \overline{n}_{\mathrm{f,eq,1}}(1) = 1 \tag{2.7}$$

   It can be appreciated that $\overline{n}_{\mathrm{f,eq,1}}(i) = i$ for an infinitely short SPAD response (i.e., $\tau_{\mathrm{r}} \rightarrow 0$). In other words, no saturation occurs in that case. It is noted that the fast spike in the single-SPAD response (see Fig. 2.2(a)) was neglected to arrive at Eqn. (2.7), as this allows the single-SPAD response to be modeled by a single-exponential decay function with time constant τ_{r}.

4. The expected value $\overline{n}_{\mathrm{f,eq,1}}$ of the equivalent number of fired SPADs for a single SPAD is now given by the weighted average of the $\overline{n}_{\mathrm{f,eq,1}}(i)$ with weights $P(i)$:

$$\overline{n}_{\mathrm{f,eq,1}} = \sum_{i=1}^{\infty} P(i) \cdot \overline{n}_{\mathrm{f,eq,1}}(i) \tag{2.8}$$

5. The expected value $\overline{n}_{\mathrm{f,eq}}$ of the equivalent number of fired SPADs for all SPADs on the SiPM can then be obtained by multiplying with N_{SPAD}:

$$\overline{n}_{\mathrm{f,eq}} = N_{\mathrm{SPAD}} \cdot \overline{n}_{\mathrm{f,eq,1}} \tag{2.9}$$

6. Eqn. (2.9) will increasingly overestimate $\overline{n}_{\mathrm{f,eq}}$ as the saturation level increases, because fewer optical crosstalk photons are emitted in case of a partial discharge and fewer crosstalk photon-induced triggers will occur. Van Dam et al. [13] showed that this can be dealt with by iteratively solving the following equation for the corrected expected value $\overline{n}_{\mathrm{tr,tot,corr}}$ of the total number of triggers:

$$\bar{n}_{\mathrm{tr,tot,corr}} = \frac{\bar{n}_{\mathrm{tr,sc}}}{1 - \lambda \cdot \bar{n}_{\mathrm{f,eq}} / \bar{n}_{\mathrm{tr,tot,corr}}} \tag{2.10}$$

Where $\bar{n}_{\mathrm{tr,tot}}$, given by Eqn. (2.5), is the initial guess for $\bar{n}_{\mathrm{tr,tot,corr}}$ in the iterative process. The value to which $\bar{n}_{\mathrm{tr,tot,corr}}$ converges is then used to recalculate $\bar{n}_{\mathrm{f,eq}}$.

2.2.4 Pulse shape model

In this section, we introduce an extension of the above-described model by Van Dam et al. [13]. The extension not only enables the calculation of the mean of the equivalent number of fired SPADs ($\bar{n}_{\mathrm{f,eq}}$), but also the distribution of that number, which is needed to compute the expected energy resolution of SiPM-based scintillation detectors. We do so by simulating many (e.g. 10^4) output pulses from a given combination of scintillator and SiPM, in response to a given energy deposition, according to the principles and assumptions of van Dam's model as described in section Sec. 2.2.3. This will also enable us to evaluate the expected pulse duration and associated rate capability. The simulation steps are as follows:

1. Given an X-ray energy deposition *E,* a set of scintillator properties (τ_{d}, *Y, f*), a value for the light collection efficiency η_{lc}, and a set of SiPM properties (η_{pd}, τ_{r}, λ, N_{SPAD}), calculate $\bar{n}_{\mathrm{tr,sc}}$ and $\bar{n}_{\mathrm{tr,tot}}$ according to Eqn. (2.1) and (2.5), respectively. Here, it is assumed that N_{SPAD} equals the pixel area divided by the SPAD pitch squared.

2. Use van Dam's model as described in Sec. 2.2.3 to determine $\bar{n}_{\mathrm{f,eq}}$ and $\bar{n}_{\mathrm{tr,tot,corr}}$, so that a corrected value for λ can be calculated:

$$\lambda_{\mathrm{corr}} = \lambda \cdot \frac{\bar{n}_{\mathrm{f,eq}}}{\bar{n}_{\mathrm{tr,tot,corr}}} \tag{2.11}$$

3. Sample a number of triggers from a generalized Poisson distribution (Eqn. (2.4)) with parameters $\bar{n}_{\mathrm{tr,sc}}$ and λ_{corr}. This can be done using Sterling's approximation with three terms and the inverse transform sampling method, for example.

4. Assign each trigger to a SPAD by sampling from a uniform distribution of integers on the interval [1, N_{SPAD}]. As a result, the number of triggers on each SPAD is known.

5. For each of the SPADs, sample the timestamps of its triggers from the scintillator emission function, i.e., Eqn. (2.2), and use these to construct the total SPAD signal. Fig. 2.3(b) shows an example of such a signal. However, note that we model the single-SPAD response (cf. Fig 2.2(a)) as a single-

exponential function characterized by the recharge time constant τ_r, so as to be consistent with Van Dam et al. [13] (see also Eqn. (2.7) and accompanying text).

6. Add up all SPAD signals to obtain the detector output pulse. An example is shown in Fig. 2.4.

7. Repeat steps 3, 4, 5 and 6 until the desired number of output pulses has been simulated.

2.2.5 Model output *I*: Energy resolution

For each simulated output pulse, we obtain the equivalent number of fired SPADs $n_{f,eq}$ by dividing the integral of the output pulse by the integral of the single-SPAD response. We subsequently make a histogram of $n_{f,eq}$ of all simulated pulses and fit it using a Gaussian function. In this way, we determine the mean ($\overline{n}_{f,eq}$) and the full width at half maximum (FWHM, $\Delta n_{f,eq}$). We then calculate the observed energy resolution R_{obs} as:

$$R_{obs} = \frac{\Delta n_{f,eq}}{\overline{n}_{f,eq}} \cdot 100\% \tag{2.12}$$

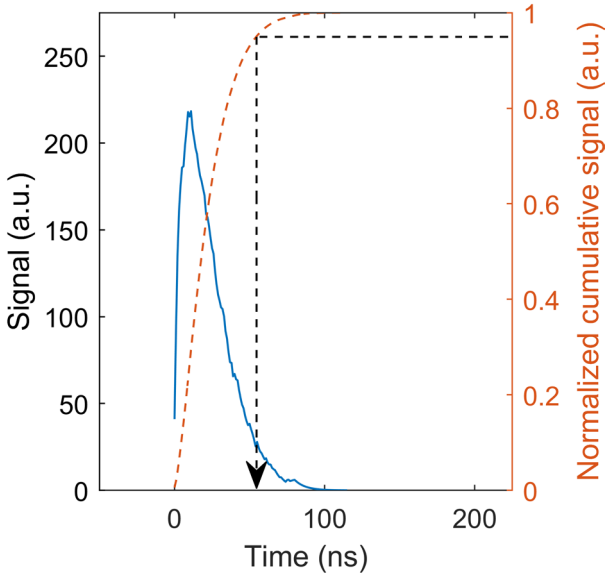

Fig. 2.4. A typical output pulse from an SiPM-based scintillation detector in response to an X-ray photon interaction in a scintillator, calculated with the model presented in this work (solid blue curve). The dashed orange curve shows the normalized cumulative signal. The pulse duration is defined as the moment in time at which the normalized cumulative signal reaches a value of 0.95 (black dashed arrow). The simulated detector consists of a $LaBr_3$:Ce scintillator (see Table 2.3) and an 0.4×0.4 mm^2 SiPM with a 15 µm SPAD pitch (see Table 2.4), exposed to 60 keV photons.

Note that R_{obs} does not represent the true energy discrimination capability of the detector, because $n_{f,eq}$ is not proportional to the number of scintillation photon-induced triggers $n_{tr,sc}$ (see Sec. 2.2.3) and, therefore, not proportional to the X-ray energy (see Eqn. (2.1)). Consequently, the simulated data must be 'backprojected' to the domain of $n_{tr,sc}$, as illustrated in Fig. 2.5. The distribution on the vertical axis is an example of a simulation result in the domain of $n_{f,eq}$. The values of $n_{f,eq}$ corresponding to the mean and the FWHM of this distribution are backprojected to the domain of $n_{tr,sc}$ (dashed black lines). The backprojection is based on a look-up table (visualized by the solid black curve) calculated using the analytical expression of Van Dam's model described in Sec. 2.2.3. This yields values for the FWHM and the mean in the domain of $n_{tr,sc}$. The ratio of these two values is considered the corrected energy resolution R_{corr}, in analogy with Eqn. (2.12). A comparison of the distributions on the horizontal axis shows that R_{corr} is worse than expected from a Poisson distribution with mean $\overline{n}_{tr,sc}$ (as given by Eqn. (2.1)) due to the non-proportional SiPM response (optical crosstalk, saturation). In addition, R_{corr} degrades more and more as the saturation level increases. R_{obs} shows the opposite behavior, which gives a misleading impression of the effect of saturation.

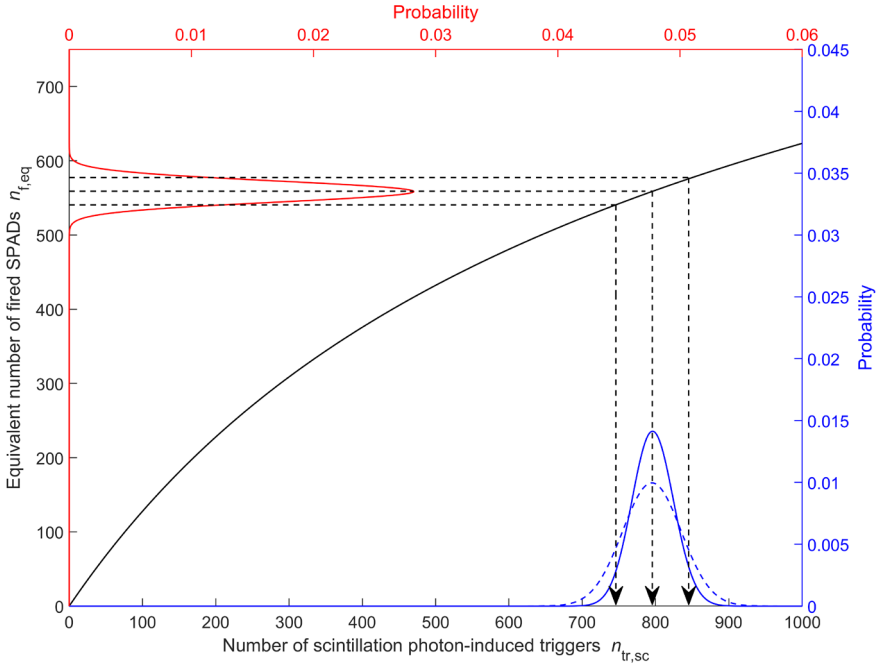

Fig. 2.5. Given a Poisson-distributed number of scintillation photon-induced triggers $n_{tr,sc}$ (solid blue curve on the horizontal axis) with mean $\overline{n}_{tr,sc}$ given by Eqn. (2.1), we first compute the expected distribution of the equivalent number of fired SPADs $n_{f,eq}$ as described in Sec. 2.2.4 and 2.2.5 (solid red curve on the vertical axis). The latter distribution is subsequently 'backprojected' to the domain of $n_{tr,sc}$ (dashed black lines), using van Dam's model of the non-proportional SiPM response described in Sec. 2.2.3 (solid black curve). The corrected energy resolution R_{corr} obtained from the resulting distribution (dashed blue curve on the horizontal axis) is clearly worse than expected from Poisson statistics, due to the non-proportional SiPM response.

It must be noted that the true energy resolution R of a scintillation detector consists of several components [14]:

$$R^2 = R_{\text{stat}}^2 + R_{\text{intr}}^2 = R_{\text{stat}}^2 + R_{\text{np}}^2 + R_{\text{inh}}^2 + R_{\text{tr}}^2 \tag{2.13}$$

Here, R_{stat} refers to the statistics of scintillation photon detection and this is the component that we compute with our model, i.e. R_{corr} is the expected R_{stat}. We obtain the expected R by Pythagorean addition of the intrinsic component R_{intr}, which combines all other contributions to the energy resolution. The most important of these contributions, R_{np}, is the excess variance caused by the non-proportionality of the scintillator's light yield. The second contribution, R_{inh}, is the excess variance due to inhomogeneity of the scintillator, e.g. spatial variation of the light yield. The last contribution, R_{tr}, is the excess variance resulting from the light transport. Since R_{intr} cannot be modeled from first principles, we rely on measured values reported in literature. These values are mainly determined by R_{np}, because R_{inh} and R_{tr} should be negligible for well-constructed detectors based on commercially grown scintillation crystals, particularly in the case of small pixels.

2.2.6 Model output *II*: Pulse duration and rate capability

The expected pulse duration and associated rate capability of a given combination of scintillator and SiPM can be derived from the set of output pulses already simulated in Sec. 2.2.4. In this study, we define the duration of a detector output pulse as the moment in time at which the integral of the pulse reaches 95% of the total area under the pulse (see Fig. 2.4). With this definition, we calculate the mean t_{95} of all pulse durations in the set. Then, we calculate the incident rate $r_{50,\text{pix}}$ at which an X-ray photon has 50% chance of arriving within t_{95} from the previous X-ray photon on the same pixel, in which case the resulting pulse is considered to be affected by pulse pile-up. Note that at the rate $r_{50,\text{pix}}$ there is also 50% chance for a given event to occur more than t_{95} later than the previous one, in which case the pulse is considered not to be affected by pile-up. Given the exponential distribution of the inter-arrival times of the X-ray photons, $r_{50,\text{pix}}$ is given by:

$$r_{50,\text{pix}} = \frac{\ln(2)}{t_{95}} \tag{2.14}$$

Finally, we translate $r_{50,\text{pix}}$ into a rate capability per mm^2, denoted by r_{50}, using the pixel size d in mm:

$$r_{50} = r_{50,\text{pix}} \cdot \left(\frac{1}{d}\right)^2 \tag{2.15}$$

2.3 Materials and methods

We first describe the experiments conducted to validate the model introduced in Sec. 2.2. We then describe the simulations performed to investigate the feasibility of developing SiPM-based scintillation detectors for use in photon-counting CT scanners.

2.3.1 Model validation *I*: Experimental set-up

A non-commercial 1×1 mm^2 SiPM from Broadcom based on the manufacturer's NUV-HD technology was used in the validation experiments. It was optically coupled to a fast 0.9×0.9×1.0 mm^3 $LuAlO_3$:Ce (LuAP:Ce) scintillation crystal (Hilger Crystals, τ_d = 17 ns) using Norland Optical Adhesive 63. Note that due to the high effective atomic number and density of LuAP:Ce (Z_{Lu}=71 and ρ_{LuAP} = 8.3 g cm^{-3}), a crystal thickness of only 1.0 mm provides an X-ray absorption efficiency of about 96%, 91% and 58% at 50, 100 and 150 keV, respectively. The scintillation crystal was covered in reflective polytetrafluoroethylene (PTFE) powder in order to increase the light collection efficiency. Two radionuclides were selected for the measurements: Am-241, with a single emission line at 59.5 keV, and Cs-137, with a single emission line at 662 keV. Although the latter energy is outside the diagnostic energy range, it helped to create a relatively high saturation level on the 1×1 mm^2 SiPM, so that we could also test our model under these potentially relevant conditions for sub-mm pixels. The current pulses from the detector were converted into voltage pulses, without substantial changes to the pulse shape, using a trans-impedance amplifier on Broadcom's AFBR-S4E001 preamplifier board. In the next step, the pulses were digitized by a Teledyne LeCroy HDO9404 digital oscilloscope operating at a bandwidth of 200 MHz and a sampling rate of 1 Gs/s. In this way, further analysis of the pulses could be done on the computer.

We characterized both the LuAP:Ce scintillator and the SiPM before conducting the validation experiments. The set-up described by Ter Weele et al. was used to determine the decay profile of the scintillator [15]. Besides the fast component with a decay time constant τ_d of approximately 17 ns, we also found a slow component with τ_d in the order of 500 ns containing ~20% of the light. Consequently, we measured the light yield with a shaping time constant of 3.0 μs following the method described by De Haas et al. [16]. Our best estimate of the light yield at 662 keV is 7.1 photons/keV, corresponding with 5.7 photons/keV in the fast component (80%). In the same experiments, we observed a very low degree of light yield non-proportionality. Therefore, values for the intrinsic resolution R_{intr} (and the non-proportionality factor f), both of which play a role in our model, were taken from work by Balcerzyk et al. [17], who determined them for LuAP:Ce with a low degree of non-proportionality. The values are shown in Table 2.1.

The 1×1 mm^2 SiPM had a SPAD pitch of 30 μm, so it contained 1089 SPADs, and was operated at 3.0 V and 5.0 V above the breakdown voltage of 27 V. An overview of the SiPM characteristics at these two overvoltages is shown in Table 2.2. Note that the photodetection efficiency η_{pd} is a function of wavelength. The values of η_{pd} given in Table 2.2 were estimated on the basis of the manufacturer's data sheet and the emission spectrum of LuAP:Ce. The values of the optical crosstalk parameter λ and the recharge

time constant τ_r were determined from measurements of dark triggers. See Appendix A2.1 for more details.

2.3.2 Model validation *II*: Data processing

About $2 \cdot 10^5$ pulses were registered for each of the four combinations of gamma-ray energy and SiPM overvoltage. We expect 99% of the integral under these pulses to fall within a time span of 200 ns, based on the values of τ_d and τ_r. The long pulse duration is due to the large τ_r, which we purposely selected as it helps to test our model under high saturation conditions. The digitized pulses were therefore integrated using a 200 ns integration window. The pulse integrals were subsequently divided by the pulse integral of the measured single-SPAD response (see Appendix A2.1) to obtain the equivalent number of fired SPADs $n_{f,eq}$. We then generated a histogram of the resulting values and fitted a Gaussian function through the full-energy peak to determine the mean of $n_{f,eq}$ and the observed energy resolution according to Eqn. (2.12). The peaks in the histograms obtained with 662 keV gamma photons were fitted with a double Gaussian, because the full-energy (FE) peak overlapped with the K-escape (KE) peak (caused by 54 keV characteristic X-rays of Lu-atoms escaping the small crystal):

$$y\left(n_{f,eq}\right) = A_{FE} \exp\left(-\frac{\left(n_{f,eq} - \overline{n}_{f,eq,FE}\right)^2}{2\sigma^2_{f,eq,FE}}\right) + A_{KE} \exp\left(-\frac{\left(n_{f,eq} - \overline{n}_{f,eq,KE}\right)^2}{2\sigma^2_{f,eq,KE}}\right) \quad (2.16)$$

The fit region was chosen in such a way that the following conditions were satisfied:

- Mean: $\overline{n}_{f,eq,KE} \geq (662 - 54) / 662 \cdot \overline{n}_{f,eq,KE} = 0.918 \cdot \overline{n}_{f,eq,KE}$
- Energy resolution: $2.355\sigma_{f,eq,KE}/\overline{n}_{f,eq,KE} \geq 2.355\sigma_{f,eq,FE}/\overline{n}_{f,eq,KE}$
- Amplitude: $A_{KE} \leq A_{FE}$

Table 2.1. Model input parameters for a LuAP:Ce scintillator (τ_d=17 ns, Y = 5.7 photons/keV) with good proportionality [17].

Energy (keV)	**59.5**	**662**
Non-proportionality factor f	0.985	1.00
Intrinsic resolution R_{intr} (%)	8.5	2.8

Table 2.2. Model input parameters for the 1×1 mm^2 SiPM (30 µm SPAD pitch) used in the validation experiments.

Overvoltage (V)	**3.0**	**5.0**
Photodetection efficiency η_{pd}	0.410	0.455
Optical crosstalk parameter λ	0.184	0.361
Recharge time constant τ_r (ns)	39.3	35.8

Note that the first condition contains the "≥" sign, because saturation may cause the peaks to be closer to each other than one would expect based on the energy difference between them.

We used the measurement at 3.0 V and 59.5 keV to determine the light collection efficiency η_{lc} of the detector – the last unknown input parameter of the model – by varying the value of η_{lc} in the model until the modeled mean of the equivalent number of fired SPADs coincided with the measured one. We selected this particular measurement because it is least influenced by optical crosstalk and saturation. For all other combinations of overvoltage and energy, the modeled and measured means of the equivalent number of fired SPADs and observed energy resolutions were compared to each other after running the model with this value of η_{lc}.

Lastly, the modeled pulse shapes were experimentally validated, as they are used to derive the pulse duration t_{95} and the associated rate capability r_{50}. To this end, we calculated the average shapes of the modeled and measured pulses for each combination of energy and overvoltage. Pulse amplitudes were normalized to 1 by dividing the mean pulses by their maximum value, so that both types of pulses could be visually compared to each other.

2.3.3 Model calculations

Once validated, the model was used to investigate the potential of SiPM-based scintillation detectors for photon-counting CT (PCCT). This was done by simulating the energy resolution, pulse shape, and associated rate capability for 59.5 keV X-ray photons incident on a single, square-shaped pixel consisting of various combinations of scintillator and SiPM. The simulations were run for light collection efficiencies η_{lc} of 0.50, 0.75 and 1.00 and for the following six pixel sizes: 200, 250, 333, 400, 500, and 1000 μm.

$Lu_{1.8}Y_{0.2}SO_5$:Ce (LYSO:Ce) is a potentially suitable scintillator for PCCT because of its high density and relatively short decay time constant τ_d = 36 ns (see Table 4.3). This scintillator is widely used in clinical positron emission tomography (PET) scanners. However, the incident photon fluence rate in CT is much higher than in PET, so an even faster scintillator could be beneficial. Therefore, $LuAlO_3$:Ce (LuAP:Ce) with τ_d = 17 ns (also see Table 4.3) was included in the study, as well. The performance of these high-density scintillators was first simulated in combination with sub-mm SiPMs based on Broadcom's NUV-HD technology. This technology is currently available with a SPAD pitch of 30 μm. The properties of this SiPM technology are listed in Table 2.4. The values at an overvoltage of 3.0 V (bold face) were used in the simulations. For comparison, the values at an overvoltage of 7.0 V are also included in Table 2.4. The main advantage of using an overvoltage of 3.0 V is that the optical crosstalk parameter is much lower, whereas the photodetection efficiency is still decent.

Table 2.3. Properties of the three fast scintillators selected for the model calculations. The required thickness is based on an X-ray absorption efficiency near 100% at 50 keV, around 90% at 100 keV and around 55% at 150 keV.

Scintillator	**LYSO:Ce[1]**	**LuAP:Ce[2,3]**	**$LaBr_3$:Ce[1]**
Light yield Y (photons/keV)	33	15	63
Non-proportionality factor f	0.845 [18,19]	0.985 [17]	0.980 [20,21]
Intrinsic resolution R_{intr} (%)	22 [18,19]	8.5 [17]	8.0 [20,21]
Decay time constant τ_d (ns)	36	17	16
Mass density (g cm^{-3})	7.1	8.3	5.1
Required thickness (mm)	1.15	1.00	3.50

Table 2.4. Properties of SiPMs based on Broadcom's NUV-HD technology.[4] The values in bold face were used for the model calculations. The other values are shown for comparison. Two values of η_{pd} are given for each combination of SPAD pitch and overvoltage: the effective photodetection efficiency for the emission spectra of the scintillators in Table 4.3 (no brackets) and the value at the wavelength of maximum sensitivity, i.e., 420 nm (values in brackets).

	SPAD pitch = 30 µm		**SPAD pitch = 15 µm**	
	Overvoltage 3.0 V	Overvoltage 7.0 V	Overvoltage 3.0 V	**Overvoltage 7.0 V**
Photodetection efficiency η_{pd}	**0.41** (0.44)	0.48 (0.55)	0.21 (0.23)	**0.28** (0.30)
Recharge time constant τ_r (ns)	**55[5]**	50	9.0	**7.0**
Optical crosstalk parameter λ[6]	**0.1235[7] [22]**	0.5753	0.0128	**0.1235**

[1] Data from datasheets of Luxium Solutions (formerly Saint Gobain Crystals), unless otherwise indicated.

[2] Data from private communication with Hilger Crystals, unless otherwise indicated.

[3] Currently available LuAP:Ce features a slow decay component, which means that part of the 15 photons/keV is not emitted with a decay time of 17 ns and does not contribute to the pulse.

[4] Data from Broadcom's datasheets and from private communication with Broadcom.

[5] The measured value of the recharge time constant in Table 2.2 differs from the values in Table 2.4, because the SiPM used in the experiments had tuned quenching resistors, which reduced the recharge time constant.

[6] The datasheets mention a crosstalk probability P_{Xtalk}, which can be converted into the crosstalk parameter λ using the following formula: $\lambda = \sum_{k=1}^{\infty} k \cdot \left(P_{Xtalk}\right)^k$.

[7] The measured value of λ in Table 2.2 differs from the value in Table 2.4. This is likely due to increased optical crosstalk in the experiments caused by the presence of a scintillator covered in reflective material on top of the SiPM.

In the next step, the performance of LYSO:Ce and LuAP:Ce coupled to sub-mm SiPMs based on Broadcom's NUV-HD technology with a reduced SPAD pitch of 15 μm was simulated. Its properties are shown in Table 2.4. An overvoltage of 7.0 V (bold face) was selected in this case, because it offers the highest photodetection efficiency and the shortest recharge time constant, while the optical crosstalk parameter is still quite low.

Finally, the performance of a third scintillator, $LaBr_3$:Ce, coupled to sub-mm SiPMs with a SPAD pitch of 15 μm was simulated. Table 2.3 shows that $LaBr_3$:Ce is interesting due to its superior combination of decay time constant, light yield, and intrinsic energy resolution.

It was already noted that the photodetection efficiency of an SiPM is a function of wavelength. However, all three scintillators included in the present study emit in the near-ultraviolet and blue part of the spectrum. Hence, when using the emission spectra of these three scintillators as weights to calculate the weighted average of η_{pd}, essentially the same value is obtained each time, viz. the value shown in Table 2.4. For comparison, the photodetection efficiency at the wavelength of maximum sensitivity (420 nm) has been added to Table 2.4 in between brackets.

2.4 Results

In the following, we first present the results of the model validation experiments and subsequently use the validated model to compute the expected performance of SiPM-based scintillation detectors for photon-counting CT.

2.4.1 Model validation

The results of the model validation experiments are summarized in Table 2.5 (mean of the equivalent number of fired SPADs, $\overline{n}_{f,eq}$) and Table 2.6 (observed energy resolution, $R_{obs,}$ i.e., the energy resolution in the domain of $n_{f,eq}$ as defined in Eqn. (2.12)). Firstly, a light collection efficiency η_{lc} of 0.57 was determined by forcing the modeled $\overline{n}_{f,eq}$ to have the same value of 92.7 that was measured with 59.5 keV gamma photons at an overvoltage of 3.0 V. The relatively low value of η_{lc} can have various causes, such as a suboptimally reflecting surface created by the PTFE powder and/or light losses in, or via, the optical glue used to attach the scintillator to the SiPM. A value of 29% for R_{obs} is expected on the basis of the model for this value of η_{lc}, in fairly good agreement with the measured value of 33%. Some mismatch between model and experiment is expected, because the measured R_{obs} is affected by the scintillator's intrinsic resolution R_{intr}, in contrast to the modeled R_{obs}. The factors contributing to R_{intr} have been discussed in the text below Eqn. (2.13). We may include R_{intr} in the modeled R_{obs} by backprojecting this R_{obs} to the domain of the number of scintillation photon-induced triggers, followed by Pythagorean addition of R_{intr} (taken from Table 2.1) and forward projection of the result to the domain of $n_{f,eq}$. Both projections are based on the method described in Sec. 2.2.5. The result is a corrected value for the modeled R_{obs}, denoted by

R_{obs}*. However, Table 2.6 shows that this procedure does not completely bridge the gap between model and experiment.

For the other three combinations of overvoltage and energy, the modeled $\overline{n}_{f,eq}$ deviates less than 5% from the measured one. Regarding the modeled R_{obs}*, a slight degradation from 30% to 31% at 59.5 keV is expected when increasing the overvoltage from 3.0 V to 5.0 V. This is because the amount of optical crosstalk increases in the model. However, this slight degradation cannot be seen in the experimental R_{obs}. At 662 keV, a change in R_{obs}* from 6.9% to 6.5% is expected when increasing the overvoltage, due to increasing saturation of the SiPM. A similar, but slightly more pronounced trend can be seen in the experimental R_{obs}.

The observed differences between model and experiment may be expected in view of the assumptions in our model and the uncertainties associated with the model input parameters and the fitting of the histograms. Furthermore, we hypothesize that mismatches between modeled R_{obs}* and measured R_{obs} may also be related to a non-negligible light transport contribution (R_{tr} in Eqn. (2.13)) to R_{intr}, for example due to a light leak in the detector that would also explain the relatively low value of η_{lc}. We conclude that the model and measurements are in sufficiently good agreement to use the

Table 2.5. Comparison of the mean equivalent number of fired SPADs $\overline{n}_{f,eq}$ computed using the model and measured in the validation experiments. The value of the light collection efficiency η_{lc} was determined by matching the modeled and measured values for an overvoltage of 3.0 V and a photon energy of 59.5 keV, i.e., under conditions of low saturation and optical crosstalk.

Energy (keV)	**Overvoltage = 3.0 V**		**Overvoltage = 5.0 V**	
	Model	Experiment	Model	Experiment
59.5	92.7	92.7	129	135
662	765	737	931	952

Table 2.6. Comparison of the observed energy resolution R_{obs} computed using the model and measured in the validation experiments. The measured R_{obs} is affected by the scintillator's intrinsic resolution R_{intr}, whereas the modeled R_{obs} is not. R_{obs}* aims to include R_{intr} (from Table 2.1) in the modeled R_{obs}.

Energy (keV)	**Overvoltage = 3.0 V**			**Overvoltage = 5.0 V**		
	Model R_{obs}	Model R_{obs}*	Experim. R_{obs}	Model R_{obs}	Model R_{obs}*	Experim. R_{obs}
59.5	29%	30%	33%	30%	31%	33%
662	6.7%	6.9%	8.0%	6.3%	6.5%	7.2%

model for the purpose of this work, i.e., to study the feasibility of using SiPM-based scintillation detectors as a potential alternative for direct-conversion detectors in photon-counting CT.

Fig. 2.6 shows the mean pulse shapes derived from the four validation experiments in comparison to the mean pulse shapes according to the corresponding model calculations. Regardless of overvoltage and energy, the simulated pulse shapes nicely follow the experimental ones in the main part of the pulse. Deviations can be observed in the tails, where the experimental mean pulse shapes return to the baseline more slowly. This is due to the slow decay component that we observed for the LuAP:Ce scintillator used in the experiments (see Sec. 2.3.1), which is not accounted for by the model. Slow components are not uncommon in scintillators and can often be reduced considerably through proper engineering of the scintillation material. It is evident that the minimization of slow components is important if a scintillator is to be used in a high count-rate application like photon-counting CT. In case slow scintillation decay components cannot be fully eliminated, implementing a baseline restorer in the read-out circuit is a possible remedy.

2.4.2 Model calculations

Fig. 2.7 shows the expected performance of sub-mm pixels of LYSO:Ce and LuAP:Ce scintillators coupled to the SiPMs with a SPAD pitch of 30 μm. It can be observed that LuAP:Ce outperforms LYSO:Ce, both in terms of rate capability and energy resolution. The former was expected, because of the shorter decay time constant. The latter shows the importance of using scintillators with a low degree of non-proportionality and associated good intrinsic resolution R_{intr}. As shown in Table 2.3, the light yield of

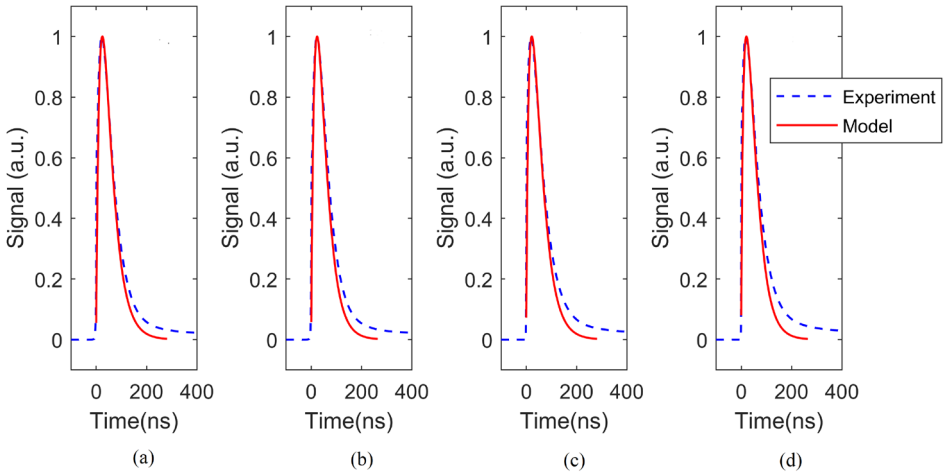

Fig. 2.6. Comparison of modeled (solid red curve) and experimental (blue dashed curve) mean pulse shapes for photon energies and overvoltages of, respectively (a) 59.5 keV and 3.0 V; (b) 59.5 keV and 5.0 V; (c) 662 keV and 3.0 V; (d) 662 keV and 5.0 V. The pulse duration is relatively long, because we selected an SiPM with a large recharge time constant, which helped to test our model under high saturation conditions.

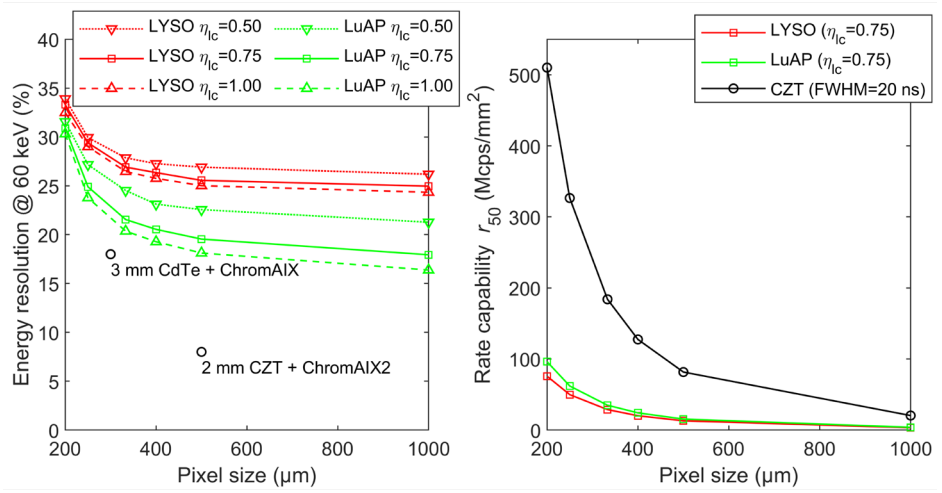

(a) (b)

Fig. 2.7. (a) Energy resolution at 60 keV and (b) rate capability r_{50}, both as a function of pixel size, for LYSO:Ce and LuAP:Ce scintillators coupled to the SiPMs with 30 µm SPAD pitch. For comparison, data for CdTe- and CZT-based photon-counting detectors are also shown [23], [24].

LuAP:Ce is at least two times as low as that of LYSO:Ce. However, its R_{intr} is much better, which compensates for the worse R_{stat} that results from its lower light yield (see Eqn. (2.13)). Fig. 2.7(a) furthermore illustrates the importance of a high light collection efficiency η_{lc} for achieving good energy resolution. Finally, it can be observed that both scintillators suffer from a degradation of the energy resolution with decreasing pixel size. This trend is due to increasing saturation of the SiPM.

To put these results into perspective, Fig. 2.7(a) shows two data points reported for CdTe- and CZT-based X-ray photon-counting detectors from Philips [23,24]. Clearly, it is impossible to get near these data points with an LYSO:Ce-based detector. However, we observe that a LuAP:Ce-based detector with high η_{lc} could get close to the '3 mm CdTe + ChromAIX' data point if the saturation effect were absent.

The plots of the rate capability r_{50} in Fig. 2.7(b) can be compared to the same Philips detectors. These detectors output Gaussian shaped pulses, so 95% of the total area under the pulses falls within four standard deviations. Given that the pulses have an FWHM of 20 ns [23], their t_{95} equals 34 ns. The r_{50} curve for CZT in Fig. 2.7(b) is based on this number. Clearly, the rate capability of the combinations of scintillator and SiPM shown in Fig. 2.7(b) are far from the rate capability of the CZT detector. Note that only the curve for $\eta_{lc} = 0.75$ is shown, as the value of η_{lc} hardly affects the pulse duration and the associated rate capability r_{50}.

It can be concluded from the above results that less saturation and shorter pulses are required to be competitive with room-temperature semiconductor detectors. Detectors

based on the advanced SiPMs with a SPAD pitch of 15 µm could potentially achieve this, because these SiPMs have a much shorter recharge time constant and a quadrupled number of SPADs for a given pixel size.

The data in Fig. 2.8(a) indeed show that sub-mm pixels of these scintillators coupled to the SiPMs with a SPAD pitch of 15 µm hardly suffer from degradation of the energy resolution with decreasing pixel size. However, for the pixel sizes that are least affected by saturation (e.g. 1000 µm), a comparison of Fig. 2.7(a) and Fig 2.8 (a) shows that the use of SiPMs with a SPAD pitch of 15 µm results in a slight worsening of the energy resolution, due to the lower photodetection efficiency of these SiPMs (see Table 2.4). This effect is less pronounced for LYSO:Ce, because the energy resolution obtained with this material is mainly determined by its relatively poor intrinsic resolution R_{intr}.

It can be appreciated from Fig. 2.8(a) that the shorter recharge time constant of the advanced SiPMs with a SPAD pitch of 15 µm leads to a considerable improvement of the rate capability. The value of the mean pulse duration t_{95} improves from 180 ns to slightly less than 60 ns for LuAP:Ce, which is in the same order of magnitude as the t_{95} of the CZT detector (34 ns). For pixel sizes ranging from 200 µm to 500 µm, a LuAP:Ce pixel would have to be made approximately 100 µm smaller than a CZT pixel of a given size to achieve the same rate capability. For example, a 400 µm LuAP:Ce pixel would have a similar rate capability as a 500 µm CZT pixel.

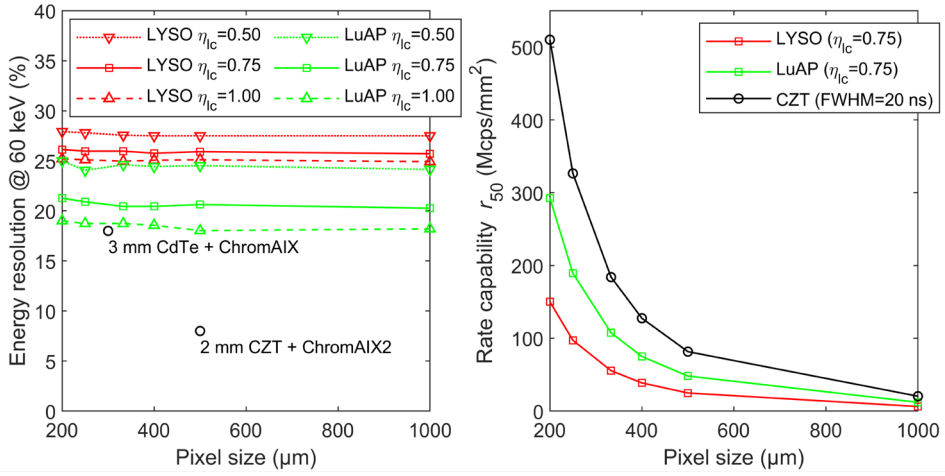

(a) (b)

Fig. 2.8. (a) Energy resolution at 60 keV and (b) rate capability r_{50}, both as a function of pixel size, for LYSO:Ce and LuAP:Ce scintillators coupled to the advanced SiPMs with a SPAD pitch of 15 µm. For comparison, data reported for CdTe- and CZT-based photon-counting detectors are also shown [23,24].

The modeled performance of detectors consisting of sub-mm $LaBr_3$:Ce crystals coupled to the advanced SiPMs with a SPAD pitch of 15 µm is graphically displayed in Fig. 2.9. The decay time constant of $LaBr_3$:Ce is 16 ns, which is only 1 ns shorter than the one of LuAP:Ce. As a result, the rate capability curve in Fig. 2.9(b) is very similar to the one of LuAP:Ce in Fig. 2.8(b). Thus, a 400 µm $LaBr_3$:Ce pixel also has a similar rate capability as a 500 µm CZT pixel, for example. However, a comparison of Fig. 2.8(a) and Fig. 2.9 (a) shows that $LaBr_3$:Ce substantially outperforms LuAP:Ce in terms of energy resolution. The achievable values of the energy resolution at 60 keV lie in between the two data points reported for the CdTe and CZT detectors. Furthermore, only a slight degradation of the energy resolution with decreasing pixel size is observed, which indicates that sub-mm pixels of the SiPMs with a SPAD pitch of 15 µm hardly suffer from saturation, even when coupled to a scintillator with a very high light yield such as $LaBr_3$:Ce.

Lastly, Fig. 2.10 shows several examples of pulses generated by 333 µm pixels of the three scintillators when coupled to the advanced SiPMs with a SPAD pitch of 15 µm, in response to 59.5 keV photons and assuming a light collection efficiency of 0.75. $LaBr_3$:Ce has a much higher light yield than LuAP:Ce, but a very similar decay time constant. This leads to a much higher pulse amplitude, but 95% of the area under the curve falls within the same window of 57-58 ns (t_{95}) for both scintillators. LYSO:Ce also has a higher light yield than LuAP:Ce, but its decay time constant is considerably larger. Thus, the scintillation photons from LYSO:Ce are more spread out in time, which results in a similar pulse amplitude, but a much longer t_{95} of 113 ns.

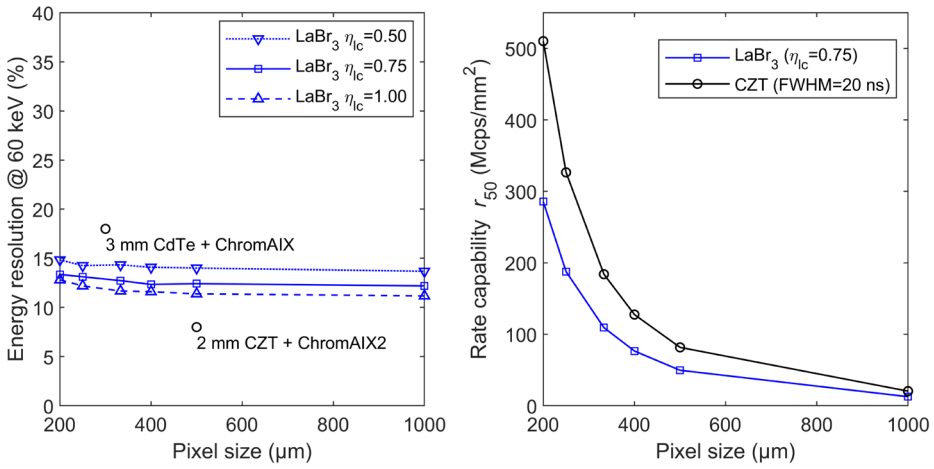

(a) (b)

Fig. 2.9. (a) Energy resolution at 60 keV and (b) rate capability r_{50}, both as a function of pixel size, for $LaBr_3$:Ce scintillators coupled to the advanced SiPMs with a SPAD pitch of 15 µm. For comparison, data for CdTe- and CZT-based photon-counting detectors are also shown [23,24].

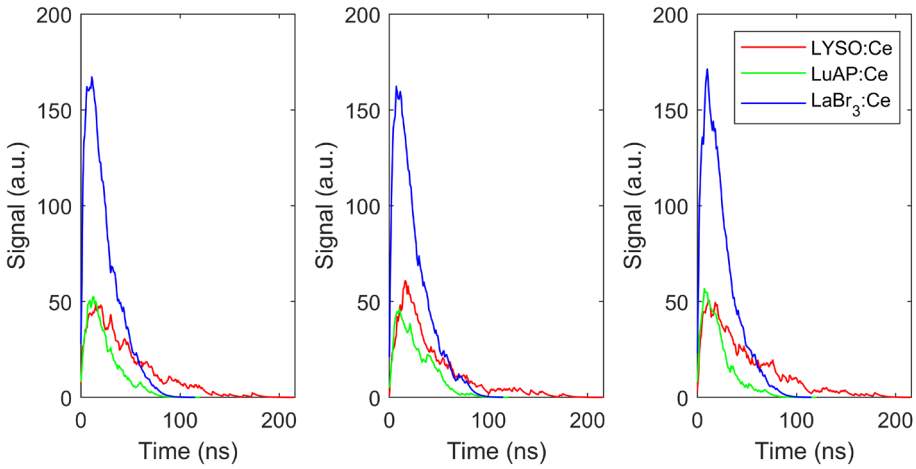

Fig. 2.10. Examples of simulated pulse shapes generated by 333 µm pixels of $LaBr_3$:Ce (solid blue curve), LuAP:Ce (dashed green curve), and LYSO:Ce (dash-dotted red curve) coupled to the advanced SiPMs with a SPAD pitch of 15 µm, in response to 59.5 keV X-ray photons and for a light collection efficiency of 0.75.

2.5 Discussion

SiPMs exhibit a non-proportional response, mainly due to the occurrence of saturation and optical crosstalk. This may substantially affect the performance of SiPM-based scintillation detectors with sub-mm pixel sizes for photon-counting CT. We therefore incorporated detailed descriptions of saturation and optical crosstalk in our model and compared the resulting model calculations to a series of validation experiments, some of which were performed under conditions in which these phenomena have a substantial influence on the measured result. Since the smallest SiPM size currently available is 1×1 mm^2, high saturation conditions were effectuated by irradiating a 0.9×0.9×1.0 mm^3 LuAP:Ce crystal coupled to such a 1×1 mm^2 SiPM with 662 keV gamma photons, in addition to irradiations with clinically more relevant 60 keV gamma photons. Good agreement between model and experiment was found in both cases, especially when the multitude of model input parameters and assumptions is considered. This gives confidence about the predictive power of the model.

According to our model calculations, LuAP:Ce and $LaBr_3$:Ce appear to be promising alternatives to CdTe- and CZT-based detectors when coupled to SiPMs with a small SPAD pitch and a very short recharge time constant, such as the advanced SiPM prototype considered in this work. While LuAP:Ce and $LaBr_3$:Ce have similarly high count rate capabilities, $LaBr_3$:Ce offers the best energy resolution. It should be noted that $LaBr_3$:Ce is hygroscopic and needs special treatment and packaging before it can be used outside a moisture-free environment. It is nevertheless used in a wide variety of detectors and applications, as is the case for other hygroscopic crystals, such as NaI:Tl.

We thus see $LaBr_3$:Ce as the most promising of the investigated materials for photon-counting CT applications in which the best possible count rate capability and energy resolution are required. Nevertheless, LuAP:Ce and LYSO:Ce could be useful alternatives in less demanding X-ray photon-counting applications.

Our model calculations furthermore indicate that rate capabilities adequate for photon-counting CT (PCCT) can be achieved when the detector pixel size equals 400 μm or less. Such pixel sizes also fulfill the spatial resolution requirements of PCCT. Yet, two challenges arise when developing a scintillation detector with such small pixels, which will need to be addressed in future work.

The first challenge concerns the escape of fluorescence and/or Compton-scattered X-rays from a detector pixel and their possible absorption in neighboring pixels (X-ray crosstalk). One of the detector properties that affect this phenomenon is the atomic number of the elements present in the detection material. Table 2.7 shows the characteristics of the fluorescence K X-rays of a few relevant elements, for example. However, the effect of secondary X-rays escaping from a pixel on the detector performance can only be studied in detail using Monte Carlo particle tracking software. Combining the distribution of energy depositions in a pixel obtained from Monte Carlo simulations with the detector response model presented in this work will yield the full spectral response of a detector pixel, for example.

Table 2.7. Characteristics of the fluorescence K X-rays of a few relevant elements. If the incident X-ray photon energy exceeds the K-edge energy, K-shell photo-electric absorption may take place. The K fluorescence yield describes which fraction of these absorptions leads to the emission of a K X-ray with energy in the tabulated range. The numbers are based on data from the NIST standard reference database 128.

Detection material	**$LaBr_3$**	**LuAP**	**LYSO**	**CdTe**	
Element	**La**	**Lu**	**Lu**	**Cd**	**Te**
K-edge energy (keV)	38.9	63.3	63.3	26.7	31.8
K fluorescence yield	0.91	0.96	0.96	0.84	0.88
Energy range of $K_{\alpha1}$, $K_{\alpha2}$, $K_{\beta1}$ X-rays (keV)	33.0 - 37.8	53.0 - 61.3	53.0 - 61.3	23.0 - 26.1	27.2 - 31.0

Secondly, scintillator-based PCCT detectors need a form of optical insulation in between the pixels in order to avoid light sharing between neighboring pixels (Fig. 2.1(a)). The use of conventional TiO_2-based reflectors with a thickness of about 100 μm can lead to a relatively large dead area and loss of dose efficiency in the case of sub-mm pixels. On the other hand, such reflectors offer excellent optical isolation. Distortion of the measurement of counts and energy, as caused by charge sharing in direct-conversion

detectors, can thus be avoided. Moreover, thinner reflectors of excellent quality exist. In particular, reflectors ranging from 38 µm to 65 µm in thickness have been used in high resolution imaging detectors based on scintillation crystals ranging from 220 µm to 430 µm in size [25,26,27]. Furthermore, innovative optical isolation techniques are under development. For example, $LaBr_3$:Ce has been grown with a columnar microstructure [28], like the CsI:Tl scintillator used in flat panel detectors for digital radiography. In research labs, laser-induced optical barriers have been created in a variety of scintillators, including LYSO:Ce [29,30]. Both techniques come with essentially no dead area, but the optical isolation may be less than what is achievable with physical reflectors. It thus needs to be evaluated if the positive effect of having zero dead area outweighs the negative effect of having some light sharing (cf. charge sharing in direct-conversion detectors).

Lastly, we note that there may be potential to further improve the rate capability of SiPM-based scintillation detectors. The pulse duration t_{95} is mainly determined by the decay time constant τ_d of the scintillator and the recharge time constant τ_r of the SiPM. The best values of these parameters encountered in the present work are 16 ns and 7 ns, respectively. However, ongoing research into fast scintillators and SiPMs may yield even smaller time constants. Fig. 2.11 shows the expected t_{95} calculated using our model, as a function of τ_d and τ_r. For combinations of τ_d and τ_r that end up below the red-dashed curve, $t_{95} \leq 34$ ns. In other words, such detectors output shorter pulses than the high-end CdTe/CZT detectors to which we compared our results in Sec. 2.4.2 [23,24].

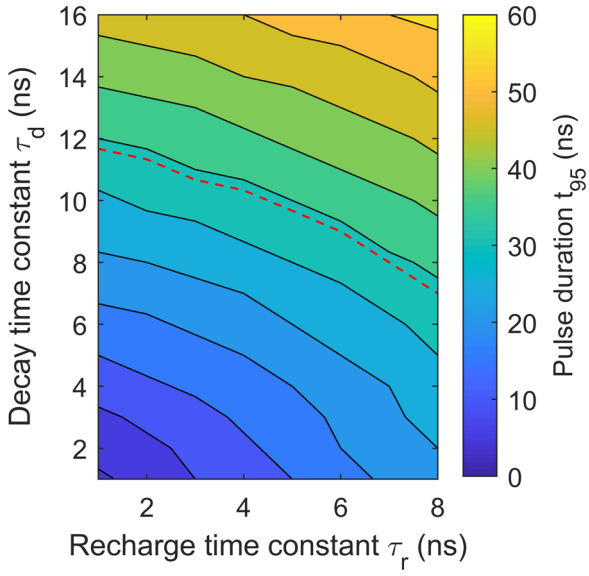

Fig. 2.11. Expected pulse duration t_{95} as a function of the decay time constant τ_d of the scintillator and the recharge time constant τ_r of the SiPM. The red-dashed curve indicates the combinations of τ_d and τ_r that yield $t_{95} = 34$ ns, which is the pulse duration of the state-of-the-art CdTe and CZT detectors to which we compared our results in Sec. 2.4.2 [23,24].

2.6 Conclusion

In this work, we investigate the feasibility of developing SiPM-based scintillation detectors for use in photon-counting CT (PCCT) scanners. To this end, we introduce and experimentally validate a model that can be used to compute the expected energy resolution as well as the expected pulse shape and associated rate capability of such detectors. The model accounts for SiPM saturation and optical crosstalk, as these phenomena may substantially affect the performance of detector pixels with sub-mm dimensions. Such small pixels are required to (1) handle the high incident X-ray photon fluence rate and (2) provide sufficient spatial resolution for PCCT.

Our model calculations indicate that the energy resolution of sub-mm pixels of fast and bright scintillators, such as LYSO:Ce, LuAP:Ce, and $LaBr_3$:Ce, when coupled to currently available SiPMs with a SPAD pitch of 30 μm, degrades with decreasing pixel size as a result of SiPM saturation. Moreover, the recharge time constant of about 55 ns of these SiPMs has a dominant influence on the detector pulse shape, resulting in relatively long detector pulse durations of about 200 ns.

Scintillation detectors based on more advanced SiPMs, having a SPAD pitch of 15 μm and a recharge time constant of 7 ns, appear to have much more favorable properties. In particular, LuAP:Ce and $LaBr_3$:Ce detectors utilizing such SiPMs will generate output pulses that last slightly less than 60 ns, which is in the same order of magnitude as the pulse duration of current PCCT direct-conversion detectors. In particular, scintillation detectors with pixels of about 400 μm or less can yield rate capabilities comparable to high-end CdTe and CZT detectors with pixels of about 500 μm. Moreover, an SiPM-based $LaBr_3$:Ce detector can achieve an energy resolution of 11.5%-13.5% at 60 keV. These numbers also compare well to those of CdTe and CZT detectors.

Based on the current findings, we conclude that it may be feasible to develop SiPM-based scintillation detectors for photon-counting CT that can compete with CdTe and CZT detectors in terms of energy resolution and rate capability.

Acknowledgements

The authors would like to thank René Bakker, Martin van Exter, and Jan Huizenga for their assistance in setting up the experiments. This research was funded in part by a financial contribution from Broadcom Inc.

References

[1] K. Taguchi and J. S. Iwanczyk, "Vision 20/20: Single photon counting x-ray detectors in medical imaging," *Medical physics,* vol. 40, no. 10, 2013, doi: https://doi.org/10.1118/1.4820371.

[2] M. J. Willemink, M. Persson, A. Pourmorteza, N. J. Pelc, and D. Fleischmann, "Photon-counting CT: Technical Principles and Clinical Prospects," (in eng), *Radiology,* vol. 289, no. 2, pp. 293-312, Nov 2018, doi: https://doi.org/10.1148/radiol.2018172656.

[3] S. Leng *et al.*, "Photon-counting Detector CT: System Design and Clinical Applications of an Emerging Technology," *RadioGraphics,* vol. 39, no. 3, pp. 729-743, 2019, doi: https://doi.org/10.1148/rg.2019180115.

[4] T. Flohr, M. Petersilka, A. Henning, S. Ulzheimer, J. Ferda, and B. Schmidt, "Photon-counting CT review," *Physica Medica,* vol. 79, pp. 126-136, 2020, doi: https://doi.org/10.1016/j.ejmp.2020.10.030.

[5] Z. Yu *et al.*, "Evaluation of conventional imaging performance in a research whole-body CT system with a photon-counting detector array," *Physics in Medicine & Biology,* vol. 61, no. 4, p. 1572, 2016, doi: https://doi.org/10.1088/0031-9155/61/4/1572.

[6] A. Pourmorteza *et al.*, "Abdominal imaging with contrast-enhanced photon-counting CT: first human experience," *Radiology,* vol. 279, no. 1, pp. 239-245, 2016, doi: https://doi.org/10.1148/radiol.2016152601.

[7] G. F. Knoll, "Radiation Detection and Measurement," 4th ed. Hoboken, NJ: John Wiley and Sons, 2010, ch. 11, pp. 365-369.

[8] S. Donati and T. Tambosso, "Single-photon detectors: From traditional PMT to solid-state SPAD-based technology," *IEEE Journal of Selected Topics in Quantum Electronics,* vol. 20, no. 6, pp. 204-211, 2014, doi: https://doi.org/10.1109/JSTQE.2014.2350836.

[9] D. R. Schaart, "Physics and technology of time-of-flight PET detectors," *Physics in Medicine & Biology,* vol. 66, no. 9, p. 09TR01, 2021, doi: https://doi.org/10.1088/1361-6560/abee56.

[10] C. Piemonte and A. Gola, "Overview on the main parameters and technology of modern Silicon Photomultipliers," *Nuclear Instruments & Methods in Physics Research A,* vol. 926, pp. 2-15, 2019, doi: https:///doi.org/10.1016/j.nima.2018.11.119.

[11] D. Marano *et al.*, "Accurate analytical single-photoelectron response of silicon photomultipliers," *IEEE Sensors Journal,* vol. 14, no. 8, pp. 2749-2754, 2014, doi: https://doi.org/10.1109/JSEN.2014.2316363.

[12] S. Vinogradov, "Analytical models of probability distribution and excess noise factor of solid state photomultiplier signals with crosstalk," *Nuclear Instruments and Methods in Physics Research A,* vol. 695, pp. 247-251, 2012, doi: https://doi.org/10.1016/j.nima.2011.11.086.

[13] H. T. Van Dam *et al.*, "A comprehensive model of the response of silicon photomultipliers," *IEEE Transactions on Nuclear Science,* vol. 57, no. 4, pp. 2254-2266, 2010, doi: https://doi.org/10.1109/TNS.2010.2053048.

[14] P. Dorenbos, J. T. M. de Haas, and C. Van Eijk, "Non-proportionality in the scintillation response and the energy resolution obtainable with scintillation crystals," *IEEE Transactions on Nuclear Science,* vol. 42, no. 6, pp. 2190-2202, 1995, doi: https://doi.org/10.1109/23.489415.

[15] D. N. ter Weele, D. R. Schaart, and P. Dorenbos, "Intrinsic scintillation pulse shape measurements by means of picosecond x-ray excitation for fast timing applications," *Nuclear Instruments and Methods in Physics Research Section A: Accelerators, Spectrometers, Detectors and Associated Equipment,* vol. 767, pp. 206-211, 2014, doi: https://doi.org/10.1016/j.nima.2014.08.019.

[16] J. T. De Haas and P. Dorenbos, "Advances in yield calibration of scintillators," *IEEE Transactions on Nuclear Science,* vol. 55, no. 3, pp. 1086-1092, 2008, doi: https://doi.org/10.1109/TNS.2008.922819.

[17] M. Balcerzyk, M. Moszynski, Z. Galazka, M. Kapusta, A. Syntfeld, and J. Lefaucheur, "Perspectives for high resolution and high light output LuAP:Ce crystals," *IEEE Transactions on Nuclear Science,* vol. 52, no. 5, pp. 1823-1829, 2005, doi: https://doi.org/10.1109/TNS.2005.856744.

[18] W. Chewpraditkul, C. Wanarak, M. Moszynski, T. Szczesniak, and L. Swiderski, "$Lu_{1.8}Y_{0.2}SiO_5$:Ce and $LaCl_3$:Ce scintillators for gamma-ray detection," in *Advanced Materials Research*, 2011, vol. 284: Trans Tech Publ, pp. 2064-2069, doi: https://doi.org/10.4028/www.scientific.net/AMR.284-286.2064.

[19] A. Phunpueok, W. Chewpraditkul, P. Limsuwan, and C. Wanarak, "Light output and energy resolution of $Lu_{0.7}Y_{0.3}AlO_3$:Ce and $Lu_{1.95}Y_{0.05}SiO_5$:Ce scintillators," *Procedia Engineering,* vol. 32, pp. 564-570, 2012, doi: https://doi.org/10.1016/j.proeng.2012.01.1309.

[20] W. Chewpraditkul and M. Moszynski, "Scintillation properties of $Lu_3Al_5O_{12}$, Lu_2SiO_5 and $LaBr_3$ crystals activated with cerium," *Physics Procedia,* vol. 22, pp. 218-226, 2011, doi: https://doi.org/10.1016/j.phpro.2011.11.035.

[21] L. Swiderski *et al.*, "Scintillation Properties of Praseodymium Doped LuAG Scintillator Compared to Cerium Doped LuAG, LSO and $LaBr_3$," *IEEE Transactions on Nuclear Science,* vol. 56, no. 4, pp. 2499-2505, 2009, doi: https://doi.org/10.1109/TNS.2009.2025040.

[22] A. Gola, A. Ferri, A. Tarolli, N. Zorzi, and C. Piemonte, "SiPM optical crosstalk amplification due to scintillator crystal: effects on timing performance," *Physics in Medicine & Biology,* vol. 59, no. 13, pp. 3615-3635, 2014, doi: https://doi.org/10.1088/0031-9155/59/13/3615.

[23] R. Steadman, C. Herrmann, O. Mülhens, and D. G. Maeding, "ChromAIX: Fast photon-counting ASIC for spectral computed tomography," *Nuclear Instruments and Methods in Physics Research Section A: Accelerators, Spectrometers, Detectors and Associated Equipment,* vol. 648, pp. S211-S215, 2011, doi: https://doi.org/10.1016/j.nima.2010.11.149.

[24] R. Steadman, C. Herrmann, and A. Livne, "ChromAIX2: A large area, high count-rate energy-resolving photon counting ASIC for a spectral CT prototype," *Nuclear Instruments and Methods in Physics Research Section A: Accelerators, Spectrometers, Detectors and Associated Equipment,* vol. 862, pp. 18-24, 2017, doi: https://doi.org/10.1016/j.nima.2017.05.010.

[25] Y. Imai *et al.*, "Development and performance evaluation of an experimental fine pitch detector multislice CT scanner," *Medical physics,* vol. 36, no. 4, pp. 1120-1127, 2009, doi: https://doi.org/10.1118/1.3086117.

[26] S. R. Cherry and J. Qi, "High resolution PET with 250 micrometer LSO detectors and adaptive zoom," Univerisity of California, Davis, CA, 2012. doi: https://doi.org/10.2172/1032741.

[27] F. Godinez, K. Gong, J. Zhou, M. S. Judenhofer, A. J. Chaudhari, and R. D. Badawi, "Development of an ultra high resolution PET scanner for imaging rodent paws: PawPET," *IEEE transactions on radiation and plasma medical sciences,* vol. 2, no. 1, pp. 7-16, 2017, doi: https://doi.org/10.1109/TRPMS.2017.2765486.

[28] H. B. Bhandari *et al.*, "Large-area crystalline microcolumnar $LaBr_3$:Ce for high-resolution gamma ray imaging," *IEEE Transactions on Nuclear Science,* vol. 60, no. 1, pp. 3-8, 2012, doi: https://doi.org/10.1109/TNS.2012.2213612.

[29] H. Sabet, L. Bläckberg, D. U. Ozsahin, A. Sitek, and G. El-Fakhri, "A sub-mm spatial resolution LYSO: Ce detector for small animal PET," in *2015 IEEE Nuclear Science Symposium and Medical Imaging Conference (NSS/MIC)*, 2015: IEEE, pp. 1-4, doi: https://doi.org/10.1109/NSSMIC.2015.7582201.

[30] L. Bläckberg *et al.*, "Exploring light confinement in laser-processed LYSO: Ce for photon counting CT application," *Physics in Medicine & Biology,* vol. 64, no. 9, p. 095020, 2019, doi: https://doi.org/10.1088/1361-6560/ab1213.

Appendix to Chap. 2

This appendix consists of two sections. In the first one, it is discussed how several input parameters of the model presented in Chap. 2 were experimentally determined. The model is used to calculate the expected performance of a detector based on a fourth promising scintillator in the second section. This scintillator is $YAlO_3$:Ce (YAP:Ce).

A2.1 Determination of SiPM parameters

In this section, it is discussed how the optical crosstalk parameter λ, the mean single-SPAD response, and the recharge time constant τ_r of the 1×1 mm^2 SiPM that was used in the model validation experiments were determined from a measurement of dark triggers (see Sec. 2.3.1 and Table 2.2). Only the methodology and the results for an overvoltage of 3.0 V are included here.

The detector was placed in a light-tight box and not exposed to ionizing radiation for the measurement of dark triggers. The 0.9×0.9×1.0 mm^3 LuAP:Ce scintillation crystal was glued to the SiPM and covered in PTFE powder, because these conditions are expected to increase the number of crosstalk photon-induced triggers per dark trigger compared to a bare SiPM [1]. The SiPM was operated at an overvoltage of 3.0 V. A histogram of the integrals of about 10^5 recorded dark pulses was generated. As shown in Fig. A2.1, such a histogram shows several equally spaced peaks. The k^{th} peak corresponds to a dark trigger plus k-1 crosstalk photon-induced triggers. The Borel distribution with $n_{\text{tr.oc}}=k$ and fitting parameter λ (see Eqn. (2.3)) was fitted through the fraction of events in each peak in order to determine the value of λ. A value of 0.184 was found.

The pulses of the events in the central part of the first peak were used to determine the mean pulse shape of the single-SPAD-response. As shown in Fig. A2.2, an exponentially decaying function with the recharge time constant τ_r as a fitting parameter was fitted through the tail of that pulse in order to determine the value of τ_r. A value of 39.3 ns was found.

Section A2.1 is based on S. J. van der Sar, S. E. Brunner, and D. R. Schaart, "Silicon photomultiplier-based scintillation detectors for photon-counting CT: A feasibility study," *Medical Physics,* vol. 48, no. 10, pp. 6324-6338, 2021, whereas section A2.2 is based on S. J. van der Sar and D. R. Schaart, "Silicon Photomultiplier-Based Scintillation Detectors for Photon-Counting X-Ray Imaging," in *Radiation Detection Systems*. Boca Raton, FL, USA: CRC Press, 2021, pp. 289-312.

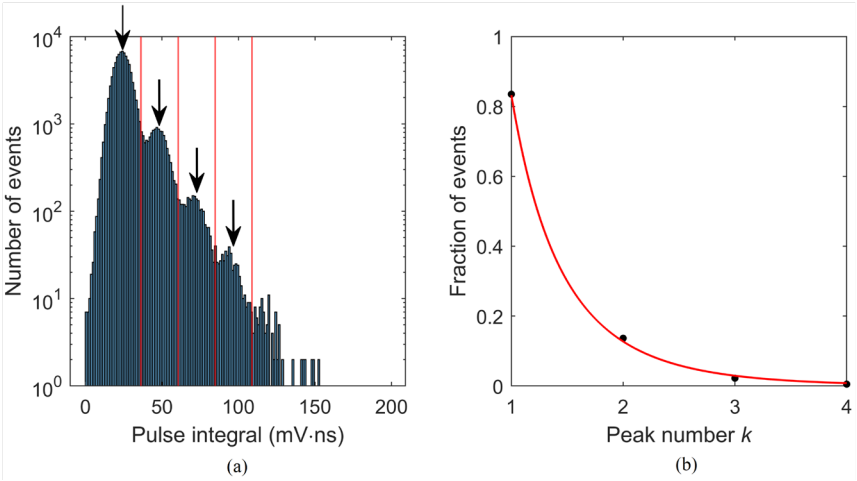

Fig. A2.1. Illustration of the method used to determine the optical crosstalk parameter λ. (a) A histogram of measured dark pulse integrals shows several equally-spaced peaks indicated by the arrows. The fraction of events in each peak is determined using the equally spaced vertical red lines as borders between the peaks. (b) The red curve is a fit of the Borel distribution with $n_{\mathrm{tr.oc}}=k$ and fitting parameter λ (see Eqn. (2.3)) through the measured fraction of events as a function of the peak number k. The value of λ was determined from this fit.

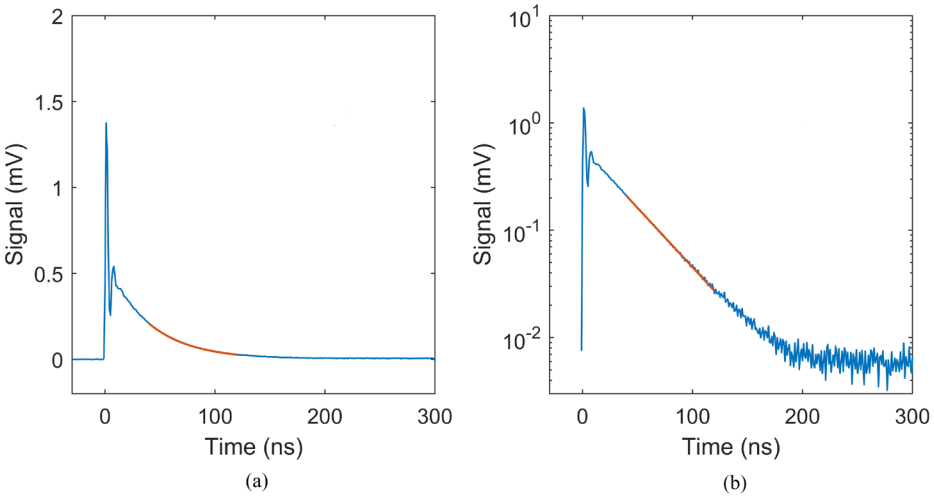

Fig. A2.2. The mean pulse shape of the single-SPAD response on (a) linear scale and (b) logarithmic scale. An exponentially decaying function with the recharge time constant τ_r as a fitting parameter was fitted through the tail of the pulse in order to determine the value of τ_r.

A2.2 Model calculations for YAP:Ce

The expected performance of $LaBr_3$:Ce, LuAP:Ce, and LYSO:Ce scintillation detectors with SiPM readout based on model calculations was presented in Sec. 2.4.2. $LaBr_3$:Ce turned out to be the most promising material, approaching the performance of state-of-the-art CdTe and CZT detectors developed and optimized for photon-counting X-ray CT. A fourth, readily available, cerium-doped, inorganic scintillator is $YAlO_3$:Ce (YAP:Ce). Here, the model calculations for YAP:Ce (and $LaBr_3$:Ce) are presented.

Table A2.1 summarizes the material properties of YAP:Ce and $LaBr_3$:Ce. Compared to $LaBr_3$:Ce, YAP:Ce has a somewhat slower scintillation response (longer decay time constant τ_d), and needs a thicker crystal to absorb equally many X-ray photons (due to the relatively low atomic number of yttrium). On the other hand, the light yield of YAP:Ce is even more proportional, and the material is not hygroscopic. The emission spectra of both scintillators are similar, so the same value for the photodetection efficiency (PDE) of the SiPM may be used for both scintillators in the model calculations. This and other SiPM parameters used in the model are given in Table 2.4 (bold face). Also in this appendix, two types of SiPM are studied, i.e., an SiPM with a SPAD pitch of 30 µm operated at an overvoltage of 3.0V, and an SiPM with a SPAD pitch of 15 µm, operated an overvoltage of 7.0 V.

Fig. A2.3 shows the outcomes of the model calculations for the combination of YAP:Ce and SiPMs with a SPAD pitch of 30 µm. As shown in Fig. A2.3(a), pixels as small as 200 µm are needed to achieve a similar rate capability as the reference CdTe/CZT detector with 500 µm pixels, for example. This is mainly due to the long recharge time constant of 55 ns of these SiPMs, which causes t_{95} (see Sec. 2.2.6 and Fig. 2.4) to be just

Table A2.1. Properties of the $LaBr_3$:Ce and YAP:Ce scintillators and input parameters for the model calculations. The required thickness is based on an X-ray absorption efficiency near 100% at 50 keV, around 90% at 100 keV and around 55% at 150 keV. $LaBr_3$:Ce data were obtained from Luxium Solutions (formerly Saint Gobain Crystals), and YAP:Ce data from Crytur, unless otherwise indicated.

Scintillator	**$LaBr_3$:Ce**	**YAP:Ce**
Light yield Y (photons/keV)	63	25
Non-proportionality factor f	0.98 [2]	1.00[3,4]
Intrinsic resolution R_{intr} (%)	8.0 [2]	4.0 [3,4]
Decay time constant τ_d (ns)	16	25
Mass density (g cm^{-3})	5.1	5.4
Required thickness (mm)	3.5	7.0

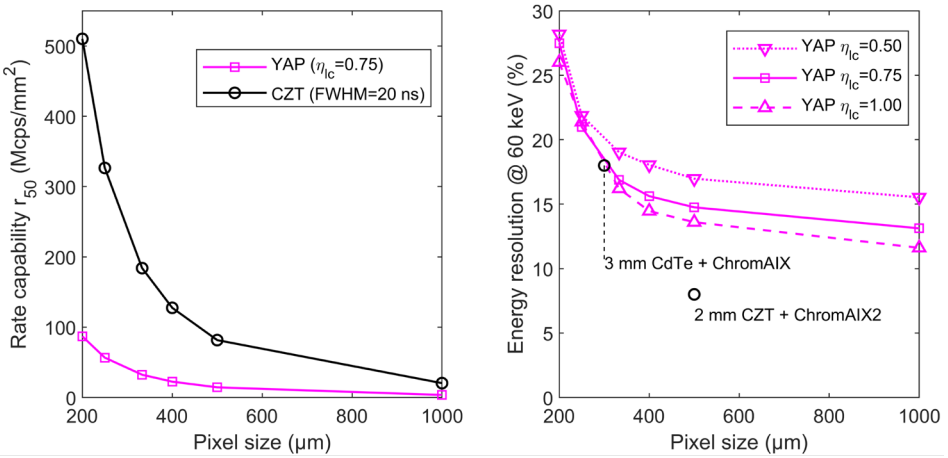

(a) (b)

Fig. A2.3. (a) Rate capability r_{50} and (b) energy resolution at 60 keV, both as a function of pixel size, and the latter also as a function of light collection efficiency (η_{lc}), for YAP:Ce scintillators coupled to the SiPMs with a SPAD pitch of 30 µm. The pulse duration, and therefore r_{50}, hardly depends on η_{lc}, so r_{50} is only shown for $\eta_{lc} = 0.75$. For comparison, data points reported for CdTe- and CZT-based photon-counting detectors are also shown [5,6].

below 200 ns. Note that the energy resolution severely degrades for such small pixels due to SiPM saturation (Fig. A2.3(b)).

Fig. A2.4 shows the results of the model computations for the same YAP:Ce scintillator, when combined with the SiPMs with a SPAD pitch of 15 µm. The rate capability has considerably improved and the negative effect of SiPM saturation has been greatly reduced. The value of t_{95} is about 80 ns, due to the much shorter recharge time constant of these SiPMs. Fig. A2.4(a) shows that a pixel size of 333 µm would provide similar rate capability as the reference CdTe/CZT detector with 500 µm pixels, for example. As shown in Fig. A2.4(b), the values of the achievable energy resolution lie in between the two reference values for CdTe/CZT detectors.

However, Fig. A2.4 also shows that the performance of the YAP:Ce detector is not as good as that of the $LaBr_3$:Ce detector, both regarding rate capability and energy resolution. Meanwhile, YAP:Ce offers better rate capability than LYSO:Ce, and better energy resolution than both LuAP:Ce and LYSO:Ce. This can be appreciated by comparing the data in Fig A2.4 to the the data in Fig. 2.8. As such, YAP:Ce may be the most interesting readily available and non-hygroscopic alternative to $LaBr_3$:Ce, especially given that the very common slow scintillation decay component in LuAP:Ce, which was also observed in Sec 2.3.1, is usually much less intense in YAP:Ce.

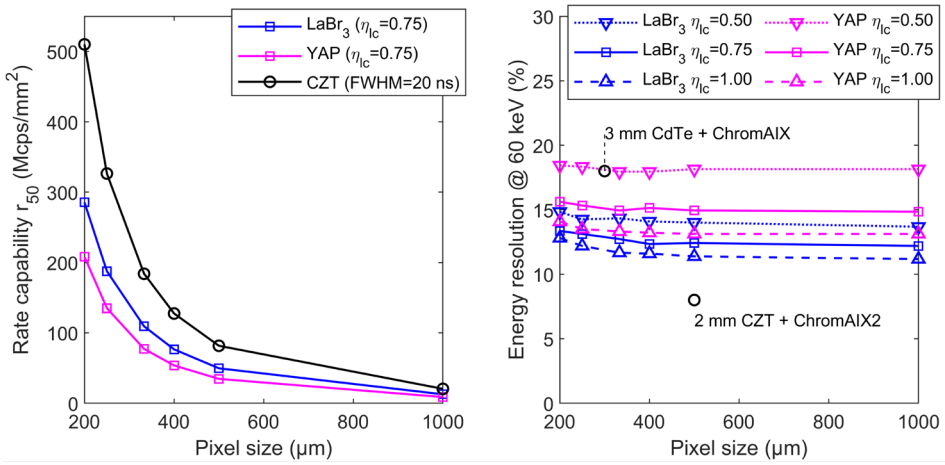

(a) (b)

Fig. A2.4. (a) Rate capability r_{50} and (b) energy resolution at 60 keV, both as a function of pixel size, and the latter also as a function of light collection efficiency (η_{lc}), for YAP:Ce and $LaBr_3$:Ce scintillators coupled to the SiPMs with a SPAD pitch of 15 µm. The pulse duration, and therefore r_{50}, hardly depends on η_{lc}, so r_{50} is only shown for $\eta_{lc} = 0.75$. Data for $LaBr_3$:Ce are the same as in Fig. 2.9. For comparison, data points reported for CdTe- and CZT-based photon-counting detectors are also shown [5,6].

References

[1] A. Gola, A. Ferri, A. Tarolli, N. Zorzi, and C. Piemonte, "SiPM optical crosstalk amplification due to scintillator crystal: effects on timing performance," *Physics in Medicine & Biology,* vol. 59, no. 13, pp. 3615-3635, 2014, doi: https://doi.org/10.1088/0031-9155/59/13/3615.

[2] L. Swiderski *et al.*, "Scintillation Properties of Praseodymium Doped LuAG Scintillator Compared to Cerium Doped LuAG, LSO and $LaBr_3$," *IEEE Transactions on Nuclear Science,* vol. 56, no. 4, pp. 2499-2505, 2009, doi: https://doi.org/10.1109/TNS.2009.2025040.

[3] M. Moszyński, M. Kapusta, D. Wolski, W. Klamra, and B. Cederwall, "Properties of the YAP: Ce scintillator," *Nuclear Instruments and Methods in Physics Research Section A,* vol. 404, no. 1, pp. 157-165, 1998, doi: https://doi.org/10.1016/S0168-9002(97)01115-7.

[4] M. Moszyński *et al.*, "Energy resolution of scintillation detectors," *Nuclear Instruments and Methods in Physics Research Section A,* vol. 805, pp. 25-35, 2016, doi: https://doi.org/10.1016/j.nima.2015.07.059.

[5] R. Steadman, C. Herrmann, O. Mülhens, and D. G. Maeding, "ChromAIX: Fast photon-counting ASIC for spectral computed tomography," *Nuclear Instruments and Methods in Physics Research Section A: Accelerators, Spectrometers, Detectors and Associated Equipment,* vol. 648, pp. S211-S215, 2011, doi: https://doi.org/10.1016/j.nima.2010.11.149.

[6] R. Steadman, C. Herrmann, and A. Livne, "ChromAIX2: A large area, high count-rate energy-resolving photon counting ASIC for a spectral CT prototype," *Nuclear Instruments and Methods in Physics Research Section A: Accelerators, Spectrometers, Detectors and Associated Equipment,* vol. 862, pp. 18-24, 2017, doi: https://doi.org/10.1016/j.nima.2017.05.010.

3 Performance of X-ray photon-counting scintillation detectors under pile-up conditions at 60 keV

Abstract

Silicon photomultiplier (SiPM)-based scintillation detectors have hardly been investigated for medical X-ray photon-counting applications. The input count rate (ICR) in these applications is so high that pulse pile-up can severely distort the measurement of counts and energies. Here, we experimentally evaluate the counting and spectral performance of SiPM-based scintillation detectors at 60 keV as a function of ICR.

We coupled 0.9×0.9×3.5 mm^3 LYSO:Ce and 0.9×0.9×4.5 mm^3 YAP:Ce scintillators to 1.0×1.0 mm^2 ultrafast SiPMs and exposed these single-pixel detectors to a 10 GBq Am-241 source. We varied the ICR from 0 to 5 Mcps/pixel and studied detector performance for paralyzable-like and nonparalyzable-like counting algorithms, after applying a second-order low-pass filter with a cut-off frequency f_c of 5 MHz, 10 MHz, or 20 MHz to the pulse trains. Counting performance was quantified by the output count rate (OCR) and the count-rate loss factor (CRLF). In addition to the traditional spectral performance measure of the full-width-at-half-maximum (FWHM) energy resolution at low ICR, we propose the spectral degradation factor (SDF) to quantify spectral effects of pile-up at any ICR.

Best counting performance is obtained with nonparalyzable-like counting and f_c = 20 MHz, for which the count-rate loss is at most 10% in the investigated range of ICRs, whereas paralyzable-like counting performs better from a spectral point-of-view. Due to less pile-up, the fastest pulses obtained with f_c = 20 MHz already provide the best SDF values at ICRs of a few Mcps/pixel, despite their worse low-rate energy resolution.

As such, the overall performance under clinical operating conditions appears to benefit more from a substantially faster pulse than from a somewhat better low-rate energy resolution. Moreover, the pulse shape of SiPM-based scintillation detectors is such that spectral degradation due to pile-up can be mitigated by integrating a dedicated peak detection window (DPDW) into the counting algorithms.

3.1 Introduction

The development of energy-resolving photon-counting detectors (PCD) as an alternative to energy-integrating detectors for hard, poly-energetic X-ray imaging applications, in particular for diagnostic X-ray computed tomography (CT), has become a hot topic of research [1,2,3]. These detectors aim to count the number of incident X-ray photons and to measure the energy of each of these photons, thereby enabling improvements in imaging quality (contrast-to-noise ratio) and creating opportunities for spectral imaging beyond dual-energy techniques.

In the case of diagnostic CT, X-ray tube voltages up to 150 kV are used and the PCDs under development typically assign the detected photons to one of a few energy bins that span the X-ray tube spectrum. A major challenge in this application is the photon fluence rate incident on the detector, which can exceed 10^8 photons/s/mm^2 [4]. Prototype diagnostic PCD-CT systems are therefore equipped with direct-conversion detectors based on the semiconductors CdTe [5], $Cd_{1-x}Zn_xTe$ (CZT, x typically 0.1 or 0.2) [6], or Si [7]. This type of detector provides a fast detector pulse (typically tens of nanoseconds wide) in response to an X-ray photon and enables relatively easy fabrication of miniaturized pixels (typically smaller than 0.5×0.5 mm^2), so that the negative effects of pulse pile-up on the correct counting of photons and on the energy determination can be mitigated to some extent.

In a direct-conversion detector, an X-ray photon releases a number of electron-hole pairs, which travel to opposite electrodes under the influence of an electric field, thereby inducing current pulses. A pixelated detector is obtained by dividing one of the electrodes into small elements, the pitch of which sets the pixel size. Stable and reliable performance of such semiconductor detectors requires good and uniform charge transport characteristics. However, issues with the cost-effectiveness of growing CdTe and CZT of the required quality may remain [1,8]. In addition, the number of manufacturers that can synthesize these high-quality materials is limited. Si does not have these drawbacks, but it has a relatively low mass density (ρ=2.3 g·cm^{-3}) and atomic number (Z=14) for hard X-ray applications. It thus remains unclear what the best choice of detector is, leaving room for developing other types of detector.

We are investigating detectors based on scintillators and silicon photomultipliers (SiPM) as an alternative to direct-conversion detectors [9,10]. Fig. 3.1(a) shows that SiPM-based scintillation detectors rely on the principle of indirect conversion, i.e., each X-ray photon absorbed in a scintillator is converted into a number of optical photons, which are in turn converted into a current pulse by an SiPM. Note that generally only one side of the scintillator is coupled to the SiPM. Since the scintillation photons are isotropically emitted, the other sides of the scintillator are usually covered in reflective material in order to optimize the light collection on the SiPM. In a pixelated detector with a one-to-one coupling of scintillator and SiPM, the reflectors also prevent light sharing between pixels. However, they can form a relatively large dead area in arrays of

miniaturized pixels, thereby reducing the dose efficiency. In previous work [9,10,11], we mentioned a few potential solutions for this issue (also see Sec. 6.3.1 of this thesis).

To a first approximation, the total number of optical photons detected by the SiPM is proportional to the energy deposited by the X-ray photon (in the order of 10^0-10^1 photons/keV), and the probability that the detection of an optical photon occurs at a time t_1 after the interaction of the X-ray photon is proportional to $\exp(-t_1/\tau_d)$. Here, τ_d is the decay time constant of the scintillator. Fig. 3.1(b) contains an example of a time distribution of detected scintillation photons.

The SiPM itself is a two-dimensional array of single-photon avalanche diodes (SPAD), as Fig. 3.1(c) shows. If an optical photon is absorbed in one of the SPADs, the resulting electron-hole pair may trigger an avalanche multiplication process, which is quenched by a resistor R (see Fig. 3.1(c)), and gives rise to an internal gain in the order of 10^5-10^6. The time profile of the resulting current pulse, which is called the single-SPAD response (SSR), may be described as being proportional to $\exp(-t_2/\tau_r)$ with t_2 the time since the absorption of the optical photon and τ_r the recharge time constant of the SiPM. Fig. 3.1(d) shows an example of an SSR. Since all SPADs on an SiPM are connected in parallel (Fig. 3.1(c)), the raw detector pulse is essentially a convolution of $\exp(-t_1/\tau_d)$ and $\exp(-t_2/\tau_r)$, the pulse height or integral of which is a measure of the energy deposited by the X-ray photon. An example of a raw detector pulse is provided in Fig. 3.1(e).

In previous work [9,11], presented in Chap. 2 and Appendix A2.2 of this thesis, we identified four scintillators that may provide reasonable count rate capability and/or energy resolution for X-ray photon-counting applications if read out by a particular SiPM with $\tau_r < 10$ ns. These scintillators offer high density and atomic number and are readily available. Moreover, scintillation detectors in general rely on light transport rather than charge transport. This potentially allows for cost-effective manufacturing of stable and reliable detectors. Indeed, the vast majority of medical imaging systems are equipped with scintillation detectors. Meanwhile, SiPMs are a rational choice of light sensor. They provide high internal gain, thereby amplifying the signal due to a single X-ray photon above the noise level of the electronics (in contrast to standard photodiodes). Moreover, they allow for pixel size miniaturization (in contrast to photomultiplier tubes). SiPMs have recently found application in the advanced (clinical) positron emission tomography (PET) scanners of all major vendors [12]. The high internal gain of SiPMs ensures that SiPM-based scintillation detectors output in the order of 10^5-10^7 electron-hole pairs per keV of deposited X-ray photon energy, whereas CdTe/CZT detectors yield in the order of 10^2 electron-hole pairs per keV. Consequently, the typical pulse processing chain for direct-conversion detectors, which consists of a charge-sensitive preamplifier, a CR-RC^n pulse shaper with a pole-zero cancellation circuit and baseline restorer, and a number of comparators with associated counters for the energy binning [13], can in principle be simplified to just a trans-impedance preamplifier, which essentially maintains the raw pulse shape, and the comparators and counters. However, due to the relatively low number of optical photons detected by the SiPM per unit time in response to a single X-ray photon absorbed in the scintillator, a typical raw

detector pulse is not a perfect convolution of two decaying exponentials, but subject to statistical fluctuations. This is visualized in Fig. 3.1(e) and negatively affects the counting of X-ray photons as well as their assignment to energy bins.

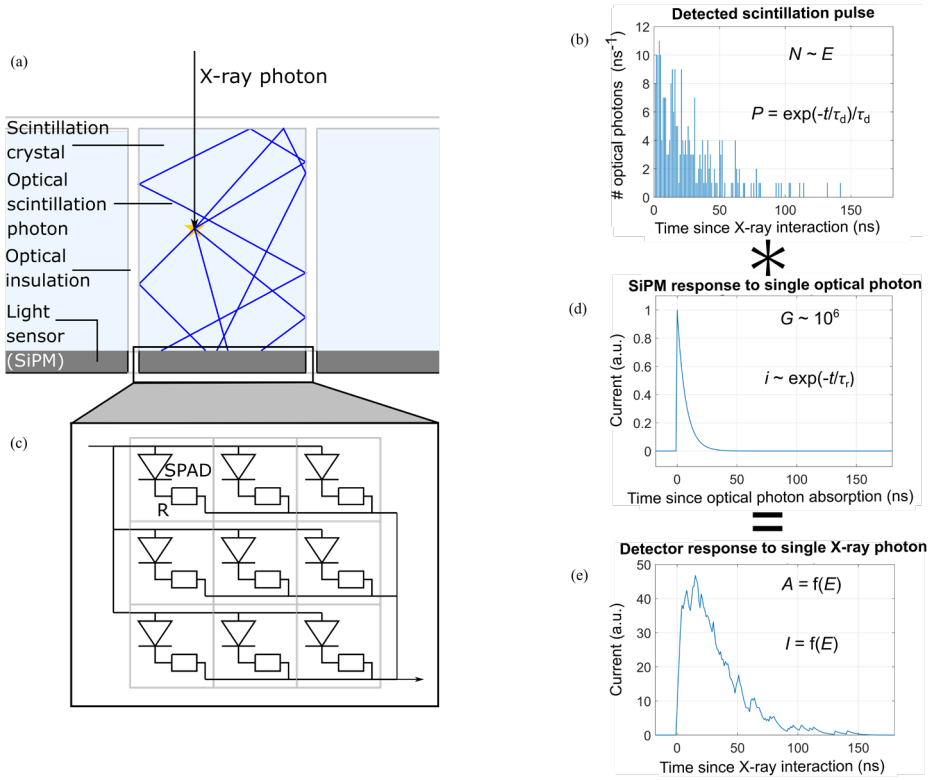

Fig. 3.1. (a) Silicon photomultiplier (SiPM)-based scintillation detectors rely on the principle of indirect conversion, i.e., an X-ray photon absorbed in a scintillator is first converted into ~10^1 optical scintillation photons per keV of deposited energy (only 5 shown here), which are isotropically emitted and guided towards the SiPM by some form of reflective optical insulation. (b) To a first approximation, the number N of optical photons detected by the SiPM (usually less than 50% of all generated scintillation photons) is proportional to the energy E deposited by the X-ray photon, and these photons are distributed in time according to an exponential probability density function P characterized by the decay time constant τ_d. Here, we show an example of such a distribution for 250 detected scintillation photons and τ_d = 30 ns. (c) The SiPM itself is a 2D array of ~10^2-10^4 single-photon avalanche diodes (SPAD, only 9 shown here) per mm^2, in which a detected optical photon initiates an avalanche multiplication process (gain G ~ 10^6) that is quenched by a resistor R. (d) The resulting current pulse is called the single-SPAD response and may be described as a decaying exponential characterized by the recharge time constant τ_r, which was set to 7 ns here. (e) Since the SPADs are connected in parallel (see (c)), the detector output current pulse is a convolution of the two decaying exponentials in (b) and (d), although affected by statistical fluctuations due to the relatively low number of scintillation photons detected per unit time. Both its amplitude A and integral I depend on E.

Therefore, our goal in this work is to evaluate different processing methods for the combined measurement of counts and energy using SiPM-based scintillation detectors. We not only do so at low fluence rates, but also under conditions of high pile-up, as can be expected in (medical) X-ray photon-counting applications. To this end, we conduct experiments in which we gradually increase the input count rate (ICR), i.e., the number of X-ray photons that deposit energy in the detector per unit time, and quantify the counting performance and spectral performance of each method as a function of ICR. We investigate an in-house developed single-pixel detector consisting of an LYSO:Ce scintillation crystal coupled to an ultrafast SiPM. LYSO:Ce has found widespread use in detectors for clinical PET scanners. As such, it is an example of a detection material that combines stable and reliable performance over time with cost-effective manufacturing. We perform a similar study for another detector consisting of a YAP:Ce scintillation crystal coupled to the same ultrafast SiPM. YAP:Ce has not found widespread use in clinical imaging systems yet. Nevertheless, it is a readily available and we expect it to perform better than LYSO:Ce based on our previous work [9,10], presented in Chap. 2 and Appendix A2.2 of this thesis.

3.2 Materials and methods

3.2.1 Data acquisition

We built two single-pixel detectors by optically coupling a 0.9×0.9×3.5 mm^3 $Lu_{1.8}Y_{0.2}SiO_5$:Ce scintillation crystal (LYSO, ρ=7.1 g/cm^3, Shanghai Project Crystal) and a 0.9×0.9×4.5 mm^3 $YAlO_3$:Ce scintillation crystal (YAP, ρ=5.4 g/cm^3, Crytur) to 1.0×1.0 mm^2 SiPMs (Broadcom Inc.) using Norland Optical Adhesive 63 and Norland Optical Adhesive 88, respectively. We selected these adhesives, because their transmission spectra match well with the emission spectra of the scintillators. We then submerged the crystals in reflective polytetrafluoroethylene (PTFE, Teflon) powder, which we compressed to increase the light collection on the SiPMs.

The SiPMs are based on Broadcom's near-ultraviolet high-density (NUV-HD) technology and feature a SPAD pitch of 15 μm and an ultrafast single-SPAD response with a recharge time constant τ_r = 7 ns. Consequently, the SSR will hardly elongate the raw detector pulses if the scintillator is LYSO or YAP, for which we measured decay time constants τ_d of 33 ns (LYSO) and 29 ns (YAP) following the method described in [14]. Furthermore, the crosstalk probability is low (<10%), and afterpulsing is negligible. However, the optical photon detection efficiency (PDE) is only between 20% and 30% in the relevant wavelength range. Information about the meaning of these SiPM characteristics can be found elsewhere, e.g., in [15].

We exposed the detectors to a 10 GBq Am-241 source that effectively functions as a mono-energetic source of 60 keV photons, because its lower-energy photon emissions are largely absorbed by the source window. Mono-energetic radiation makes it more straightforward to evaluate spectral detector performance than a poly-energetic photon

beam from an X-ray tube does, as the true energy of every detected photon is known a priori. By varying the source-detector distance (SDD), we were able to study the detector performance for various input count rates and pile-up levels. It should be noted that the selected crystal thicknesses of 3.5 mm (LYSO) and 4.5 mm (YAP) were not selected with a specific X-ray photon-counting application in mind, but allowed to minimize the SDD given the specific geometry of the Am-241 source.

The raw detector signals were amplified by an AD8099 trans-impedance amplifier with a gain of 10. The amplifier's output was fed into a Teledyne LeCroy HDO9409 digital oscilloscope operating at a bandwidth of 200 MHz and a sampling rate of 1 GS/s. In this way, ten pulse trains of 100 ms were digitized for each detector and SDD. Various processing methods were then applied to the digitized pulse trains. They are described in more detail in the next two subsections. However, we first checked, for both detectors, if there was a baseline shift in the pulse trains measured at the longest SDD. If so, we subtracted that offset from all pulse trains measured by that detector.

3.2.2 Pulse processing *I*: Second-order low-pass filters

The use of low-pass filters is a straightforward and practical way to get rid of the fluctuations on the raw pulses that were discussed in Sec. 3.1 and shown in Fig. 3.1(e). Such filters are characterized by their cut-off frequency f_c. A filter with a lower value of f_c more strongly reduces the fluctuations on the pulses, but also gives rise to more amplitude loss and pulse elongation. Vice versa, we expect higher count rate capability, but worse pulse height (i.e., energy) resolution from a filter with a higher value of f_c.

The number of low-pass filters applied in succession is called the order of the filter. Higher-order filters achieve with higher values of f_c a remaining level of pulse fluctuations that is comparable to that of a first-order filter, thereby producing faster pulses. As such, they seem well suited for high-rate X-ray photon-counting applications. However, higher-order filters also lead to more pulse amplitude loss, so the useful range of filter orders is limited. Hence, we only worked with second-order low-pass filters in this study.

In a histogram of the maximum signal recorded between each positive and subsequent negative crossing of a predefined threshold, pulse fluctuations appear as a peak just above the threshold level (see Sec. 3.2.3 for how we determined these levels). We found that this peak remained absent up to values of f_c around 20 MHz, for both the LYSO and the YAP detector. We also found that the pulse amplitude loss became too large for values of f_c less than 5 MHz. We therefore studied second-order low-pass filters with three values of f_c, namely 5 MHz, 10 MHz, and 20 MHz. The effect of these filters on a measured pulse train can be observed in Fig. 3.2.

All filters were implemented in the time domain. The differential equation that describes how the output voltage V_{out} of a first-order low-pass filter depends on the input voltage V_{in}, the time derivative of V_{out} and f_c reads:

$$V_{\text{out}}(t) = V_{\text{in}}(t) - \frac{1}{2\pi f_c}\frac{dV_{\text{out}}}{dt} \tag{3.1}$$

This was discretized into the following form using the backward differentiation method:

$$V_{\text{out}}[n] = \frac{2\pi f_c \Delta t}{1+2\pi f_c \Delta t} V_{\text{in}}[n] + \frac{1}{1+2\pi f_c \Delta t} V_{\text{out}}[n-1] \tag{3.2}$$

Here, n indicates the sample number and Δt the sampling period (1 ns in our case as the sampling rate of the digital oscilloscope was 1 GS/s). We applied Eqn. (3.2) twice to emulate the effect of a second-order filter.

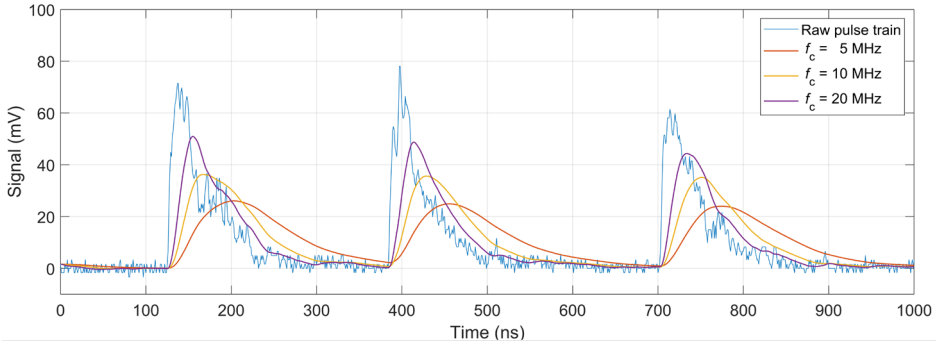

Fig. 3.2. Example of a part of a raw pulse train measured with the LYSO detector and its second-order low-pass filtered versions for cut-off frequencies f_c equal to 5 MHz, 10 MHz, and 20 MHz. The higher f_c., the faster the pulses and the smaller the pulse amplitude loss. On the other hand, the fluctuations on the pulses are less dampened by filters with a higher value of f_c.

3.2.3 Pulse processing *II*: Counting algorithms

We implemented two counting algorithms to extract energy-resolved photon-counting data from the filtered pulse trains. These algorithms are described in the following.

Paralyzable-like (p-like) counting

A count is registered when a filtered pulse train causes a positive crossing of a threshold. We call the maximum signal between this positive threshold crossing and the subsequent negative threshold crossing the pulse height (see Fig. 3.3(a)). It is usually a good measure of the energy deposited by the X-ray photon. However, if a pulse piles up on the tail of the previous pulse, as shown in Fig. 3.3(b), the pulse height yields a wrong measurement of the energy. Furthermore, if an X-ray photon interacts in the detector before the previous pulse has dropped below the threshold level, the new pulse will not cause a positive threshold crossing and only one count, with an incorrect energy, is registered (see Fig. 3.3(c)). This type of counting gives rise to paralyzable-like (p-like) behavior, which means that the number of registered counts per unit time, i.e., the output count rate (OCR), is proportional to the input count rate at low values of ICR,

but starts to deviate at higher values, until it reaches a maximum. The OCR then starts to decrease and approaches zero for very high values of ICR. In that case, the pulse train is above threshold almost all the time, so hardly any threshold crossings occur, and hardly any counts are registered.

In this work, we set the count detection threshold to a voltage level equivalent to about 25 keV, which we calculated for each value of the cut-off frequency by multiplying the mean pulse height as determined from a Gaussian fit to the histogram of pulse height values measured at the longest SDD with that cut-off frequency by a factor 25/60 ≈ 0.4167. Thresholds in the range of 20 keV to 30 keV are commonly implemented in CdTe- and CZT-based PCDs for diagnostic CT, because they are above the noise floor of these detectors and at the lower end of the (hardened) X-ray tube spectra typically used in this application. It is noted that spectral PCDs additionally have multiple higher (often adjustable) thresholds. These are only used to assign the counts to energy bins, and do not limit the count rate capability of the detectors [16,17], so they are not of interest to this study.

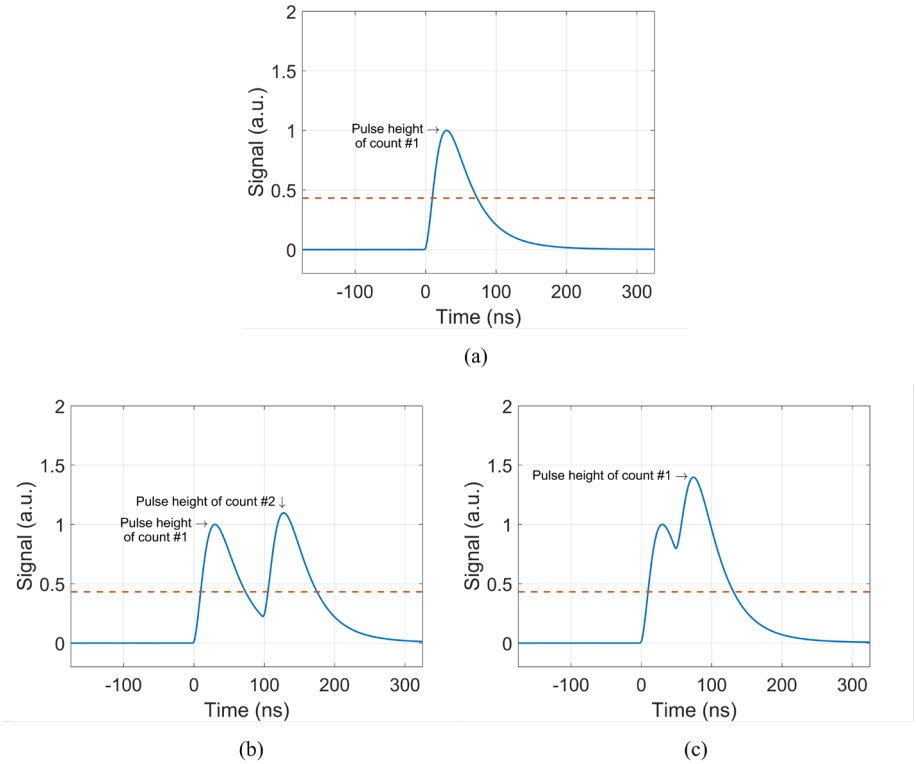

Fig. 3.3. (a) The paralyzable-like counting algorithm registers a count when a positive threshold (dashed line) crossing takes place. The maximum signal before the next negative threshold crossing is considered the pulse height of that count and therefore a measure of the energy deposited by the absorbed 60 keV photon. (b) When a pulse piles up on the tail of a previous one, the pulse height associated with the second count is distorted. (c) When a pulse is generated before the previous one has decayed to below the threshold level, only one count is registered and the pulse height of that count is distorted.

The peak in each pulse height histogram measured with the YAP detector was found to be asymmetric, mainly due to K-escape events. We therefore fitted two Gaussians through such peaks. Since the energy of the K X-rays of yttrium (Y) is about 15 keV, the K-escape peak is located around 45 keV. We therefore implemented a constraint that the Gaussian corresponding to the K-escape peak must be centered around 45/60×100% = 75% of the mean value of the main Gaussian.

Nonparalyzable-like (np-like) counting

A nonparalyzable-like (np-like) counting algorithm allows to register two counts for the superposition of the two pulses in Fig. 3.3(c). It can be implemented by evaluating, after a fixed time period of length τ_{np} following a positive threshold crossing (the first count), whether or not the pulse train is still above threshold [18]. If so, a second count is registered and the same evaluation will be repeated after another period of length τ_{np} (see Fig. 3.4(a)). If the outcome of the evaluation is negative, the next count is only registered when the next positive threshold crossing occurs. In the case of very high ICR, the pulse train is above threshold more or less all the time, so the outcome of almost every evaluation is positive, and OCR approaches an asymptotic value of $1/\tau_{np}$. This is nonparalyzable behavior. We refer to the maximum signal within a time window of length τ_{np} as the pulse height and consider it a measure of the energy associated with the corresponding count. Distorted energy measurements are therefore still possible under pile-up conditions (see Fig. 3.4(a)).

It is important that τ_{np} exceeds the time-over-threshold (ToT) of the pulses in order to prevent double counting of a single X-ray photon, as visualized in Fig. 3.4(b). We therefore created histograms of the ToT of all pulses registered as counts by the p-like algorithm at the longest SDD, for all three values of f_c and for both detectors. The histograms contained a dominant peak, which means that (almost) all pulses had a ToT less than a certain ToT_{max}, i.e., the ToT corresponding to the right side of the peak. We defined τ_{np} to be 110% of ToT_{max} in order to ensure that, in the case of pile-up, when the ToT of the second pulse may be elongated, the algorithm still registers two counts instead of three. The values of τ_{np} obtained in this way are 99 ns (f_c = 20 MHz), 121 ns (f_c = 10 MHz), and 176 (f_c = 5 MHz) for the LYSO detector, and 88 ns (f_c = 20 MHz), 115 ns (f_c = 10 MHz), and 170 (f_c = 5 MHz) for the YAP detector. The faster scintillation decay of YAP (see Sec. 3.2.1) explains the lower values for this detector.

3.2.4 Performance measure *I*: Spectral

We first determined the best achievable spectral performance of the two detectors, at low input count rate, using a digital signal processing technique that may not be trivial to implement in practical imaging systems with a high channel density. This method is called the ‘gold-standard method’ in this work. We filtered the pulse trains recorded at the longest source-detector distance using a median filter of 21st order. Such a filter preserves the steep rising edges of the raw detector pulses, but still suppresses the fluctuations on these pulses. The median filtered pulse trains can therefore be used to determine accurately the number of pulses in the pulse train and the timestamp of the

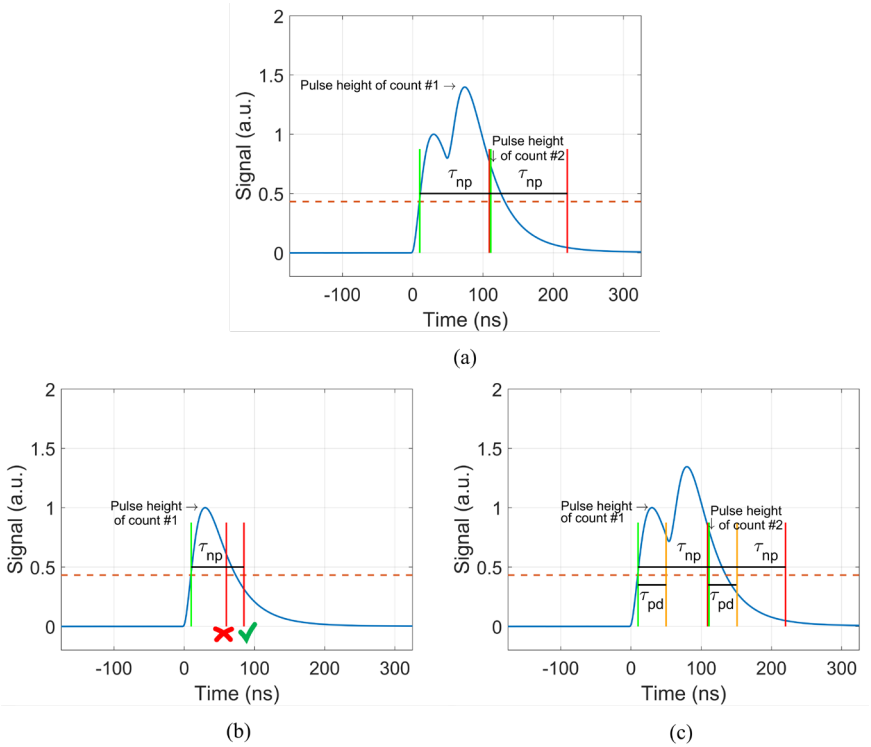

Fig. 3.4. (a) The nonparalyzable-like counting algorithm evaluates, at the end of a window of length τ_{np} following a positive threshold crossing, if the signal is still above threshold (dashed line) or not. If so, a second count is registered and a new window of length τ_{np} is started, and so on. The maximum signal within each window is considered the pulse height associated with that count. Although this algorithm allows to correctly count the number of pulses, the pulse height measurement is still distorted. (b) It is very important that τ_{np} exceeds the time-over-threshold of the pulses, so that no two counts are registered for a single pulse. (c) The pulse height measurement may be improved by determining the maximum signal within a shorter peak detection window of length τ_{pd} starting at the beginning of the window of length τ_{np}. Note that this dedicated peak detection window can also be integrated in the p-like algorithm.

positive threshold crossing of each pulse. After the timestamps had been determined, each raw pulse was numerically integrated for a subsequent period of time equal to five scintillation decay time constants τ_d. We fitted a Gaussian through the photopeak in a histogram of pulse integral values in order to determine the energy resolution as the ratio of the mean pulse integral μ and the full width at half maximum (FWHM = 2.355σ, with σ the standard deviation of the Gaussian). It is noted that, in the case of the YAP detector, a double Gaussian was fitted under the constraint described in Sec. 3.2.3 in order to account for K-escape events. The results can be considered the best FWHM energy resolutions achievable with these detectors, as almost all optical photons from the scintillator (i.e., 99% of them) are collected on the SiPM within this $5\tau_d$ window.

At higher ICRs, pulse pile-up will cause counts to end up outside the photopeak. Under those conditions, the FWHM energy resolution no longer provides a full description of

the spectral performance of a detector. We therefore propose an additional metric, the *spectral degradation factor* (SDF), which can be calculated in the following way:

Step 1. Determine for a given detector the gold-standard FWHM fraction (p_0) as the fraction of all counts registered at the longest SDD using the gold-standard method that falls within a bin centered around the mean pulse integral μ with a width equal to the FWHM of the Gaussian distribution of pulse integrals.

Step 2. Store the width of this so-called gold-standard FWHM bin relative to μ and use it to determine for each pulse processing method (which value of f_c and p- or np-like counting?) a FWHM bin that is equally wide relative to that method's mean pulse height, around which the bin is centered. This mean pulse height must be obtained from a (double) Gaussian fit to the peak in the pulse height histogram recorded at the longest SDD.

Step 3. Determine the FWHM fraction (p_{FWHM}) for a combination of pulse processing method and SDD as the fraction of all counts registered at this SDD using this processing method that falls within this method's FWHM bin.

Step 4. Calculate the SDF as:

$$\mathrm{SDF} = \frac{p_{\mathrm{FWHM}}}{p_0} \tag{3.3}$$

The p_{FWHM}, and therefore the SDF, of a given detector provide insight into the fraction of full-energy events that can be considered correctly classified as such both under low and high pile-up conditions. The advantage of the SDF is that the contributions to spectral degradation already contained in p_0, such as the number of K-escape and Compton scattering events and the width of the photopeak under low pile-up conditions, are cancelled out. As such, the value of the SDF is always close to 1 at low ICR and does not depend on, e.g., scintillator dimensions and probe energy, thereby enabling a clean comparison of the different pulse processing methods as a function of ICR.

We also used the SDF concept to investigate if and how much the spectral performance improves by regarding the maximum signal within a dedicated peak detection window of length τ_{pd} after a positive threshold crossing (p-like counting) or after the start of a time window of length τ_{np} (np-like counting, with $\tau_{\mathrm{pd}}<\tau_{\mathrm{np}}$) as the pulse height associated with that count. This idea relies on the fact that the peak of a pulse (unaffected by pile-up) from an SiPM-based scintillation detector is always reached relatively early on in the pulse. Hence, when two pulses pile up, it should still be possible to determine the correct pulse height of the first pulse provided the second pulse occurs more than τ_{pd} after the first one (see Fig. 3.4(c)). In order to choose proper values of τ_{pd}, we generated histograms of the time differences between the moment each pulse crosses the threshold and the moment it reaches its maximum value determined by the p-like counting algorithm applied to the measurement at the longest SDD. Fig. 3.5 shows that these crossing-to-peak times have a Gaussian-like distribution and reduce with increasing cut-off frequency f_c. We selected values of τ_{pd} that correspond to the right-hand side end

points of these distributions, i.e., τ_{pd} = 40 ns (f_c = 20 MHz), τ_{pd} = 50 ns (f_c = 10 MHz), and τ_{pd} = 65 ns (f_c = 5 MHz) for both detectors. In the remainder of this work, we refer to this method as p/np-like counting with a dedicated peak detection window (DPDW). It can be implemented in real detectors using clocked comparators, for example [19].

3.2.5 Performance measure *II*: Counting

For counting photons, we first evaluated the number of registered counts per unit time, which we refer to as the output count rate. Instead of studying this quantity as well as the spectral performance measures as a function of SDD, it is more valuable to study them as a function of ICR. However, the Am-241 source is a disk source and both its active area and location within the housing are not accurately known. The active area is surely larger than the cross-sectional area of the scintillation crystals (0.9×0.9 mm^2), which, combined with the non-zero thickness of the crystals, means that, for the shorter SDDs in particular, 60 keV photons also enter the crystals through the side faces. These circumstances make it hard to use an analytic formula to determine ICR for each SDD.

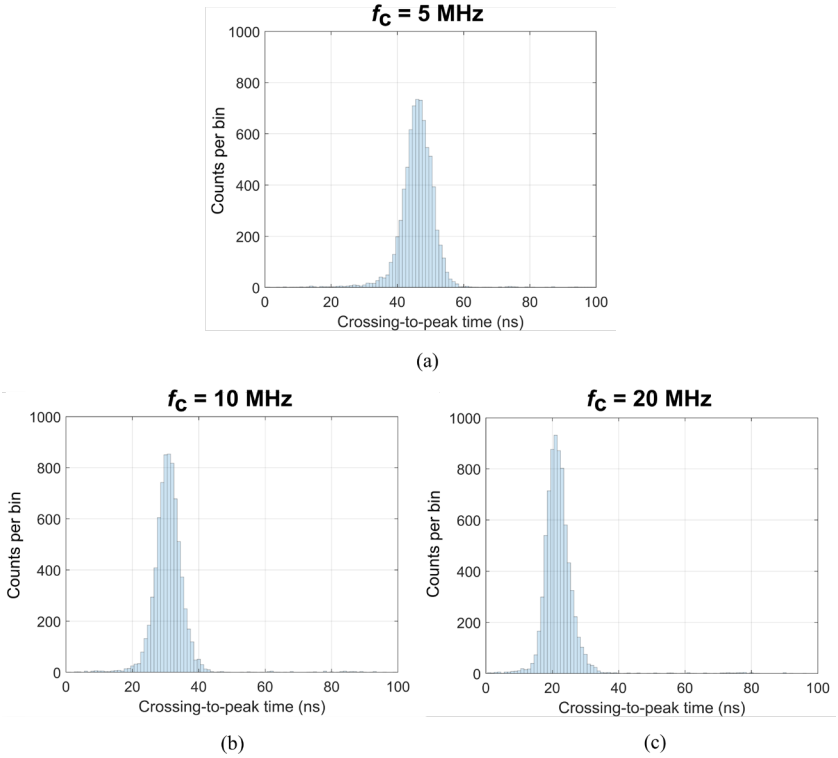

Fig. 3.5. (Positive threshold) crossing-to-peak time histograms (bin width = 1 ns; measurement time = 100 ms) for the LYSO detector and cut-off frequencies f_c of the second-order low-pass filter applied to the raw pulse trains equal to (a) 5 MHz, (b) 10 MHz, and (c) 20 MHz. The lengths τ_{pd} of the dedicated peak detection windows were chosen such that all pulses reach their peak in this period of time, i.e., 65 ns for f_c = 5 MHz, 50 ns for f_c = 10 MHz, and 40 ns for f_c = 20 MHz.

We therefore performed pulse train simulations to determine which OCRs to expect for a series of ICRs. For each ICR, ten trains of delta pulses were generated. The pulse trains were 100 ms in length and had a sample period of 1 ns. The number of pulses in each train was sampled from a Poisson distribution with an expectation value equal to the product of the ICR and 0.1 s (100 ms), while the timestamp of each pulse was sampled from a uniform distribution. Each delta pulse train was convolved with the mean pulse shape determined from the low-pass filtered (f_c = 20 MHz) experimental data. The detection threshold was again set to a level equivalent to 25 keV and the OCR was determined using both the p-like and the np-like algorithms. The OCRs obtained for each of the ten pulse trains were then averaged. These mean OCRs were stored in a look-up table alongside their corresponding ICR. By linearly interpolating the data in this table, we estimated the ICR for each measured OCR.

It is noted that some counts registered by the YAP detector correspond to K-escape events with an energy of about 45 keV instead of 60 keV. By comparing the areas under both Gaussians of the double Gaussian fit described in Sec. 3.2.3, we determined that the Gaussian centered at 45 keV contained about 15% of the total number of events in the YAP detector. We therefore made sure 15% of the pulses in the pulse train simulations had a pulse height of only 45/60×100% = 75% of that of the pulses corresponding to 60 keV photons.

Once the estimated ICR for each SDD was known, we determined the *count-rate loss factor* (CRLF), the ratio of OCR to ICR, as a function of ICR, in analogy with the SDF.

3.3 Results

3.3.1 Counting performance

Fig. 3.6 shows the (mean) output count rate, as well as the count-rate loss factor, as a function of estimated input count rate, counting algorithm, and cut-off frequency f_c for the LYSO detector. As expected, nonparalyzable-like counting achieves a better CRLF, and therefore a higher (mean) OCR than paralyzable-like counting for a given value of f_c. The fact that that np-like counting with f_c = 5 MHz even yields a better CRLF, and, consequently, a higher OCR than p-like counting with f_c = 20 MHz already for ICRs in the order of 0.1 Mcps/pixel is somewhat remarkable though. Again in accordance with expectations, higher values of f_c provide higher OCRs for a given counting algorithm. Nevertheless, the curves for np-like counting with f_c = 10 MHz and f_c = 20 MHz are remarkably close to each other. For both values of f_c, it can be appreciated that the OCR is at least about 90% of the ICR up to the maximum ICR of 4.6 Mcps/pixel that we could achieve with the present experimental set-up. Very similar, although slightly better, OCRs and CRLFs were measured for the YAP detector. These plots can be found in the Appendix (Fig. A3.1). The similarity is due to the small difference in the decay time constants τ_d of both scintillators (see Sec. 3.2.1).

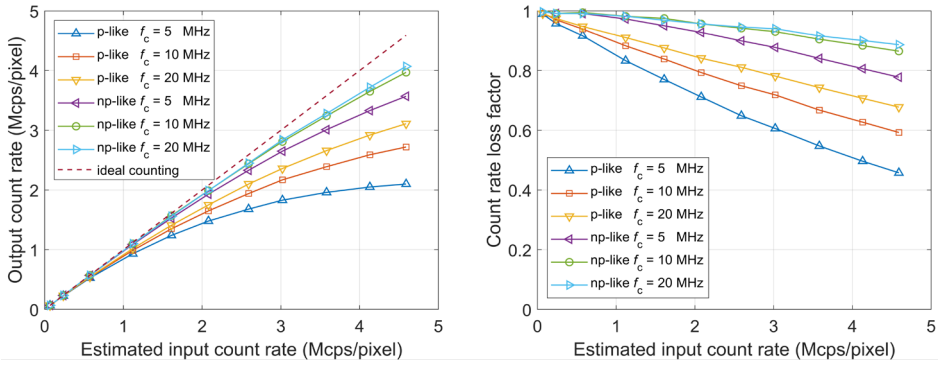

(a) (b)

Fig. 3.6. (a) The output count rate of the LYSO detector as a function of the estimated input count rate, the cut-off frequency f_c of the second-order low-pass filter applied to the raw pulse trains, and the counting algorithm (paralyzable-like (p-like) or nonparalyzable-like (np-like)). The line labeled 'ideal counting' is defined as OCR = ICR. (b) The count-rate loss factor, defined as OCR divided by estimated ICR for a given algorithm and value of f_c, as a function of ICR.

3.3.2 Spectral performance

Fig. 3.7 shows the results obtained with the gold-standard method described in Sec. 3.2.4. The measured FWHM energy resolutions at 60 keV are 28% and 31% for the YAP detector and the LYSO detector, respectively. Remarkably, the energy resolution of the YAP detector is better, although the mean pulse integrals of both detectors indicate that about twice as many optical photons were detected by the LYSO detector. In general, Poisson statistics imply that the more scintillation photons are detected, the better the energy resolution. However, the so-called non-proportionality of the scintillator also affects the energy resolution [20]. The more the number of generated optical photons deviates from being proportional to the energy deposited, the larger the negative effect on the energy resolution. Whereas YAP is known to be a proportional scintillator, LYSO is rather non-proportional [21]. This should largely explain the observed difference in measured energy resolution here. As described in Sec. 3.2.4, we also determined the values of p_0 from these two measurements. These turned out to be 0.638 for the YAP detector, and 0.723 for the LYSO detector. The lower value for the YAP detector is mainly due to the K-escape events.

Fig. 3.8(a) shows the spectral degradation factor (defined in Eqn. (3.3)) as a function of estimated ICR, counting algorithm, and value of f_c for the LYSO detector. The inset shows a zoomed-in version of the data for low values of the ICR. As expected, the highest SDF at the lowest ICR is achieved for f_c = 5 MHz, followed by f_c = 10 MHz and f_c = 20 MHz. This is because a lower value of f_c usually implies a better FWHM energy resolution. Indeed, we determined FWHM resolutions at 60 keV of 31.6% for f_c = 5 MHz, 32.6% for f_c = 10 MHz and 33.5% for f_c = 20 MHz for this particular LYSO detector. The value of 31.6% for f_c = 5 MHz is close to the above-mentioned FWHM energy resolution of 31% at 60 keV obtained with the gold-standard method. However,

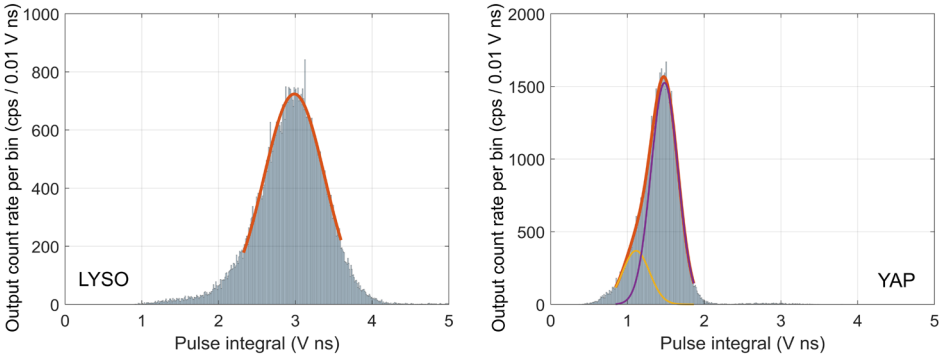

Fig. 3.7. Pulse integral histograms determined using the gold-standard method explained in Sec. 3.2.4 for (a) the LYSO detector, and (b) the YAP detector. Despite yielding an approximately twice as weak scintillation signal, the YAP detector provides a somewhat better energy resolution (28% versus 31% FWHM at 60 keV) due to its better proportionality [21]. Details about the double Gaussian fit in (b) were given in Sec. 3.2.3.

as the ICR starts to increase, a lower pile-up level due to the faster pulses offered by a higher value of f_c starts to become more beneficial for the spectral performance than the low-rate FWHM energy resolution. For p-like counting, f_c = 5 MHz indeed only has the highest SDF up to ICR ≈ 0.3 Mcps/pixel. Then, f_c = 10 MHz provides the best spectral performance up to ICR ≈ 1.0 Mcps/pixel. If ICR > 1.0 Mcps/pixel, f_c = 20 MHz is optimal from a spectral point-of-view. Similar trends are observed for np-like counting, the turning points being located at ICR ≈ 0.2 Mcps/pixel and ICR ≈ 0.7 Mcps/pixel.

Similar plots for the YAP detector can be found in Fig. 3.8(b). The data show that the dependency of the SDF at low ICRs on the value of f_c is somewhat more pronounced for the YAP detector. Indeed, we determined that the FWHM energy resolution at 60 keV ranges from 29.5% for f_c = 5 MHz to 33.5% for f_c = 20 MHz. That is a difference of 4 percentage point, or twice the difference observed for the LYSO detector, likely because of the more proportional response of YAP discussed above in the context of Fig. 3.7. In addition, the pile-up level for a given ICR is slightly lower in the YAP detector due to a somewhat faster scintillation decay (see Sec. 3.2.1). As a result of both facts, the turning points occur at higher values of ICR, i.e., at 0.5 Mcps/pixel and 1.7 Mcps/pixel for p-like counting and at 0.4 Mcps/pixel and 1.2 Mcps/pixel for np-like counting.

3.3.3 Optimal cut-off frequency and counting algorithm

In summary, f_c = 20 MHz already provides the best spectral performance at ICR values greater than about 1 Mcps/pixel, the exact value depending on detector and counting algorithm. The spectral disadvantage of a high f_c value at low ICRs is quite small and does not appear to outweigh the advantages at higher ICRs. f_c = 20 MHz anyway yields the best counting performance (see Fig. 3.6), so the highest value of f_c that still

sufficiently suppresses the pulse fluctuations is most likely optimal for most X-ray imaging applications.

The question remains whether p-like or np-like counting is to be preferred. Fig. 3.6 showed that np-like counting is better from a counting perspective, whereas Fig. 3.8 indicated that the spectral degradation for given ICR and f_c is more severe for this counting algorithm. This is visually explained in Fig. 3.9 (top row), which contains pulse height spectra measured by the LYSO detector, for f_c = 20 MHz, for both counting

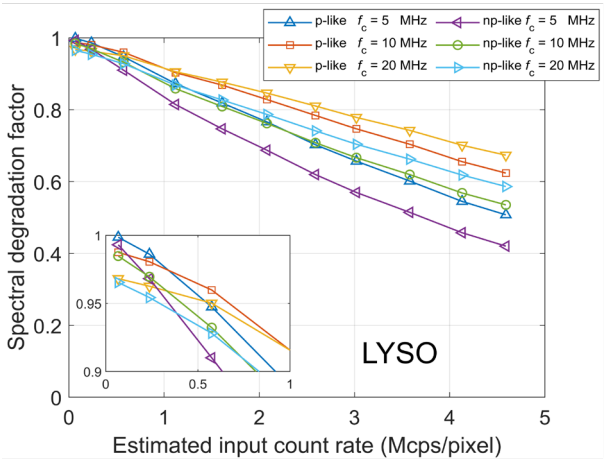

(a)

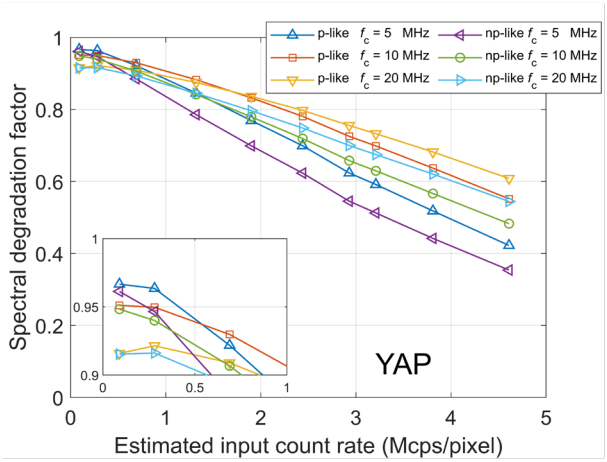

(b)

Fig. 3.8. (a) The spectral degradation factor of the LYSO detector, for which p_0=0.723 (see Eqn. (3.3), as a function of the estimated input count rate, the counting algorithm (paralyzable-like (p-like) or nonparalyzable-like (np-like)), and the cut-off frequency f_c of the second-order low-pass filter applied to the raw pulse trains. (b) The corresponding data set for the YAP detector, for which p_0=0.638. This lower value of p_0 is mainly due to K-escape events in the YAP detector.

algorithms, and for low (0.068 Mcps/pixel), intermediate (1.1 Mcps/pixel) and high (4.6 Mcps/pixel) values of the estimated ICR. For the lowest ICR, the only feature of the spectra is the full-energy peak and the spectra for p-like counting and np-like counting fully overlap. As the ICR increases, pile-up becomes more likely. For both p-like and np-like counting, counts affected by pile-up typically end up to the right of the FWHM bin in the pulse height spectra, thereby reducing the fraction of counts in that bin. Because of the exponential distribution of the inter-arrival times between two 60 keV photons and the finite energy resolution of the detector, these counts do not lead to well-resolved sum peaks, but rather to a continuum of counts. In addition, a shift of the most probable pulse height towards higher values can be observed for both counting algorithms as the ICR increases. The main difference between the spectra for p-like counting and np-like counting in the top row of Fig. 3.9 can be observed on the left-hand side of the FWHM bin. If two pulses pile up and the p-like algorithm registers only one count, the np-like algorithm can still detect a second count (see Fig. 3.3(c) and Fig. 3.4(a)). This explains why the count-rate loss factor for np-like counting in Fig. 3.6(b) stays closer to 1 than that for p-like counting. However, the maximum signal within the time window of length τ_{np} of the second count will usually be located on the falling edge of a pulse (see Fig. 3.4(a)). Consequently, the pulse height associated with this count is typically much lower than the (mean) pulse height corresponding to 60 keV, so the count ends up to the left of the FWHM bin in the spectra. This explains why the spectral performance of the np-like counting algorithm is worse. In the end, a choice between p-like counting and np-like counting depends on whether one prefers better counting or better spectral performance.

For completeness, Fig. 3.9 also contains the pulse height spectra for the other two values of f_c, i.e., 10 MHz and 5 MHz. In general, the trends observed for f_c = 20 MHz can also be seen for these lower f_c. The spectral distortion due to pile-up just gets stronger with decreasing f_c, which manifests as a stronger reduction of the height of the photopeak with increasing ICR, as well as a more dominant presence of the 'triple pile-up' continuum visible on the far right-hand side of the spectra measured at an estimated ICR of 4.6 Mcps/pixel.

3.3.4 Dedicated peak detection window

The effect of integrating a dedicated peak detection window into the counting algorithms (as described in Sec. 3.2.4 and visualized in Fig. 3.4(c)) on the pulse height spectra is depicted in Fig. 3.10(a) for the LYSO detector with f_c = 20 MHz, at an estimated ICR of 4.6 Mcps/pixel. The spectra indicate that the DPDW increases the probability that a registered count ends up inside the FWHM bin rather than to the right-hand side of it. This is reflected in an overall improvement of the spectral degradation factors shown in Fig. 3.10(b) compared to those obtained without the DPDW shown in Fig. 3.8(a).

Fig. 3.10(a) shows that np-like counting with the dedicated peak detection window also increases the chance that a registered count ends up on the left-hand side of the FWHM bin. Thus, the positive effect of the DPDW is larger for p-like counting than for np-like

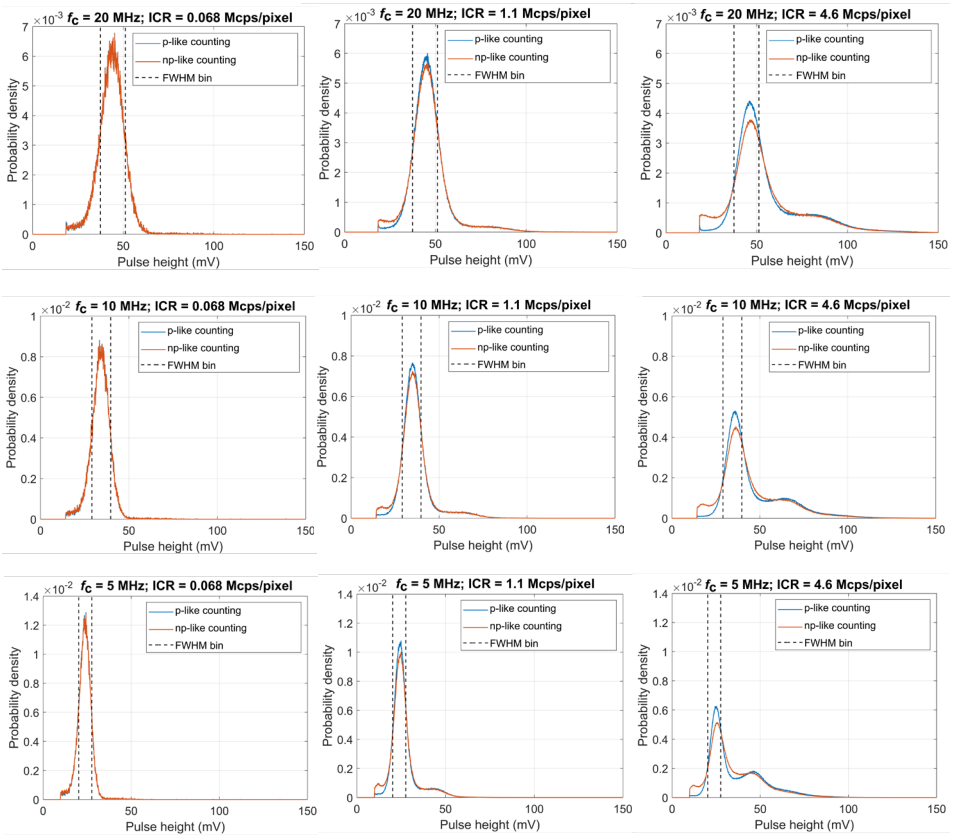

Fig. 3.9. Normalized pulse height spectra, which represent the probability that a registered count gets associated with a certain pulse height, measured with the LYSO detector and both the paralyzable-like (p-like) and nonparalyzable-like (np-like) counting algorithm. From left to right, the estimated input count rate (ICR) is increasing. From top to bottom, the cut-off frequency f_c of the second-order low-pass filter applied to the raw pusle trains is decreasing. The FWHM bin, used to calculate the spectral degradation factor (see Sec. 3.2.4 and Eqn. (3.3)) is visualized by means of the vertical dashed lines.

counting. This is also reflected in the spectral degradation factors. Whereas np-like counting with f_c = 20 MHz has a better SDF than p-like counting with f_c = 5 MHz for the higher values of the ICR in the case without DPDW (Fig. 3.8(a)), the SDFs of p-like counting with DPDW are better than those of np-like counting with DPDW regardless of f_c for these values of the ICR (Fig. 3.10(b)).

Due to the better spectral performance obtained with the DPDW, higher cut-off frequencies become optimal from a spectral point-of-view at higher values of ICR than before. For example, we note that the SDFs of p-like counting with DPDW for f_c = 10 MHz and f_c = 20 MHz in Fig. 3.10(b) are very close to each other over the whole range of investigated ICRs and that f_c = 20 MHz only becomes slightly better than f_c = 10

MHz for ICRs exceeding 2.4 Mcps/pixel (was 1.0 Mcps/pixel without DPDW). P-like counting with DPDW and a cut-off frequency of 5 MHz yields the best spectral performance for values of ICR up to 0.7 Mcps/pixel as the inset in Fig. 3.10(b) shows (was 0.3 Mcps/pixel without DPDW). Nevertheless, we may still conclude that the highest possible value of f_c is most beneficial for practical systems, because it provides better counting performance (see Fig. 3.6) and the spectral disadvantages at low ICR remain small. This conclusion also remains valid for np-like counting. A choice between p-like counting and np-like counting still depends on whether counting performance or spectral performance is preferred.

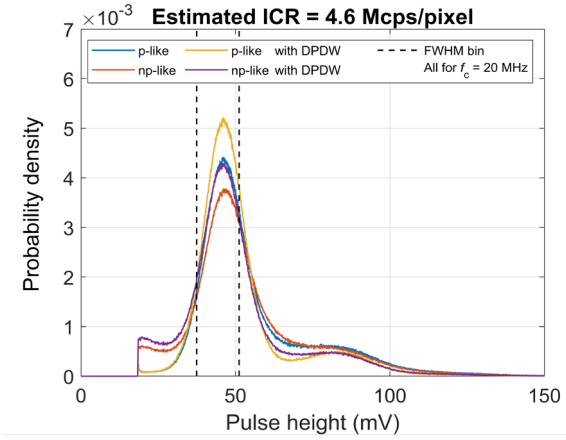

(a)

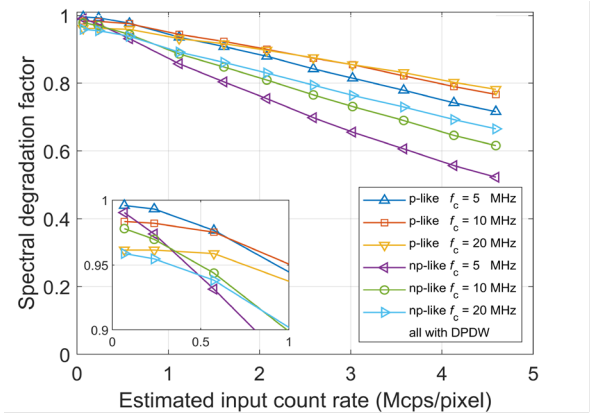

(b)

Fig. 3.10. (a) The effect of integrating a dedicated peak detection window (DPDW) into the paralyzable-like (p-like) and nonparalyzable-like (np-like) counting algorithms on normalized pulse height spectra, which represent the probability that a registered count has a certain pulse height. Here, spectra measured at an estimated input count rate (ICR) of 4.6 Mcps/pixel with the LYSO detector and a second-order low-pass filter with a cut-off frequency f_c = 20 MHz are plotted with a bin width of 0.1 mV. See Sec. 3.2.3 and Fig. 3.4(c) for an explanation of the counting algorithms with a DPDW. (b) The resulting spectral degradation factor (see Sec. 3.2.4 and Eqn. (3.3)) as a function of input count rate for the pulse processing methods with DPDW.

Data on the effect of the dedicated peak detection window on the performance of the YAP detector can be found in the Appendix (Fig. A3.2). Qualitatively, the same trends as for the LYSO detector were found. For example, the values of the ICR for which the different cut-off frequencies are optimal from a spectral point-of-view also increased. Quantitatively, f_c = 5 MHz is optimal until 1.1 Mcps/pixel, f_c = 10 MHz between 1.1 Mcps/pixel and 2.8 Mcps/pixel, and f_c = 20 MHz for higher values of ICR in the case of p-like counting. For np-like counting, the turning points occur at 0.5 Mcps/pixel and 1.5 Mcps/pixel, respectively.

3.4 Discussion

We experimentally evaluated the counting and spectral performance of single-pixel, ultrafast SiPM-based LYSO and YAP scintillation detectors for X-ray photon-counting applications, as a function of input count rate and pulse processing method. Regarding the latter, we investigated the effects of the cut-off frequency f_c (5 MHz, 10 MHz, 20 MHz) of a second-order low-pass filter applied to the raw pulse trains and the effects of paralyzable-like and nonparalyzable-like counting algorithms. Evaluating spectral performance is more straightforward with a mono-energetic radiation source, so we placed a 10 GBq Am-241 source (60 keV) at various distances from the detector in order to vary ICR. Despite this high activity, the geometry of the set-up only allowed us to investigate ICRs up to 5 Mcps/pixel. This may be a low ICR for diagnostic CT, but we argue in Appendix A3.1 that it can be close to the maximum ICR in another X-ray imaging application, namely cone beam CT in radiotherapy.

We determined the output count rate and the count-rate loss factor as a function of ICR in order to evaluate counting performance. As expected, nonparalyzable-like counting with the highest value of f_c is optimal from this point-of-view.

Regarding spectral performance, we first evaluated the traditional measure of the low-rate FWHM energy resolution and found values around 30% at 60 keV for both detectors. A characteristic of the SiPM that has a substantial effect on the achievable energy resolution is the optical photon detection efficiency. The ultrafast SiPMs that we currently use have a relatively low PDE of 20% to 30%. However, it is possible to increase the PDE of ultrafast SiPMs to about 60% [22]. If twice as many optical photons are detected, the energy resolution improves by at best a factor $\sqrt{2}$. Especially the YAP detector, the energy resolution of which strongly depends on the number of detected scintillation photon due to its proportional response, may therefore obtain an energy resolution closer to 20% FWHM at 60 keV, approaching that of at least one CdTe detector with miniaturized pixels developed for a photon-counting CT prototype [23]. Moreover, many spectral imaging tasks require only two energy bins, which lowers the requirement on the energy resolution. Also note that the higher number of detected scintillation photons per unit time due to a higher PDE may allow for applying filters with higher values of f_c, thereby improving the counting performance, too.

We supplemented the traditional measure of the low-rate FWHM energy resolution with the spectral degradation factor, with the aim to better characterize detector performance under the pile-up conditions that are typically found in X-ray photon-counting applications. The SDF has been defined in Eqn. (3.3). It can be seen as an easy-to-calculate measure of spectral performance, providing insight into the fraction of full-energy events that can be considered correctly classified as such under high pile-up conditions. We obtained the most favorable SDF values with paralyzable-like counting. However, we note that the SDF does not quantify the spread in the energies associated with the counts.

Another finding is that spectral degradation due to pulse pile-up already kicks in at relatively low input count rates and that, therefore, the FWHM energy resolution at low ICR has limited predictive value for the spectral performance under pile-up conditions. For example, when increasing f_c from 5 MHz to 20 MHz, the FWHM energy resolution of the LYSO detector at low ICR worsened by about 2 percentage point, while the worsening was about 4 percentage point for the YAP detector. At the same time, the full width at tenth maximum (FWTM) of the mean detector pulse, which is a typical characteristic of pulse duration, improved from 230 ns to 132 ns for the LYSO detector and from 228 to 116 ns for the YAP detector. As a result, the spectral detector performance was much less affected by pile-up for f_c = 20 MHz. In fact, f_c = 20 MHz already appeared optimal from a spectral point-of-view for ICR values greater than a few Mcps/pixel, the exact value depending on the detector and the counting algorithm. This finding may also be applied when selecting an optimal detection material. A faster detection material appears more important than a material that offers somewhat better FWHM energy resolution under low fluence-rate conditions for high-rate spectral X-ray photon-counting applications.

Lastly, we found a positive effect of integrating a dedicated peak detection window into the counting algorithms (see Fig. 3.10). This improvement of spectral performance by determining the pulse height in a short window of length τ_{pd} following the detection of a count (see Fig. 3.4(c)) is more pronounced for p-like counting than for np-like counting. However, Fig. 3.5 shows that the lengths of the peak detection windows that we used are rather conservative. About 5 ns lower values of τ_{pd} are possible, which may further improve spectral detector performance.

3.5 Conclusion

Aiming to develop spectral photon-counting scintillation detectors for hard X-ray applications such as medical imaging, we investigated the counting and spectral performance of two 1×1 mm^2 single-pixel detectors based on the fast and widely available LYSO and YAP scintillators coupled to an ultrafast silicon photomultiplier, as a function of the input count rate, the counting algorithm (paralyzable-like / nonparalyzable-like) and the cut-off frequency f_c (5 MHz, 10 MHz, and 20 MHz) of a second-order low-pass filter applied to the raw signals.

Nonparalyzable-like counting in general yields better counting performance than paralyzable-like counting. For f_c = 20 MHz, the count-rate loss of both detectors is limited to 10% for ICRs up to 5 Mcps/pixel. However, the spectral performance is generally better for paralyzable-like counting. Moreover, we found that spectral degradation due to pile-up kicks in at relatively low ICRs, so that the faster pulses offered by f_c = 20 MHz, which yield somewhat worse FWHM energy resolution at low ICR, already provide the best spectral performance at ICRs greater than just a few Mcps/pixel, the exact value depending on the detector and the counting algorithm. We also showed that spectral degradation due to pile-up can be further mitigated by integrating a dedicated peak detection window into the counting algorithms. This is facilitated by the specific shape of the pulses from an SiPM-based scintillation detector.

These findings were obtained using the spectral degradation factor proposed in this work. The SDF supplements the low-rate FWHM energy resolution and quantifies the fraction of full-energy events that can be considered correctly classified as such at any ICR. Thus, the SDF appears to be a useful measure of spectral performance for X-ray photon-counting detectors exposed to clinically relevant ICRs.

Our findings imply that not only pulse processing methods, but also detection materials that provide considerably faster pulses may yield better SDF values in high-rate applications than those that offer somewhat better low-rate FWHM energy resolution at the expense of a longer pulse duration. The results presented in this work thus offer important guidance for the selection of both suitable detection materials and pulse processing methods for X-ray photon-counting detectors.

References

[1] T. Flohr, M. Petersilka, A. Henning, S. Ulzheimer, J. Ferda, and B. Schmidt, "Photon-counting CT review," *Physica Medica,* vol. 79, pp. 126-136, 2020, doi: https://doi.org/10.1016/j.ejmp.2020.10.030.

[2] S. S. Hsieh, S. Leng, K. Rajendran, S. Tao, and C. H. McCollough, "Photon counting CT: Clinical applications and future developments," *IEEE Transactions on Radiation and Plasma Medical Sciences,* vol. 5, no. 4, pp. 441-452, 2020, doi: https://doi.org/10.1109/TRPMS.2020.3020212.

[3] M. Danielsson, M. Persson, and M. Sjölin, "Photon-counting x-ray detectors for CT," *Physics in Medicine & Biology,* vol. 66, no. 3, p. 03TR01, 2021, doi: https://doi.org/10.1088/1361-6560/abc5a5.

[4] M. Persson *et al.*, "Upper limits of the photon fluence rate on CT detectors: Case study on a commercial scanner," *Medical physics,* vol. 43, no. 7, pp. 4398-4411, 2016, doi: https://doi.org/10.1118/1.4954008.

[5] K. Rajendran *et al.*, "First clinical photon-counting-detector CT system: Technical evaluation," *Radiology,* vol. 303, no. 1, p. 130, 2022, doi: https://doi.org/10.1148/radiol.212579.

[6] S. Si-Mohamed *et al.*, "Feasibility of lung imaging with a large field-of-view spectral photon-counting CT system," *Diagnostic and Interventional Imaging,* vol. 102, no. 5, pp. 305-312, 2021, doi: https://doi.org/10.1016/j.diii.2021.01.001.

[7] J. da Silva *et al.*, "Resolution characterization of a silicon-based, photon-counting computed tomography prototype capable of patient scanning," *Journal of Medical Imaging,* vol. 6, no. 4, p. 043502, 2019, doi: https://doi.org/10.1117/1.JMI.6.4.043502.

[8] U. N. Roy *et al.*, "Role of selenium addition to CdZnTe matrix for room-temperature radiation detector applications," *Scientific reports,* vol. 9, no. 1, pp. 1-7, 2019, doi: https://doi.org/10.1038/s41598-018-38188-w.

[9] S. J. van der Sar, S. E. Brunner, and D. R. Schaart, "Silicon photomultiplier-based scintillation detectors for photon-counting CT: A feasibility study," *Medical physics,* vol. 48, no. 10, pp. 6324-6338, 2021, doi: https://doi.org/10.1002/mp.14886.

[10] S. J. van der Sar and D. R. Schaart, "Silicon Photomultiplier-Based Scintillation Detectors for Photon-Counting X-Ray Imaging," in *Radiation Detection Systems*. Boca Raton, FL, USA: CRC Press, 2021, pp. 289-312, doi: https://doi.org/10.1201/9781003147633-10.

[11] S. Van Der Sar, S. Brunner, and D. Schaart, "X-ray photon-counting using silicon photomultiplier-based scintillation detectors at high X-ray tube currents," in *SPIE Medical Imaging 2022: Physics of Medical Imaging*, 2022, vol. 12031: SPIE, pp. 118-124, doi: https://doi.org/10.1117/12.2611365.

[12] S. Surti and J. S. Karp, "Update on latest advances in time-of-flight PET," *Physica Medica,* vol. 80, pp. 251-258, 2020, doi: https://doi.org/10.1016/j.ejmp.2020.10.031.

[13] R. Ballabriga *et al.*, "Review of hybrid pixel detector readout ASICs for spectroscopic X-ray imaging," *J. Instrum,* vol. 11, no. 01, p. P01007, 2016, doi: https://doi.org/10.1088/1748-0221/11/01/P01007.

[14] D. N. ter Weele, D. R. Schaart, and P. Dorenbos, "Intrinsic scintillation pulse shape measurements by means of picosecond x-ray excitation for fast timing applications," *Nuclear Instruments and Methods in Physics Research Section A: Accelerators, Spectrometers, Detectors and Associated Equipment,* vol. 767, pp. 206-211, 2014, doi: https://doi.org/10.1016/j.nima.2014.08.019.

[15] C. Piemonte and A. Gola, "Overview on the main parameters and technology of modern Silicon Photomultipliers," *Nuclear Instruments & Methods in Physics Research A,* vol. 926, pp. 2-15, 2019, doi: https:///doi.org/10.1016/j.nima.2018.11.119.

[16] S. Kappler, A. Henning, B. Kreisler, F. Schoeck, K. Stierstorfer, and T. Flohr, "Photon counting CT at elevated X-ray tube currents: contrast stability, image noise and multi-energy performance," in *Medical imaging 2014: Physics of medical imaging*, 2014, vol. 9033: SPIE, pp. 368-375, doi: https://doi.org/10.1117/12.2043511.

[17] R. Steadman, C. Herrmann, and A. Livne, "ChromAIX2: A large area, high count-rate energy-resolving photon counting ASIC for a spectral CT prototype," *Nuclear Instruments and Methods in Physics Research Section A: Accelerators, Spectrometers, Detectors and Associated Equipment,* vol. 862, pp. 18-24, 2017, doi: https://doi.org/10.1016/j.nima.2017.05.010.

[18] T. Loeliger, C. Brönnimann, T. Donath, M. Schneebeli, R. Schnyder, and P. Trüb, "The new PILATUS3 ASIC with instant retrigger capability," in *2012 IEEE Nuclear Science Symposium and Medical Imaging Conference (NSS/MIC)*, 2012: IEEE, pp. 610-615, doi: https://doi.org/10.1109/NSSMIC.2012.6551180.

[19] M. Gustavsson, F. U. Amin, A. Bjorklid, A. Ehliar, C. Xu, and C. Svensson, "A high-rate energy-resolving photon-counting ASIC for spectral computed tomography," *IEEE Transactions on Nuclear Science,* vol. 59, no. 1, pp. 30-39, 2011, doi: https://doi.org/10.1109/TNS.2011.2169811.

[20] P. Dorenbos, J. T. M. de Haas, and C. Van Eijk, "Non-proportionality in the scintillation response and the energy resolution obtainable with scintillation crystals," *IEEE Transactions on Nuclear Science,* vol. 42, no. 6, pp. 2190-2202, 1995, doi: https://doi.org/10.1109/23.489415.

[21] I. V. Khodyuk and P. Dorenbos, "Trends and patterns of scintillator nonproportionality," *IEEE Transactions on Nuclear Science,* vol. 59, no. 6, pp. 3320-3331, 2012, doi: https://doi.org/10.1109/TNS.2012.2221094.

[22] E. Engelmann, W. Schmailzl, P. Iskra, F. Wiest, E. Popova, and S. Vinogradov, "Tip avalanche photodiode—A new generation silicon photomultiplier based on non-planar technology," *IEEE Sensors Journal,* vol. 21, no. 5, pp. 6024-6034, 2020, doi: https://doi.org/10.1109/JSEN.2020.3041556.

[23] R. Steadman, C. Herrmann, O. Mülhens, and D. G. Maeding, "ChromAIX: Fast photon-counting ASIC for spectral computed tomography," *Nuclear Instruments and Methods in Physics Research Section A: Accelerators, Spectrometers, Detectors and Associated Equipment,* vol. 648, pp. S211-S215, 2011, doi: https://doi.org/10.1016/j.nima.2010.11.149.

Appendix to Chap. 3

This appendix contains two sections. It is shown in the first section that the maximum input count rate (ICR) of almost 5 Mcps/pixel that was achieved in the experiments with the 10 GBq Am-241 source may be about the maximum ICR in cone-beam CT systems on radiotheraphy gantries. The second section includes the data acquired with the YAP detector that were discussed, but not shown, in the main text of Chap. 3.

A3.1 Input count rate in cone-beam CT for radiotherapy

The highest X-ray photon fluence rate incident on the detector of a diagnostic CT system is found in head scans [1]. The protocol for such a scan prescribes a tube voltage V of 120 kVp and a tube current I of 300 mA, while the tube-to-detector distance r is 95 cm. This gives rise to a fluence rate φ of at most 3.4×10^8 photons/s/mm^2. On the other hand, standard head scan protocols for cone-beam CT systems on radiation therapy gantries prescribe V = 100 kVp, and a tube current of 10-20 mA, so $I \approx 15$ mA [2,3]. This twenty times as low tube current is sufficient, because the system rotates at a much lower speed than in diagnostic CT. Meanwhile, r can be varied in many cone-beam CT systems. For a certain clinical system [3], the tube-to-isocenter distance can be set to 80-100 cm, and the isocenter-to-detector distance to 0-80 cm. In order to create room for the patient, setting the latter to 54 cm seems reasonable. Adding this to the minimum tube-to-isocenter distance of 80 cm yields r = 134 cm, which is $\sqrt{2}$ times as large as r in the diagnostic CT system. Moreover, the dependency of φ on V, I and r is:

$$\varphi \sim \frac{V^2 I}{r^2}$$

We therefore expect a forty times as low maximum fluence rate in cone-beam CT systems on radiotherapy gantries based on the differences in I and r only, and a 57.6 times as low maximum fluence rate when we also include the difference in V, compared to diagnostic CT systems. This yields maximum fluence rates of 8.5×10^6 photons/s/mm^2 and 5.9×10^6 photons/s/mm^2, respectively. This simple analysis neglects factors that increase the required rate capability in cone-beam CT, such as a higher scatter-to-primary ratio than in diagnostic CT, as well as factors that lower this requirement, such as an X-ray absorption efficiency less than 1 for the higher-energy photons and the fact that the maximum rates only occur in the less important beam paths with hardly any attenuation by the patient. It nevertheless indicates that (clinical) X-ray imaging systems exist in which the maximum input count rate (ICR) is in the order of 10^6 counts/s/mm^2.

A3.2 Additional data acquired with the YAP detector

Some figures containing data acquired with the YAP detector are shown here. These have been discussed in the main text of Chap. 3, so there is no accompanying text, other than the figure captions, included here.

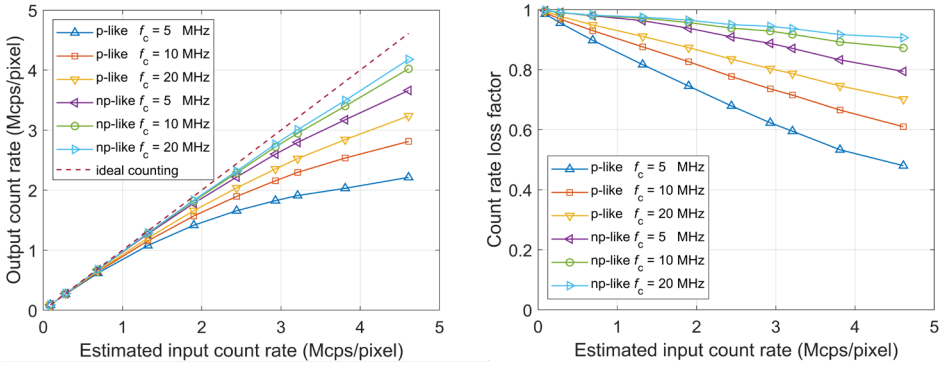

(a) (b)

Fig. A3.1. (a) The output count rate (OCR) of the YAP detector as a function of the estimated input count rate (ICR), the cut-off frequency f_c of the second-order low-pass filter applied to the raw pulse trains, and the counting algorithm (paralyzable-like (p-like) or nonparalyzable-like (np-like)). The line labeled 'ideal counting' is defined as OCR = estimated ICR. (b) The count-rate loss factor, defined as OCR divided by estimated ICR for a given algorithm and value of f_c, as a function of ICR.

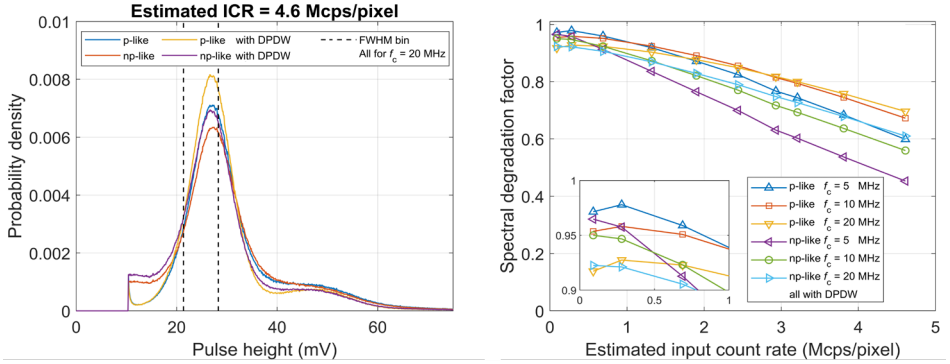

(a) (b)

Fig. A3.2. (a) The effect of integrating a dedicated peak detection window (DPDW) into the paralyzable-like (p-like) and nonparalyzable-like (np-like) counting algorithms on normalized pulse height spectra, which represent the probability that a registered count gets associated with a certain pulse height. Here, spectra measured at an estimated input count rate (ICR) of 4.6 Mcps/pixel with the YAP detector and a second-order low-pass filter with a cut-off frequency f_c = 20 MHz are plotted with a bin width of 0.1 mV. See Sec. 3.2.3 and Fig. 3.4(c) for an explanation of the counting algorithms with DPDW. (b) The resulting spectral degradation factor (see Sec. 3.2.4 and Eqn. (3.3)) as a function of ICR for the pulse processing methods with DPDW.

References

[1] M. Persson *et al.*, "Upper limits of the photon fluence rate on CT detectors: Case study on a commercial scanner," *Medical physics,* vol. 43, no. 7, pp. 4398-4411, 2016, doi: https://doi.org/10.1118/1.4954008.

[2] D. Hyer, "Imaging doses in radiation therapy from kilovoltage cone-beam computed tomography," 2011. [Online]. Available: https://www.aapm.org/meetings/amos2/pdf/60-15015-86048-515.pdf.

[3] Varian Medical Systems, "Varian On Board Imager specifications," 2012. [Online]. Available: http://photonix.com.ar/wp-content/uploads/2018/10/obi-specs.pdf.

4 Characterization of three silicon photomultiplier-based X-ray photon-counting scintillation detectors for medical imaging

Abstract

We are investigating scintillation detectors with silicon photomultiplier (SiPM) readout for X-ray photon-counting applications. Here, we experimentally evaluate the counting and spectral performance of detectors based on three different scintillation materials and compare the results to those reported for CdTe- and CZT-based direct-conversion detectors developed for diagnostic photon-counting computed tomography (PCCT).

We built three 1×1 mm^2 single-pixel detectors by coupling the readily available and fast scintillators LYSO:Ce, YAP:Ce, and $LaBr_3$:Ce to ultrafast SiPMs, and optimized the pulse processing for count rate capability rather than energy resolution. We first exposed the detectors to three radio-isotopes to determine the proportionality of the energy response and the energy resolution, and then to an X-ray tube to measure count rate curves, i.e., output count rate (OCR) as a function of input count rate.

The energy resolutions of the LYSO:Ce and YAP:Ce detectors both exceed 30% FWHM at 60 keV, the YAP:Ce detector showing a more proportional energy response. For a 30 keV count detection threshold, the maximum OCR of the YAP:Ce detector is 5.4 Mcps/pixel for paralyzable-like counting, while the OCR approaches 12.5 Mcps/pixel for nonparalyzable-like counting, whereas the LYSO:Ce detector reaches 4.5 Mcps/pixel and 10 Mcps/pixel, respectively. The $LaBr_3$:Ce detector achieves about twice as high values of 10.4 Mcps/pixel and 22 Mcps/pixel for both counting modes, corresponding to almost 80% of the rate capability of abovementioned direct-conversion detectors. Moreover, it shows high proportionality and its energy resolution of about 20% FWHM at 60 keV is comparable to that of at least one CdTe detector developed for PCCT.

In conclusion, $LaBr_3$:Ce-based scintillation detectors may be a viable alternative to direct-conversion detectors for diagnostic PCCT, whereas LYSO:Ce- and YAP:Ce-based detectors appear better suited for less demanding applications. Possibilities for further improvement of the performance of SiPM-based X-ray photon-counting scintillation detectors are also discussed.

This chapter is an extension of S.J. van der Sar, S.E. Brunner, and D.R. Schaart, "X-ray photon-counting using silicon photomultiplier-based scintillation detectors at high X-ray tube currents," in *SPIE Medical Imaging 2022: Physics of Medical Imaging*, 2022, vol. 12031: SPIE, pp. 118-124 and of S. J. van der Sar, D. Leibold, S. E. Brunner, and D. R. Schaart, "$LaBr_3$:Ce and silicon photomultipliers: towards the optimal scintillating photon-counting detector," in *7th International Conference on Image Formation in X-Ray Computed Tomography*, 2022, vol. 12304: SPIE, pp. 55-60.

4.1 Introduction

X-ray photon-counting detectors (PCD) for medical X-ray imaging aim to count the number of X-ray photons incident on each detector pixel. Based on a measurement of the energy deposited by each photon, each count can furthermore be assigned to one of several (typically 2-8) energy bins that collectively cover the entire X-ray tube spectrum. PCDs have the potential to improve the contrast-to-noise ratio and/or to reduce the radiation dose and contrast agent load compared to traditional X-ray imaging systems equipped with energy-integrating detectors. Moreover, they facilitate dual-energy imaging, open up opportunities for multi-energy imaging, and, thereby, allow for quantitative imaging of multiple contrast agents in a single acquisition [1,2,3].

Most PCDs developed to date are direct-conversion detectors based on the semiconductor CdTe or $Cd_{1-x}Zn_xTe$ (CZT, x typically 0.1-0.2), and X-ray computed tomography (CT) systems that are equipped with CdTe/CZT detectors and capable of patient scanning have been built [4,5]. In such detectors, X-ray photons are directly converted into electric charges, which migrate to pixelated electrodes under the influence of an electric field. CdTe and CZT have a reasonably high density ($\rho \approx 5.8$ g cm^{-3}) and effective atomic number ($Z_{\text{eff}} \approx 50$), so that a detector thickness of 1.5-3.0 mm is sufficient in the diagnostic energy range ($E < 150$ keV). In addition, this type of detector produces fast pulses (tens of nanoseconds) and enables a relatively easy reduction of the pixel size to 0.5×0.5 mm^2 or smaller, both of which help to mitigate the negative effects of pulse pile-up, such as a loss of counts and incorrect energy measurement (see Fig. 4.1). This is necessary because of the high X-ray fluence rate typically encountered in medical X-ray imaging applications. For example, it can exceed 10^8 photons/s/mm^2 in a very demanding application such as diagnostic CT [6]. However, reliable and stable detector performance at high fluence rates requires CdTe/CZT with a low density of charge trapping centers, uniformly distributed throughout the detector [2,7].

The investigation of other types of detector thus appears warranted. One such alternative is direct conversion in silicon. Although high-quality Si is widely available, it has a much lower density (2.3 g cm^{-3}) and Z_{eff} (14) than CdTe/CZT. Consequently, 3.0-6.0 cm of material is needed to absorb enough X-ray photons for dose-efficient imaging. Furthermore, Compton scattering is the dominant interaction mechanism in a Si detector. A relatively complex detector design is needed to account for these facts [8]. Nevertheless, a CT system that is equipped with Si detectors and capable of patient scanning has also been built [9].

As another potential alternative, we investigate a detector concept based on indirect conversion using a scintillator [10,11]. In such a detector, X-ray photons are first converted into optical scintillation photons, which are in turn converted into electric charges by a light sensor. Since the detector relies on the transport of optical photons rather than electric charges, it may be easier to synthesize detector-grade materials in a cost-effective way. This claim is supported by the fact that the vast majority of detectors

employed in present medical imaging systems are scintillation detectors. Furthermore, various scintillators that combine high density and Z_{eff} with a fast response to incoming radiation are readily available.

In first approximation, the response of a scintillation detector can be described as follows: If an X-ray photon deposits an amount of energy E (in keV) in a scintillation crystal, the mean number $\bar{N}$ of generated scintillation photons will equal:

$$\bar{N} = E \cdot Y(E) \tag{4.1}$$

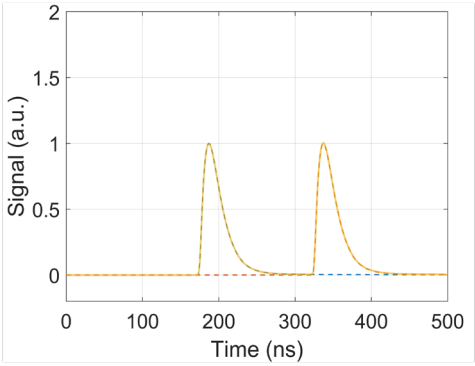

(a)

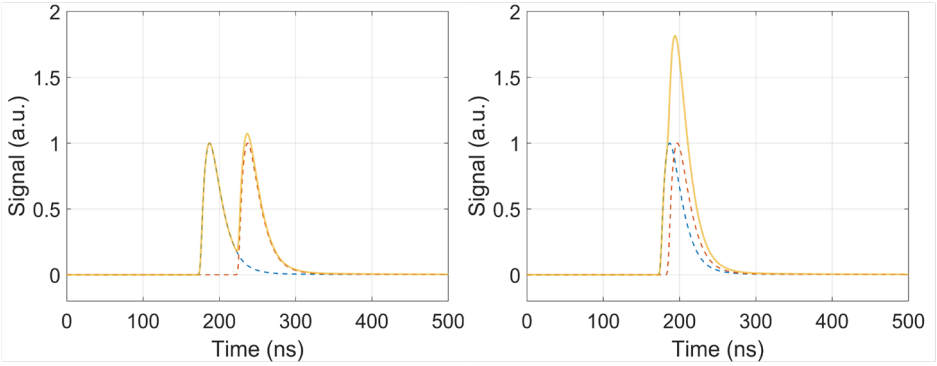

(b) (c)

Fig 4.1. An X-ray detector outputs a pulse in response to each absorbed X-ray photon. Here, two pulses are shown (blue and red dashed curves) as well as their sum (yellow solid curve) for three scenarios: (a) There is sufficient time between the absorption of both X-ray photons so that the pulses do not pile up and the measurement of the X-ray photon count and energy (i.e., the pulse height, for example) remains undistorted. (b) The time between the absorption of both photons is shorter, so that the second pulse piles up on the tail of the first pulse. It may still be possible to observe the correct number of pulses, but the energy measurement is distorted. (c) The X-ray photons are absorbed very shortly after each other, so that the two pulses look like a single pulse. The measurement of both the number of X-ray photons and their energy is distorted.

Here, Y is the light yield of the scintillator in photons/keV. The actual number of photons N is Poisson-distributed at best, but typically shows a variance larger than $\overline{N}$. The deviation from Poisson statistics is larger for a scintillator that exhibits a higher degree of non-proportionality, i.e., a stronger dependency of Y on E [12,13]. Interestingly, Y is often only a function of E for E<100 keV, i.e., in the diagnostic energy range. A fraction < 1 of the generated scintillation photons is detected by the light sensor and it is the statistics of the *detected* scintillation photons that ultimately determines the detector energy resolution. Finally, the generated and detected scintillation photons are distributed in time according to an exponential distribution:

$$P(\Delta t_1) = {}^{1}\!/_{\tau_d} \exp\left({}^{-\Delta t_1}\!/_{\tau_d}\right) \tag{4.2}$$

Here, Δt_1 is the time since the X-ray interaction, and τ_d the decay time constant of the scintillator, which has a major influence on the pulse duration.

Our choice of light sensor is the silicon photomultiplier (SiPM). This light sensor provides an internal gain in the order of 10^5-10^6, thereby lifting the relatively weak signal in the order of 10^0-10^1 detected scintillation photons/keV generated by a single X-ray photon substantially above the (electronic) noise level of the detector (as opposed to photodiodes). In addition, SiPMs can be miniaturized to the sub-mm level (in contrast to photomultiplier tubes). Moreover, they have found their way into clinical imaging systems, such as the high-end positron emission tomography (PET) scanners of all major vendors [14].

An SiPM consists of many single-photon avalanche diodes (SPAD). If a single scintillation photon is absorbed in a SPAD, it may trigger an avalanche multiplication process that provides the aforementioned internal gain. The fraction of photons incident on the SiPM that trigger such an avalanche process is called the photon detection efficiency (PDE). A triggered SPAD ultimately yields a current pulse $i(\Delta t_2)$ that may be described as a decaying exponential characterized by the recharge time constant τ_r:

$$i(\Delta t_2) \sim \exp\left({}^{\Delta t_2}\!/_{\tau_r}\right) \tag{4.3}$$

Here, Δt_2 is the time since the absorption of the scintillation photon in the SPAD. Since the SPADs on a single SiPM are connected in parallel, the current pulses produced by SiPM-based scintillation detectors are in essence a convolution of the exponentially decaying scintillator and SPAD responses, although subject to statistical variations due to the limited number of scintillation photons detected per unit time. Moreover, unless $\tau_r << \tau_d$, the SPAD response will substantially elongate the pulse duration, increasing the pile-up level in the detector. Fortunately, ultrafast SiPMs with τ_r < 10 ns are currently available [15].

Our goal in this work is to evaluate experimentally the counting and spectral performance of three single-pixel, X-ray photon-counting detectors consisting of such an ultrafast SiPM coupled to either a LYSO:Ce, YAP:Ce, or $LaBr_3$:Ce scintillation crystal. These materials were selected with the aid of a previously developed model of the expected detector performance, outlined in Chap. 2 of this thesis [10,11]. Each of these scintillators are readily available and have a high density and Z_{eff}, as well as a fast response to X-ray photons. We optimize pulse processing for count rate capability rather than energy resolution, and measure count rate curves using an X-ray tube, and energy resolutions at 60 keV using an Am-241 source. Such experiments are commonly done to assess the counting and spectral performance of CdTe and CZT detectors for medical X-ray photon-counting applications. Hence, we can compare the performance of the three scintillation detectors to the reported performance of direct-conversion detectors optimized for photon-counting CT, for example. We also acquire data with two other radionuclides that emit photons at other energies in the diagnostic energy range to study the proportionality of the energy response of our detectors.

4.2 Materials and methods

4.2.1 Detectors

We built single-pixel detectors based on 1.5 mm thick $Lu_{1.8}Y_{0.2}SiO_5$:Ce (LYSO, from Project Shanghai Crystals), 4.5 mm thick $YAlO_3$:Ce (YAP, from Crytur) and 3.5 mm thick $LaBr_3$:Ce ($LaBr_3$, from Luxium Solutions, formerly Saint Gobain Crystals) scintillation crystals, all with a cross-sectional area of 1×1 mm^2. In the case of LYSO and $LaBr_3$, these thicknesses provide an X-ray absorption efficiency in the diagnostic energy range (E < 150 keV) that is comparable to that of 2.5 mm CZT, whereas the 4.5 mm thick YAP crystal has a absorption efficiency similar to that of 1.5 mm CZT. A few relevant properties of these scintillators as specified by major manufacturers are given in Table 4.1.

Each scintillation crystal was coupled to a 1×1 mm^2 ultrafast SiPM from Broadcom (Fig. 4.2(a)). The SiPMs feature a SPAD pitch of 15 µm. At a bias voltage of 34 V, they have a recharge time constant of 7 ns (YAP and $LaBr_3$ detectors) or 9 ns (LYSO detector), an (optical) photon detection efficiency of about 20%-30% in the relevant wavelength range, a dark count rate in the order of 0.1 Mcps (per mm^2, also see Sec. 4.3.1), a crosstalk probability below 10%, and negligible afterpulsing. More information on these SiPM properties can be found in review papers [16].

We used Norland Optical Adhesive 63 (NOA 63) for the LYSO detector and NOA 88 for the YAP detector to make an optical coupling between scintillation crystal and SiPM. The two NOAs were selected because of their optimal transmittance at the emission wavelength of each scintillator. Since $LaBr_3$ is a hygroscopic scintillator, the $LaBr_3$ detector was built in a glovebox and the very low outgassing, optically transparent MasterBond EP30-2 epoxy was used for the optical coupling. As shown in

Fig. 4.2(b), we subsequently submerged the crystals in highly reflective polytetrafluoroethylene (Teflon) powder and compressed it to increase the light collection efficiency on the SiPM. Lastly, we sealed the $LaBr_3$ detector using a two-component epoxy, so that we were able to conduct experiments outside the glovebox with this detector. See Fig. 4.2(c) for a picture of the resulting detector, and Fig. 4.2(d) for a schematic drawing.

Table 4.1. A few relevant scintillator properties as specified by major manufacturers of the materials, i.e., Luxium Solutions (formerly Saint Gobain Crystals) for LYSO:Ce and $LaBr_3$:Ce and Crytur for YAP:Ce, unless otherwise indicated. The emission wavelength is that with the maximum intensity in the spectrum.

	$Lu_{1.8}Y_{0.2}SiO_5$:Ce (LYSO)	**$YAlO_3$:Ce (YAP)**	**$LaBr_3$:Ce (hygroscopic)**
Decay time constant τ_d (ns)	36	25	16
Light yield Y (photons/keV)	33	25	63
Emission wavelength (nm)	420	370	380
Mass density ρ (g cm^{-3})	7.1	5.4	5.1
Effective atomic number[1] [17]	65	33	46

4.2.2 Signal processing

The current signals from the SiPMs were amplified (gain = 10) and converted into voltage signals by an Analog Devices AD8099 trans-impedance amplifier, which has sufficient bandwidth (380 MHz) to maintain the shape of the raw detector pulses. These voltage signals were then digitized by a TeledyneLeCroy HDO9409 digital oscilloscope operating at a bandwidth of 200 MHz and a sampling rate of 1 GS/s. Subsequent signal processing was done offline. We first applied an offset correction to measurements conducted at low incident rates, if needed. The same correction was applied to measurements at higher rates, so that baseline shifts due to a higher incident rate were not corrected for. We subsequently applied a second-order low-pass filter with cut-off frequency f_c to suppress the statistical fluctuations on the pulses, which occur due to the

[1] The effective atomic number was calculated as $Z_{\mathrm{eff}} = \sqrt[3.5]{\sum_i a_i Z_i^{3.5}}$, where a and Z are the atomic weight fraction and the atomic number of the i^{th} element in the detection material, respectively. This formula is valid when the photo-electric effect is the dominant interaction mechanism, which is the case for the detection materials and the energy range ($E \leq 122$ keV) studied here.

finite number of scintillation photons detected per unit time, as explained in Sec. 4.1. Fig. 4.3 shows that filters with higher values of f_c lead to shorter pulses, which provide higher count rate capability, while they are less effective in suppressing the fluctuations on the pulses. Insufficient suppression will too often result in multiple counts for a single pulse, if a count is registered for every positive crossing of a predefined threshold, for example. Since we aim to push the rate capability in this work, we selected values of f_c that just sufficiently suppress the fluctuations. 25 MHz turns out to be the highest possible value of f_c for the LYSO and YAP detectors. In contrast, the raw pulses from the $LaBr_3$ detector intrinsically have a lower level of statistical fluctuations, because this scintillator provides at least two times as many scintillation photons in about twice as short a time (see Table 4.1), allowing f_c not only to be 25 MHz, but also to be increased to 100 MHz (see Fig. 4.3).

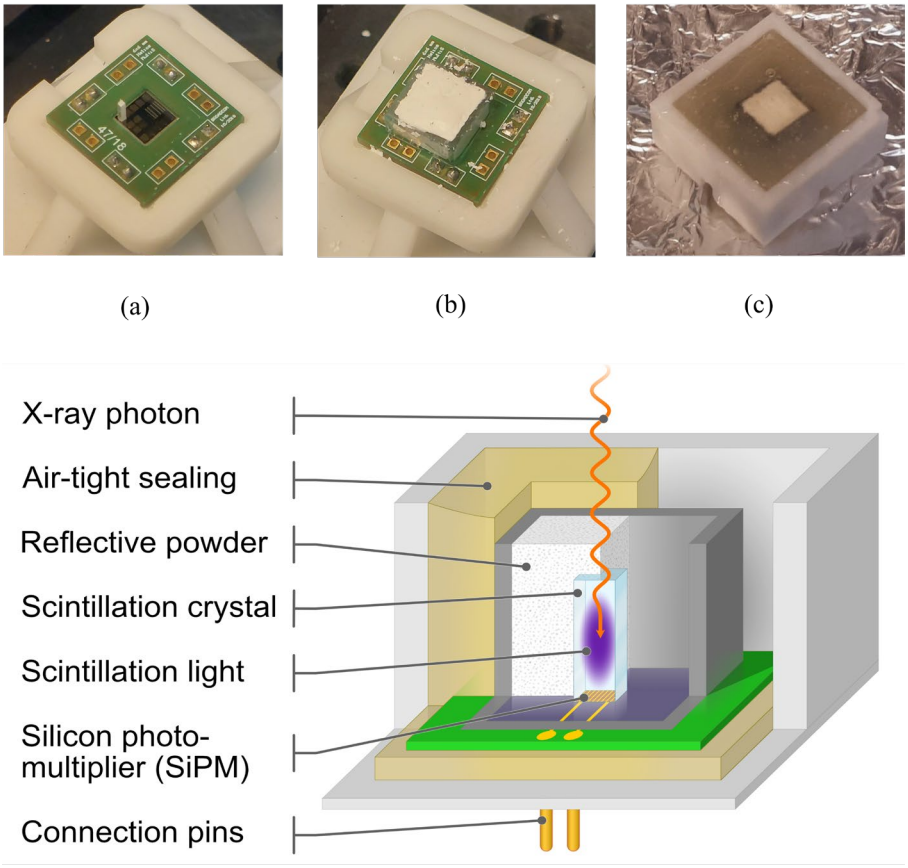

Fig. 4.2. Overview of the assembly process of a single-pixel detector. (a) We first glued a scintillation crystal on a silicon photomultiplier (SiPM) using optically transparent glue. (b) Next, we covered the crystal in white polytetrafluoroethylene (PTFE, Teflon) powder, which was then compressed to increase reflectivity. (c) Only in the case of the hygroscopic $LaBr_3$ scintillator, we additionally applied an air-tight epoxy sealing around the detector. (d) A schematic drawing of the fully assembled $LaBr_3$ detector.

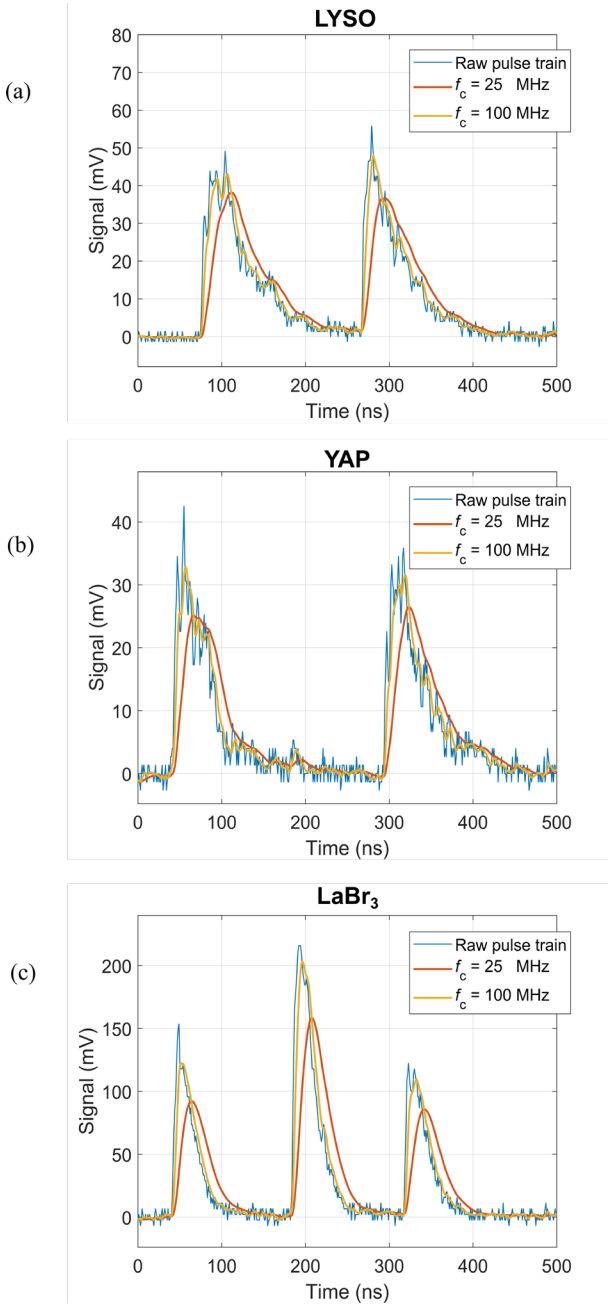

Fig. 4.3. The effect of applying second-order low-pass filters with different cut-off frequencies f_c on the raw pulse trains coming from (a) the LYSO detector, (b) the YAP detector, and (c) the $LaBr_3$ detector. Higher values of f_c lead to shorter pulses, but are less effective in reducing the random fluctuations on the pulses. The figure shows that $f_c = 100$ MHz only gives rise to smooth pulses in the case of the $LaBr_3$ detector, whereas $f_c = 25$ MHz is the maximum value that can be used with the LYSO and YAP detectors.

4.2.3 Experiments with radioactive sources

We exposed each detector to three radioactive sources: Am-241 (~10^2 kBq), Ba-133 (~10^2 kBq), and Co-57 (~10^3 kBq) and recorded 10^5 pulses per combination of source and detector. We then applied second-order low-pass filters as described in Sec. 4.2.2. For each filtered pulse, we determined the maximum signal, i.e., the pulse height, as a measure of the energy deposited. We used these data to construct pulse height histograms and identified the photopeaks associated with the following photon emissions: 14 keV (Co-57), 32 keV (Ba-133), 60 keV (Am-241), 81 keV (Ba-133), and 122 keV (Co-57). We then determined the mean pulse height μ for each energy E from Gaussian fits to these peaks. We furthermore plotted μ as a function of E and calculated the non-proportionality factor $f_{\text{non-pr}}$ with respect to the detector response at the highest energy of 122 keV as follows:

$$f_{\text{non-pr}}(E) = \frac{122\ \text{keV} \cdot \mu(E)}{\mu(122\ \text{keV}) \cdot E} \tag{4.4}$$

The more $f_{\text{non-pr}}$ deviates from 1, the stronger the dependency of the scintillator's light yield on energy, which negatively affects the energy resolution (see Eqn. (4.1) and accompanying text). We also calculated the low-rate FWHM energy resolution R of each detector at E = 60 keV. We did so from the μ and the standard deviation σ obtained from the Gaussian fit to the photopeak in the Am-241 pulse height histogram in the following way:

$$R = \frac{2.355\,\sigma(60\text{keV})}{\mu(60\text{keV})} \tag{4.5}$$

4.2.4 X-ray tube experiments

We also exposed each detector to an Yxlon Y.TU 320-D03 X-ray tube, which had a tungsten target and an anode angle of 20°. The sum of the intrinsic and additional filtration was equal to 3.0 mm Be and 7.5 mm Al, and the tube voltage was set to 120 kV. The resulting X-ray spectrum as calculated by the SpekCalc software [18] is shown in Fig. 4.4.

We gradually increased the tube current from 0.5 mA to the maximum value of 20 mA, while keeping the detector at a fixed distance from the source. This source-detector distance (SDD) was chosen such that hardly any pulse pile-up occurred in the measurement at 0.5 mA. We collected ten pulse trains of 100 ms for each tube current. These pulse trains were analyzed by means of a paralyzable-like (p-like) counting algorithm and a nonparalyzable-like (np-like) counting algorithm. Both algorithms make use of a count detection threshold, which we set to either 15 keV or 30 keV (covering the range of lowest-energy thresholds, which limit the count rate capability of a detector, commonly applied in CdTe and CZT detectors). We determined the corresponding voltage levels by linearly interpolating between the mean pulse heights measured at 14 keV and 32 keV with the radioactive sources (see Sec. 4.2.3).

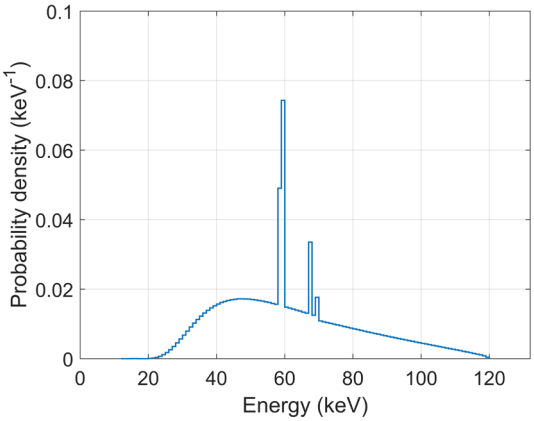

Fig. 4.4. X-ray spectrum as calculated by the SpekCalc software [18] for an X-ray tube operating at a tube voltage of 120 kV, and having a tungsten target, an anode angle of 20 degrees, and 3.0 mm Be and 7.5 mm Al filtration in total. This spectrum, which has a mean energy of 61.2 keV, was used in the experiments.

The p-like algorithm registers a count whenever the pulse train causes a positive threshold crossing. The maximum signal before the subsequent negative threshold crossing, which we refer to as the pulse height, is considered a measure of the energy associated with that count. The np-like algorithm, on the other hand, registers a count when a positive threshold crossing takes place, and evaluates whether or not the pulse train is still above threshold at the end of a window of duration τ_{np} following that threshold crossing. If so, a new count is registered and the evaluation is repeated a period of time τ_{np} later. This cycle is repeated until the outcome of the evaluation is negative. Then, the algorithm registers a new count when the next positive threshold crossing takes place. The maximum signal within τ_{np} ("the pulse height") is considered a measure of the energy associated with that count. In order to prevent counting single X-ray photons twice, it is crucial that the $\tau_{np,x}$ for an x keV threshold exceeds the maximum time-over-the x keV threshold ($ToT_{max,x}$) of the pulses. Fig. 4.5 contains the five mean pulse shapes of events that ended up in the five full-energy peaks measured with the $LaBr_3$ detector (f_c=100 MHz) and the three radioactive sources mentioned in Sec. 4.2.3. It shows that the larger the energy deposition in the scintillator, the larger ToT_x. Since the maximum X-ray energy in the experiments is 120 keV (see Fig. 4.4), we determined $ToT_{max,15keV}$ and $ToT_{max,30keV}$ for all detectors from the mean pulse shape of events that ended up in the 122 keV peak measured with the Co-57 source. We then selected values of $\tau_{np,15keV}$ and $\tau_{np,30keV}$ that just exceeded the values of $ToT_{max,x}$ found in this way. These $\tau_{np,x}$ values are given in Table 4.2.

Using a combination of counting algorithm and threshold, we determined the number of counts in each of the ten pulse trains of 100 ms acquired at a certain tube current. We then calculated the output count rate for each pulse train and averaged these OCRs to obtain a mean OCR at that tube current. We repeated this for each tube current in order

to be able to plot a count rate curve, i.e., (mean) OCR as a function of tube current. However, it is more insightful to plot OCR as a function of input count rate (ICR). We therefore estimated an ICR for each tube current by assuming ICR=OCR for a tube current of 0.5 mA and a 15 keV threshold, and by making use of the fact that the ICR is proportional to the tube current. The former is a valid assumption, because we made sure there was hardly any pulse pile-up occurring at 0.5 mA and the minimum energy in the X-ray tube spectra exceeded 20 keV (see Fig. 4.4). We plot these estimated ICRs along the top horizontal axes of the count rate curve diagrams.

Furthermore, we show histograms of the pulse heights associated with the counts registered at the lowest ICR, i.e. at a tube current of 0.5 mA. Using linear interpolation of the data on pulse height as a function of photon energy (see Sec. 4.2.3), we plot X-ray energy along the top horizontal axes of these diagrams.

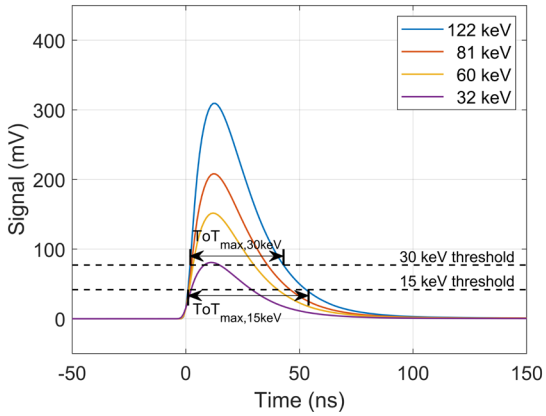

Fig. 4.5. Mean shape of the pulses due to the full absorption of photons of various energies in the $LaBr_3$ detector (f_c = 100 MHz). The 15 keV and 30 keV thresholds are also visualized, as well as the maximum time-over-the x keV thresholds ($ToT_{max,x}$) in these experiments, i.e., the ToT_x for the 122 keV pulse. We chose τ_{np} values for the np-like counting algorithm that just exceeded these values of $ToT_{max,x}$ (see Table 4.2).

Table 4.2. The values of the "nonparalyzable-like dead time" τ_{np}, for 15 keV and 30 keV thresholds, and for each detection material and cut-off frequency f_c of the second-order low-pass filter applied to the raw pulse trains.

Detection material	f_c **(MHz)**	$\tau_{np,15keV}$ **(ns)**	$\tau_{np,30keV}$ **(ns)**
LYSO	25	130	100
YAP	25	100	80
$LaBr_3$	25	70	60
$LaBr_3$	100	55	45

4.3 Results

4.3.1 Pulse height spectra

Fig. 4.6(a), (b) and (c) show the pulse height spectra of the three radioactive sources measured with the LYSO:Ce, YAP:Ce, and $LaBr_3$:Ce detectors, respectively.

The peaks resulting from the full absorption of 122 keV photons from the Co-57 source can be appreciated on the far right side of the corresponding spectra. These peaks are typically accompanied by satellite peaks located somewhat more to the left, which represent photo-electric absorption events in which the resulting K X-ray escapes from the crystal. The average K X-ray energy equals 55 keV and 34 keV for the elements Lu and La, respectively, so this K-escape peak occurs at 67 keV in case of the LYSO detector (Fig. 4.6(a)) and 88 keV in case of the $LaBr_3$ detector (Fig. 4.6(c)). Yttrium K X-rays have an average energy of only 15 keV, so the counts in the Co-57 spectrum of the YAP detector (Fig. 4.6(b)) around 40 mV are too far away from the 122 keV peak to represent K-escape events. It is more likely that these are due to 122 keV photons that have Compton-scattered in the materials surrounding the scintillator, i.e., mainly in the compressed Teflon powder (with a low effective atomic number) in the case of the YAP detector (see Fig. 4.2(b)). The maximum energy loss due to Compton scattering in these materials is 39 keV for 122 keV photons, meaning that this continuum of counts starts at an energy of 83 keV. K X-rays from the lead shielding of the set-up (with an average energy of 77 keV) may also contribute to this continuum of counts. It is noted that similar counts have likely been registered by the LYSO and $LaBr_3$ detectors, but they cannot be clearly resolved from the K-escape peaks in these cases.

Co-57 also emits 14 keV photons, giving rise to the indicated peaks at the left side of the spectra. In the case of the YAP detector (Fig. 4.6(b)), this peak overlaps with what is likely a Compton plateau, which extends to 39 keV for incident photons with an energy of 122 keV. Because of the relatively low Z_{eff} of YAP (33, see Table 4.1), Compton scattering is much more likely (37% of all interactions) than in LYSO and $LaBr_3$ (6.6% and 15%, respectively). Thus, the corresponding features in Fig. 4.6(a) and (c), although present, are much weaker. Especially in the case of the $LaBr_3$ detector (Fig. 4.6(c)), the Compton plateau is hardly visible, because it is spread out over many more 1 mV bins.

There is an additional feature, which is not only present in the Co-57 spectrum, but in all spectra measured with the YAP detector, namely the small peaks at 2 mV (see Fig. 4.6(b)). These are due to SiPM dark counts, which generally constitute the main source of noise in SiPM-based detectors [16]. There is hardly any overlap between this noise peak and the 14 keV peak, so dark counts can be effectively rejected during data/image acquisition by setting the lowest threshold to a voltage level equivalent to 10 keV, for example. The LYSO and $LaBr_3$ detectors output stronger pulses in response to a single X-ray or gamma photon (see Fig. 4.6), due to the higher light yield of these scintillators, for example (see Table 4.1). The dark counts with a pulse height around 2 mV therefore coincide with counts due to photons with an energy much lower than 10 keV for these

(a)

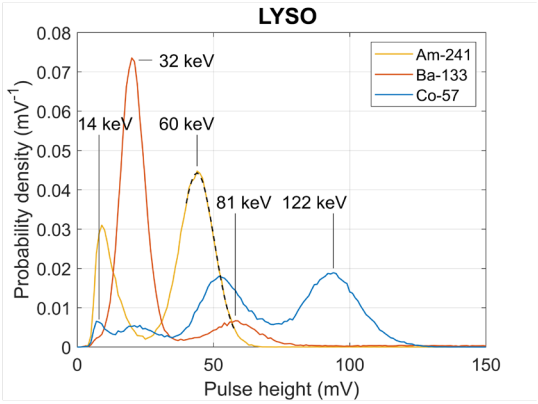

(b)

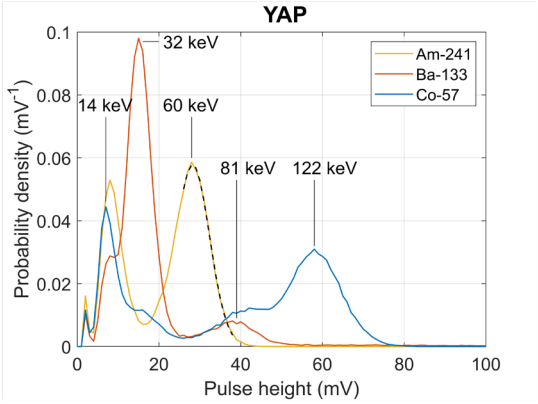

(c)

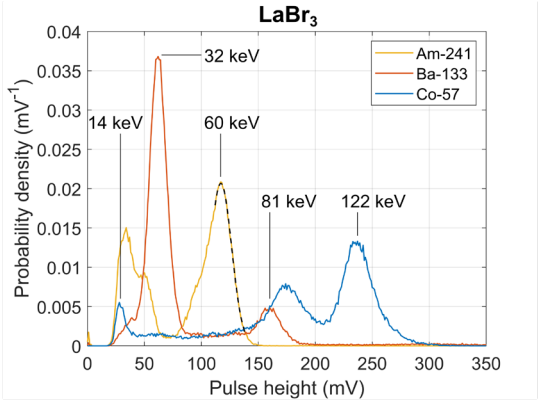

Fig. 4.6. Pulse height spectra of the Am-241, Ba-133, and Co-57 sources as measured with (a) the LYSO detector, (b) the YAP detector, and (c) the $LaBr_3$ detector. All raw pulses were first filtered by a second-order low-pass filter with a cut-off frequency of 25 MHz before the pulse heights were determined. The dashed curves are Gaussian fits to the 60 keV peak, which were used to determine the FWHM energy resolution. They run from 90% of the maximum on the left side to 10% of the maximum on the right side of the peak, in order to exclude the effect of the asymmetry of the peak on the energy resolution. The asymmetry is due to photons that Compton scattered in the materials surrounding the scintillator (see Fig. 4.2) before being detected.

detectors. This means a lowest threshold far below 10 keV is sufficient to reject dark counts during acquisition. Indeed, we could set a trigger threshold on the digital oscilloscope that completely rejected the dark counts, without removing part of the 14 keV peak. That is why the noise peak is absent in the spectra shown in Fig. 6(a) and (c).

The main peaks in the Ba-133 spectra are due to a narrow band of X-ray emissions centered at 32 keV and a gamma-ray emission at 81 keV. Overlapping K-escape peaks can be seen on the left-hand side of the 32 keV peaks in Fig. 4.6(b) and (c). These are caused by the escape of bromine and yttrium K X-rays with average energies of 12 keV and 15 keV, respectively. In the LYSO detector (Fig. 4.6(a)), K-escape is negligible at an incident photon energy of 32 keV, because this is below the K-edge energy of Lu (63 keV). For incident photons with an energy of 81 keV, on the other hand, K-escape leads to an average energy deposition of 26 keV in the LYSO detector. As a result, the corresponding peak cannot be distinguished from the 32 keV peak. In the case of the YAP detector, the 81 keV peak is asymmetric because it overlaps with a K-escape peak around 66 keV. The K-escape peak lies at 47 keV in the case of the $LaBr_3$ detector and contributes to the continuum of counts observed between the 32 keV and 81 keV peaks. Compton scattering of 81 keV photons in the low-Z_{eff} materials surrounding the $LaBr_3$ crystal, such as epoxy and Teflon powder (see Fig. 4.2(b) and (c)), may also contribute to this continuum. For the LYSO and YAP detectors, this effect likely contributes to the asymmetric shape of the 81 keV photopeak.

In the case of the Am-241 source, the 60 keV photopeak is of main interest. The other peak is due to X-ray emissions with energies ranging from 11 keV to 22 keV, so it is less useful for determining pulse height as a function of energy. The spectrum measured with the $LaBr_3$ detector (Fig. 4.6(c)) contains a lanthanum K-escape peak at 26 keV, which overlaps with the X-ray peak. The K-escape peak should be around 45 keV for the YAP detector, but cannot be distinguished from the 60 keV peak. Instead, it may contribute to the somewhat asymmetric shape of this peak (Fig. 4.6(b)). However, Compton scattering of 60 keV photons in the materials surrounding the scintillators, which leads to counts of at least 49 keV, also contributes to this asymmetry, given the clearly asymmetric shape of the 60 keV peak in the spectrum measured with the $LaBr_3$ detector. K-escape from the LYSO crystal is again negligible for incident photon energies below the K-edge energy of 63 keV, so any asymmetry in the 60 keV peak in Fig. 4.6(a) must be due to Compton scattering, as well.

4.3.2 Energy resolution

The FWHM energy resolution of the 60 keV photopeak in an Am-241 spectrum is a commonly reported measure of spectral performance of X-ray photon-counting detectors. However, as discussed above and visualized in Fig. 4.6, counts due to photons that have Compton-scattered in low-Z_{eff} materials surrounding the crystal tend to make this peak asymmetric in our experiments. However, such counts are unlikely in a pixel array, because Compton scattering hardly occurs in the investigated scintillation materials at 60 keV due to their higher Z_{eff}. We therefore tried to minimize the effect of these counts on the FWHM energy resolution. We did so by determining the energy

resolution from a Gaussian fit to the 60 keV peak starting at 90% of the maximum on the left-hand side and running down till 10% of the maximum on the right-hand side of the peak (see Fig. 4.6). We thus found FWHM energy resolutions at 60 keV of 34% (LYSO, f_c = 25 MHz), 35% (YAP, f_c = 25 MHz), 19% ($LaBr_3$, f_c = 25 MHz), and 22% ($LaBr_3$, f_c = 100 MHz). A lower f_c leads to a somewhat better energy resolution for the $LaBr_3$ detector, because it is more effective in reducing the pulse height variation among pulses. Fig. 4.6 furthermore shows that the superior energy resolution of the $LaBr_3$ detector clearly provides better spectral separation between 60 keV and 81 keV photons, for example. This may allow for an additional energy bin in practice (see Sec. 4.1), without too many photons being registered in a wrong bin.

4.3.3 (Non-)proportionality

We determined the (mean) pulse height and the non-proportionality factor $f_{non\text{-}pr}$ (see Eqn. (4.4)) as a function of energy for each detector from the data presented in Fig. 4.6. The results are shown in Fig. 4.7. It can be noticed that the LYSO detector is considerably less proportional than the YAP and $LaBr_3$ detectors. Non-proportionality is a well-known characteristic of LYSO [13]. The same holds for the remarkable behavior of $f_{non\text{-}pr}$ around the K-edge of lutetium at 63 keV. The relatively large deviation of $f_{non\text{-}pr}$ from 1 largely explains why the above-mentioned energy resolution of the LYSO detector is similar to that of the YAP detector despite a much stronger signal from the LYSO detector, i.e., more detected optical scintillation photons, caused by the higher light yield of LYSO, for example (see Eqn. (4.1) and accompanying text, and Table 4.1). $f_{non\text{-}pr}$ only substantially deviates from 1 for the YAP and $LaBr_3$ detectors around 14 keV. This finding is unexpected and may be related to the fact that $f_{non\text{-}pr}$ becomes sensitive to small errors in the fitted value of the mean pulse height when the photon energy becomes low compared to the reference energy of 122 keV (see Eqn. (4.4)).

4.3.4 X-ray tube spectra

Fig. 4.8 shows the X-ray tube spectra measured with the three detectors, using the paralyzable-like counting algorithm with a 15 keV threshold, at the lowest tube current of 0.5 mA. The top horizontal axes show the energy in keV, derived from the data in Fig. 4.7. The tube voltage was 120 kV in all measurements. We notice little spectral overflow to energies above 120 keV, confirming that the pile-up level is low at this tube current. The few counts registered above 120 keV also result from the finite energy resolution of the detectors. Comparing the spectra in Fig. 4.8 to the ground truth in Fig. 4.4, we notice two main differences. Firstly, the K X-ray lines of the tungsten target are blurred by the energy resolution of the detectors. They are best resolved from the underlying Bremsstrahlung spectrum by the $LaBr_3$ detector, because this detector offers the best energy resolution (see Sec. 4.3.2). Secondly, we note that the spectral intensity does not drop to zero around 20 keV, as expected based on Fig. 4.4. The registered counts around this energy probably result from X-ray photons that first scattered in the materials surrounding the scintillation crystals (see Fig. 4.2) and X-ray photons that deposited only part of their energy in the scintillator during a Compton interaction. K-escape can also result in counts around 20 keV. For example, the high count rate

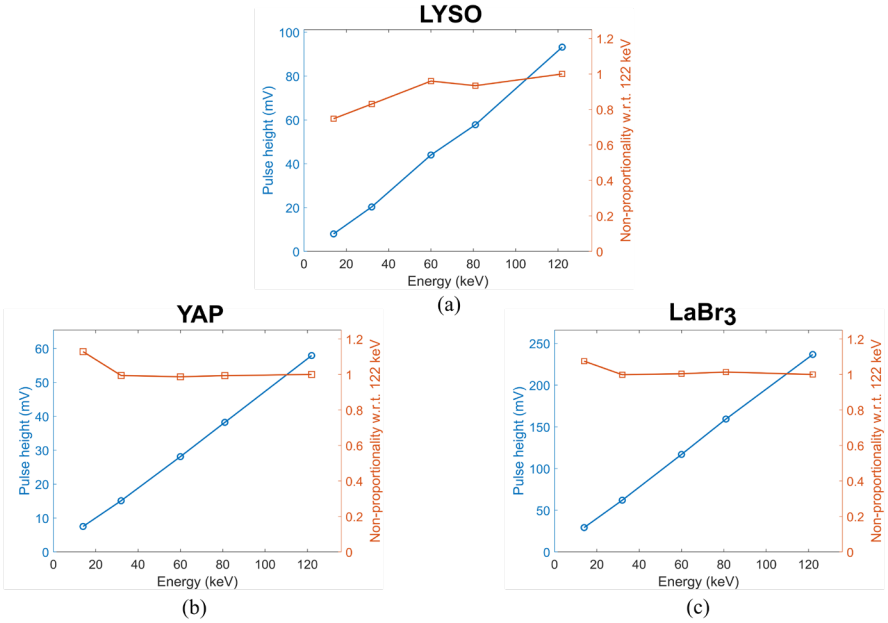

Fig. 4.7. (Mean) pulse height as a function of energy, determined from Gaussian fits to the data in Fig. 6 for (a) the LYSO detector, (b) the YAP detector, and (c) the $LaBr_3$ detector , with the cut-off frequency set to 25 MHz in all cases. The right axes show the non-proportionality factor $f_{\text{non-pr}}$ with respect to (w.r.t) 122 keV, as defined in Eqn. (4.4).

registered by the LYSO detector at 15 keV (see Fig. 4.8(a)) may be due to K-escape following the photo-electric absorption of photons with an energy around 70 keV.

4.3.5 Count rate performance

Fig. 4.9 shows the count rate curves obtained with the LYSO and YAP detectors. The curves for p-like counting indeed show paralyzable-like behavior, i.e., the maximum output count rate reaches a maximum, before it starts to decrease towards 0. The LYSO detector reaches maximum OCRs of 3.5 Mcps/pixel and 4.5 Mcps/pixel for 15 keV and 30 keV count detection thresholds, respectively, while the YAP detector achieves OCRs of at most 4.3 Mcps/pixel and 5.4 Mcps/pixel for these thresholds. The corresponding estimated input count rates are about 2.5 times as large. The detectors should only be used up to these values of ICR, so that the conversion of a measured OCR into an ICR, which is needed to determine the transmission by the object to be imaged, remains unambiguous. However, the closer ICR to this maximally allowed ICR, the lower the contrast sensitivity.

Likewise, the curves for np-like counting show typical nonparalyzable behavior, i.e., they approach asymptotic values defined by OCR = $1/\tau_{\text{np}}$. The used values of τ_{np} were provided in Table 4.2. In the case of the LYSO detector, the asymptotic values equal 7.7 Mcps/pixel and 10 Mcps/pixel for 15 keV and 30 keV thresholds, respectively. The curves for the YAP detector approach 10 Mcps/pixel and 12.5 Mcps/pixel for these

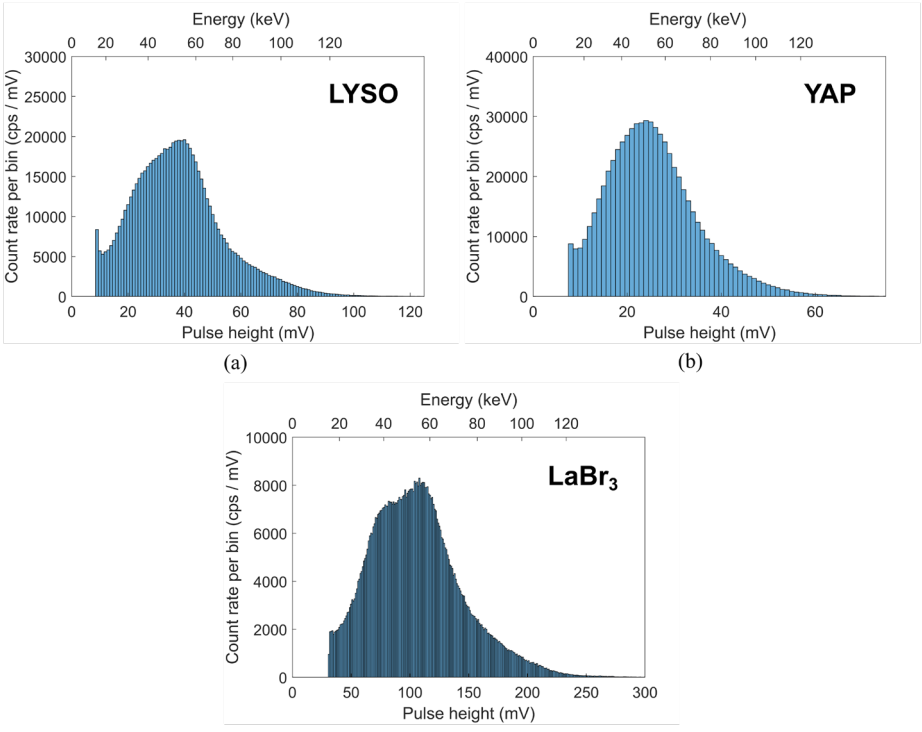

Fig. 4.8. X-ray tube spectra measured by (a) the LYSO detector, (b) the YAP detector, and (c) the $LaBr_3$ detector (f_c = 25 MHz). See Fig. 4.4 for a ground truth spectrum The spectra shown here were acquired at a tube current of 0.5 mA, using a paralyzable-like counting algorithm with a 15 keV threshold. The conversion from pulse height (bottom horizontal axis) to energy (top horizontal axis) is based on the curves shown in Fig. 4.7.

thresholds. Since the curves do not have a maximum, there is no limit on the usable range of ICRs, although it again holds that the contrast sensitivity is lower in the flatter parts of the curves.

Comparing the results for the LYSO and YAP detectors, we observe that the latter performs somewhat better from a count-rate capability point-of-view. Not only the (slightly) faster decay time constant of YAP explains this observation, but also its more proportional energy response (see Fig. 4.7(a) and (b)). This can be understood as follows: If an X-ray photon with an energy of, say, 60 keV deposits its energy in a scintillator, the resulting detector pulse will be longer above the threshold when $f_{\text{non-pr}}(E_{\text{threshold}}) < f_{\text{non-pr}}(60\text{ keV})$, compared to when $f_{\text{non-pr}}(E_{\text{threshold}}) \geq f_{\text{non-pr}}(60\text{ keV})$ (also see Eqn. (4.4)).

The count rate curves of the $LaBr_3$ detector are shown in Fig. 4.10. For a cut-off frequency of 25 MHz (Fig. 4.10(a)) and p-like counting, we observe maximum OCRs of 6.0 Mpcs/pixel and 7.4 Mcps/pixel for 15 keV and 30 keV thresholds, respectively. The corresponding estimated ICRs are about 2.5 times as large. The curves for np-like

counting approach an asymptotic value just exceeding 14.0 Mcps/pixel in the case of a 15 keV threshold, and a value around 16.5 Mcps/pixel for a 30 keV threshold, in accordance with expectations based on calculating $1/\tau_{np}$ for the values of τ_{np} listed in Table 4.2.

Although the scintillation decay of $LaBr_3$ is about twice as fast as that of LYSO and YAP, we do not yet observe twice as high OCRs. This is because we kept the cut-off

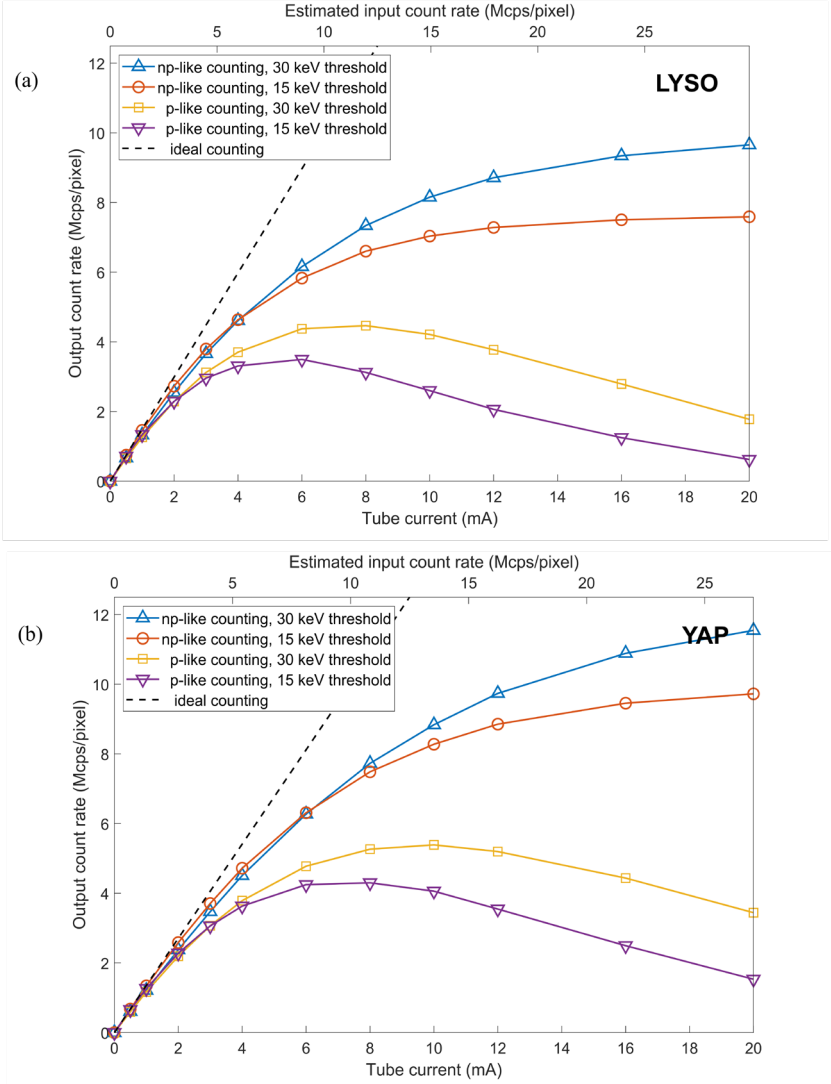

Fig. 4.9. Count rate curves, i.e. output count rate as a function of tube current (bottom horizontal axis) / (estimated) input count rate (top horizontal axis), for paralyzable-like (p-like) and nonparalyzable-like (np-like) counting algorithms and two low-energy count detection thresholds, measured with (a) the LYSO detector, and (b) the YAP detector. The dashed line for ideal counting represents the case of the OCR equaling the estimated ICR.

frequency of the second-order low-pass filter at 25 MHz, which results in a noticeable elongation of the pulse duration compared to the raw pulses (see Fig. 4.3(c)). Hence, in order to increase the count rate capability by a factor two, one should also reduce the time constant of the low-pass filter by a factor two. Since f_c of a low-pass filter is inversely proportional to that time constant, an f_c of at least 50 MHz is needed. Fortunately, we showed in Fig. 4.3(c) that the high number of scintillation photons emitted and detected per unit time in the $LaBr_3$ detector makes it possible to increase f_c

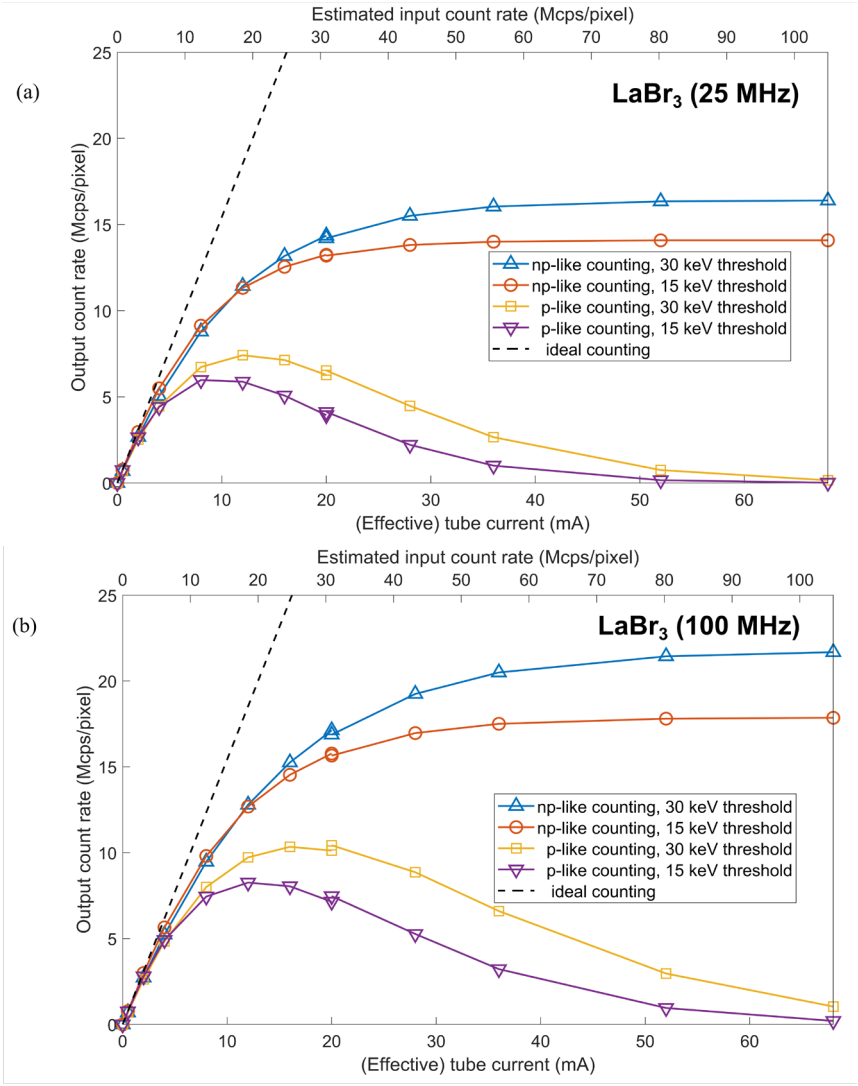

Fig. 4.10. Count rate curves, i.e. output count rate as a function of tube current (bottom x-axis) / (estimated) input count rate (top x-axis), for two counting algorithms and two low-energy thresholds, measured using (a) the $LaBr_3$ detector with f_c = 25 MHz, and (b) the same detector with f_c=100 MHz. The dashed line is the case of output count rate equaling input count rate.

to 100 MHz. Fig 4.10(b) shows the count rate curves for f_c = 100 MHz. The maximum OCRs for p-like counting now increase to 8.3 Mcps/pixel and 10.4 Mcps/pixel for the 15 keV and 30 keV thresholds, respectively, while the curves for np-like counting approach 18 Mcps/pixel and 22 Mcps/pixel for these thresholds. Those values are indeed about twice as high as the corresponding values for the LYSO and YAP detectors, and again in agreement with expectations based on calculating $1/\tau_{np}$ for the values of τ_{np} listed in Table 4.2.

For completion, we note that the curves in Fig. 4.10 feature a small discontinuity at the maximum tube current of 20 mA. Since the $LaBr_3$ detector in np-like counting mode appeared to be able to deal with considerably higher ICRs than could be reached with this tube current at the initial source-detector distance, we performed additional measurements at a two-fold reduced SDD (which should yield a four-times as high ICR), starting a new tube current sweep at 5 mA (which should yield a four-times as low ICR). This is the reason why the horizontal axes in Fig. 4.10 are labelled *effective* tube current. The small discontinuities in the curves indicate that we did not manage to reduce the SDD by exactly a factor two.

4.4 Discussion

We measured the count rate curves and the low-fluence rate spectral performance, i.e., the proportionality of the energy response and the FWHM energy resolution at 60 keV, of 1×1 mm^2 single-pixel detectors consisting of LYSO, YAP, and $LaBr_3$ scintillation crystals coupled to very fast SiPMs for (clinical) X-ray photon-counting applications, such as photon-counting CT systems. Pulse processing consisted of current-to-voltage conversion, a second-order low-pass filter with cut-off frequency f_c optimized for counting performance rather than energy resolution, and either a paralyzable-like or nonparalyzable-like counting algorithm. Both algorithms consider pulse height as a measure of energy deposited.

As expected on the basis of scintillator characterization studies available in literature [13], the YAP and $LaBr_3$ detectors showed a very proportional response within the energy range investigated (14 keV - 122 keV). However, the $LaBr_3$ detector showed the best spectral performance overall, achieving FWHM energy resolutions at 60 keV of 19% for f_c = 25 MHz and 22% for f_c = 100 MHz. The former is comparable to at least one CdTe detector developed for diagnostic PCCT [19].

A factor limiting the number of detected scintillation photons, and therefore the energy resolution achieved with the present detectors, is the rather low (20-30%) photon detection efficiency (PDE) of the SiPMs. This means that only 20-30% of the scintillation photons incident on the SiPM are actually detected. Recently, a new, very fast (recharge time constant < 5 ns) SiPM was reported with a PDE of 60% in the relevant wavelength range [20]. A twice to thrice as high PDE can lead to a factor √2 to √3 better energy resolution. Especially the energy resolutions of detectors based on

proportional scintillators, such as YAP and $LaBr_3$ (see Fig. 4.7), are likely to benefit from a higher PDE. Thus, an energy resolution better than 15% FWHM at 60 keV may be feasible with a $LaBr_3$-based X-ray photon-counting detector.

In addition, we stress that the present detectors are prototypes. Further improvements in reflector and optical coupling between scintillator and SiPM may therefore be possible. This would also increase the number of detected scintillation photons and improve the energy resolution.

In this early stage of development, we opted for a few mm of compressed PTFE (Teflon) powder as a reflector around the scintillation crystal. In the case of the hygroscopic $LaBr_3$ detector, there was also an air-tight epoxy sealing around the detector (see Fig. 4.2). The 60 keV photopeaks, from which the energy resolution were determined, were somewhat asymmetric, because some of the incident photons underwent Compton scattering in these surrounding materials with a low effective atomic number before hitting the crystal. This effect will be absent in a practical imaging detector, which primarily consists of a scintillation crystal array and typically contains relatively few low-Z_{eff} materials. Although we tried to mitigate the influence of the photopeak asymmetry on the energy resolution by fitting Gaussian functions only to the high-energy side of the peaks (see Fig. 4.6), the values of the energy resolution found in this way may still be worse than those obtained with a detector containing fewer low-Z_{eff} materials.

The best count rate performance in this work was also obtained with the $LaBr_3$ detector, using f_c = 100 MHz. The scintillator's high light yield of 63 photons/keV, in combination with its short decay time constant τ_d of 16 ns, enables this high value of f_c by increasing the number of optical photons emitted per unit time, thereby reducing the statistical fluctuations on the pulses (see Sec. 4.2.2 and Fig. 2.3). When operated in p-like counting mode with a 30 keV threshold, the detector achieves a maximum observed count rate of 10.4 Mcps/pixel, while the output count rate approaches an asymptotic value of 22 Mcps/pixel in np-like mode with the same threshold (see Fig. 4.2(b)). These values are about 80% of the corresponding values reported for state-of-the-art CdTe and CZT detectors developed and (extensively) optimized for diagnostic photon-counting CT (prototype) scanners, i.e., 13 Mcps/pixel for p-like counting with a 30 keV threshold [21] and 28-29 Mcps/pixel for np-like counting with a 25 keV threshold [22], which corresponds to $\tau_{np} \approx 35$ ns. Thus, equal count rate performance could be achieved at the imaging system level using only marginally smaller pixels [10]. Alternatively, given that the recharge time constant of the SiPM used in this work is less than the decay time constant of $LaBr_3$, higher OCRs per pixel could be achieved using a (not necessarily readily available) scintillator with $\tau_d < 16$ ns. However, in order to benefit from a faster scintillation decay, such a scintillator should have a sufficiently high light yield that f_c need not be reduced to keep the level of pulse fluctuation on an acceptable level. Fortunately, this requirement can be mitigated by using the aforementioned ultrafast SiPMs that have a PDE of 60%, which is two to three times as high than that of the SiPMs used here.

We have thus shown that an SiPM-based $LaBr_3$ detector can approach both the counting and spectral performance of CdTe/CZT detectors for diagnostic photon-counting CT systems. However, we note that comparing both detector concepts is not straightforward, because they are different concepts and the performance may depend on factors such as pixel dimensions, operating conditions etc.

Furthermore, it is to be noted that $LaBr_3$ is a hygroscopic material, thus requiring an air-tight sealing. Practical $LaBr_3$ detectors are typically sealed using a thin layer of aluminum, as is the case for other hygroscopic scintillators. One example is NaI:Tl, which is commonly used in nuclear medicine imaging systems, such as single-photon emission computed tomography (SPECT). The other two scintillators investigated here, LYSO and YAP, have the advantage that they are not hygroscopic, but their energy resolutions exceed 30% FWHM at 60 keV and their maximum OCRs per pixel are approximately twice as low as that of the $LaBr_3$ detector (see Fig. 4.9 and 4.10(b)). Consequently, they would need about twice as many pixels per unit area to achieve a similar rate capability per mm^2, which comes with a number of drawbacks, including a larger dead area occupied by the reflectors around each pixel. However, we pointed towards a few examples of existing, finely pixelated scintillation crystal arrays with sub-65 nm reflectors in previous work [10,11]. We also mentioned a few other innovative methods to deal with this challenge there. All these examples and methods are discussed in Sec. 6.3.1 of this thesis, as well. Alternatively, the LYSO and YAP detectors may be useful for X-ray imaging systems that are less demanding in terms of rate capability and pixel size than diagnostic CT. Moreover, it also holds for the LYSO and YAP detectors that the aforementioned SiPMs with a PDE of 60% will yield a better energy resolution, and likely allow for a cut-off frequency exceeding 25 MHz, thereby reducing the pulse duration and improving the rate capability of these detectors.

4.5 Conclusion

The count rate curve and (low fluence-rate) energy resolution are commonly used to describe the performance of X-ray photon-counting detectors for medical imaging applications. Here, we measured these parameters for three 1×1 mm^2 single-pixel detectors consisting of LYSO, YAP or $LaBr_3$ scintillation crystals coupled to ultrafast silicon photomultipliers.

The LYSO and YAP detectors reach maximum output count rates per pixel of about 40% of those reported for CdTe- and CZT-based direct-conversion detectors developed and (extensively) optimized for prototype diagnostic photon-counting CT systems, while their energy resolutions exceed 30% FWHM at 60 keV. The $LaBr_3$ detector, on the other hand, achieves maximum OCRs of 10.4 Mcps/pixel and 22 Mcps/pixel in paralyzable-like and nonparalyzable-like mode, respectively. These numbers are about 80% of those of the aforementioned direct-conversions detectors. Thus, equal count rate performance may be achieved at the imaging system level using marginally smaller pixels. Moreover, the $LaBr_3$ detector shows a proportional energy response and its

energy resolution of about 20% FWHM at 60 keV is similar to that of at least one CdTe detector developed for diagnostic CT.

These results indicate that $LaBr_3$-based detectors may be a viable alternative for direct-conversion detectors for diagnostic photon-counting CT, whereas LYSO- and YAP-based detectors appear more suitable for less demanding applications. Looking forward, considerable improvements in both counting and spectral performance are to be expected if the SiPMs used here are replaced by a recently developed version with a two to three times as high optical photon detection efficiency. Moreover, research into faster scintillators for this application appears warranted, because the scintillation decay time constant is the main factor limiting the rate capability of SiPM-based X-ray photon-counting scintillation detectors.

Acknowledgements

We thank Luxium Solutions (formerly Saint Gobain Crystals) for providing us with the $1\times1\times3$ mm^3 $LaBr_3$:Ce scintillation crystals, and Broadcom Inc. for supplying the ultrafast SiPMs. Furthermore, we are grateful to Hugo van der Kort and Martin van Exter for designing the tools that allowed us to couple these small scintillators to the SiPMs. We also thank Martijn de Boer and Jan Huizenga for their assistance in setting up the experiments.

References

[1] S. Leng *et al.*, "Photon-counting Detector CT: System Design and Clinical Applications of an Emerging Technology," *RadioGraphics,* vol. 39, no. 3, pp. 729-743, 2019, doi: https://doi.org/10.1148/rg.2019180115.

[2] T. Flohr, M. Petersilka, A. Henning, S. Ulzheimer, J. Ferda, and B. Schmidt, "Photon-counting CT review," *Physica Medica,* vol. 79, pp. 126-136, 2020, doi: https://doi.org/10.1016/j.ejmp.2020.10.030.

[3] M. Danielsson, M. Persson, and M. Sjölin, "Photon-counting x-ray detectors for CT," *Physics in Medicine & Biology,* vol. 66, no. 3, p. 03TR01, 2021, doi: https://doi.org/10.1088/1361-6560/abc5a5.

[4] K. Rajendran *et al.*, "First clinical photon-counting-detector CT system: Technical evaluation," *Radiology,* vol. 303, no. 1, p. 130, 2022, doi: https://doi.org/10.1148/radiol.212579.

[5] S. Si-Mohamed *et al.*, "Feasibility of lung imaging with a large field-of-view spectral photon-counting CT system," *Diagnostic and Interventional Imaging,* vol. 102, no. 5, pp. 305-312, 2021, doi: https://doi.org/10.1016/j.diii.2021.01.001.

[6] M. Persson *et al.*, "Upper limits of the photon fluence rate on CT detectors: Case study on a commercial scanner," *Medical physics,* vol. 43, no. 7, pp. 4398-4411, 2016, doi: https://doi.org/10.1118/1.4954008.

[7] U. N. Roy *et al.*, "Role of selenium addition to CdZnTe matrix for room-temperature radiation detector applications," *Scientific reports,* vol. 9, no. 1, pp. 1-7, 2019, doi: https://doi.org/10.1038/s41598-018-38188-w.

[8] H. Bornefalk and M. Danielsson, "Photon-counting spectral computed tomography using silicon strip detectors: a feasibility study," *Physics in Medicine & Biology,* vol. 55, no. 7, p. 1999, 2010, doi: https://doi.org/10.1088/0031-9155/55/7/014.

[9] J. da Silva *et al.*, "Resolution characterization of a silicon-based, photon-counting computed tomography prototype capable of patient scanning," *Journal of Medical Imaging,* vol. 6, no. 4, p. 043502, 2019, doi: https://doi.org/10.1117/1.JMI.6.4.043502.

[10] S. J. van der Sar, S. E. Brunner, and D. R. Schaart, "Silicon photomultiplier-based scintillation detectors for photon-counting CT: A feasibility study," *Medical physics,* vol. 48, no. 10, pp. 6324-6338, 2021, doi: https://doi.org/10.1002/mp.14886.

[11] S. J. van der Sar and D. R. Schaart, "Silicon Photomultiplier-Based Scintillation Detectors for Photon-Counting X-Ray Imaging," in *Radiation Detection Systems*. Boca Raton, FL, USA: CRC Press, 2021, pp. 289-312, doi: https://doi.org/10.1201/9781003147633-10.

[12] P. Dorenbos, J. T. M. de Haas, and C. Van Eijk, "Non-proportionality in the scintillation response and the energy resolution obtainable with scintillation crystals," *IEEE Transactions on Nuclear Science,* vol. 42, no. 6, pp. 2190-2202, 1995, doi: https://doi.org/10.1109/23.489415.

[13] I. V. Khodyuk and P. Dorenbos, "Trends and patterns of scintillator nonproportionality," *IEEE Transactions on Nuclear Science,* vol. 59, no. 6, pp. 3320-3331, 2012, doi: https://doi.org/10.1109/TNS.2012.2221094.

[14] S. Surti and J. S. Karp, "Update on latest advances in time-of-flight PET," *Physica Medica,* vol. 80, pp. 251-258, 2020, doi: https://doi.org/10.1016/j.ejmp.2020.10.031.

[15] F. Acerbi, G. Paternoster, A. Gola, V. Regazzoni, N. Zorzi, and C. Piemonte, "High-density silicon photomultipliers: Performance and linearity evaluation for high efficiency and dynamic-range applications," *IEEE Journal of Quantum Electronics,* vol. 54, no. 2, pp. 1-7, 2018, doi: https://doi.org/10.1109/JQE.2018.2802542.

[16] C. Piemonte and A. Gola, "Overview on the main parameters and technology of modern Silicon Photomultipliers," *Nuclear Instruments & Methods in Physics Research A,* vol. 926, pp. 2-15, 2019, doi: https:///doi.org/10.1016/j.nima.2018.11.119.

[17] A. J. J. Bos, F. S. Draaisma, and W. J. C. Okx, "Hoofdstuk 3: Wisselwerking van Straling met Materie," in *Inleiding tot de Stralingshygiëne*: Sdu Uitgevers, 2007, p. 64, doi: ISBN: 978 90 12 11 905 4.

[18] G. Poludniowski, G. Landry, F. Deblois, P. Evans, and F. Verhaegen, "SpekCalc: a program to calculate photon spectra from tungsten anode x-ray tubes," *Physics in Medicine & Biology,* vol. 54, no. 19, p. N433, 2009, doi: https://doi.org/10.1088/0031-9155/54/19/N01.

[19] R. Steadman, C. Herrmann, O. Mülhens, and D. G. Maeding, "ChromAIX: Fast photon-counting ASIC for spectral computed tomography," *Nuclear Instruments and Methods in Physics Research Section A: Accelerators, Spectrometers, Detectors and Associated Equipment,* vol. 648, pp. S211-S215, 2011, doi: https://doi.org/10.1016/j.nima.2010.11.149.

[20] E. Engelmann, W. Schmailzl, P. Iskra, F. Wiest, E. Popova, and S. Vinogradov, "Tip avalanche photodiode—A new generation silicon photomultiplier based on non-planar technology," *IEEE Sensors Journal,* vol. 21, no. 5, pp. 6024-6034, 2020, doi: https://doi.org/10.1109/JSEN.2020.3041556.

[21] R. Steadman, C. Herrmann, and A. Livne, "ChromAIX2: A large area, high count-rate energy-resolving photon counting ASIC for a spectral CT prototype," *Nuclear Instruments and Methods in Physics Research Section A: Accelerators, Spectrometers, Detectors and Associated Equipment,* vol. 862, pp. 18-24, 2017, doi: https://doi.org/10.1016/j.nima.2017.05.010.

[22] S. Kappler, A. Henning, B. Kreisler, F. Schoeck, K. Stierstorfer, and T. Flohr, "Photon counting CT at elevated X-ray tube currents: contrast stability, image noise and multi-energy performance," in *Medical imaging 2014: Physics of medical imaging*, 2014, vol. 9033: SPIE, pp. 368-375, doi: https://doi.org/10.1117/12.2043511.

5 X-ray transport in scintillator- and semiconductor-based photon-counting detectors with miniaturized pixels

Abstract

Detectors for medical X-ray imaging have pixel sizes ≤ 1×1 mm^2 and are a few mm thick. Consequently, secondary radiation often escapes the pixel in which a primary X-ray has interacted. In spectral photon-counting detectors (PCD), this leads to, e.g., detection efficiency loss, count multiplicity, and incorrectly measured energies. We recently demonstrated that $LaBr_3$:Ce, LSO:Ce, and YAP:Ce scintillators, coupled to fast silicon photomultipliers, may be reasonable alternatives to the CZT semiconductor for PCDs. Here, we investigate the influence of X-ray transport in above-mentioned scintillators and CZT on detector performance.

We perform Monte Carlo simulations of X-ray transport in pixel arrays with thicknesses chosen such that the absorption efficiency for an RQA9 spectrum equals that of 2 mm CZT (0.937). Two cases are studied: *A) equal spatial resolution*: a fixed pixel size of 1×1 mm^2, and *B) equal count rate capability*: material-specific pixel sizes ≤ 0.5×0.5 mm^2. The detectors are uniformly irradiated by mono-energetic X-rays of energy E_{in}. We determine the zero-frequency detective quantum efficiency DQE(0) as a measure of counting performance, and the full-energy peak fraction under uniform irradiation $f_{full\text{-}E}$ as a measure of spectral performance, for various E_{in} and a 25 keV detection threshold. We then calculate spectrally-weighted averages $\overline{DQE(0)}$ and $\overline{f_{full\text{-}E}}$, taking weights from an RQA9 spectrum.

In *A)*, we found that YAP yields a $\overline{DQE(0)}$ of 0.911, outperforming CZT (0.898), $LaBr_3$ (0.870), and LSO (0.818), whereas CZT provides a higher $\overline{f_{full\text{-}E}}$ of 0.831 than YAP (0.823), $LaBr_3$ (0.796) and LSO (0.718). In *B)*, YAP yields, despite smaller pixels, a superior $\overline{DQE(0)}$ of 0.910 compared to CZT (0.879), $LaBr_3$ (0.842), and LSO (0.811). CZT offers a $\overline{f_{full\text{-}E}}$ of 0.736, followed by YAP (0.691), $LaBr_3$ (0.644), and LSO (0.547).

In conclusion, our framework provides basic insights into how X-ray transport in the detector affects PCD performance, given an X-ray spectrum and pixel size requirement.

5.1 Introduction

Energy-resolving X-ray photon-counting detectors (PCD) aim to count the number of X-ray photons incident on each detector pixel and to measure the energy of the individual photons. Currently, PCDs are considered a promising alternative to the energy-integrating detectors traditionally used in computed tomography (CT) and other forms of medical X-ray imaging, because they are expected to improve the contrast-to-noise ratio for a given radiation dose and/or contrast agent load and enable multi-energy imaging, for example [1,2,3].

In an X-ray detector, the energy deposited by an X-ray photon leads to a current pulse. The pulse processing chain of PCDs under development for medical X-ray imaging typically first converts this pulse into a smooth voltage pulse, the pulse height of which can be considered a measure of the energy deposited. The pulse is then registered as a count in one of the predefined energy bins that cover the X-ray tube spectrum. The number of bins typically ranges from two (sufficient for dual-energy imaging) to eight.

The high X-ray photon fluence rates incident on the detector in medical X-ray imaging, i.e., up to ~10^8 $mm^{-2}s^{-1}$ in a very demanding application such as diagnostic CT [4], have hampered the development of PCDs for a long time. Under such conditions, pulse pile-up can severely distort a measurement of counts and energies. Pile-up occurs when two pulses are generated very briefly after each other, so that the pulses overlap. Consequently, they may be mistakenly regarded as a single pulse by the detector, or as two pulses, but with an erroneous pulse height for the second one. The latter case is visualized in Fig. 5.1(a). The negative effects of pile-up can be mitigated by selecting a absorption material that yields faster pulses (Fig. 5.1(b)) and/or by increasing the number of pixels per unit area, so that the two X-ray photons are processed by separate channels (Fig. 5.1(c)). Fast pulses and straightforward pixel size miniaturization, as well as room-temperature operation and high mass density and effective atomic number, are offered by direct-conversion detectors based on the semiconductors CdTe and $Cd_{1-x}Zn_xTe$ (CZT, x typically 0.1-0.2). However, detector-grade CdTe and CZT has only recently become available. This has led to the release of the first clinical photon-counting CT scanners [5]. Nevertheless, the cost-effective synthesis of such high-quality CdTe and CZT remains an issue and the number of manufacturers that can grow these detector-grade materials is very limited. Silicon has been proposed as an alternative absorption material, but it has a low density and atomic number for medical applications in which energies up to 150 keV are used, thus requiring intricate detector designs [6,7].

We are investigating scintillation detectors with silicon photomultiplier (SiPM) readout as an alternative detector concept for medical X-ray photon-counting applications. In previous work [8,9], we identified $LaBr_3$:Ce, LSO:Ce, and YAP:Ce as readily-available scintillators with a relatively high density and effective atomic number that may provide sufficiently fast pulses and reasonable energy resolution (also see Chap. 2 and Appendix A2.2 of this thesis). However, these are not the only factors that determine the counting and spectral performance of PCDs. Most X-ray imaging applications require pixel sizes

of at most 1×1 mm^2 to meet the associated spatial resolution requirements, while even smaller sizes may be needed to reduce the pile-up level in the detector, as explained above. Moreover, a thickness of only a few mm may be sufficient for dose-efficient X-ray absorption. A consequence of such small pixel dimensions is that K-fluorescence and Compton-scattered X-ray photons (secondary radiation / secondary X-ray photons) have a fair chance to leave a pixel, either escaping the detector or being absorbed in another pixel (inter-pixel X-ray crosstalk). Here, we study the associated consequences for the counting and spectral performance of scintillator- and CZT-based PCDs under low fluence-rate conditions by means of Monte Carlo simulations.

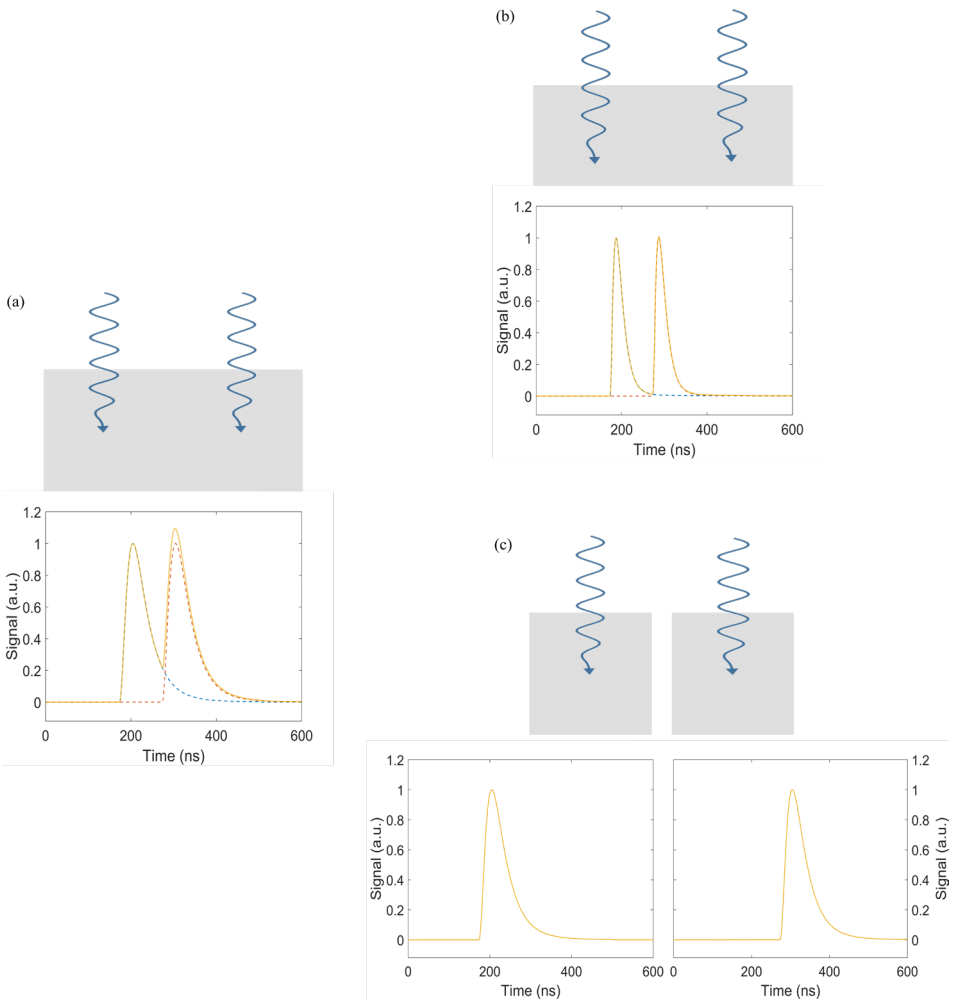

Fig. 5.1. (a) Two pulses (dashed curves) that pile up on each other, giving rise to a total pulse (solid curve), which may be regarded as a single pulse by the detector read-out system, or as two pulses with a wrong pulse height for the second one. The pulse pile-up level can be reduced by having (b) faster detector pulses, and/or (c) more pixels per unit area.

5.2 Methodology

5.2.1 Simulation set-up

We performed Monte Carlo simulations of X-ray transport in pixelated detectors. To this end, we built pixel arrays in the Monte Carlo software GATE [10,11], version 9.0, which is based on the Monte Carlo code Geant4 [12,13], version 10.6.1. The detectors were either made of the semiconductor $Cd_{0.9}Zn_{0.1}Te$ (CZT, mass density ρ = 5.8 g cm^{-3}, effective atomic number Z_{eff} = 50 [1] [14]) or of one of the following three scintillation host materials: $LaBr_3$ (ρ = 5.1 g cm^{-3}, Z_{eff} = 46), Lu_2SiO_5 (LSO, ρ = 7.4 g cm^{-3}, Z_{eff} = 66), and $YAlO_3$ (YAP, ρ = 5.4 g cm^{-3}, Z_{eff} = 33). These scintillators are activated by means of cerium doping. However, the Ce concentration is smaller than 1 mol% in LSO:Ce and YAP:Ce, while Ce (Z = 58) occupies La (Z = 57) lattice sites in $LaBr_3$:Ce, with little effect on its density and Z_{eff}, even at high Ce concentrations. Therefore, we did not include any dopants in the simulated materials.

5

The required thickness of the detectors depends on the X-ray energy range used in a particular imaging system. In this work, we focus on systems that make use of an X-ray tube with a tungsten anode and a tube voltage around 120 kVp. Such imaging systems can be used for head, chest (thorax), abdomen and pelvis imaging, for example. A typical spectrum of the X-rays that have traversed a patient in these systems is the RQA9 spectrum [15], shown in Fig. 5.2(a). CZT-based photon-counting detectors developed for such systems typically have a thickness d_{czt} of 2.0 mm. In order to determine the equivalent scintillator thickness $d_{sci,eq}$, we first split the RQA9 spectrum into eleven intervals around energies E_{in} and determined the fraction of X-ray photons w in each interval (see Table 5.1). We then minimized the absolute value of the weighted sum of the differences in X-ray absorption efficiency η_{abs} at each E_{in} between a scintillator with a thickness d_{sci} and CZT with d_{czt} = 2.0 mm:

$$\begin{aligned} d_{sci,eq} &= \arg\min_{d_{sci}} \left| \sum_{E_{in}} w(E_{in}) \left(\eta_{abs}(d_{sci}, E_{in}) - \eta_{abs}(d_{czt}, E_{in}) \right) \right| \\ &= \arg\min_{d_{sci}} \left| \sum_{E_{in}} w(E_{in}) \left(\exp(-\mu_{czt}(E_{in})\, d_{czt}) - \exp(-\mu_{sci}(E_{in})\, d_{sci}) \right) \right| \end{aligned} \quad (5.1)$$

[1] The effective atomic number was calculated as $Z_{eff} = \sqrt[3.5]{\sum_i a_i Z_i^{3.5}}$, where a and Z are the atomic weight fraction and the atomic number of the i^{th} element in the absorption material, respectively. This formula is valid if the photo-electric effect is the dominant interaction mechanism, which is the case for the absorption materials and the energy range ($E \leq 120$ keV) studied here.

Here, μ is the linear attenuation coefficient (without coherent scattering), which we obtained from the NIST XCOM database [16]. The $d_{sci,eq}$ were determined with 0.1 mm precision and are shown in Fig. 5.2(b) along with the corresponding curves for the X-ray absorption efficiency as a function of E_{in}. We note that the curve of LSO considerably differs from that of the other materials. This is due the fact that LSO is the only material with a K-edge in the relevant energy range, namely the K-edge of lutetium at 63 keV.

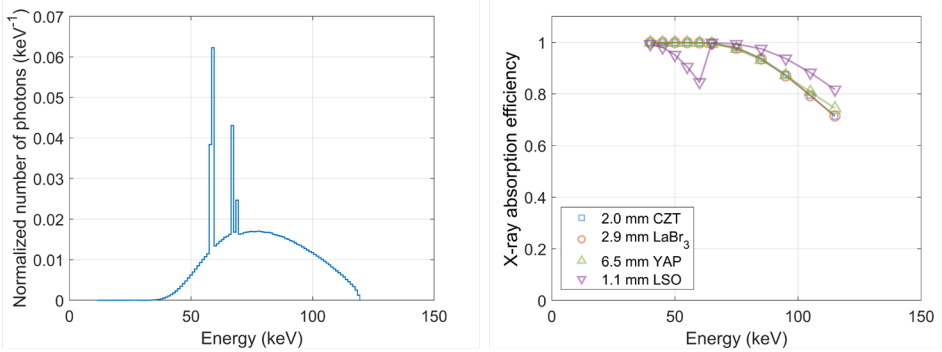

(a) (b)

Fig. 5.2. (a) The RQA9 spectrum as calculated by the SpekCalc software [17]. (b) X-ray absorption efficiency as a function of the energy of the incident X-ray photons, for a CZT detector with a thickness of 2.0 mm and for the three scintillation detectors with thicknesses equivalent to 2.0 mm CZT as determined using Eqn. (5.1).

Table 5.1. Overview of the eleven intervals around energies E_{in} into which we split up the RQA9 spectrum shown in Fig. 5.2(a). The fraction w of X-ray photons in each interval is also tabulated. If two adjacent intervals share an endpoint energy, as denoted by a ⟨ or ⟩ sign, the number of photons at that energy is shared between both intervals.

E_{in} (keV)	Interval (keV)	Fraction w of X-ray photons		E_{in} (keV)	Interval (keV)	Fraction w of X-ray photons
40	⟨0, 42]	0.0047				
45	[43, 47]	0.0145		75	⟨70, 80⟩	0.1680
50	[48, 52]	0.0312		85	⟨80, 90⟩	0.1608
55	[53, 57]	0.0500		95	⟨90, 100⟩	0.1342
60	[58, 62⟩	0.1425		105	⟨100, 110⟩	0.0957
65	⟨62, 70⟩	0.1552		115	⟨110, 120]	0.0432

The detectors consisted of 101×101 pixels. As mentioned in Sec. 5.1, the pixel size can either be set by a spatial resolution requirement or by a maximally allowed level of pulse pile-up in the detector. Hence, we studied two scenarios:

Scenario A: Equal pixel size.
The pixel size is fixed to 1×1 mm^2. This case represents applications in which the fluence rate incident on the detector is low enough for pile-up to be of limited concern in all absorption materials studied here, so the choice of pixel size is primarily dictated by a spatial resolution requirement. One could think of cone-beam CT on a radiotherapy gantry as an example of an application where such a scenario may apply.

Scenario B: Material-specific pixel size.
The pixel size is determined by a maximally allowed level of pile-up and, therefore, depends on the choice of absorption material. In previous work [8,9], presented in Chap. 2 and Appendix A2.2 of this thesis, we studied the pulse shape of detectors based on the materials studied here. Based on that work, we expect equal pile-up levels for 0.50×0.50 mm^2 CZT pixels, 0.40×0.40 mm^2 $LaBr_3$ pixels, 0.33×0.33 mm^2 YAP pixels, and 0.29×0.29 mm^2 LSO pixels. Here, one could think of diagnostic CT systems as an example application.

The first scenario allows to study how only the absorption material affects X-ray transport and the associated consequences for the detector performance. In the second one, the effect of different pixel sizes is also included. Although the different pixel sizes are necessary to create equal pile-up levels in practice, we emphasize that this Monte Carlo simulation study aims to study detector performance degradation due to X-ray transport only and not due to pile-up. Thus, an infinitely low fluence rate was assumed.

For each combination of absorption material and pixel size, we uniformly irradiated the central detector pixel with perpendicularly-incident, mono-energetic X-ray beams of energy E_{in}, simulating $4{\cdot}10^6$ primary photons at each E_{in} listed in Table 5.1. X-ray transport was governed by the emstandard_opt4 physics list with a range cut of 1 μm. For each photonic interaction in the detector, we registered from which primary photon it originated, in which pixel it occurred, and how much energy was deposited. We then summed the energies deposited in events that originated from the same primary photon and occurred in the same pixel. This gave rise to a count with energy E_{out}, provided $E_{out}>E_{thr}$, where E_{thr} is the threshold energy used for count detection. As such, we did not simulate the transport of electron-hole pairs in the case of CZT and optical photons in the case of a scintillator, and we did not insert (reflective) material in between pixels.

5.2.2 Outcome measures

Firstly, we evaluated how X-ray transport affects the *counting performance* of photon-counting detectors using the concept of the zero-frequency detective quantum efficiency DQE(0) in the limit of no pile-up.

The DQE(0) is defined as $\mathrm{SNR}^2_{\mathrm{out}}(0)/\mathrm{SNR}^2_{\mathrm{in}}(0)$, where SNR(0) stands for the zero-frequency signal-to-noise ratio and the subscripts refer to the output and input data, respectively. When a PCD is irradiated with N photons, Poisson statistics dictate that $\mathrm{SNR}^2_{\mathrm{in}}(0) = N$. An ideal PCD detects all incident photons, so $\mathrm{SNR}^2_{\mathrm{out}}(0) = N$, and therefore DQE(0) = 1.

Practical PCDs do not detect all incident photons. Some incident X-rays are not absorbed in the detector, i.e., they traverse the detector without depositing energy in it (see Fig. 5.3(a)). The fraction of incident photons that does deposit energy in the detector is the X-ray absorption efficiency. Only this fraction contributes to $\mathrm{SNR}_{\mathrm{out}}$. Hence, $\mathrm{SNR}^2_{\mathrm{out}}(0) = \eta_{\mathrm{abs}} N$ and DQE(0) = η_{abs}. When determining the equivalent scintillator thicknesses using Eqn. (5.1), we actually found the scintillator thicknesses for which this DQE(0), averaged over the RQA9 spectrum, is as close as possible to that of 2.0 mm CZT, i.e., to a value of 0.937.

There are more ways in which X-ray transport affects DQE(0). For example, if a primary photon deposits energy in a pixel, and the secondary radiation escapes the detector, and the energy deposition by the primary photon is below the count detection threshold, the primary will not be registered as a count (see Fig. 5.3(b)). Likewise, if a primary photon deposits energy in multiple pixels and the energy deposition in each of these pixels is lower than the threshold energy for count detection, the photon will not be counted (see Fig. 5.3(c)). In practice, E_{thr} must be set above the noise level of the electronics and below the lowest E_{in} that the detector is exposed to. CZT detectors developed for imaging systems that make use of RQA9-like spectra typically use a threshold between 20 keV and 30 keV. In this work, we therefore assume a 25 keV threshold. Denoting the fraction of absorbed primary photons that deposits more energy than E_{thr} in a pixel by the threshold crossing efficiency η_{thr}, $\mathrm{SNR}^2_{\mathrm{out}}(0) = \eta_{\mathrm{abs}}\eta_{\mathrm{thr}} N$, and DQE(0) = η_{abs} η_{thr}. This product of the absorption and the threshold crossing efficiency can be considered the X-ray detection efficiency.

On the other hand, a primary photon can also give rise to energy depositions that exceed E_{thr} in multiple pixels due to the transport of secondary radiation through the pixel array (see Fig. 5.3(d)). If this happens in m pixels, the detector registers m counts for that primary photon. As such, m is called the count multiplicity. When the count multiplicity averaged over all detected primary photons, i.e., those for which $m \geq 1$, is denoted by $\overline{m}$, $\mathrm{SNR}^2_{\mathrm{out}}(0) = \eta_{\mathrm{abs}}\eta_{\mathrm{thr}}\, \overline{m}^2 / \overline{m^2}\, N$ [18]. Moreover,

$$\mathrm{DQE}(0) = \eta_{\mathrm{abs}}\eta_{\mathrm{thr}}\, \overline{m}^2 / \overline{m^2} \tag{5.2}$$

Using the simulation output described in Sec. 5.2.1, we evaluated Eqn. (5.2) for each detector and E_{in} listed in Table 5.1. However, a single number is convenient for comparing the detectors with each other. We therefore calculated an average DQE(0) for each detector, weighted by the RQA9 spectrum:

$$\overline{\mathrm{DQE}(0)} = \sum_{E_{\mathrm{in}}} \left(w \, \mathrm{DQE}(0) \right) \tag{5.3}$$

The values of w were taken from Table 5.1. This $\overline{\mathrm{DQE}(0)}$ can be seen as the ratio of what the output data of a detector exposed to an RQA9 spectrum is worth ($\mathrm{SNR}^2_{\mathrm{out}}(0)$) to what it costs ($\mathrm{SNR}^2_{\mathrm{in}}(0) = N$). A detector for which $\overline{\mathrm{DQE}(0)} = 0.5$ requires twice as many X-ray photons to obtain a desired $\mathrm{SNR}^2_{\mathrm{out}}(0)$ than an ideal detector. $\overline{\mathrm{DQE}(0)}$ can therefore be considered a measure of dose efficiency.

Secondly, we quantified how X-ray transport affects the *spectral performance* of a uniformly irradiated detector using the concept of the full-energy peak fraction $f_{\text{full-E}}$, in the limit of zero pile-up.

We obtained $f_{\text{full-E}}$ from the simulation output for each detector and E_{in} listed in Table 5.1 by determining the fraction of all registered counts for which $E_{\mathrm{out}} = E_{\mathrm{in}}$. Since X-ray transport is point symmetric, $f_{\text{full-E}}$ determined in this way equals the expected fraction of counts in the full-energy peak for any pixel of a uniformly irradiated detector, provided the distance from the pixel to the edge of the detector is large compared to the free path length of the secondary radiation. As such, $f_{\text{full-E}}$ is a useful measure to describe the influence of X-ray transport on the spectral performance of a detector.

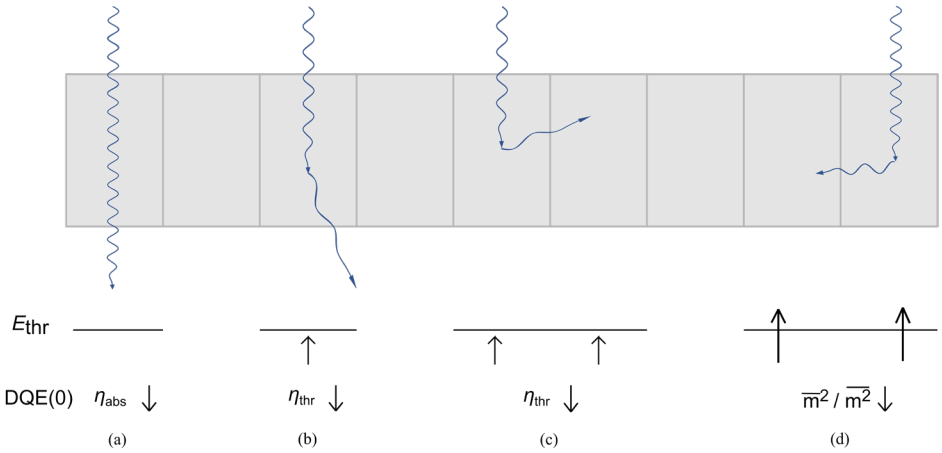

Fig. 5.3. The various ways in which X-ray transport through a detector can degrade the zero-frequency detective quantum efficiency DQE(0) are: (a) A primary photon traverses the detector without depositing energy in it, lowering the absorption efficiency η_{abs}. (b) The initial energy deposition by the primary photon does not exceed the count detection threshold energy E_{thr}, while the secondary X-ray escapes the detector, decreasing the threshold crossing efficiency η_{thr}. (c) The initial energy deposition by the primary X-ray does not exceed the threshold energy, while the secondary photon is absorbed in another pixel. However, its energy is also below the threshold, so η_{thr} drops. (d) Both the energy deposition of the primary photon and that of the secondary photon in another pixel exceed the threshold, reducing DQE(0) via the count multiplicity term $\overline{m^2}/\overline{m^2}$.

A single number for the spectral performance of each detector is again convenient for comparing the detectors with each other. We therefore calculated an average $f_{\text{full-E}}$ for each detector, weighted by the RQA9 spectrum:

$$\overline{f_{\text{full-E}}} = \sum_{E_{\text{in}}} \left(w f_{\text{full-E}} \right) \tag{5.4}$$

The values of w were again taken from Table 5.1.

5.3 Results

5.3.1 Scenario *A*: Equal pixel size

Fig. 5.4 shows the zero-frequency detective quantum efficiency for 1×1 mm^2 pixels of each absorption material, as a function of the energy of the incident X-ray photons. The data in Fig. 5.4(a) were obtained without applying an energy threshold for count detection, i.e., E_{thr} = 0 keV, whereas the data in Fig. 5.4(b) were obtained with E_{thr} = 25 keV. The corresponding values of $\overline{\text{DQE}(0)}$ can be found in Table 5.2.

It can be appreciated in Table 5.2 that the YAP detector benefits most from the 25 keV threshold. In fact, the $\overline{\text{DQE}(0)}$ of the YAP detector becomes superior to that of the CZT, $LaBr_3$ and LSO detectors when this threshold is used. The improvement of DQE(0) is present over the whole energy range, as shown in Fig. 5.4. This is because the K X-rays generated in photo-electric interactions in YAP have energies around 15 keV, which is lower than the threshold energy. As such, the absorption of this type of secondary radiation in pixels other than the one in which the corresponding primary photon has interacted does not give rise to counts, and the count multiplicity for many primary photons equals 1. This brings $\overline{m}^2/\overline{m^2}$ in the expression for DQE(0) (see Eqn. (5.2)) close to 1.

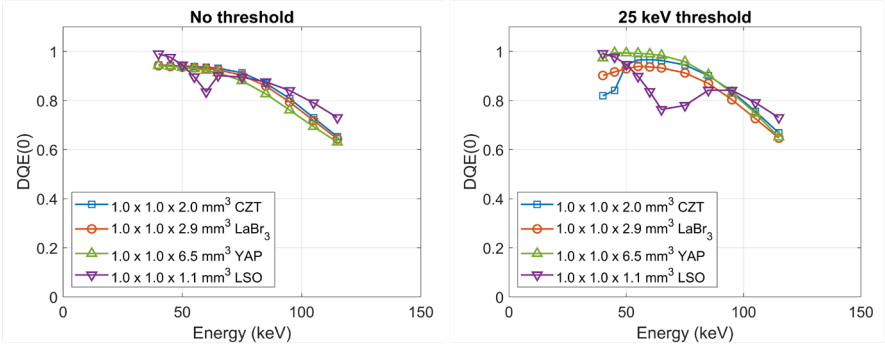

(a) (b)

Fig. 5.4. Zero-frequency detective quantum efficiency DQE(0) as a function of the energy of the X-rays incident on four different detectors, either determined (a) without an energy threshold for count detection, i.e., E_{thr} = 0 keV, or (b) with a 25 keV threshold.

Table 5.2. The weighted-average zero-frequency detective quantum efficiency $\overline{\mathrm{DQE}(0)}$, calculated for the data in Fig. 5.4 using Eqn. (5.3), and the weighted-average full-energy peak fraction $\overline{f_{\text{full-E}}}$ under uniform detector irradiation, calculated for the data in Fig. 5.5 using Eqn. (5.4). The weights for each X-ray photon energy were taken from Table 5.1 and represent the intensity of the RQA9 spectrum.

	$\overline{\mathrm{DQE}(0)}$		$\overline{f_{\text{full-E}}}$	
Pixel dimensions and absorption material	**Without threshold**	**With 25 keV threshold**	**Without threshold**	**With 25 keV threshold**
1.0×1.0×2.0 mm^3 CZT	0.8720	0.8985	0.7760	0.8310
1.0×1.0×2.9 mm^3 $LaBr_3$	0.8628	0.8701	0.7547	0.7962
1.0×1.0×6.5 mm^3 YAP	0.8433	0.9115	0.7001	0.8226
1.0×1.0×1.1 mm^3 LSO	0.8633	0.8176	0.6179	0.7175

Table 5.2 shows that the $\overline{\mathrm{DQE}(0)}$ of the CZT detector also benefits from the 25 keV threshold in this way, although to a lesser extent. This is because some of the K X-rays of cadmium and tellurium have energies below 25 keV, whereas others have energies exceeding 25 keV. In addition, the DQE(0) at 40 keV and 45 keV considerably decreases compared to the case without threshold (see Fig. 5.4). This is because the energy deposited in a photo-electric interaction of a primary photon with such a low energy is less than the threshold energy. If the interaction results in a K X-ray that is not absorbed in the same pixel, but escapes the detector or is absorbed in another pixel in which it does not lead to a count because its energy is too low, no count at all will be registered (see Fig. 5.3(b) and (c)). This lowers the threshold crossing efficiency in the formula for DQE(0) given in Eqn. (5.2). However, the effect on $\overline{\mathrm{DQE}(0)}$ is small, because there are not many 40-45 keV photons in an RQA9 spectrum (see Table 5.1).

Since the K X-rays of lanthanum have a mean energy of 34 keV, one expects a similar drop in the DQE(0) of the $LaBr_3$ detector at 40, 45, 50, and 55 keV after applying the 25 keV threshold. However, Fig. 5.4 shows that this drop is less severe than for the CZT detector. This is because η_{thr} of the $LaBr_3$ detector is only lowered when K X-rays escape from the detector (as in Fig. 5.3(b)). If a K X-ray is absorbed in another pixel, it will always give rise to a count, because all K X-ray energies exceed the 25 keV threshold. On the other hand, the positive effect of the threshold on DQE(0) at higher incident energies via the factor $\bar{m}^2/\overline{m^2}$, as observed for YAP and CZT, is limited for $LaBr_3$, because of the relatively high K X-ray energies of La. The net result of these trends is that the $\overline{\mathrm{DQE}(0)}$ of the $LaBr_3$ detector is hardly affected by the 25 keV threshold (see Table 5.2).

Similar reasoning applies to the LSO detector. However, the drop in DQE(0) via η_{thr} occurs between 65 keV and 85 keV (see Fig. 5.4), because lutetium has a K-edge at 63 keV and its K X-rays have energies ranging from 53 keV to 63 keV. Moreover, the drop is more substantial than for $LaBr_3$, which indicates that the escape of K X-rays from the

detector is more likely in the case of LSO. This makes sense, because the higher atomic number of Lu implies a higher fluorescence yield, higher K X-ray energies, longer mean free paths of the K X-rays in the absorption material, and a thinner detector. In addition, the RQA9 spectrum is more intense in the 65-85 keV region than in the 40-55 keV region (see Fig. 5.2(a) and Table 5.1), so the effect on $\overline{\mathrm{DQE}(0)}$ is larger. Indeed, Table 5.2 shows that LSO is the only material for which $\overline{\mathrm{DQE}(0)}$ decreases after applying the 25 keV threshold.

Fig. 5.5 shows the full-energy peak fraction under uniform detector irradiation for 1×1 mm^2 pixels of the four absorption materials as a function of the energy of the incident X-ray photons. The data in Fig. 5.5(a) were obtained without applying an energy threshold for count detection, whereas the data in Fig. 5.5(b) were obtained with a 25 keV threshold. The corresponding values of $\overline{f_{\text{full-E}}}$ can be found in Table 5.2.

Without a threshold, the best $\overline{f_{\text{full-E}}}$ is achieved by the CZT detector, closely followed by the $LaBr_3$ detector. Since $f_{\text{full-E}}$ is a fraction of the number of registered counts instead of a fraction of the number of incident photons, the curves in Fig. 5.5 for these detectors do not shows signs of the typical shape of the absorption efficiency curves shown in Fig. 5.2(b), in contrast to the DQE(0) data in Fig. 5.4. Nevertheless, the $f_{\text{full-E}}$ of the YAP detector considerably decreases with increasing X-ray energy. This can be attributed to a growing probability of Compton scattering, because YAP consists of relatively low atomic number elements. Compton-scattered photons have a higher energy than K X-rays, so they increase the chance of inter-pixel crosstalk, thereby lowering $f_{\text{full-E}}$. The data of the LSO detector show a considerable discontinuity around the K-edge energy of Lu, due to a sudden increase in inter-pixel crosstalk via K X-rays. For the other absorption materials, this discontinuity lies below the energy range studied here and seems to be smaller. Both are due to the fact that these materials consist of lower-Z elements, so the fluorescence yield and the K X-ray energies are lower, and the mean free paths of the K X-rays are shorter.

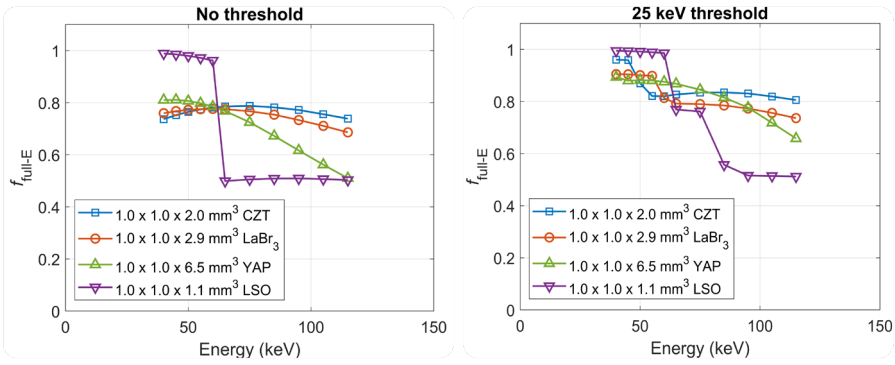

(a) (b)

Fig. 5.5. The full-energy peak fraction $f_{\text{full-E}}$ under uniform detector irradiation as a function of the energy of the X-rays incident on four different detectors, either determined (a) without an energy threshold for count detection, or (b) with a 25 keV threshold.

The 25 keV count detection threshold rejects counts that anyways have an incorrect energy, so it improves the $f_{\text{full-E}}$ of all detectors over the whole energy range (see Fig. 5.5). This improvement is most substantial at the incident photon energies for which the DQE(0) dropped via η_{thr}, i.e., from the K-edge energy of Cd/Te, La, and Lu up to 25 keV above the K X-ray energies of these elements. Note that this energy range for YAP is below the energy range studied here. For higher energies, the energy deposited in a photo-electric interaction of a primary photon is never less than 25 keV. This reduces the number of counts that is rejected by the threshold, resulting in a smaller improvement of $f_{\text{full-E}}$. At these higher energies, the threshold only rejects a fraction of the counts due to Compton scattering of the primary photon and the counts due to inter-pixel crosstalk via K X-rays with an energy less than 25 keV. Hence, the improvement of $f_{\text{full-E}}$ is largest for the lower-Z materials in this energy range. The net result of both trends and the fact that the RQA9 spectrum is most intense between 60 keV and 100 keV (see Fig. 5.2(a) and Table 5.1) is that the $\overline{f_{\text{full-E}}}$ of the YAP detector (see Table 5.2) becomes greater than that of the $LaBr_3$ detector after applying the threshold, but remains just less than that of the CZT detector, while the LSO detector again has the worst value of $\overline{f_{\text{full-E}}}$.

5.3.2 Scenario *B*: Material-specific pixel size

Fig. 5.6 shows the DQE(0) with a 25 keV threshold as a function of incident X-ray energy for the material-specific pixel sizes that are expected to give rise to equal pile-up levels in practice. The corresponding values of $\overline{\text{DQE(0)}}$ can be found in Table 5.3. As expected for smaller pixel sizes, these values are all less than the ones for scenario *A* with a 25 keV threshold presented in Table 5.2.

The $\overline{\text{DQE(0)}}$ of the YAP detector only slightly decreases compared to scenario *A*. Moreover, the YAP detector remains the best detector in terms of $\overline{\text{DQE(0)}}$, despite the fact that it has a smaller pixel size than the CZT and $LaBr_3$ detectors. This is because all energy depositions by the 15 keV K X-rays of yttrium in other pixels than the one in which the primary photon interacted remain below the count detection threshold, so the increased inter-pixel crosstalk via this mechanism because of a pixel size reduction does not lead to a DQE(0) loss. This is different for CZT and $LaBr_3$, for which some or all K X-rays have energies that exceed the threshold. Increased inter-pixel crosstalk via Compton scattering (mainly in YAP) also hardly leads to a DQE(0) loss, because the energy deposition in a Compton interaction remains below the threshold energy of 25 keV for incident photon energies up to 95 keV. For energies between 95 keV and 120 keV, the majority of the Compton plateau still falls below the threshold.

The LSO detector has the smallest pixel size in this scenario, but its $\overline{\text{DQE(0)}}$ of 0.8112 is much closer to the value of 0.8176 obtained for 1×1 mm^2 pixels than in the case of the CZT and $LaBr_3$ detectors. This may have multiple causes. First, hardly any inter-pixel crosstalk or detector escape takes place at incident photon energies up to the K-edge energy of 63 keV. It can be derived from Table 4.1 that X-rays with such energies form almost 25% of an RQA9 spectrum. Consequently, the DQE(0) for a fairly large fraction

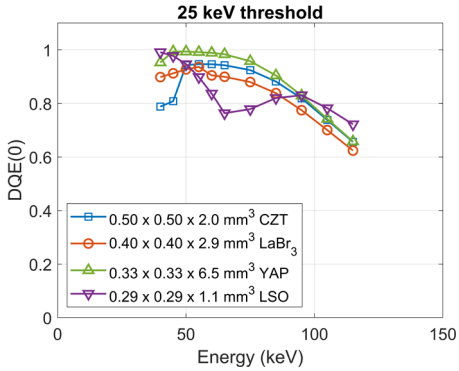

Fig. 5.6. Zero-frequency detective quantum efficiency DQE(0) as a function of the energy of the X-rays incident on four different detectors, determined with a 25 keV threshold.

Table 5.3. The weighted-average zero-frequency detective quantum efficiency $\overline{\mathrm{DQE}(0)}$, calculated for the data in Fig. 5.6. using Eqn. (5.3), and the weighted-average full-energy peak fraction $\overline{f_{\text{full-E}}}$ under uniform detector irradiation, calculated for the data in Fig. 5.7 using Eqn. (5.4). The weights for each X-ray photon energy were taken from Table 5.1 and represent the intensity of the RQA9 spectrum.

Pixel dimensions and absorption material	$\overline{\mathbf{DQE(0)}}$ **with 25 keV threshold**	$\overline{f_{\text{full-E}}}$ **with 25 keV threshold**
0.50×0.50×2.0 mm^3 CZT	0.8793	0.7359
0.40×0.40×2.9 mm^3 $LaBr_3$	0.8423	0.6442
0.33×0.33×6.5 mm^3 YAP	0.9109	0.6910
0.29×0.29×1.1 mm^3 LSO	0.8112	0.5466

of this spectrum is hardly affected by the difference in pixel size between scenario *A* and *B* spectrum. For incident photon energies exceeding 63 keV, the DQE(0) loss of the LSO detectors due to X-ray transport and the 25 keV threshold was more severe than for the other detectors in the case of 1×1 mm^2 pixels, so the additional contribution from reducing the pixel size is relatively small.

Fig. 5.7 shows $f_{\text{full-E}}$ with a 25 keV threshold as a function of incident X-ray energy for the material-specific pixel sizes that are expected to give rise to equal pile-up levels in practice. Compared to the data for equal pixel sizes of 1×1 mm^2 presented in Fig. 5.5(b), a decrease over the whole energy range can be observed (although hardly in the cases in which secondary radiation is unlikely to escape from a pixel, such as the case of the LSO detector at energies up to the 63 keV K-edge of Lu). This is different behavior than observed for DQE(0) above. For example, the DQE(0) of the YAP detector was unaffected by the increased inter-pixel crosstalk via K X-rays due to the pixel size

reduction, whereas the $f_{\text{full-E}}$ of this detector considerably drops. The reason behind this observation is that DQE(0) needs one count for a single primary photon in order not to degrade. The energy associated with that count does not matter. $f_{\text{full-E}}$, on the other hand, needs one count with a correct associated energy in order not to degrade. Thus, the rejection of potential second counts due to inter-pixel crosstalk via K X-rays by the threshold is not sufficient to keep $f_{\text{full-E}}$ unaffected.

As a result, the corresponding values of $\overline{f_{\text{full-E}}}$ in Table 5.3 are, for all absorption materials, considerably lower than in the case of 1×1 mm^2 pixels and a 25 keV threshold (see Table 5.2). Interestingly, YAP remains on top of $LaBr_3$ despite a smaller pixel size.

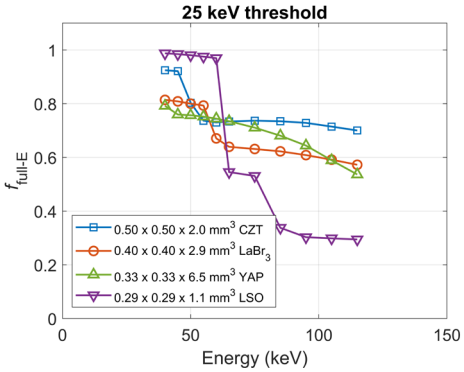

Fig. 5.7. The full-energy peak fraction $f_{\text{full-E}}$ under uniform detector irradiation as a function of the energy of the X-rays incident on four different detectors, determined with a 25 keV threshold.

5.4 Discussion

The performance of energy-resolving X-ray photon-counting detectors is primarily determined by the count rate capability and energy resolution of the detector. In our quest to find suitable scintillators for use in PCDs for medical X-ray applications, we previously found (also see Chap. 2 and Appendix A2.2 of this thesis) that materials such as $LaBr_3$, LSO and YAP may be reasonable alternatives to semiconductors such as CZT with respect to those performance parameters [8,9].

However, medical X-ray imaging typically requires pixels of at most 1×1 mm^2 due to spatial resolution requirements, while smaller pixels may be needed to increase the input count rate per mm^2 that the detector can handle with an acceptable level of pulse pile-up (see Fig. 5.1). Consequently, the escape of secondary radiation, such as K X-rays and Compton-scattered X-rays, from the pixel in which the primary X-ray interacted is likely. This affects detector performance.

In this work, we aimed to gain first-order, quantitative insights into how X-ray transport in the abovementioned high-density scintillators, which span a rather wide range of

atomic numbers, affects the performance of pixelated detectors, and how that compares to CZT detectors, by means of Monte Carlo simulations. We evaluated the zero-frequency detective quantum efficiency as a measure of counting performance, and the full-energy peak fraction under uniform detector irradiation as a measure of spectral performance. We did so for X-ray energies that are present in an RQA9 spectrum, in the limit of zero pile-up, and with a 25 keV count detection threshold.

An example of a first-order insight obtained from this study is that both performance metrics tend to be better for absorption materials consisting of elements with a relatively low atomic number, such as YAP and CZT, than for materials containing higher-Z elements, such as $LaBr_3$ and, in particular, LSO. This even holds when the lower-Z material requires a smaller pixel size to achieve sufficient count rate capability. The reason is that a lower value of Z implies lower K X-ray energies E_{KX}. If $E_{KX} < E_{thr}$, the threshold will reject potential counts due to K X-rays only, which helps to reduce performance degradation due to X-ray transport.

This indicates that the choice of E_{thr} affects the quantitative data presented in this work, especially for CZT, which has K X-ray energies ranging from 23 keV to 32 keV. Since we used a 25 keV threshold, which is halfway the usual range of count detection thresholds (20-30 keV) used in photon-counting CT systems equipped with CdTe or CZT detectors, some K X-ray energies of Cd and Te are below this threshold, while others exceed it. As such, we neither present very optimistic nor very pessimistic numbers for CZT detectors. In fact, the DQE(0) framework can be used to optimize the count detection threshold for each absorption material [18]. However, it should be noted that this threshold also affects other aspects of detector performance, such as the count rate capability [19].

In future work, detectors that appear favorable based on our first-order analysis may be studied in more detail. For example, the generation and transport of electron-hole pairs (CZT) or optical photons (scintillators) may be included in the simulation. In the case of CZT detectors, this requires that the electron-hole pair creation energy and the Fano factor are known, and that a charge transport model is selected. Not only rather simple models exist [20,21], but also potentially very accurate ones based on the Shockley-Ramo theorem [22]. In the case of scintillation detectors, it mainly requires a model of the mean and variance of the number of generated optical photons as a function of deposited energy, a model of optical photon transport [23], and a choice for a method to confine the scintillation light as good as possible to a single pixel. If the traditional method of having reflectors between pixels is chosen, the DQE(0) framework can be used to evaluate how the associated loss of X-ray absorption efficiency due to dead area compares to the DQE loss due to charge sharing, and to determine which reflector thickness yields the same dose efficiency as a CZT detector. Alternatively, if innovative methods, such as laser-induced optical barriers [24], are chosen, the DQE(0) framework can be used to analyze how the resulting light sharing among pixels compares to charge sharing in CZT detectors.

The generation and transport of electron-hole pairs and optical photons blur the spectral response functions. Hence, taking these into account in the simulation offers a more realistic model of the processing of photonic interactions with an associated energy deposition around the threshold energy of 25 keV. Including these in the simulation is therefore crucial to evaluate the performance of the various absorption materials in multi-threshold detectors, which PCDs for medical X-ray imaging typically are (see Sec. 5.1). For such systems, a frequency-dependent spectral DQE that combines counting and spectral performance has been derived by others [25,26,27]. This DQE also includes the negative effects of inter-pixel crosstalk on the spatial resolution achievable with the detectors.

A last effect of inter-pixel X-ray crosstalk is the increase in the number of photons per second to be processed by a pixel for a given rate of primary photons, making distortions in the measurement of counts and energies due to pulse pile-up more likely. Pile-up makes the system non-linear, so it cannot be included in a (spectral) DQE framework. Alternatively, spectra under pile-up conditions can be calculated, either using analytical models [28,29,30], or time-resolved Monte Carlo simulations [31]. However, a figure-of-merit to compare the spectra from different detectors to each other is not straightforward to derive.

5.5 Conclusion

By means of Monte Carlo simulations, we gained first-order, quantitative insights into how X-ray transport affects the zero-frequency detective quantum efficiency and the full-energy peak fraction under uniform detector irradiation of $LaBr_3$-, YAP-, and LSO-based scintillation detectors, which we are investigating as alternatives to CdTe/CZT-based detectors for medical X-ray photon-counting applications. For an RQA9 spectrum incident on the detectors and a 25 keV count detection threshold, YAP provides the best DQE(0), followed by CZT, $LaBr_3$ and LSO, in the limit of zero pulse pile-up. However, CZT comes out on top regarding $f_{\text{full-E}}$, before YAP, $LaBr_3$ and LSO. These rankings remain the same when a fixed pixel size of 1×1 mm^2 is replaced by material-specific pixel sizes ≤ 0.5×0.5 mm^2, which we expect to provide equal pile-up levels in practice, despite YAP requiring smaller pixels than CZT and $LaBr_3$. Thus, the X-ray transport properties of a material, such as the atomic numbers of the elements it consists of, appear to have more influence on DQE(0) and $f_{\text{full-E}}$ than the pixel size, at least for the pixel sizes studied here.

References

[1] T. Flohr, M. Petersilka, A. Henning, S. Ulzheimer, J. Ferda, and B. Schmidt, "Photon-counting CT review," *Physica Medica,* vol. 79, pp. 126-136, 2020, doi: https://doi.org/10.1016/j.ejmp.2020.10.030.

[2] M. Danielsson, M. Persson, and M. Sjölin, "Photon-counting x-ray detectors for CT," *Physics in Medicine & Biology,* vol. 66, no. 3, p. 03TR01, 2021, doi: https://doi.org/10.1088/1361-6560/abc5a5.

[3] A. Esquivel *et al.*, "Photon-Counting Detector CT: Key Points Radiologists Should Know," *Korean Journal of Radiology,* vol. 23, 2022, doi: https://doi.org/10.3348/kjr.2022.0377.

[4] M. Persson *et al.*, "Upper limits of the photon fluence rate on CT detectors: Case study on a commercial scanner," *Medical physics,* vol. 43, no. 7, pp. 4398-4411, 2016, doi: https://doi.org/10.1118/1.4954008.

[5] K. Rajendran *et al.*, "First clinical photon-counting-detector CT system: Technical evaluation," *Radiology,* vol. 303, no. 1, p. 130, 2022, doi: https://doi.org/10.1148/radiol.212579.

[6] H. Bornefalk and M. Danielsson, "Photon-counting spectral computed tomography using silicon strip detectors: a feasibility study," *Physics in Medicine & Biology,* vol. 55, no. 7, p. 1999, 2010, doi: https://doi.org/10.1088/0031-9155/55/7/014.

[7] J. da Silva *et al.*, "Resolution characterization of a silicon-based, photon-counting computed tomography prototype capable of patient scanning," *Journal of Medical Imaging,* vol. 6, no. 4, p. 043502, 2019, doi: https://doi.org/10.1117/1.JMI.6.4.043502.

[8] S. J. van der Sar, S. E. Brunner, and D. R. Schaart, "Silicon photomultiplier-based scintillation detectors for photon-counting CT: A feasibility study," *Medical physics,* vol. 48, no. 10, pp. 6324-6338, 2021, doi: https://doi.org/10.1002/mp.14886.

[9] S. J. van der Sar and D. R. Schaart, "Silicon Photomultiplier-Based Scintillation Detectors for Photon-Counting X-Ray Imaging," in *Radiation Detection Systems*. Boca Raton, FL, USA: CRC Press, 2021, pp. 289-312, doi: https://doi.org/10.1201/9781003147633-10.

[10] S. Jan *et al.*, "GATE: a simulation toolkit for PET and SPECT," *Physics in Medicine & Biology,* vol. 49, no. 19, p. 4543, 2004, doi: https://doi.org/10.1088/0031-9155/49/19/007.

[11] S. Jan *et al.*, "GATE V6: a major enhancement of the GATE simulation platform enabling modelling of CT and radiotherapy," *Physics in Medicine & Biology,* vol. 56, no. 4, p. 881, 2011, doi: https://doi.org/10.1088/0031-9155/56/4/001.

[12] S. Agostinelli *et al.*, "GEANT4—a simulation toolkit," *Nuclear instruments and methods in physics research section A: Accelerators, Spectrometers, Detectors and Associated Equipment,* vol. 506, no. 3, pp. 250-303, 2003, doi: https://doi.org/10.1016/S0168-9002(03)01368-8.

[13] J. Allison *et al.*, "Recent developments in Geant4," *Nuclear instruments and methods in physics research section A: Accelerators, Spectrometers, Detectors and Associated Equipment,* vol. 835, pp. 186-225, 2016, doi: https://doi.org/10.1016/j.nima.2016.06.125.

[14] A. J. J. Bos, F. S. Draaisma, and W. J. C. Okx, "Hoofdstuk 3: Wisselwerking van Straling met Materie," in *Inleiding tot de Stralingshygiëne*: Sdu Uitgevers, 2007, p. 64, doi: ISBN: 978 90 12 11 905 4.

[15] *Medical diagnostic X-ray equipment - Radiation conditions for use in the determination of characteristics*, International standard IEC 61267:2005 IEC, Geneva, Switzerland, September 11 2005. [Online]. Available: https://webstore.iec.ch/publication/5079

[16] M. J. Berger *et al.* "XCOM: Photon Cross Section Database (version 1.5)." National Institute of Standards and Technology. https://physics.nist.gov/xcom (accessed April 1, 2022).

[17] G. Poludniowski, G. Landry, F. Deblois, P. Evans, and F. Verhaegen, "SpekCalc: a program to calculate photon spectra from tungsten anode x-ray tubes," *Physics in Medicine & Biology,* vol. 54, no. 19, p. N433, 2009, doi: https://doi.org/10.1088/0031-9155/54/19/N01.

[18] T. Michel *et al.*, "A fundamental method to determine the signal-to-noise ratio (SNR) and detective quantum efficiency (DQE) for a photon counting pixel detector," *Nuclear*

Instruments and Methods in Physics Research Section A: Accelerators, Spectrometers, Detectors and Associated Equipment, vol. 568, no. 2, pp. 799-802, 2006, doi: https://doi.org/10.1016/j.nima.2006.08.115.

[19] S. J. van der Sar, D. Leibold, S. E. Brunner, and D. R. Schaart, "LaBr3:Ce and silicon photomultipliers: towards the optimal scintillating photon-counting detector," in *7th International Conference on Image Formation in X-Ray Computed Tomography*, 2022, vol. 12304: SPIE, pp. 55-60, doi: https://doi.org/10.1117/12.2646519.

[20] K. Taguchi, C. Polster, O. Lee, K. Stierstorfer, and S. Kappler, "Spatio-energetic cross talk in photon counting detectors: Detector model and correlated Poisson data generator," *Medical physics,* vol. 43, no. 12, pp. 6386-6404, 2016, doi: https://doi.org/10.1118/1.4966699.

[21] K. Taguchi, K. Stierstorfer, C. Polster, O. Lee, and S. Kappler, "Spatio-energetic cross-talk in photon counting detectors: Numerical detector model (Pc TK) and workflow for CT image quality assessment," *Medical physics,* vol. 45, no. 5, pp. 1985-1998, 2018, doi: https://doi.org/10.1002/mp.12863.

[22] K. P. Cronin, M. A. Kupinski, H. B. Barber, and L. R. Furenlid, "Simulations and analysis of fluorescence effects in semiconductor x-ray and gamma-ray detectors," in *Medical Imaging 2022: Physics of Medical Imaging*, 2022, vol. 12031: SPIE, pp. 1209-1215, doi: https://doi.org/10.1117/12.2610686.

[23] E. Roncali, M. A. Mosleh-Shirazi, and A. Badano, "Modelling the transport of optical photons in scintillation detectors for diagnostic and radiotherapy imaging," *Physics in Medicine & Biology,* vol. 62, no. 20, p. R207, 2017, doi: https://doi.org/10.1088/1361-6560/aa8b31.

[24] L. Bläckberg *et al.*, "Exploring light confinement in laser-processed LYSO: Ce for photon counting CT application," *Physics in Medicine & Biology,* vol. 64, no. 9, p. 095020, 2019, doi: https://doi.org/10.1088/1361-6560/ab1213.

[25] M. Persson, P. L. Rajbhandary, and N. J. Pelc, "A framework for performance characterization of energy-resolving photon-counting detectors," *Medical physics,* vol. 45, no. 11, pp. 4897-4915, 2018, doi: https://doi.org/10.1002/mp.13172.

[26] P. L. Rajbhandary, M. Persson, and N. J. Pelc, "Detective efficiency of photon counting detectors with spectral degradation and crosstalk," *Medical physics,* vol. 47, no. 1, pp. 27-36, 2020, doi: https://doi.org/10.1002/mp.13889.

[27] J. Tanguay, D. Richtsmeier, C. Dydula, J. A. Day, K. Iniewski, and M. Bazalova-Carter, "A detective quantum efficiency for spectroscopic X-ray imaging detectors," *Medical physics,* vol. 48, no. 11, pp. 6781-6799, 2021, doi: https://doi.org/10.1002/mp.15194.

[28] K. Taguchi, E. C. Frey, X. Wang, J. S. Iwanczyk, and W. C. Barber, "An analytical model of the effects of pulse pileup on the energy spectrum recorded by energy resolved photon counting x-ray detectors," *Medical physics,* vol. 37, no. 8, pp. 3957-3969, 2010, doi: https://doi.org/10.1118/1.3429056.

[29] K. Taguchi *et al.*, "Modeling the performance of a photon counting x-ray detector for CT: Energy response and pulse pileup effects," *Medical physics,* vol. 38, no. 2, pp. 1089-1102, 2011, doi: https://doi.org/10.1118/1.3539602.

[30] J. Cammin, J. Xu, W. C. Barber, J. S. Iwanczyk, N. E. Hartsough, and K. Taguchi, "A cascaded model of spectral distortions due to spectral response effects and pulse pileup effects in a photon-counting x-ray detector for CT," *Medical physics,* vol. 41, no. 4, p. 041905, 2014, doi: https://doi.org/10.1118/1.4866890.

[31] D. Leibold, S. van der Sar, M. Goorden, and D. Schaart, "Point spread function of photon-counting detectors under pile-up conditions: a proposed framework," in *Medical Imaging 2022: Physics of Medical Imaging*, 2022, vol. 12031: SPIE, pp. 1223-1230, doi: https://doi.org/10.1117/12.2612861.

6 General discussion and conclusion

6.1 Context of this work

X-ray imaging plays a major role in both the diagnosis and image-guided treatment of diseases. One of its key features is the high image acquisition speed, enabled by powerful X-ray tubes that are able to generate X-ray fluence rates exceeding 10^8 photons/s/mm^2 incident on the detector [1]. A measurement of the number of X-ray photons and their energy is therefore severely distorted by pulse pile-up and detector dead time effects, unless detectors with a very fast temporal response and sub-mm pixels (in order to distribute the incident fluence rate over multiple channels per mm^2) are used. In addition, the detectors must stably and reliably perform under these high-rate conditions, have reasonable energy resolution, efficiently absorb X-ray photons with energies up to 150 keV, and operate at room temperature. Since (spectral) photon-counting detectors (PCD) fulfilling these requirements have long been unavailable, medical X-ray imaging traditionally relies on energy-integrating detectors (EID). However, PCDs offer a number of advantages over EIDs, such as improvements in contrast-to-noise ratio for a given radiation dose and contrast agent load, and spectral X-ray imaging beyond the currently available dual-energy imaging techniques [2,3,4]. It is thus desirable that photon-counting X-ray imaging becomes widely available.

Presently, the general opinion in the field is that the above-mentioned requirements can only be met by direct-conversion detectors based on the semiconductors CdTe and $Cd_{1-x}Zn_xTe$ (CZT, x typically 0.1-0.2). In recent decades, the reliability and stability of these detectors under high-rate conditions has substantially improved. This has led to the release of several (prototype) photon-counting, diagnostic computed tomography (CT) systems capable of patient scanning by various vendors [5,6,7]. However, the cost-effectiveness of producing CdTe and CZT of the required quality may remain an issue [8,9], and the number of manufacturers is very limited. These circumstances may hamper the wide availability of medical X-ray photon-counting imaging systems in the coming years. Direct-conversion detectors based on silicon have been proposed as an alternative [10] and a prototype CT scanner has been built [11]. However, the density (2.3 g/cm^3) and atomic number (14) of Si are relatively low for medical X-ray imaging.

Indirect-conversion detectors based on scintillators may combine the high density and atomic number of CdTe and CZT with the cost-effectiveness of production of Si that is

needed for a widely available medical imaging system. The latter is supported by the fact that both the EIDs in currently available X-ray imaging systems as well as the PCDs in nuclear medicine imaging systems are predominantly based on scintillators. This thesis therefore focused on the question whether or not scintillation detectors, in particular with silicon photomultiplier (SiPM) readout, can offer the detector performance needed for X-ray photon-counting applications. The answer to this question is yes. However, it is not straightforward to build suitable pixelated detectors, so this last chapter mainly focuses on which challenges have to be overcome, and how to do that. Furthermore, it contains a general discussion of the results presented in Chap. 2, 3, and 4.

6.2 Achievable count rate capability and energy resolution

Chap. 2, 3, and 4 all dealt with the achievable count rate capability and energy resolution of SiPM-based scintillation detectors. Only single-pixel detectors (with a maximum pixel size of 1×1 mm^2) were studied in these chapters. This is not only convenient for initial investigations into a new detector concept, but also sufficient to get a good sense of the achievable count rate capability and energy resolution, which are very important performance metrics for X-ray photon-counting detectors.

In Chap. 2, a model was developed that calculates the expected pulse duration, which is, to a first approximation, inversely proportional to the count rate capability, and the energy resolution of any combination of scintillator and SiPM. Four fast and readily available scintillators with high density and atomic number were identified, namely $LaBr_3$:Ce ($LaBr_3$), $LuAlO_3$:Ce (LuAP), $Lu_{1.8}Y_{0.2}SiO_5$:Ce (LYSO), and $YAlO_3$:Ce (YAP), as well as an ultrafast SiPM. The expected pulse duration and energy resolution at 60 keV as a function of pixel size were calculated. Importantly, an SiPM-based LuAP detector was built, which was used for successful model validation experiments.

The model calculations showed that it is hard to outperform CdTe/CZT detectors highly optimized for photon-counting diagnostic CT systems with these four scintillators and this SiPM. Nevertheless, the $LaBr_3$ and LuAP detectors provide pulse durations in the order of 10^1 ns, which is in the same order of magnitude as the direct-conversion detectors, while the $LaBr_3$ and YAP detectors can yield energy resolutions at 60 keV that are in the same range as these of CdTe/CZT detectors, i.e., roughly between 10% and 20% full-width at half maximum (FWHM). In addition, the model calculations showed that the energy resolution is hardly degraded by SiPM saturation when the pixel size has to be reduced to the sub-mm level for rate capability reasons. This is due to the high dynamic range of the SiPMs used in this work.

6.2.1 Count rate capability

Measurements of actual count rate curves performed at an X-ray tube facility were presented in Chap. 4. The results confirm that the rate capability of the $LaBr_3$ detector

can come close to that of the high-end CdTe/CZT detectors, with maximum output count rates (OCR) per pixel being 80% of those of the direct-conversion detectors. This means that, in first-order approximation, the count rate capability per mm^2 of a $LaBr_3$ detector will be similar to that of a CdTe/CZT detector, if the pixel area of the former is 80% of the pixel area of the latter. The LYSO and YAP detectors indeed lag behind with maximum OCRs per pixel around 35% and 45% of those of the CdTe/CZT detectors, respectively. Based on these findings, $LaBr_3$ seems to be suitable for the most demanding applications in terms of incident fluence rate, such as diagnostic CT, whereas LYSO and YAP can be used for less demanding applications, such as cone-beam CT on the radiotherapy gantry. It was shown in Appendix A3.1 of Chap. 3 that the maximum fluence rate incident on the detector in the latter application may be two orders of magnitude lower than in diagnostic CT, i.e., in the order of 10^6 s^{-1} mm^2.

6.2.2 Energy resolution

The experimentally determined energy resolutions of the $LaBr_3$, LYSO, and YAP detectors presented in Chap. 3 and 4 were in general considerably worse than the modeled values from Chap. 2, in particular for the YAP detector. Only the $LaBr_3$ detector achieved an energy resolution around 20% FWHM at 60 keV, which is similar to that of at least one CdTe detector developed for a photon-counting diagnostic CT system [12]. There are a few possible reasons for the differences between model and experiments:

- In Chap. 2 (the model), the best achievable energy resolution based on pulse integrals was determined, whereas the pulse height was used as measure of energy in Chap. 3 and 4 (the experiments), after the raw pulse trains had been processed by a second-order low-pass filter with cut-off frequency f_c. This was done because it allowed for higher output count rates.

- The energy resolution was modelled as the quadratic sum of a component due to the statistics of optical photon detection (R_{stat}) and an intrinsic component (R_{intr}), which is ideally only determined by the non-proportionality of the scintillator. R_{stat} was modelled in detail, whereas values for R_{intr} were taken from literature (see Eqn. (2.13) and accompanying text). However, R_{intr} may also depend on the crystal dimensions in the case of crystals with a high aspect ratio, such as the 1.0×1.0×3.5 mm^3 $LaBr_3$ and 1.0×1.0×4.5 mm^3 YAP crystals used in the experiments. It typically degrades with increasing aspect ratio, as the fraction of optical photons that make it to the SiPM becomes a stronger function of the depth-of-interaction.

- The measurements of the light yield in Chap. 2 showed that the light yield of LuAP was lower than specified by the manufacturer of the crystals. The light yields of LYSO and YAP also turned out to be lower than the values given by the manufacturers, which were used for the model calculations. The resulting lower number of detected optical photons worsens the energy resolution.

- The scintillators were covered in compressed, reflective powder for the experiments. In the case of the hygroscopic $LaBr_3$ crystal, the detector was also surrounded by an air-tight epoxy sealing. It was discussed in Chap. 4 that counts due to photons that have first Compton scattered in these surrounding materials cause a broadening of the full-energy peak, thereby degrading the energy resolution.

Nevertheless, the model validation experiments with the LuAP detector in Chap. 2 were successful. This is for a few reasons: Firstly, the pulse integral was considered a measure of the energy associated with a count in these experiments, just as in the model. Secondly, the LuAP crystal was almost cube-shaped, so it had a low aspect ratio. Thirdly, the light yield of the crystal was measured, and the measured value was put into the model. Lastly, the light yield turned out to be rather low, while the proportionality was high, so R_{stat} dominated over R_{intr}, making the model calculations less dependent on a value for R_{intr} taken from literature.

LuAP detectors were not used in Chap. 3 and 4 though, because the characterization experiments needed for model validation not only showed that the light yield was worse than expected, but also that the decay time profile had a substantial slow component, which likely results in baseline shifts at high incident fluence rates. Hence, the raw signal from LuAP was not considered suitable for further studies.

6.2.3 Outperforming CdTe and CZT detectors?

The question remains whether or not scintillation detectors can outperform CdTe/CZT detectors developed and optimized for photon-counting diagnostic CT systems.

Regarding count rate capability, the decay time constant τ_d of the scintillators is currently the limiting factor. However, faster, although not necessarily readily available, scintillators exist. An interesting example reported in literature is $PrBr_3$:Ce ($PrBr_3$), which is similar to $LaBr_3$ in terms of density and effective atomic number, but twice as fast (τ_d = 8 ns versus τ_d = 16 ns) [13]. However, the light yield of $PrBr_3$ is three to four times as low as that of $LaBr_3$ (16-21 photons/keV versus (at least) 63 photons/keV). Hence, the number of detected scintillation photons per unit time in a $PrBr_3$ detector is one and a half to two times as small. It may therefore be needed to lower the cut-off frequency f_c of the second-order low-pass filter from 100 MHz, as used for the $LaBr_3$ detector, to 50 MHz, for example. The associated pulse elongation prohibits a factor two improvement in count rate capability compared to the $LaBr_3$ detector, despite the twice as fast scintillation decay. Nevertheless, it is still likely that the filtered pulses from a $PrBr_3$ detector are sufficiently fast to bridge the small gap between the rate capabilities of $LaBr_3$ and CdTe/CZT detectors.

Interestingly, a new type of SiPM with tip avalanche photodiodes was recently developed [14]. It has a recharge time constant τ_r of 4 ns, which is about twice as fast as that of the SiPMs used in this work, and an optical photon detection efficiency (PDE) around 60%, which is two to three times as high as that of the SiPMs used in this work.

As such, this new SiPM considerably reduces the level of pulse fluctuations. This may allow for $f_c \geq 100$ MHz for the $PrBr_3$ detector, and therefore for a rate capability that greatly exceeds that of CdTe/CZT detectors. However, lowering the optical crosstalk probability of these SiPM is desirable.

It should be noted that, if a scintillation detector provides higher rate capability per pixel than CdTe/CZT detectors, this does not necessarily mean that it is acceptable to use larger pixels in order to deal with a given incident fluence rate. This is because the improvement in spatial resolution offered by sub-mm pixels is considered one of the main advantages of photon-counting detectors by radiologists [15].

Regarding energy resolution, the two to three times as high PDE of the above-mentioned SiPMs with tip avalanche photodiodes in principle improves the R_{stat} of a scintillation detector by a factor $1/\sqrt{3}$ to $1/\sqrt{2}$. This brings the energy resolution of the $LaBr_3$ detector well within the range of energy resolutions reported for CdTe/CZT detectors optimized for photon-counting diagnostic CT systems, i.e., roughly between 10% and 20% FWHM at 60 keV [12,16]. However, the higher PDE will make it more likely that R_{stat} degrades due to SiPM saturation, in particular when the pixel size is reduced to the sub-mm level. On the other hand, the twice as low value of the recharge time constant of these new SiPMs helps to reduce saturation. The overall effect can be studied with the model presented in Chap. 2.

Despite the higher PDE, the low-rate energy resolution of a detector consisting of a $PrBr_3$ scintillator read out by the new SiPMs with tip avalanche photodiodes is likely somewhat worse than that of the $LaBr_3$ detector presented in this work, because of the much lower light yield of $PrBr_3$. However, one of the main findings of Chap. 3 is that pile-up already degrades spectral performance at relative low incident fluence rates, and that it may have a bigger influence on spectral performance than the low-rate FWHM energy resolution under clinically realistic conditions. The faster pulse of the $PrBr_3$ detector may thus be preferred over the better energy resolution of the $LaBr_3$ detector.

Besides $PrBr_3$, the currently investigated two-dimensional hybrid lead halide perovskite scintillators are also promising materials to increase the count rate capability of SiPM-based scintillation detectors beyond that of CdTe/CZT detectors and the way these materials are synthesized is cost-effective [17]. However, their density and effective atomic number are rather low compared to those of CdTe, CZT, $LaBr_3$ and $PrBr_3$. An example of such a material is benzylammonium lead bromide. This material was recently grown and characterized [18]. In that study, it was shown that this scintillator has a value of τ_d of only 4.2 ns and the model described in Chap. 2 of this thesis was applied to a detector consisting of this material and the SiPM with τ_r=7 ns. A value of the raw pulse duration t_{95} of 26 ns, which is considerably less than that of CZT (34 ns), was found. Interestingly, since $\tau_d < \tau_r$, the level of pulse fluctuations is so low that hardly any low-pass filtering, and therefore hardly any unwanted pulse elongation, is needed.

6.3 Towards pixel arrays

Pixel arrays were only investigated in Chap. 5 by means of Monte Carlo simulations. Because of the small pixel size of at most 1×1 mm^2 required for medical X-ray imaging applications, a characteristic or Compton-scattered X-ray escaping the pixel in which the primary X-ray had a photo-electric or Compton interaction is quite likely. This can substantially affect the counting and spectral detector performance. The zero-frequency detective quantum efficiency DQE(0) was evaluated as a measure of the counting performance, and the full-energy peak fraction under uniform detector irradiation $f_{\text{full-E}}$ as a measure of the spectral performance. This was done for YAP, CZT, $LaBr_3$, and Lu_2SiO_5 (LSO) detectors, which are ordered here from low to high (effective) atomic number and therefore from low to high energy characteristic X-rays. The YAP detector yielded the best DQE(0), even when it had smaller pixels than the other detectors. This is because energy deposited by the 15 keV characteristic X-rays of yttrium in other pixels than the one in which the primary X-ray interacted, did not lead to a count with the count detection threshold having been set to a commonly used value of 25 keV. Nevertheless, the CZT detector yielded the highest values of $f_{\text{full-E}}$. Interestingly, higher (effective) atomic number materials are generally preferred for other medical imaging modalities in which photons are counted, such as single-photon emission computed tomography (SPECT) and positron emission tomography (PET). However, the lower incident energies (≤140 keV) and smaller pixel sizes (≤1×1 mm^2) in medical X-ray imaging caused the LSO detector to perform worst here.

6.3.1 Dose-efficient optical insulation in finely pixelated detectors

More detector aspects than only the influence of secondary X-ray transport on detector performance have to be considered when moving on towards pixel arrays. For example, a method to confine the scintillation photons as well as possible to a single pixel must be selected. Traditionally, reflective material is inserted between two pixels to this end. For example, diagnostic CT scanners with energy-integrating detectors typically have a pixel pitch of 1 mm, i.e., 0.9×0.9 mm^2 pixels of scintillation material with a 0.1 mm thick TiO_2 reflector between adjacent pixels. However, this method requires that pixels of 1×1 mm^2 or smaller can be cut from bulk $LaBr_3$, L(Y)SO or YAP materials. Alternatively, the scintillation crystals may be grown inside a reflective matrix. However, the reflective material is insensitive to X-rays (dead area), so it reduces the geometric detection efficiency η_{geo} of the detector, and thereby the DQE and the dose efficiency. In order to maintain the same η_{geo} as an EID for a particular application, the reflector thickness must be reduced in accordance with the reduction in pixel size that is needed to achieve the necessary rate capability per mm^2. For example, if the pixel dimensions are reduced by a factor two, the reflector thickness must also be reduced by a factor two.

Finely pixelated arrays with thin reflectors have mainly been developed for L(Y)SO-based detectors so far, in the context of high-resolution, small-animal PET, and not yet for detectors based on the other scintillators discussed in this thesis. Examples from

literature include 0.43×0.43 mm^2 LSO pixels separated by 0.050 mm thick reflectors [19] and 0.22×0.22 mm^2 LSO pixels separated by 0.064 mm thick reflectors [20]. Using a scintillator that is not suitable for X-ray photon-counting applications, Canon has managed to produce a clinical CT system, equipped with a high-resolution EID in which both the pixel size and the reflector thickness have been reduced by a factor two compared to the traditional system [21].

CdTe/CZT detectors do not have dead area at all, which gives them an advantage in terms of DQE and dose efficiency. On the other hand, the DQE and dose efficiency of direct-conversion detectors is reduced due to charge sharing. It may therefore be interesting to investigate in future research what reflector thickness gives rise to the same DQE as a CdTe/CZT detector with charge sharing. To this end, it is important to include the generation and transport of electron-hole pairs (CdTe/CZT) and optical photons (scintillators) in the simulation set-up of Chap. 5. Various ways to do so were proposed in Sec. 5.4.

Ideally, pixel arrays with reflectors do not suffer from light sharing among pixels. However, they come with dead area and production challenges, as explained above. Alternatively, specific structures that give rise to some light sharing, but virtually no dead area, can be created in the scintillators. Two examples are:

- Columnar microstructure. The scintillator consists of densely packed, needle-like structures, which are called microcolumns. Total internal reflection at the surface of a microcolumn guides the scintillation light towards the light sensor. Energy-integrating, flat-panel detectors for medical X-ray imaging based on the CsI:Tl scintillator have such a microstructure, for example. It has been shown that $LaBr_3$ with a thickness of a few mm, as required for medical X-ray imaging, can also be grown in this way, with microcolumns of 15-20 μm in diameter [22]. The light output was rather high and uniform as a function of lateral position and depth-of-interaction, resulting in an energy resolution that was only a few percentage point worse than that of a standard $LaBr_3$ detector. However, the light spread is somewhat problematic for sub-mm pixels at the moment. Exposing a 1 mm thick microcolumnar $LaBr_3$ detector to a 50 μm wide line source of 122 keV photons (Co-57) yielded a line spread function with a FWHM of 659 μm. A FWHM of 138 μm was obtained with some form of cluster processing, but this comes at the cost of lower count rate capability.

- Laser-induced optical barriers (LIOB). A laser beam is used to locally modify the crystal structure. In this way, a region with a lower refractive index than the bulk material is created, which starts to act as an optical barrier, guiding the light towards the light sensor. For 1×1×2 mm^3 LYSO pixels, it was found that the light confinement to a single pixel is at most 80%, i.e. on average 80% of the *detected* scintillation photons are detected in the pixel in which the X-ray interaction took place [23]. The overall light collection efficiency (LCE) is only 50%, however. Confinement up to 90% is possible when LIOBs are

combined with laser ablation, but the LCE drops to just above 40%. In this scenario, the upper and lower part of the barrier are complete removed by the laser and filled with reflective material. The LIOB (and laser ablation) technique can also be applied to other materials than LYSO, including hygroscopic ones [24], but it is heavily material-dependent. In other words, it needs to be carefully optimized for each material.

These and other techniques that give rise to virtually no dead area are very interesting for X-ray photon-counting scintillation detectors, and should be further developed and investigated in future research. Since they lead to some light sharing among pixels, a DQE analysis of how the light sharing compares to the charge sharing in CdTe/CZT detectors is very valuable, for example. This again requires that the generation and transport of electron-hole pairs (CdTe/CZT) and optical photons (scintillators) is included in the simulation set-up of Chap. 5. Ways to do so were identified in Sec. 5.4.

6.3.2 Detector readout

Furthermore, an application specific integrated circuit (ASIC) must be developed for pulse processing, digitization and readout, before experiments with pixel arrays can be performed. In the experiments conducted for this thesis with single-pixel detectors, raw pulse trains from the detector were digitized by a digital oscilloscope, giving rise to 12 GB of data per second. These data were further processed offline. This is a feasible approach for single-pixel detectors, but very unpractical for pixel arrays.

6.4 Ultimate comparison of detectors

In all chapters of this thesis, various aspects of the counting and spectral performance of a scintillation detector were separately evaluated, and often compared to those of other scintillation detectors and CdTe/CZT detectors. However, an ultimate comparison of detectors may require a single figure-of-merit that combines the counting and spectral detector performance. To this end, the detective quantum efficiency, which was used to evaluate the counting performance in Chap. 5, can be extended to a spectral DQE [25]. However, a few difficulties arise when evaluating this spectral DQE in simulation:

- The spectral DQE requires a choice for the number of energy thresholds/bins, which is usually between two and eight, implemented in the detector. The higher the number of energy bins, the more important to include the generation and transport of electron-hole pairs in the case of CdTe/CZT detectors and optical photons in the case of scintillation detectors in the simulation to obtain accurate results (see Sec. 5.4). This is because these phenomena blur the spectral response functions, contributing to overlap between bins. It also means that a method to confine the scintillation photons as well as possible to a single pixel must be selected (see Sec. 6.3.1). Moreover, the optimal values of the thresholds may depend on the detection material.

- The spectral DQE is hard to interpret. Whereas the zero-frequency DQE can be plotted as a function of X-ray energy (see Sec. 5.3), the spectral DQE is a function of two energies. It can therefore be represented by a matrix. The diagonal elements of this matrix can be considered the dose efficiency at a particular X-ray energy for detecting a spectral change at that energy. The off-diagonal elements describe how the other energies in the spectrum positively or negatively contribute to detecting this spectral change. A complete description of detector performance also requires the non-zero frequencies. Consequently, the spectral DQE becomes a three-dimensional matrix, which is even harder to interpret. Only by defining a simplified imaging task, which assigns weights to the matrix elements, the three-dimensional matrix can be reduced to a single number, which allows to compare detectors.

- The spectral DQE can only be used in the limit of zero fluence rate, because it assumes a linear-shift invariant system. This assumption no longer holds in the presence of count losses due to pile-up and dead time effects. As such, a comparison of detectors based on the spectral DQE may not be valid under clinically realistic operating conditions.

The last issue can be addressed by time-resolved Monte Carlo simulations, which allow to include pile-up and dead time effects [26] [27]. However, it remains necessary to define a few simplified imaging tasks, so that, for example, Cramér-Rao lower bound analyses can be performed to compare detectors with each other [27]. Moreover, the first bullet point above also applies to this approach. It is worth noting that analytical models to calculate a spectrum under pile-up conditions exist, as well [28,29,30]. These may speed up the calculations, if they are suitable for this type of study.

Given the difficulties with the abovementioned methods, it seems more fruitful to start building pixel arrays with scintillators and SiPMs that appear promising based on preliminary studies such as those presented in this thesis, as soon as the issues mentioned in Sec. 6.3 have been addressed, than to find the optimal detector by means of a simulation model first. Small phantom imaging studies can already be done with relatively small pixel arrays, so that the detectors can be compared to each other by means of image quality metrics.

6.5 Conclusion

The goal of this thesis was to investigate if it is feasible to obtain sufficient detector performance for medical X-ray photon-counting applications with SiPM-based scintillation detectors, with an emphasis on count rate capability, energy resolution, and inter-pixel X-ray crosstalk.

The results of this research indicate that LYSO:Ce and YAP:Ce detectors do not approach the performance of CdTe/CZT detectors developed for photon-counting

diagnostic CT. Nevertheless, the performance of these scintillation detectors can be sufficient for other applications, e.g., cone-beam CT in radiotherapy (CBCT). YAP is the more promising of the two, due to higher count rate capability, potentially better energy resolution, and more promising inter-pixel X-ray crosstalk properties. Building a YAP detector with 1×1 mm^2 pixels for CBCT is a quick way to move forward with this detector concept.

The results also indicate that $LaBr_3$:Ce detectors approach the performance of CdTe/CZT detectors. They are thus useful for diagnostic CT, provided arrays of pixels with sizes ≤ 0.5×0.5 mm^2 can be built in a dose-efficient way. Laser-induced optical barriers, potentially combined with the laser ablation technique, are very promising to this end. These and other methods to do so should be further investigated.

Given the small gap between the count rate capabilities of $LaBr_3$ and CdTe/CZT detectors, faster, but not readily available scintillators, such as $PrBr_3$:Ce and lead halide perovskites, can outperform CdTe and CZT in terms of rate capability. Further development of these and other fast scintillators thus appears warranted.

References

[1] M. Persson *et al.*, "Upper limits of the photon fluence rate on CT detectors: Case study on a commercial scanner," *Medical physics,* vol. 43, no. 7, pp. 4398-4411, 2016, doi: https://doi.org/10.1118/1.4954008.

[2] T. Flohr, M. Petersilka, A. Henning, S. Ulzheimer, J. Ferda, and B. Schmidt, "Photon-counting CT review," *Physica Medica,* vol. 79, pp. 126-136, 2020, doi: https://doi.org/10.1016/j.ejmp.2020.10.030.

[3] M. Danielsson, M. Persson, and M. Sjölin, "Photon-counting x-ray detectors for CT," *Physics in Medicine & Biology,* vol. 66, no. 3, p. 03TR01, 2021, doi: https://doi.org/10.1088/1361-6560/abc5a5.

[4] A. Esquivel *et al.*, "Photon-Counting Detector CT: Key Points Radiologists Should Know," *Korean Journal of Radiology,* vol. 23, 2022, doi: https://doi.org/10.3348/kjr.2022.0377.

[5] K. Rajendran *et al.*, "First clinical photon-counting-detector CT system: Technical evaluation," *Radiology,* vol. 303, no. 1, p. 130, 2022, doi: https://doi.org/10.1148/radiol.212579.

[6] S. Si-Mohamed *et al.*, "Feasibility of lung imaging with a large field-of-view spectral photon-counting CT system," *Diagnostic and Interventional Imaging,* vol. 102, no. 5, pp. 305-312, 2021, doi: https://doi.org/10.1016/j.diii.2021.01.001.

[7] T. Fan *et al.*, "Preliminary performance evaluation of a prototype whole body photon counting CT using moderate detector pixel design," presented at the 2022 IEEE Nuclear Science Symposium and Medical Imaging Conference (NSS/MIC), 2022. [Online]. Available: https://www.eventclass.org/contxt_ieee2022/scientific/online-program/session?s=M-10#e381.

[8] U. N. Roy *et al.*, "Role of selenium addition to CdZnTe matrix for room-temperature radiation detector applications," *Scientific reports,* vol. 9, no. 1, pp. 1-7, 2019, doi: https://doi.org/10.1038/s41598-018-38188-w.

[9] U. N. Roy, G. S. Camarda, Y. Cui, R. Gul, G. Yang, and R. B. James, "Charge-transport properties of as-grown $Cd_{1-x}Zn_xTe_{1-y}Se_y$ by the traveling heater method," *AIP Advances,* vol. 8, no. 12, p. 125015, 2018, doi: https://doi.org/10.1063/1.5064373.

[10] H. Bornefalk and M. Danielsson, "Photon-counting spectral computed tomography using silicon strip detectors: a feasibility study," *Physics in Medicine & Biology,* vol. 55, no. 7, p. 1999, 2010, doi: https://doi.org/10.1088/0031-9155/55/7/014.

[11] J. da Silva *et al.*, "Resolution characterization of a silicon-based, photon-counting computed tomography prototype capable of patient scanning," *Journal of Medical Imaging,* vol. 6, no. 4, p. 043502, 2019, doi: https://doi.org/10.1117/1.JMI.6.4.043502.

[12] R. Steadman, C. Herrmann, O. Mülhens, and D. G. Maeding, "ChromAIX: Fast photon-counting ASIC for spectral computed tomography," *Nuclear Instruments and Methods in Physics Research Section A: Accelerators, Spectrometers, Detectors and Associated Equipment,* vol. 648, pp. S211-S215, 2011, doi: https://doi.org/10.1016/j.nima.2010.11.149.

[13] M. D. Birowosuto, P. Dorenbos, C. Van Eijk, K. Kramer, and H. Gudel, "$PrBr_3:Ce^{3+}$: A New Fast Lanthanide Trihalide Scintillator," *IEEE transactions on nuclear science,* vol. 53, no. 5, pp. 3028-3030, 2006, doi: https://doi.org/10.1109/TNS.2006.880969.

[14] E. Engelmann, W. Schmailzl, P. Iskra, F. Wiest, E. Popova, and S. Vinogradov, "Tip avalanche photodiode—A new generation silicon photomultiplier based on non-planar technology," *IEEE Sensors Journal,* vol. 21, no. 5, pp. 6024-6034, 2020, doi: https://doi.org/10.1109/JSEN.2020.3041556.

[15] C. H. McCollough, K. Rajendran, and S. Leng, "Standardization and Quantitative Imaging With Photon-Counting Detector CT," *Investigative Radiology,* p. 10.1097, 2023, doi: https://doi.org/10.1097/RLI.0000000000000948.

[16] R. Steadman, C. Herrmann, and A. Livne, "ChromAIX2: A large area, high count-rate energy-resolving photon counting ASIC for a spectral CT prototype," *Nuclear Instruments and Methods in Physics Research Section A: Accelerators, Spectrometers, Detectors and Associated Equipment,* vol. 862, pp. 18-24, 2017, doi: https://doi.org/10.1016/j.nima.2017.05.010.

[17] A. Xie *et al.*, "Library of two-dimensional hybrid lead halide perovskite scintillator crystals," *Chemistry of Materials,* vol. 32, no. 19, pp. 8530-8539, 2020, doi: https://doi.org/10.1021/acs.chemmater.0c02789.

[18] J. J. van Blaaderen *et al.*, "$(BZA)_2PbBr_4$: A potential scintillator for photon-counting computed tomography detectors," *Journal of Luminescence,* p. 120012, 2023, doi: https://doi.org/10.1016/j.jlumin.2023.120012.

[19] F. Godinez, K. Gong, J. Zhou, M. S. Judenhofer, A. J. Chaudhari, and R. D. Badawi, "Development of an ultra high resolution PET scanner for imaging rodent paws: PawPET," *IEEE transactions on radiation and plasma medical sciences,* vol. 2, no. 1, pp. 7-16, 2017, doi: https://doi.org/10.1109/TRPMS.2017.2765486.

[20] S. R. Cherry and J. Qi, "High resolution PET with 250 micrometer LSO detectors and adaptive zoom," Univerisity of California, Davis, CA, 2012. doi: https://doi.org/10.2172/1032741.

[21] Canon. "Aquilion Precision. Ultra-High Resolution CT. Precision in Every Detail." https://global.medical.canon/products/computed-tomography/aq_precision (accessed 18 September, 2022).

[22] H. B. Bhandari *et al.*, "Large-area crystalline microcolumnar $LaBr_3$:Ce for high-resolution gamma ray imaging," *IEEE Transactions on Nuclear Science,* vol. 60, no. 1, pp. 3-8, 2012, doi: https://doi.org/10.1109/TNS.2012.2213612.

[23] L. Bläckberg *et al.*, "Exploring light confinement in laser-processed LYSO: Ce for photon counting CT application," *Physics in Medicine & Biology,* vol. 64, no. 9, p. 095020, 2019, doi: https://doi.org/10.1088/1361-6560/ab1213.

[24] H. Sabet, L. Bläckberg, D. U. Ozsahin, A. Sitek, and G. El-Fakhri, "A sub-mm spatial resolution LYSO: Ce detector for small animal PET," in *2015 IEEE Nuclear Science Symposium and Medical Imaging Conference (NSS/MIC)*, 2015: IEEE, pp. 1-4, doi: https://doi.org/10.1109/NSSMIC.2015.7582201.

[25] M. Persson, P. L. Rajbhandary, and N. J. Pelc, "A framework for performance characterization of energy-resolving photon-counting detectors," *Medical physics,* vol. 45, no. 11, pp. 4897-4915, 2018, doi: https://doi.org/10.1002/mp.13172.

[26] D. Leibold, S. van der Sar, M. Goorden, and D. Schaart, "Point spread function of photon-counting detectors under pile-up conditions: a proposed framework," in *Medical Imaging 2022: Physics of Medical Imaging*, 2022, vol. 12031: SPIE, pp. 1223-1230, doi: https://doi.org/10.1117/12.2612861.

[27] K. Taguchi and J. S. Iwanczyk, "Assessment of multi-energy inter-pixel coincidence counters for photon-counting detectors at the presence of charge sharing and pulse pileup: A simulation study," *Medical physics,* vol. 48, no. 9, pp. 4909-4925, 2021, doi: https://doi.org/10.1002/mp.15112.

[28] K. Taguchi, E. C. Frey, X. Wang, J. S. Iwanczyk, and W. C. Barber, "An analytical model of the effects of pulse pileup on the energy spectrum recorded by energy resolved photon counting x-ray detectors," *Medical physics,* vol. 37, no. 8, pp. 3957-3969, 2010, doi: https://doi.org/10.1118/1.3429056.

[29] K. Taguchi *et al.*, "Modeling the performance of a photon counting x-ray detector for CT: Energy response and pulse pileup effects," *Medical physics,* vol. 38, no. 2, pp. 1089-1102, 2011, doi: https://doi.org/10.1118/1.3539602.

[30] J. Cammin, J. Xu, W. C. Barber, J. S. Iwanczyk, N. E. Hartsough, and K. Taguchi, "A cascaded model of spectral distortions due to spectral response effects and pulse pileup effects in a photon-counting x-ray detector for CT," *Medical physics,* vol. 41, no. 4, p. 041905, 2014, doi: https://doi.org/10.1118/1.4866890.

Acknowledgements

Although pursuing a PhD degree sometimes felt like a somewhat lonely journey to me, there were actually many great people around, who helped me on this trip and made it an enjoyable time. Many thanks to all of you! However, I would like to express my gratitude to some people in particular in this acknowledgements section.

First of all, I say thank you to Dennis, my promotor and supervisor. You offered me the opportunity to work for (more than) four years on an exciting and largely unexplored topic in my field of interest after I had finished my Master's thesis under your supervision. At the start, it was not easy to meet with you due to your full agenda and many travels, but this changed after the outbreak of the coronavirus, and I sometimes jokingly say that your increased availability for meetings was the only positive side effect of the pandemic. Meetings with you were always good, and I think I never left one feeling bad. Your chatting about non-work related topics kept me smiling, your optimism kept me motivated, and your creative ideas kept me going. Moreover, I learned a lot from you regarding concise writing without leaving out important parts of a story. I also offer my thanks to Pieter, my other promotor, and Marlies, my copromotor. Whereas Dennis may have a tendency to diverge, you kept an eye on the time planning and the end goal. It was great to work with three experts and nice people!

I would like to thank Stefan for his involvement in the project, too. Your leaving Delft and moving to Broadcom paved the way for this research. I appreciate your insights from an industry point of view and your vast knowledge of silicon photomultipliers.

There are more people that contributed to the project. I would like to show appreciation to the lab technicians Jan, Johan and Martijn, and to the technical designers of the Dienst Elektronische and Mechanische Ontwikkeling (DEMO), in particular Hugo, Martin and René. Your hands-on experience in the labs and your creative solutions to technical problems are indispensable for a clumsy physicist like me. Rob, despite the fact that we hardly worked together, I would like to thank you for the coffee breaks we had together with Jan! Next, I thank all the people of the Stralingsbeschermingsdienst (SBD), among whom Bouke, Henk, and Marlies. Being able to work with intense sources of ionizing radiation was crucial to the project, and you greatly supported me in working with a 10 GBq americium-241 source and a 4.2 kW X-ray tube. I would like to mention Anouk here, as well. Your ever so quick and excellent support when it comes to everything that is not related to science is very much appreciated!

I now move on to my fellow PhD students and the PostDocs that I worked with. First of all, I thank Eelco. You were a great daily supervisor during my Master's thesis project,

made me enthusiastic about scientific research, and encouraged me to pursue a PhD degree. Jeremy, your rants about academia, on the other hand, may have lowered my enthusiasm for doing science, but the Australian idiom that I learned from you still makes me laugh. “Hey, how are you doing? Well, same sh*t, different day” remains my favorite, and is a pretty accurate description of daily life as a PhD candidate at times. David, you are a very helpful guy. Many thanks for your assistance when I was working in the glovebox, for your incredibly nice cover design, and for the times you cheered me up when I was a bit down. The conference in San Diego and our subsequent road trip through California are definitely among the best events during my time as a PhD student. If you ever wonder about my future plans, going there again is definitely on my bucket list! Jack, your arrival in Delft, supposedly from space, was a bit unexpected to both David and me. I remember how we quickly cleaned your desk, and how I caught you swiping left and right in the Tinder app on your very first day in our office. It was fun to work with you! Also thanks to Beien, Casper, Celebrity, Huanhuan, Jasper, Justin, Max, Minh, Rogier, Yuan, and to any PhD student I have unintentionally forgotten to mention here, for the nice chats during work time, the coffee and lunch breaks, and the Friday afternoon beers. I also say thank you to the Master students that I worked with. Anne-Maaike and Orestis, it was a nice learning experience for both you and me, and I enjoyed how we could also get along a bit outside office hours.

I am also grateful to my new colleagues at the Nuclear Research and consultancy Group (NRG). You are all nice persons, who have made me feel welcome and have often shown interest in the progress of my thesis. It is great that (some of) you have come to Delft to celebrate this PhD degree with me!

Fortunately, there is also life outside work, even for PhD students. I am lucky to have some good friends that I would like to thank here. First of all, Marco, my friend since the first day of primary school. It is incredible how long our friendship lasts! Talking with you about our favorite football club Feyenoord and the Dutch national team is a great distraction from work. We played football so often when we were younger, and have watched so many matches over the years. I hope there are many more to come!

Sander and Tom, we have known each other since the first day of secondary school. Our Latin classes inspired us to refer to ourselves as the Triumviratus Magnificus. Although history shows that the members of a triumvirate do not always live in harmony with each other, we have proven differently! Our holidays together were amazing and a welcome break from work. Many thanks! During my PhD defense, both of you serve as paranymphs. We have long been looking forward to dressing up in a white tie dress suit, decorated with cufflinks that show the coat of arms of our Triumviratus. Let’s enjoy this special day together!

I have known Ahmad, Bart, and Mathijs since my first day at TU Delft. We formed a mentor group, which consisted of about eight people at the start of our physics program. A few guys left, one even after one day, but we became good friends! I really enjoyed the many dinners and drinks that we had after a long day of studying or working.

Cycling became our “shared” passion, and we climbed so many famous hills and mountain passes together. In the words of the Live Slow Ride Fast podcast, I thank you for “life on and especially off the bike!”

Besides cycling, I like spending my free time on the tennis court and on the dance floor. Thanks to everyone that made me forget research for a while during these activities!

Finally, I say thank you to my family, and to some members in particular in Dutch. Allereerst mijn oma. Ondanks dat u natuurlijk niet begreep wat ik allemaal deed aan de TU Delft, toonde u wel altijd belangstelling en vroeg hoe het ging. Ik ben heel blij dat u het afronden van mijn promotieonderzoek en het behalen van de bijbehorende titel tijdens een bijzondere ceremonie mag meemaken! Wim, ook jou wil ik bedanken voor je aanmoedigingen en je interesse in mijn onderzoek. Onze bezoekjes aan De Kuip en Thialf waren een fijne onderbreking van het werk! Natuurlijk ben ik ook mijn zus Lisette en haar vriend Guido erg dankbaar. Niet alleen voor alle steun die jullie mij gegeven hebben, maar ook voor alle keren dat jullie mij gevraagd hebben om samen iets leuks te gaan doen! Tot slot wil ik mijn ouders enorm bedanken! Jullie hebben de afgelopen jaren altijd voor mij klaargestaan, en het is ontzettend fijn om te weten dat ik altijd bij jullie terecht kan. Jullie steun is onmisbaar geweest voor mij. Laten we samen van het behalen van deze doctorstitel genieten!

Stefan van der Sar
Oktober 2023

About the author

Stefan Jens van der Sar was born on 4 May 1994 in Rotterdam, the Netherlands, and grew up in the north-eastern neighborhoods of the city, where he received primary education at the ds. J.J. Buskesschool from 1998 until 2006. He then moved on to the Marnix Gymnasium, a school for pre-university education with additional courses on the languages and cultures of classical antiquity, located in the city center. In 2012, Stefan joined the Delft University of Technology (TUD), where he studied Applied Physics, and obtained a BSc degree in 2015, and an MSc degree in 2018. Early on, Stefan developed an interest in the medical applications of physics. As such, he followed the minor program Medicine for Engineering Students at the Erasmus Medical Center, the academic hospital in Rotterdam, and did an internship at the research and development department of Abbott Medical Optics in Groningen, where he worked on adaptive optics for intra-ocular lens development. Moreover, his MSc thesis was about range verification in proton radiation therapy by prompt-gamma detection. That research was conducted under supervision of dr. ir. Dennis R. Schaart, head of the Medical Physics and Technology (MPT) section of TUD, in the context of the newly-built Holland Proton Therapy Center in Delft. After graduation, Stefan decided to stay with the Delft University of Technology to perform doctoral research on X-ray photon-counting scintillation detectors for medical imaging applications, again under supervision of dr. ir. Dennis R. Schaart. The results of that research are presented in this PhD thesis.

List of publications

Written publications, including thesis chapters based on these publications in brackets:

S. J. van der Sar and D. R. Schaart, "Silicon Photomultiplier-Based Scintillation Detectors for Photon-Counting X-Ray Imaging," in *Radiation Detection Systems*. Boca Raton, FL, USA: CRC Press, 2021, pp. 289-312, doi: https://doi.org/10.1201/9781003147633-10 (Chapter 1 and Appendix A2.2).

S. J. van der Sar, S. E. Brunner, and D. R. Schaart, "Silicon photomultiplier-based scintillation detectors for photon-counting CT: A feasibility study," *Medical Physics,* vol. 48, no. 10, pp. 6324-6338, 2021, doi: https://doi.org/10.1002/mp.14886 (Chapter 2 and Appendix A2.1).

S. J. van der Sar, S. E. Brunner, and D. R. Schaart, "X-ray photon-counting using silicon photomultiplier-based scintillation detectors at high X-ray tube currents," in *SPIE Medical Imaging 2022: Physics of Medical Imaging*, 2022, vol. 12031: SPIE, pp. 118-124, doi: https://doi.org/10.1117/12.2611365 (Chapter 4).

S. J. van der Sar, D. Leibold, S. E. Brunner, and D. R. Schaart, "$LaBr_3$:Ce and silicon photomultipliers: Towards the optimal scintillating photon-counting detector," in *7th International Conference on Image Formation in X-Ray Computed Tomography*, 2022, vol. 12304: SPIE, pp. 55-60, doi: https://doi.org/10.1117/12.2646519 (Chapter 4).

Other written publications:

W. Shi, M. Theelen, A. Illiberti, S.J. van der Sar, M. Butterling, H. Schut, M. Zeman, E.H. Brück, S.W.H. Eijt, "Evolution and role of vacancy clusters at grain boundaries of ZnO:Al during accelerated degradation of Cu(In,Ga)Se_2 solar cells revealed by positron annihilation," *Physical Review Materials,* vol. 2, no. 10, pp. 1-18, 2018, doi: https://doi.org/10.1103/PhysRevMaterials.2.105403.

D. Leibold, S.J. van der Sar, M.C. Goorden, and D.R. Schaart, "Point spread function of photon-counting detectors under pile-up conditions: A proposed framework," in *SPIE Medical Imaging 2022: Physics of Medical Imaging*, 2022, vol. 12031: SPIE, pp. 1223-1230, doi: https://doi.org/10.1117/12.2612861.

J.J. van Blaaderen, S.J. van der Sar, D. Onggo, M.A.K. Sheikh, D.R. Schaart, M. Birowosuto, and P. Dorenbos, "$(BZA)_2PbBr_4$: A potential scintillator for photon-counting computed tomography detectors," *Journal of Luminescence,* vol. 263, 120012, 2023, doi: https://doi.org/10.1016/j.jlumin.2023.120012.

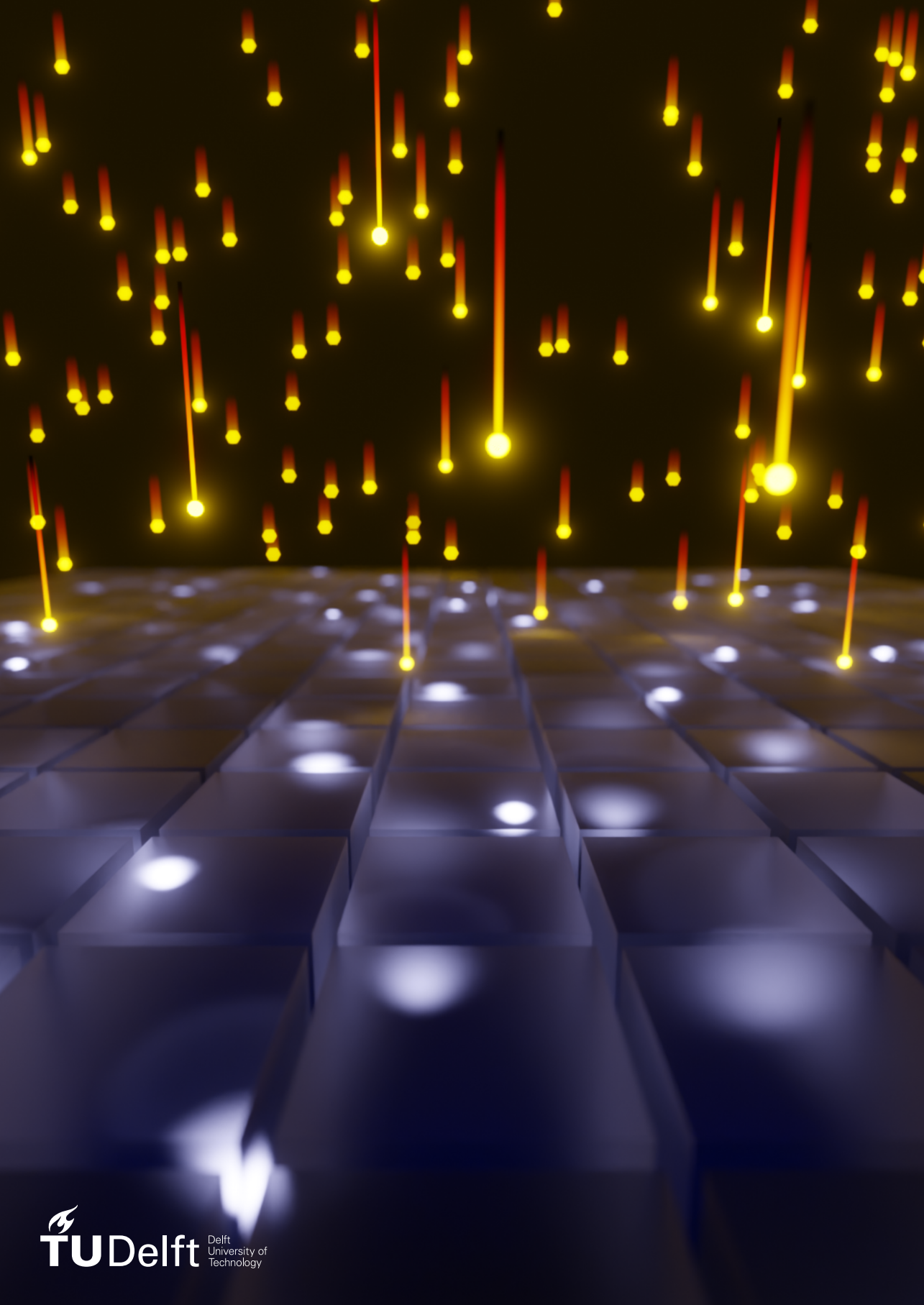
TU Delft
Delft
University of
Technology